FERMILAB-FN-0825-E

June 2, 2008

The FP420 R&D Project: Higgs and New Physics with forward protons at the LHC

M. G. Albrow[1], R. B. Appleby[2], M. Arneodo[3], G. Atoian[4], R. Barlow[2], W. Beaumont[5], L. Bonnet[6], A. Brandt[7], P. Bussey[8], C. Buttar[8], J. M. Butterworth[9], M. Carter[10], B.E. Cox[2,], D. Dattola[11], C. Da Via[12], J. de Favereau[6], D. d'Enterria[13], P. De Remigis[11], A. De Roeck[13,5,*], E.A. De Wolf[5], P. Duarte[7,†], J. R. Ellis[13], B. Florins[6], J. R. Forshaw[12], J. Freestone[12], K. Goulianos[14], J. Gronberg[15], M. Grothe[16], J. F. Gunion[17], J. Hasi[12], S. Heinemeyer[18], J. J. Hollar[15], S. Houston[8], V. Issakov[4], R. M. Jones[2], M. Kelly[12], C. Kenney[19], V.A. Khoze[20], S. Kolya[12], N. Konstantinidis[9], H. Kowalski[21], F. Lanni[22], H.E. Larsen[23], S.-L. Liu[24], A. Lyapine[9], F.K. Loebinger[12], R. Marshall[12], A. D. Martin[20], J. Monk[9], I. Nasteva[12], P. Nemegeer[6], M. M. Obertino[3], R. Orava[25], V. O'Shea[8], A. Pal[7], S. Parker[19], J. Pater[12], A.-L. Perrot[26], T. Pierzchala[6], A. D. Pilkington[12], J. Pinfold[24], K. Piotrzkowski[6], W. Plano[12], A. Poblaguev[4], V. Popov[27], K. M. Potter[2], V. Radeka[22], S. Rescia[22], F. Roncarolo[2], A. Rostovtsev[27], X. Rouby[6], M. Ruspa[3], M.G. Ryskin[20], A. Santoro[28], N. Schul[6], G. Sellers[2], A. Solano[23], S. Spivey[7], W.J. Stirling[20], D. Swoboda[26], M. Tasevsky[29], R. Thompson[12], T. Tsang[22], P. Van Mechelen[5], A. Vilela Pereira[23], S.J. Watts[12], M. R. M. Warren[9], G. Weiglein[20], T. Wengler[12], S.N. White[22], B. Winter[10], Y. Yao[24], D. Zaborov[27], A. Zampieri[11], M. Zeller[4], A. Zhokin[5,27]*

FP420 R&D Collaboration

[1]Fermilab, [2]University of Manchester and the Cockcroft Institute, [3]Università del Piemonte Orientale, Novara, and INFN, Torino, [4]Yale University, [5]Universiteit Antwerpen, [6]Université Catholique de Louvain, [7]University of Texas at Arlington, [8]University of Glasgow, [9]University College London (UCL), [10]Mullard Space Science Laboratory (UCL), [11]INFN Torino, [12]University of Manchester, [13]CERN, PH Department, [14]Rockefeller University, NY, [15]Lawrence Livermore National Laboratory (LLNL), [16]University of Wisconsin, Madison, [17]UC Davis, [18]IFCA (CSIC-UC, Santander), [19]Molecular Biology Consortium, Stanford University, [20]Institute for Particle Physics Phenomenology, Durham, [21]DESY, [22]Brookhaven National Lab (BNL), [23]Università di Torino and INFN, Torino, [24]University of Alberta, [25]Helsinki Institute of Physics, [26]CERN, TS/LEA, [27]ITEP Moscow, [28]Universidade do Estado do Rio De Janeiro (UERJ), [29]Institute of Physics, Prague

---

[*] Contact persons: Brian.Cox@manchester.ac.uk, Albert.de.Roeck@cern.ch

[†] Now at Rice University

Abstract

We present the FP420 R&D project, which has been studying the key aspects of the development and installation of a silicon tracker and fast-timing detectors in the LHC tunnel at 420 m from the interaction points of the ATLAS and CMS experiments. These detectors would measure precisely very forward protons in conjunction with the corresponding central detectors as a means to study Standard Model (SM) physics, and to search for and characterise New Physics signals. This report includes a detailed description of the physics case for the detector and, in particular, for the measurement of Central Exclusive Production, $pp \to p + \phi + p$, in which the outgoing protons remain intact and the central system ϕ may be a single particle such as a SM or MSSM Higgs boson. Other physics topics discussed are $\gamma\gamma$ and γp interactions, and diffractive processes. The report includes a detailed study of the trigger strategy, acceptance, reconstruction efficiencies, and expected yields for a particular $pp \to pHp$ measurement with Higgs boson decay in the $b\bar{b}$ mode. The document also describes the detector acceptance as given by the LHC beam optics between the interaction points and the FP420 location, the machine backgrounds, the new proposed connection cryostat and the moving ("Hamburg") beam-pipe at 420 m, and the radio-frequency impact of the design on the LHC. The last part of the document is devoted to a description of the 3D silicon sensors and associated tracking performances, the design of two fast-timing detectors capable of accurate vertex reconstruction for background rejection at high-luminosities, and the detector alignment and calibration strategy.

Contents

1 Introduction . . . 6
1.1 Executive summary . . . 6
1.2 Outline . . . 7
1.3 Integration of 420 m detectors into ATLAS and CMS forward physics programs . . . 8
2 The Physics Case for Forward Proton Tagging at the LHC . . . 9
2.1 Introduction . . . 9
2.2 The theoretical predictions . . . 11
2.3 Standard Model Higgs boson . . . 13
2.4 h,H in the MSSM . . . 14
2.5 Observation of Higgs bosons in the NMSSM . . . 18
2.6 Invisible Higgs boson decay modes . . . 20
2.7 Conclusion of the studies of the CEP of h,H . . . 21
2.8 Photon-photon and photon-proton physics . . . 22
2.9 Diffractive physics . . . 34
2.10 Physics potential of p_T measurements in FP420 . . . 38
2.11 Other physics topics . . . 39
3 Simulated measurement of $h \to b\bar{b}$ in the MSSM . . . 41
3.1 Trigger strategy for $h \to b\bar{b}$ . . . 43
3.2 Experimental cuts on the final state . . . 44
3.3 Results and significances . . . 46
3.4 Inclusion of forward detectors at 220 m . . . 48
3.5 Comparison of the $h,H \to b\bar{b}$ analyses . . . 50
3.6 Recent improvements in background estimation . . . 51
4 LHC Optics, acceptance, and resolution . . . 53
4.1 Introduction . . . 53
4.2 Detector acceptance . . . 54
4.3 Mass resolution . . . 58
4.4 Optics summary . . . 61
5 Machine Induced Backgrounds . . . 62
5.1 Introduction . . . 62
5.2 Near beam-gas background . . . 62
5.3 Beam halo . . . 63

5.4 Halo from distant beam-gas interactions . . . 69
5.5 Secondary interactions . . . 70
5.6 Machine background summary . . . 75
6 A new connection cryostat at 420 m . . . 77
6.1 Cryostat summary . . . 80
7 Hamburg beam-pipe . . . 82
7.1 Introduction . . . 82
7.2 FP420 moving pipe design . . . 82
7.3 Pocket Design and Tests . . . 83
7.4 Test beam prototype . . . 87
7.5 Motorization and detector system positioning . . . 87
7.6 System operation and safeguards . . . 90
7.7 Hamburg pipe summary and outlook . . . 91
8 RF impact of Hamburg pipe on LHC . . . 93
8.1 Motivation and introduction . . . 93
8.2 Longitudinal impedance . . . 94
8.3 Transverse impedance and beam instability . . . 98
8.4 Coupling with detectors . . . 99
8.5 RF summary . . . 99
9 Silicon Tracking Detectors . . . 100
9.1 Introduction . . . 100
9.2 3D silicon detector development . . . 101
9.3 Tracking detector mechanical support system . . . 109
9.4 High-voltage and low-voltage power supplies . . . 121
9.5 Readout and infrastructure at the host experiment . . . 132
9.6 Thermal Design . . . 134
9.7 Performance of the tracking system . . . 140
10 Fast Timing Detectors . . . 146
10.1 Overlap background and kinematic constraints . . . 146
10.2 Timing . . . 146
10.3 Timing detectors . . . 148
10.4 Detector simulations . . . 150
10.5 Performance in test-beam measurements . . . 150

10.6 Electronics and data acquisition 154
10.7 Reference time system 155
10.8 Central detector timing 156
10.9 Timing summary and future plans 157
11 Alignment and calibration 159
11.1 Alignment requirements 159
11.2 Beam and proton transfer calculations 162
11.3 Machine alignment 163
11.4 Mass scale and resolution measurement with physics processes 163
11.5 Alignment summary 168
12 Near detector infrastructure and detector services 169
13 Conclusions 172
14 Costing 175

1 Introduction

1.1 Executive summary

Although forward proton detectors have been used to study Standard Model (SM) physics for a couple of decades, the benefits of using proton detectors to search for New Physics at the LHC have only been fully appreciated within the last few years [1, 2, 3, 4, 5, 6]. By detecting both outgoing protons that have lost less than 2% of their longitudinal momentum [7], in conjunction with a measurement of the associated centrally produced system using the current ATLAS and/or CMS detectors, a rich programme of studies in QCD, electroweak, Higgs and Beyond the Standard Model physics becomes accessible, with the potential to make unique measurements at the LHC. A prime process of interest is Central Exclusive Production (CEP), $pp \rightarrow p + \phi + p$, in which the outgoing protons remain intact and the central system ϕ may be a single particle such as a Higgs boson. In order to detect both outgoing protons in the range of momentum loss appropriate for central systems in the ~ 100 GeV/c^2 mass range during nominal high-luminosity running, proton tagging detectors must be installed close to the outgoing beams in the high-dispersion region 420 m from the interaction points on each side of the ATLAS and CMS experiments. The FP420 R&D project is a collaboration including members from ATLAS, CMS, TOTEM and the accelerator physics community, with support from theorists, aimed at assessing the feasibility of installing such detectors.

The proposed FP420 detector system is a magnetic spectrometer. The LHC magnets between the interaction points and the 420 m regions bend protons that have lost a small fraction of their initial momentum out of the beam envelope. The FP420 detector consists of a silicon tracking system that can be moved transversely and measures the spatial position of these protons relative to the LHC beam line and their arrival times at several points in a 12 m region around 420 m. The proposed instrumentation of the 420 m region includes the replacement of the existing 14 m long connection cryostat with a warm beam-pipe section and a cryogenic bypass. To this purpose, a new connection cryostat has been designed, based on a modified arc termination module, so as to minimise the impact on the machine. The FP420 detector must be moveable because it should be parked at a large distance from the beams during injection and luminosity tuning, but must operate at distances between 4 mm and 7 mm from the beam centre during data taking, depending on the beam conditions. A measurement of the displacement and angle of the outgoing protons relative to the beam allows the momentum loss and transverse momentum of the scattered protons to be reconstructed. This in turn allows the mass of the centrally produced system ϕ to be reconstructed by the missing mass method [1] with a resolution (σ) between 2 GeV/c^2 and 3 GeV/c^2 *per event* irrespective of the decay products of the central system.

The detector position relative to the beam can be measured both by employing beam position monitors and by using a high-rate physics process which produces protons of a known momentum loss (from a central detector measurement of the central system) in the FP420 acceptance range. The second method has the advantage that the magnetic field between the central detectors and FP420 does not have to be precisely known *a priori*.

The cross sections for CEP of the SM Higgs boson and other new physics scenarios are expected to be small, on the femtobarn scale. FP420 must therefore be designed to operate up to the highest LHC instantaneous luminosities of $10^{34}\mathrm{cm}^{-2}\mathrm{s}^{-1}$, where there will be on average 35 overlap interactions per bunch crossing (assuming σ_{tot} = 110 mb). These overlap events can result in a large fake background, consisting of a central system from one interaction and protons from other interactions in the same bunch crossing. Fortunately, there are many kinematic and topological constraints which offer a large factor of background rejection. In addition, a measurement of the difference in the arrival times of the two protons at FP420 in the 10 picosecond range allows for matching of the detected protons with a central vertex within $\sim$2 mm, which will enable the rejection of most of the residual overlap background, reducing it to a manageable level.

Studies presented in this document show that it is possible to install detectors in the 420 m region with no impact on the operation or luminosity of the LHC (Section 9). These detectors can be calibrated to the accuracy required to measure the mass of the centrally produced system to between 2 and 3 GeV/c^2. This would allow an observation of new particles in the $60-180$ GeV/c^2 mass range in certain physics scenarios during 3 years of LHC running at instantaneous luminosities of 2×10^{33} cm^{-2} s^{-1}, and in many more scenarios at instantaneous luminosities of up to 10^{34} cm^{-2} s^{-1}. Events can be triggered using the central detectors alone at Level 1, using information from the 420 m detectors at higher trigger levels to reduce the event rate. Observation of new particle production in the CEP channel would allow a direct measurement of the quantum numbers of the particle and an accurate determination of the mass, irrespective of the decay channel of the particle. In some scenarios, these detectors may be the primary means of discovering new particles at the LHC, with unique ability to measure their quantum numbers. There is also an extensive, high-rate $\gamma\gamma$ and γp baseline physics program.

We therefore conclude that the addition of such detectors will, for a relatively small cost, enhance the discovery and physics potential of the ATLAS and CMS experiments.

1.2 Outline

The outline of this document is as follows. In Section 2 we provide a brief overview of the physics case for FP420. In Section 3 we describe in detail a physics and detector simulation of a particular scenario which may be observable if 420 m detectors are installed. The acceptance and mass resolutions used in this analysis are presented in Section 4. In Section 5 we describe the machine-induced backgrounds at 420 m such as beam-halo and beam-gas backgrounds. We then turn to the hardware design of FP420. Section 6 describes the new 420 m connection cryostat which will allow moving near-beam detectors with no effects on LHC operations. The design of the beam pipe in the FP420 region and the movement mechanism are described in Section 7, and the studies of the radio-frequency impact of the design on the LHC are described in Section 8. Section 9 describes the design of the FP420 3D silicon sensors, detectors and detector housings and off-detector services such as cabling and power supplies. Section 10 describes two complementary fast timing detector designs, both of which are likely to be used at FP420. Section 11 describes the alignment and calibration strategy, using both physics and beam position monitor techniques. We present our conclusions and future plans in Section 13.

1.3 Integration of 420 m detectors into ATLAS and CMS forward physics programs

This report focuses primarily on the design of 420 m proton tagging detectors. CMS will have proton taggers installed at 220 m around its IP at startup, provided by the TOTEM experiment and for which common data taking with CMS is planned [8]. ATLAS also has an approved forward physics experiment, ALFA, with proton taggers at 240m designed to measure elastic scattering in special optics runs [9].

There are ideas to upgrade the currently approved TOTEM detectors and a proposal to install FP420-like detectors at 220 m around ATLAS [10]. Adding detectors at 220 m capable of operating at high luminosity increases the acceptance of FP420 for central masses of $\sim$120 GeV/c^2 and upwards, depending on the interaction point[1] and the distance of approach of both the 220 m and 420 m detectors to the beam (see chapter 4). Throughout this document we present results for 420 m detectors alone and where appropriate for a combined 220 m + 420 m system. It is envisaged that FP420 collaboration members will become parts of the already existing ATLAS and CMS forward physics groups, and will join with them to propose forward physics upgrade programmes that will be developed separately by ATLAS and CMS, incorporating the findings of this report.

---

[1] For 220 m detectors, the acceptance is different around IP1 (ATLAS) and IP5 (CMS).

2 The Physics Case for Forward Proton Tagging at the LHC

2.1 Introduction

A forward proton tagging capability can enhance the ability of the ATLAS and CMS detectors to carry out the primary physics program of the LHC. This includes measurement of the mass and quantum numbers of the Higgs boson, should it be discovered via traditional searches, and augmenting the discovery reach if nature favours certain plausible beyond the Standard Model scenarios, such as its minimal supersymmetric extension (MSSM). In this context, the central exclusive production (CEP) of new particles offers unique possibilities, although the rich photon-photon and photon-proton physics program also delivers promising search channels for new physics. These channels are described in Section 2.8.

By central exclusive production we refer to the process $pp \to p + \phi + p$, where the '+' signs denote the absence of hadronic activity (that is, the presence of a rapidity gap) between the outgoing protons and the decay products of the central system ϕ. The final state therefore consists *solely* of the two outgoing protons, which we intend to detect in FP420, and the decay products of the central system which will be detected in the ATLAS or CMS detectors. We note that gaps will not typically be part of the experimental signature due to the presence of minimum bias pile-up events, which fill in the gap but do not affect our ability to detect the outgoing protons. Of particular interest is the production of Higgs bosons, but there is also a rich and more exotic physics menu that includes the production of many kinds of supersymmetric particles, other exotica, and indeed any new object which has 0^{++} (or 2^{++}) quantum numbers and couples strongly to gluons [2, 11] or to photons [12]. The CEP process is illustrated for Higgs boson production in Fig. 1. The Higgs boson is produced as usual through gluon-gluon fusion, while another colour-cancelling gluon is exchanged, and no other particles are produced.

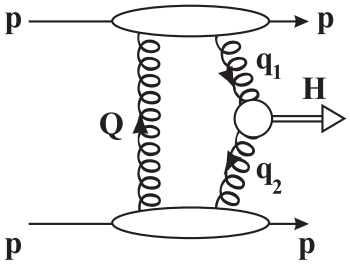

Fig. 1: Central Exclusive Production (CEP): $pp \to p + H + p$.

There are three important reasons why CEP is especially attractive for studies of new heavy objects. Firstly, if the outgoing protons remain intact and scatter through small angles then, to a very good approximation, the primary active di-gluon system obeys a $J_z = 0$, C-even, P-even, selection rule [13]. Here J_z is the projection of the total angular momentum along the proton beam axis. This selection rule readily permits a clean determination of the quantum numbers of any new resonance, which is predominantly 0^{++} in CEP. Secondly, because the process is exclusive, the energy loss of the outgoing protons is directly related to the invariant mass of the central system, allowing an excellent mass measurement irrespective of the decay mode of the central system. Even final states containing jets and/or one or more neutrinos are measured with $\sigma_M \sim 2$ GeV/c^2. Thirdly, in many topical cases and in particular for Higgs boson production, a signal-to-background ratio of order 1 or better is achievable [14, 15, 16, 17, 18]. This ratio becomes significantly larger for Higgs bosons in certain regions of MSSM parameter space [15, 19, 20].

There is also a broad, high-rate QCD and electro-weak physics program; by tagging both of the outgoing protons, the LHC is effectively turned into a gluon-gluon, photon-proton and photon-photon collider [6, 21]. In the QCD sector, detailed studies of diffractive scattering, skewed, unintegrated gluon densities and the rapidity gap survival probability [2, 22, 23, 24] can be carried out. In addition, CEP would provide a source of practically pure gluon jets, turning the LHC into a 'gluon factory' [13] and providing a unique laboratory in which to study the detailed properties of gluon jets, especially in comparison with quark jets. Forward proton tagging also provides unique capabilities to study photon-photon and photon-proton interactions at centre-of-mass energies never reached before. Anomalous top production, anomalous gauge boson couplings, exclusive dilepton production, or quarkonia photoproduction, to name a few, can be studied in the clean environment of photon-induced collisions.

In what follows we will give a brief overview of the theoretical predictions including a survey of the uncertainties in the expected cross sections. We will then review the possibilities of observing Higgs bosons in the Standard Model, MSSM and NMSSM for W, τ and b-quark decay channels. A major potential contribution of FP420 to the LHC program is the possibility to exploit the $b\bar{b}$ decay channel of the Higgs particle, which is not available to standard Higgs analyses due to overwhelming backgrounds. The combination of the suppression of the $b\bar{b}$ background, due to the $J_z = 0$ selection rule, and the superior mass resolution of the FP420 detectors opens up the possibility of exploiting this high branching ratio channel. Although the penalty for demanding two forward protons makes the discovery of a Standard Model Higgs boson in the $b\bar{b}$ channel unlikely despite a reasonable signal-to-background ratio, the cross section enhancements in other scenarios indicate that this could be a discovery channel. For example, it has recently been shown that the heavy CP-even MSSM Higgs boson, H, could be detected over a large region of the $M_A - \tan\beta$ plane; for $M_A \sim 140$ GeV/c^2, discovery of H should be possible for all values of $\tan\beta$. The 5σ discovery reach extends beyond $M_A = 200$ GeV/c^2 for $\tan\beta > 30$ [25, 19]. We discuss the MSSM Higgs bosons measurements in the $b\bar{b}$ decay channel in detail in Section 2.4.

In addition, for certain MSSM scenarios, FP420 provides an opportunity for a detailed line-shape analysis [15, 26]. In the NMSSM, the complex decay chain $h \to aa \to 4\tau$ becomes viable in CEP, and even offers the possibility to measure the mass of the pseudoscalar Higgs boson [27]. Another attractive feature of the FP420 programme is the ability to probe the CP-structure of the Higgs sector either by measuring directly the azimuthal asymmetry of the outgoing tagged protons [28] or by studying the correlations between the decay products [26].

2.2 The theoretical predictions

In this section we provide a very brief overview of the theoretical calculation involved in making predictions for CEP. We shall, for the sake of definiteness, focus upon Higgs boson production. A more detailed review can be found in [5]. Referring to Fig. 1, the dominant contribution comes from the region $\Lambda^2_{\mathrm{QCD}} \ll Q^2 \ll M_h^2$ and hence the amplitude may be calculated using perturbative QCD techniques [29, 13]. The result is

$$\mathcal{A}_h \simeq N \int \frac{dQ^2}{Q^6} V_h \, f_g(x_1, x_1', Q^2, \mu^2) \, f_g(x_2, x_2', Q^2, \mu^2), \tag{1}$$

where the $gg \to h$ vertex factor for the 0^+ Higgs boson production is (after azimuthal-averaging) $V_h \simeq Q^2$ and the normalization constant N can be written in terms of the $h \to gg$ decay width [2, 29]. Equation (1) holds for small transverse momenta of the outgoing protons, although including the full transverse momentum dependence is straightforward [30, 15].

The f_g's are known as 'skewed unintegrated gluon densities' [31, 32]. They are evaluated at the scale μ, taken to be $\sim M_h/2$. Since $(x' \sim Q/\sqrt{s}) \ll (x \sim M_h/\sqrt{s}) \ll 1$, it is possible to express $f_g(x, x', Q^2, \mu^2)$, to single logarithmic accuracy, in terms of the gluon distribution function $g(x, Q^2)$. The f_g's each contain a Sudakov suppression factor, which is the probability that the gluons which fuse to make the central system do not radiate in their evolution from Q up to the hard scale. The apparent infrared divergence of Equation (1) is nullified by these Sudakov factors and, for the production of $J_z = 0$ central systems with invariant mass above 50 GeV/c^2, there is good control of the unknown infrared region of QCD.

Perturbative radiation associated with the $gg \to h$ subprocess, which is vetoed by the Sudakov factors, is not the only way to populate and to destroy the rapidity gaps. There is also the possibility of soft rescattering in which particles from the underlying proton-proton event (i.e. from other parton interactions) populate the gaps. The production of soft secondaries caused by the rescattering is expected to be almost independent of the short-distance subprocess and therefore can be effectively accounted for by a multiplicative factor S^2, usually termed the soft gap survival factor or survival probability [33]. The value of S^2 is not universal and depends on the centre-of-mass energy of the collision and the transverse momenta, p_T, of the outgoing forward protons; the most sophisticated of the models for gap survival use a two [23] and three-channel [22] eikonal model incorporating high mass diffraction. To simplify the discussion it is common to use a fixed value corresponding to the average over the p_T acceptance of the forward detectors (for a 120 GeV/c^2 Higgs boson, S^2 is about 0.03 at the LHC). Taking this factor into account, the calculation of the production cross section for a 120 GeV/c^2 Standard Model Higgs boson via the CEP process at the LHC yields a central value of 3 fb.

The primary uncertainties in the predicted cross section come from two sources. Firstly, since the gluon distribution functions $g(x, Q^2)$ enter to the fourth power, the predictions are sensitive to the choice of parton distribution function (PDF) in the proton and in particular to the gluon densities at $x = \mathcal{O}(0.01)$. These are currently obtained from fits to data from HERA and the Tevatron. Figure 2 shows the prediction for the cross section for the CEP of a SM Higgs boson as a

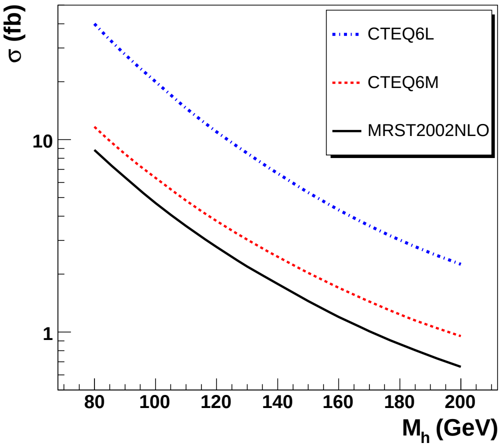

Fig. 2: The cross section for the central exclusive production of a Standard Model Higgs boson as a function of M_h, for three different proton parton distribution functions.

function of M_h for three different choices of PDF at the LHC [20]. The cross section varies from 2.8 fb to 11 fb for a 120 GeV/c^2 SM Higgs boson, although the highest prediction comes from a leading order PDF choice and, since the calculation includes an NLO K-factor (K=1.5), one might conclude that this choice is the least favoured. Secondly, there is some uncertainty in the calculation of the soft survival factor S^2. Until recently, the consensus was that S^2 has a value between 2.5% and 4% at LHC energies [34], but a lower value has been discussed [24, 35] (although these have been challenged in [22]). Early LHC data on various diffractive processes should settle this issue [36].

The reliability of the theoretical calculations can be checked to some extent at the Tevatron. The CDF collaboration has observed a 6σ excess of events in the exclusive dijet sample, $p\bar{p} \to p + jj + \bar{p}$ [37], which is well described by the theory. CDF has also observed several candidates for central exclusive di-photon production, $p\bar{p} \to p + \gamma\gamma + \bar{p}$, at the predicted rates [38], although the invariant mass of the di-photon pair is approximately 10 GeV/c^2 and the infrared region may not be under good control. Both of these predictions include calculations for the soft survival factor at Tevatron energies.

The CDF measurements give some confidence in the predicted cross sections at the LHC. However, the theoretical uncertainties are approximately a factor of three, giving a predicted cross section range for a 120 GeV/c^2 SM Higgs boson of 1 to 9 fb.

2.3 Standard Model Higgs boson

The calculations of the previous section give a central cross section value of 3 fb for a 120 GeV/c^2 SM Higgs boson, falling to 1 fb for a mass of 200 GeV/c^2 (Fig. 2, where we take the more conservative case obtained with the MRST PDFs). Out of the two dominant decay channels ($h \to b\bar{b}$, WW^*), the WW^* channel is the simplest way to observe the SM Higgs boson in CEP because the events are easy to trigger for the semi-leptonic and fully leptonic decay modes. A study taking into account basic experimental cuts was performed in [16] assuming that forward proton detectors were operational at 220 m and 420 m from the interaction point. With Level 1 trigger thresholds of $p_T > 25$ GeV/c for single electrons and $p_T > 20$ GeV/c for single muons, and reduced thresholds for dileptons, it was found that there should be $\sim$3 events in 30 fb^{-1} for 140 GeV/c$^2 < M_h <$ 200 GeV/c^2. For a lighter Standard Model Higgs boson, $M_h = 120$ GeV/c^2, there would be $\sim$0.5 events per 30 fb^{-1}, and it was concluded that the event rate is marginal at low luminosity for $M_h < 140$ GeV/c^2. The event yields are similar for ATLAS and CMS. All background processes, primarily from either photon-photon fusion or W-strahlung from the CEP of light-quark dijets, were studied and the conclusion was that signal-to-background ratio of one (or better) should be achievable, although below the 2-W threshold there is a potentially dangerous background in the case where the off-shell W^* from the Higgs boson decays hadronically. For the gold-plated doubly-leptonic decay modes, there would be approximately one event per 30 fb^{-1} with no appreciable backgrounds.

Since above analysis was published, it has become clear that it will not be necessary to impose such high leptonic trigger thresholds because forward proton detector information can be employed at higher trigger levels to reduce the rates significantly, allowing for higher Level 1 input rates (as discussed in Section 3.1). If the trigger thresholds are reduced to 15 GeV/c for both electrons and muons (which could also be achieved by demanding a coincidence with one or two jets) then the signal rates double. Detector effects have been investigated using the fast simulations of CMS (ATLAS) for the CEP of a 165 (160) GeV/c^2 Higgs boson [39]. These studies showed that the experimental efficiency of the fully leptonic channel is in good agreement with the analysis presented in [16], but that the semi-leptonic event rates may be reduced by up to a factor of four during data taking at instantaneous luminosities in excess of 5×10^{33}cm^{-2} s^{-1} due to kinematic cuts necessary to reduce the luminosity dependent ‘overlap’ backgrounds, which are discussed in Section 3. Taking into account the increase in integrated luminosity, it is expected that 10 events could be observed in the gold-plated fully leptonic decay channel for 300 fb^{-1} of data. Note that these events have the striking characteristic of a dilepton vertex with no additional tracks allowing for excellent background suppression and will afford a measurement of the Higgs mass to within $\sim$2 GeV/c^2 (the mass measurement by FP420 is not affected by the two undetected neutrinos). For a 120 GeV/c^2 Higgs boson, there will be a total of 5 events for 300 fb^{-1}.

The conclusion is that the CEP of a SM Higgs boson should be observable in the WW^* decay channel for all masses in 300 fb^{-1} with a signal to background ratio of one or better. This will provide confirmation that any observed resonance is indeed a scalar with quantum numbers

0^{++}, and allow for a mass measurement[2] on an event-by-event basis of better than 3 GeV/c^2 even in the doubly-leptonic decay channels in which there are two final state neutrinos. This will be a vitally important measurement at the LHC, where determining the Higgs quantum numbers is extremely difficult without CEP. Furthermore, in certain regions of MSSM parameter space, in particular for 140 GeV/c^2$< M_A <$ 170 GeV/c^2 and intermediate tanβ, the CEP rate for $h \to WW^*$ may be enhanced by up to a factor of four [19]. We discuss the MSSM in more detail in the following section for the $b\bar{b}$ decay channel.

For the Standard Model Higgs boson, the $b\bar{b}$ decay channel is more challenging. It is the conclusion of [8, 20] that this channel will be very difficult to observe for $M_h = 120$ GeV/c^2 using FP420 alone, but may be observable at the 3σ level if 220 m detectors are used in conjunction with FP420 and the cross sections are at the upper end of the theoretical expectations and/or the experimental acceptance and trigger and b-tagging efficiencies are improved beyond the currently assumed values. This should not be dismissed, because such an observation would be extremely valuable, since there may be no other way of measuring the b-quark couplings of the SM Higgs at the LHC. We discuss the experimental approach to observing Higgs bosons in the $b\bar{b}$ decay channel in detail in Section 3.

2.4 h, H in the MSSM

In many MSSM scenarios, the additional capabilities brought to the LHC detectors by FP420 would be vitally important for the discovery of the Higgs bosons[3] and the measurement of their properties. The coupling of the lightest MSSM Higgs boson to b quarks and τ leptons may be strongly enhanced at large tan β and small M_A, opening up both modes to FP420. The cross sections may become so large in CEP that one could carry out a lineshape analysis to distinguish between different models [15, 26] and to make direct observations of CP violation in the Higgs sector [26, 28]. If the widths are a few GeV/c^2, a direct width measurement may be possible, a unique capability of FP420.

2.4.1 $h, H \to b\bar{b}$ *decay modes*

In [19] (Heinemeyer *et al.*) a detailed study of the additional coverage in the $M_A -$ tanβ plane afforded by FP420 and 220 m detectors was carried out for several benchmark MSSM scenarios. In particular, the observation of the CP-even Higgs bosons (h, H) in the b-quark decay channel was investigated. Figure 3 shows the ratio of the MSSM to SM cross sections × the branching-ratio for the $h \to b\bar{b}$ channel within the M_h^{max} scenario [40] as a function of M_A and tanβ. For example, at tan$\beta = 33$ and $M_A = 120$ GeV/c^2, the cross section for $h \to b\bar{b}$ in the MSSM is enhanced by a factor of five with respect to the Standard Model. The results shown are for $\mu = +200$ GeV, where the parameter μ determines the size and effect of higher order corrections; negative (positive) μ leads

---

[2] The mass resolution of FP420 is discussed in detail in Section 4.

[3] Here we are dealing with the lightest MSSM Higgs boson h and the heavier state H. Note that production of the pseudo-scalar Higgs, A, is suppressed in CEP due to the $J_z = 0$ selection rule.

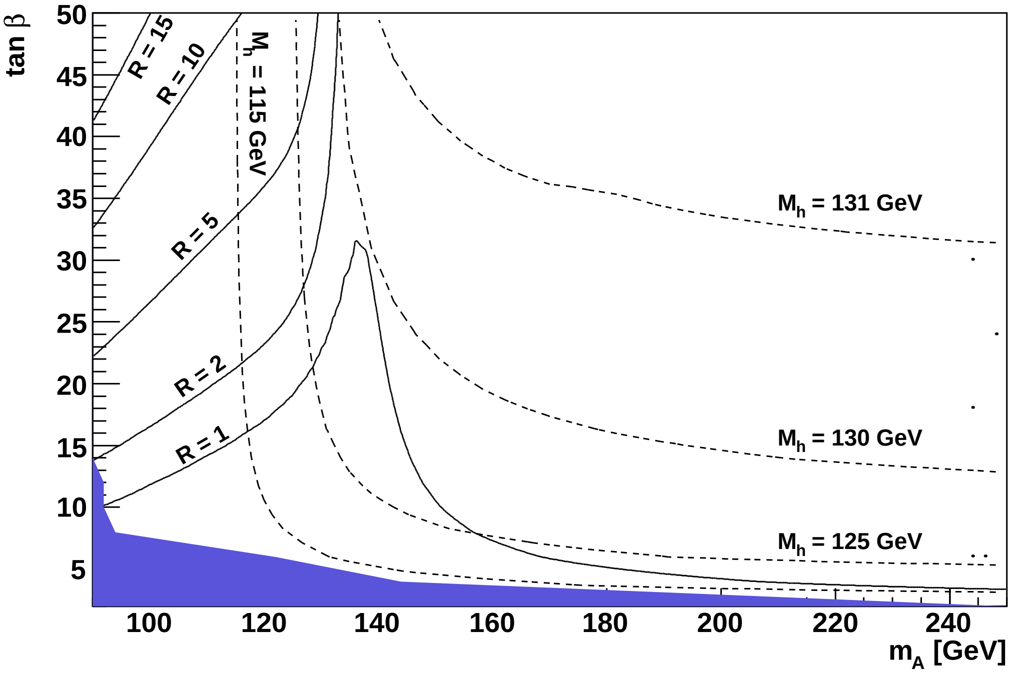

Fig. 3: The ratio, R, of cross section × branching ratio in the CEP $h \to b\bar{b}$ channel in the M_A - tanβ plane of the MSSM within the M_h^{max} benchmark scenario (with $\mu = +200$ GeV) to the SM Higgs cross section [19]. The dark shaded (blue) region corresponds to the parameter region that is excluded by the LEP Higgs boson searches [41, 42].

to enhanced (suppressed) bottom Yukawa couplings.

Figure 4 shows the 5σ discovery contours (upper plot) and the 3σ contours (lower plot) for this scenario. The discovery contours were calculated using an experimental efficiency based on the simulated analysis in the CMS-TOTEM studies [8], with a full simulation of the acceptance of both FP420 and 220 m forward proton detectors. The Level 1 trigger strategy was based on information only from the central detectors and 220 m detectors. Full details can be found in [19]. Curves are shown for several luminosity scenarios; $\int \mathcal{L} = 60$ fb^{-1} corresponds to 3 years of data taking by ATLAS and CMS at 10^{33} cm^{-2} s^{-1}, and $\int \mathcal{L} = 600$ fb^{-1} corresponds to 3 years of data taking by both experiments at 10^{34} cm^{-2} s^{-1}. For example, if $\tan\beta = 40$ and $M_A = 120$ GeV/c^2, $h \to b\bar{b}$ would be observed with more than 3σ confidence with 60 fb^{-1} of data (lower plot), but would require twice the experimental efficiency or more integrated luminosity to be observed with 5σ confidence (upper plot). Figure 5 shows the 5σ discovery contours (upper plot) and the 3σ contours (lower plot) for the heavy scalar, H, in the same scenario. With sufficient integrated luminosity (few

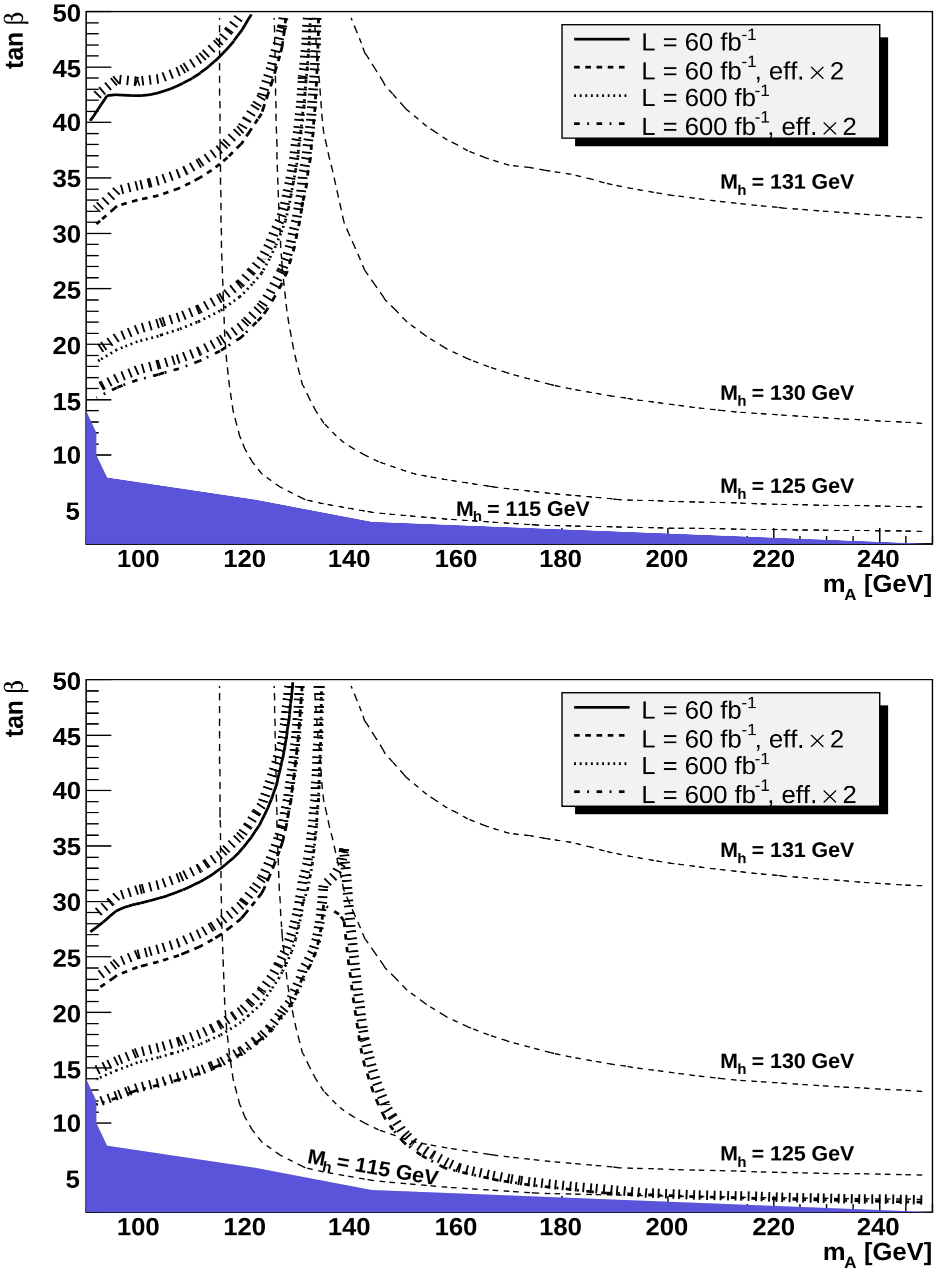

Fig. 4: 5σ discovery contours (upper plot) and contours of 3σ statistical significance (lower plot) for the $h \to b\bar{b}$ channel in CEP in the M_A - tanβ plane of the MSSM within the $M_h^{\max}$ benchmark scenario for different luminosity scenarios as described in the text [19]. The values of the mass of the light CP-even Higgs boson, M_h, are indicated by contour lines. No pile-up background assumed. The dark shaded (blue) region corresponds to the parameter region that is excluded by the LEP Higgs boson searches [41, 42].

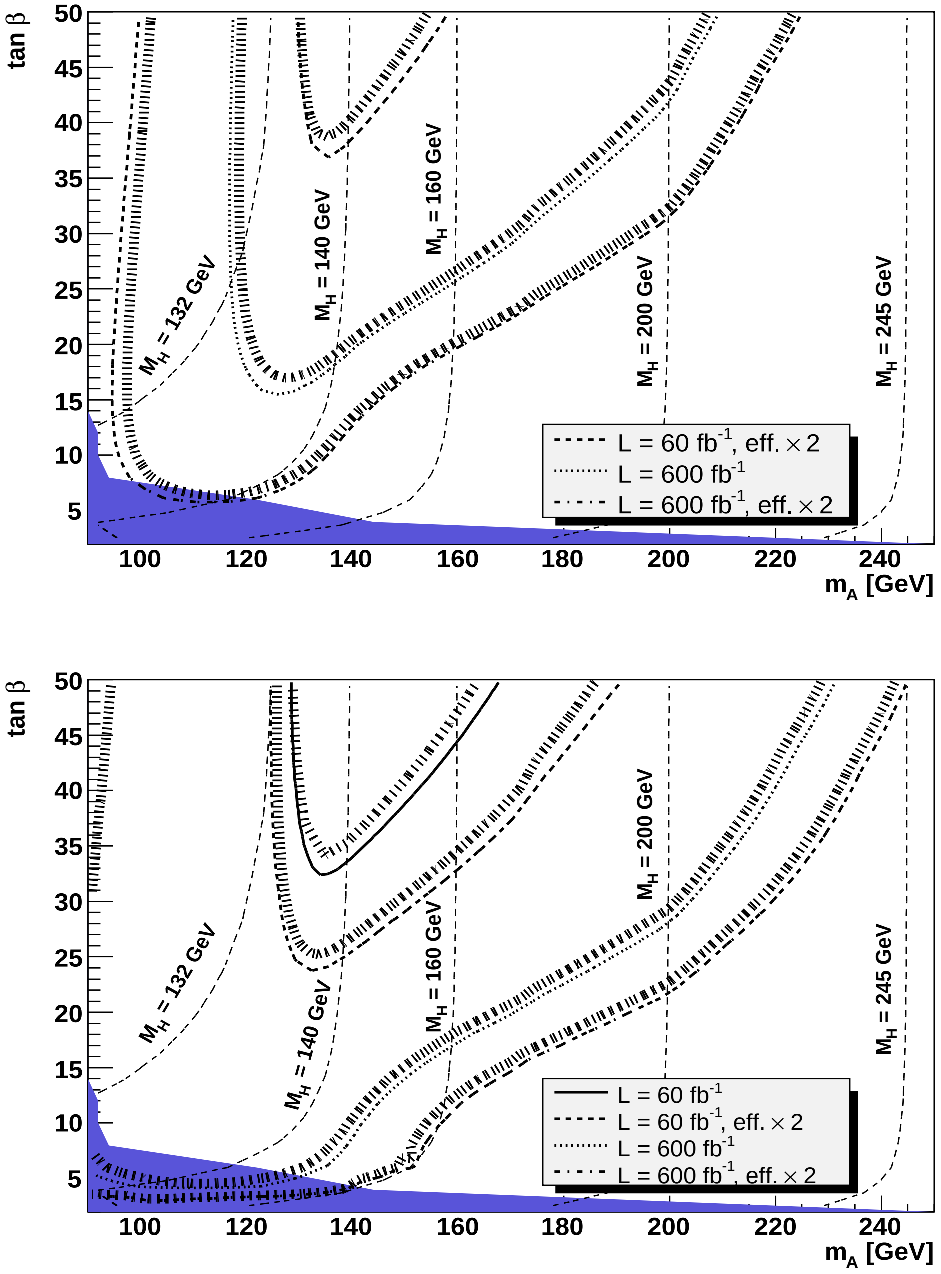

Fig. 5: 5σ discovery contours (upper plot) and contours of 3σ statistical significance (lower plot) for the CEP $H \rightarrow b\bar{b}$ channel in the M_A - tanβ plane of the MSSM within the M_h^{max} benchmark scenario (with $\mu = +200$GeV) for different luminosity scenarios as described in the text [19]. The values of the mass of the heavier CP-even Higgs boson, M_H, are indicated by contour lines. No pile-up background assumed. The dark shaded (blue) region corresponds to the parameter region that is excluded by the LEP Higgs boson searches [41, 42].

hundreds fb^{-1}), all values of $\tan\beta$ are covered for $M_A \sim 140$ GeV/c^2 and at high $\tan\beta$ observation remains possible for Higgs bosons with masses in excess of 200 GeV/c^2.

An important challenge of the $b\bar{b}$ channel measurement at the LHC is the combinatorial 'overlap' background caused by multiple proton-proton interactions in the same bunch crossing. The analysis presented above uses the selection efficiencies discussed in [8] which are based on stringent cuts that are expected to reduce such pile-up contributions. This background is indeed negligible at low luminosities ($\sim 10^{33}$ cm^{-2} s^{-1}), but becomes more problematic at the highest luminosities. For the latter cases, additional software as well as hardware improvements in rejecting the background have been assumed. Such improvements are presented in the analysis of [20] (Cox et al.) which examines the MSSM point given by $\tan\beta = 40$ and $M_A = 120$ GeV/c^2 in detail. Figure 4 indicates that, for this choice of parameters, $h \to b\bar{b}$ should be observable with a significance close to 4σ for 60 fb^{-1} of data. Section 3 summarises the results obtained in [20] and demonstrates the experimental procedure and hardware requirements needed to reduce the overlap backgrounds. We compare the results of the two independent $h \to b\bar{b}$ analyses in Section 3.5.

2.4.2 $h, H \to \tau\tau$ decay modes

In the standard (non-CEP) search channels at the LHC, the primary means of detecting the heavy CP-even Higgs boson H (and the CP-odd A) in the MSSM is in the b-quark associated production channel, with subsequent decay of the Higgs boson in the $\tau\tau$ decay mode. This decay mode is also open to CEP and was studied in [19]. The branching ratio of the Higgs bosons to $\tau\tau$ is approximately 10% for $M_{H/A} > 150$ GeV/c^2 and 90% to $b\bar{b}$, if the decays to light SUSY particles are not allowed. Note that τ's decay to 1-prong (85%) or 3-prong (15%); requiring no additional tracks on the $\tau\tau$ vertex is very effective at reducing non-exclusive background.

Figure 6 shows the 5σ discovery contours and the 3σ contours in the $M_A - \tan\beta$ plane for the M_h^{max} benchmark scenario for different luminosity scenarios. The discovery region is significantly smaller than for the $b\bar{b}$ case, although the decay channel can be observed at 3σ across a large area of parameter space. This would be an important complementary measurement to the standard search channels, affording a direct measurement of the quantum numbers of the H. Furthermore, in this region of parameter space, the A is very close in mass to the H and, since the A is heavily suppressed in CEP, a clean high-precision measurement of the H mass in the $\tau\tau$ channel will be possible using forward proton tagging. Heinemeyer *et al.* [19] also investigated the coverage for the di-tau decay channel of the light h, and found that a 3σ observation could be made in the region $\tan\beta \geq 15$, $M_h < 130$ GeV/c^2 at high luminosity.

2.5 Observation of Higgs bosons in the NMSSM

The Next-to-Minimal Supersymmetric Standard Model (NMSSM) extends the MSSM by the inclusion of a singlet superfield, $\hat{S}$ [43]. This provides a natural solution to the μ problem through the $\lambda\hat{S}\hat{H}_u\hat{H}_d$ superpotential term when the scalar component of $\hat{S}$ acquires a vacuum expectation value. The Higgs sector of the NMSSM contains three CP-even and two CP-odd neutral Higgs bosons,

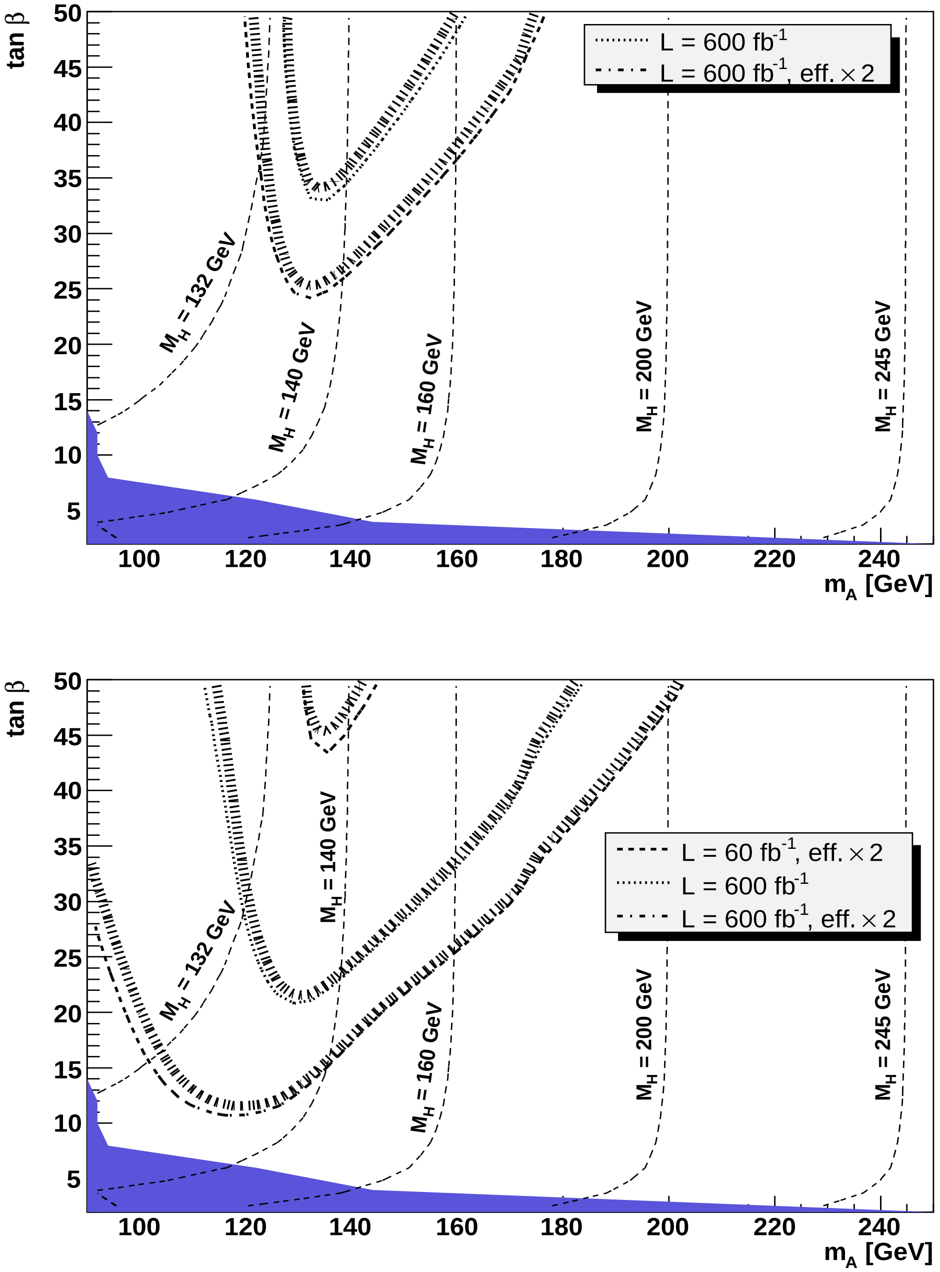

Fig. 6: 5σ discovery contours (upper plot) and contours of 3σ statistical significance (lower plot) for the $H \to \tau^+\tau^-$ channel in CEP in the M_A–tanβ plane of the MSSM within the M_h^{max} benchmark scenario (with $\mu = +200$GeV) for different luminosities. The values of the mass of the heavier CP-even Higgs boson, M_H, are indicated by contour lines. No pile-up background assumed. The dark shaded (blue) region corresponds to the parameter region that is excluded by the LEP Higgs boson searches.

and a charged Higgs boson. According to [44] the part of parameter space that has no fine-tuning problems results in the lightest scalar Higgs boson decaying predominantly via $h \to aa$, where a is the lightest pseudo-scalar. The scalar Higgs boson has a mass of $\sim$100 GeV/c^2. If the a has a mass of $2m_\tau \lesssim m_a \lesssim 2m_b$, which is in fact preferred, then the decay channel $h \to aa \to 4\tau$ would become the dominant decay chain. This is not excluded by LEP data. In such a scenario the LHC could fail to discover any of the Higgs bosons [44].

Subsequently, however, it was shown in [27] that the lightest Higgs boson could be discovered in CEP using FP420. The parameter point chosen was similar to scenario 1 in [45] and resulted in $M_h = 92.9$ GeV/c^2 and $m_a = 9.7$ GeV/c^2, with $\mathrm{BR}(h \to aa) = 92\%$ and $\mathrm{BR}(a \to \tau\tau) = 81\%$. The analysis uses mainly tracking information to define the 4τ final state and triggers on a single muon with a transverse momentum greater than 10 GeV/c, although the analysis still works for an increased muon threshold of 15 GeV/c. The final event rates are low, approximately 3-4 events after all cuts at ATLAS or CMS over three years of data taking if the instantaneous luminosity is greater than 10^{33} cm^{-2} s^{-1}. There is however no appreciable background. Figure 7(a) shows the combined significance of observation at ATLAS and CMS after three years of data taking at a specific instantaneous luminosity. The mass of the h is obtained using FP420 to an accuracy of $2-3$ GeV/c^2 (per event). Furthermore, using FP420 and the tracking information from the central detector, it is possible to make measurements of the a mass on an event-by-event basis. This is shown in Figure 7(b) for an example pseudo-data set corresponding to 150 fb^{-1} of integrated luminosity. From examining many such pseudo-data sets, the mass of the a in this scenario would be measured as 9.3 ± 2.3 GeV/c^2.

A complementary, independent trigger study has also been performed for this decay channel using the CMS fast simulation. Using only the standard CMS single muon trigger of 14 GeV/c, a trigger efficiency of 13% for the $h \to aa \to 4\tau$ was observed. This is in reasonably good agreement with the study presented above, which observed a 12% efficiency for a 15 GeV/c trigger (assuming ATLAS efficiencies). Furthermore, the study also observed that the analysis presented above would benefit from additional triggers, which were not considered in [27]. The total trigger efficiency increases to $\sim$28% if a combination of lepton triggers are used. It is likely that the majority of these events will pass the analysis cuts presented in [27] and so would boost the event rate by up to a factor of two. If the lepton trigger thresholds can be reduced, which could be possible at low luminosities, the trigger efficiency increases to 45% resulting in a factor of 3.5 increase in the event rate.

2.6 Invisible Higgs boson decay modes

In some extensions of the SM, the Higgs boson decays dominantly into particles which cannot be directly detected, the so called invisible Higgs. The prospects of observing such Higgs boson via the forward proton mode are quite promising [46] assuming that the overlap backgrounds can be kept under control. Note that contrary to the conventional parton-parton inelastic production, the mass of such invisible Higgs boson can be accurately measured by the missing mass method.

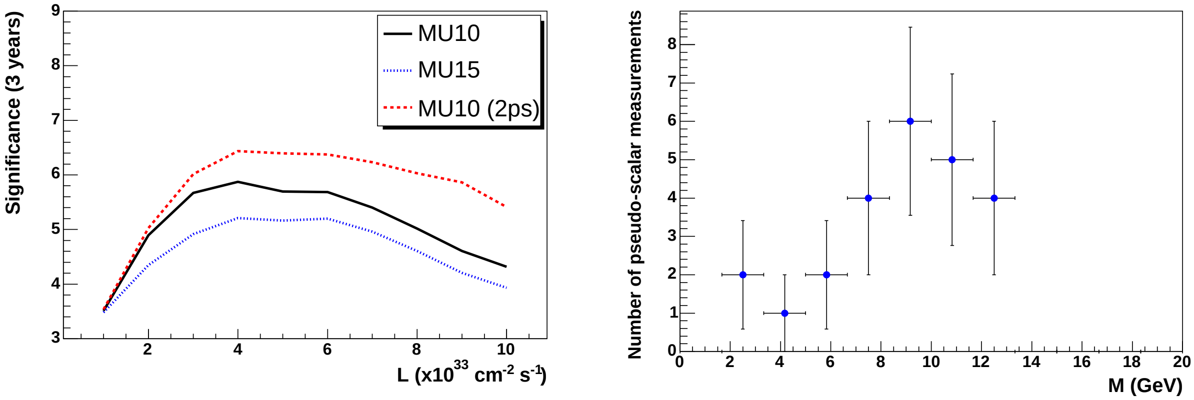

(a) (b)

Fig. 7: (a) The significance of observation of $h \rightarrow aa \rightarrow 4\tau$ using a muon p_T trigger threshold of 10 GeV/c (or 15 GeV/c) for three years of data taking at ATLAS and CMS. Also shown is the increase in the significance due to a factor of five improvement in background rejection from a 2 ps proton time-of-flight measurement, see Sections 3 and 10, or a comparable gain across all of the rejection variables [27]. (b) A typical a mass measurement for 150 fb^{-1} of data.

2.7 Conclusion of the studies of the CEP of h, H

It is a general feature of extended Higgs sectors that the heavy Higgs bosons decouple from the gauge bosons and therefore decay predominantly to heavy SM fermions. Adding the possibility to detect the $b\bar{b}$ decay channel and enhancing the capacity to detect the $\tau\tau$ channel would therefore be of enormous value. In the M_h^{max} scenario of the MSSM, if forward proton detectors are installed at 420 m and 220 m and operated at all luminosities, then nearly the whole of the $M_A - \tan\beta$ plane can be covered at the 3σ level. Even with only 60 fb^{-1} of luminosity the large $\tan\beta$ / small M_A region can be probed. For the heavy CP-even MSSM Higgs boson with a mass of approximately 140 GeV/c^2, observation should be guaranteed for all values of $\tan\beta$ with sufficient integrated luminosity. At high $\tan\beta$, Higgs bosons of masses up to ~ 240 GeV/c^2 should be observed with 220 m proton taggers. The coverage and significance are further enhanced for negative values of the μ parameter. For scenarios in which the light (heavy) Higgs boson and the A boson are nearly degenerate in mass, FP420 (together with the 220 proton tagger) will allow for a clean separation of the states since the A cannot be produced in central exclusive production. In the NMSSM, forward proton tagging could become the discovery channel in the area of parameter space in which there are no fine-tuning issues through the decay chain $h \rightarrow aa \rightarrow 4\tau$. Using the information from FP420, the mass of both the h and a can be obtained on an event-by-event basis.

Observation of any Higgs state in CEP allows for direct observation of its quantum numbers and a high-precision mass measurement. As we shall see in Section 3, it will be possible in many scenarios to measure the mass with a precision of better than 1 GeV/c^2 and a width measurement may also be possible. Installation of FP420 would therefore provide a significant enhancement in the discovery potential of the current baseline LHC detectors.

2.8 Photon-photon and photon-proton physics

2.8.1 Introduction

Photon-induced interactions have been extensively studied in electron-proton and electron-positron collisions at HERA and LEP, respectively. A significant fraction of pp collisions at the LHC will also involve quasi-real (low-Q^2) photon interactions, occurring for the first time at centre-of-mass energies well beyond the electroweak scale. The LHC will thus offer a unique possibility for novel research – complementary to the standard parton-parton interactions – via photon-photon and photon-proton processes in a completely unexplored regime. The much larger effective luminosity available in parton-parton scatterings will be compensated by the better known initial conditions and much simpler final states in photon-induced interactions. The distinct experimental signatures of events involving photon exchanges are the presence of very forward scattered protons and of large rapidity gaps (LRGs) in forward directions. Dedicated very forward detectors are thus required in order to efficiently *tag* photon-induced events and keep the backgrounds under control [6]. Very recently, exclusive two-photon production of lepton pairs [47] and diffractive photoproduction of quarkonia [48] have been successfully measured in $p\bar{p}$ collisions at Tevatron (and also in heavy-ion collisions at RHIC [49]) using LRGs. In both measurements, clear signals were obtained with low backgrounds. Apart from their intrinsic interest, these exclusive processes p + p $\to$ p + e^+e^- + p, p + $\mu^+\mu^-$ + p, both through $\gamma\gamma \to l^+l^-$ and $\gamma + p \to \Upsilon + p$ provide a source of forward protons with momenta known to better than 1 GeV/c (dominated by the incoming beam momentum spread $dp/p \sim 10^{-4}$). They therefore give an important calibration of the FP420 momentum scale and resolution, even though usually only one proton is detected (see Section 11.4).

The equivalent photon (or Weizsäcker-Williams) approximation (EPA) [50] provides the appropriate framework to describe processes involving photon exchange with proton beams at the LHC. In this approximation, one photon is emitted by one (or both) incoming proton(s) which then subsequently collides with the other proton (photon) producing a system X. Here, we will only consider[4] *elastic* photon-photon collisions, $\gamma\gamma \to X$, where both proton "emitters" remain intact (i.e. $pp \to ppX$) and *inelastic* photoproduction, $\gamma p \to X$, where the "target" proton dissociates into a state Y (i.e. $pp \to pXY$). In both cases, we ignore additional parton interactions which destroy the rapidity gaps. The probability that the gaps survive (gap survival probability, see Section 2.2) is much larger in the case of photon-photon interactions – which occur at relatively large impact parameters – compared to exclusive Pomeron- or gluon- induced processes [2, 21]. In the EPA, the photon spectrum is a function of the photon energy E_γ and its virtuality Q^2 [50]:

$$\mathrm{d}N = \frac{\alpha}{\pi}\frac{\mathrm{d}E_\gamma}{E_\gamma}\frac{\mathrm{d}Q^2}{Q^2}\left[\left(1-\frac{E_\gamma}{E}\right)\left(1-\frac{Q^2_{min}}{Q^2}\right)F_E + \frac{E_\gamma^2}{2E^2}F_M\right], \qquad (2)$$

---

[4] A third class of events where the two colliding protons dissociate is not considered here.

where α is the fine-structure constant, E is the incoming proton energy and the minimum photon virtuality $Q^2_{min} \simeq [M_Y^2 E/(E-E_\gamma) - M_p^2]E_\gamma/E$, where M_p is the proton mass and M_Y is the invariant mass of the final state Y, and F_M and F_E for the elastic production are given by the proton form factors, in the dipole approximation: $F_M = G_M^2$ and $F_E = (4M_p^2 G_E^2 + Q^2 G_M^2)/(4M_p^2 + Q^2)$, where $G_E^2 = G_M^2/7.78 = (1 + Q^2/0.71\mathrm{GeV}^2)^{-4}$. The spectrum is strongly peaked at low E_γ, therefore photon-photon centre-of-mass energies $W \simeq 2\sqrt{E_{\gamma_1} E_{\gamma_2}}$ are usually much smaller than the total centre-of-mass energy of $2E = 14$ TeV. In the elastic case, the photon virtuality is usually low, $\langle Q^2 \rangle \approx 0.01$ GeV^2, and therefore the proton scattering angle is very small, $\lesssim 20$ μrad. The luminosity spectrum of photon-photon collisions, $d\mathcal{L}_{\gamma\gamma}/dW_{\gamma\gamma}$, can be obtained by integration of the product of the photon spectra, given by Eq. (2), over the photon virtualities and energies keeping fixed W. The elastic $\gamma\gamma$ luminosity spectrum (Fig. 8) peaks strongly at low values of W, but extends to large values, even beyond[5] 1 TeV. The integrated spectrum directly gives a fraction of the pp LHC luminosity available in $\gamma\gamma$ collisions at $W > W_0$. The relative photon-photon effective luminosity amounts to 1% for $W_{\gamma\gamma} > 23$ GeV and to 0.1% for $W_{\gamma\gamma} > 225$ GeV. Given the very large LHC luminosity, this leads to significant event rates for high-energy processes with relatively small photon-photon cross-sections. This is even more true for γp interactions, where both energy reach and effective luminosities are much higher than for the $\gamma\gamma$ case. Finally, photon physics can be studied also in ion collisions at the LHC [51], where the lower ion luminosities are largely compensated by the high photon fluxes due to the Z^2 enhancement (for each nucleus), where Z is the ion charge.

In this section, we will consider the following exclusive photon-induced processes accessible to measurement at the LHC with very forward proton tags:

1. two-photon production of lepton pairs (an excellent LHC “luminometer” process),
2. two-photon production W and Z pairs (as a means to investigate anomalous triple and quartic gauge couplings),
3. two-photon production of supersymmetric pairs; as well as
4. associated WH photoproduction, and
5. anomalous single top photoproduction.

Realistic studies of all these processes – computed with dedicated packages (MADGRAPH / MADEVENT [52], CALCHEP [53], LPAIR [54]) including typical ATLAS/CMS acceptance cuts and a modified version of the Pythia generator [55] for all processes involving final-state partons – are discussed in detail in a recent review on photon-induced interactions at the LHC [12]. A summary of this work is presented in the following subsections.

---

[5] Note that the W-pair invariant mass coverage in $\gamma\gamma$ reactions is much larger than in the hard exclusive central diffractive processes where the cross sections at large masses are strongly suppressed by the QCD Sudakov form factor [2].

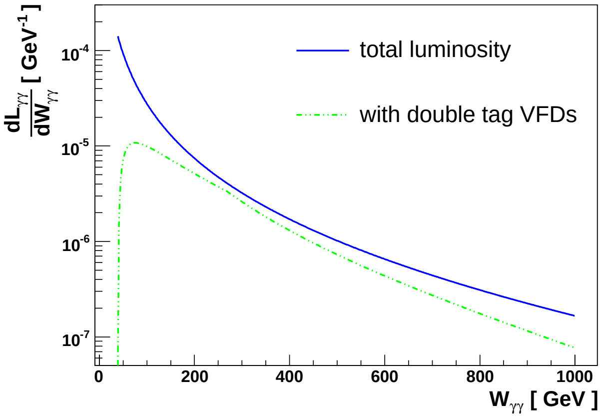

Fig. 8: Relative elastic luminosity spectrum of photon-photon collisions at the LHC in the range $Q^2_{min} < Q^2 < 2$ GeV^2 (solid blue line) compared to the corresponding luminosity if the energy of each photon is restricted to the forward detector (VFD) tagging range 20 GeV $< E_\gamma <$ 900 GeV (dashed green curve) [12].

2.8.2 Two-photon processes

Elastic two photon interactions yield very clean event topologies at the LHC: two very forward protons measured far away from the IP plus some centrally produced system. In addition, the photon momenta can be precisely measured using the forward proton taggers, allowing the reconstruction of the event kinematics. To illustrate the photon physics potential of the LHC, various pair production cross sections in two-photon collisions have been computed using a modified version [12] of MADGRAPH/MADEVENT [52]. The corresponding production cross sections are summarised in Table 1. Since the cross sections for pair production depend only on charge, spin and mass of the produced particles, the results are shown for charged and colourless fermions and scalars of two different masses. These cross sections are shown as a function of the minimal $\gamma\gamma$ centre-of-mass energy W_0 in Fig. 9.

Clearly, interesting $\gamma\gamma$ exclusive cross sections at the LHC are accessible to measurement. In particular, the high expected statistics for exclusive W pair production should allow for precise measurements of the $\gamma\gamma WW$ quartic couplings. The production of new massive charged particles such as supersymmetric pairs [56], is also an intriguing possibility. Similarly, the exclusive production of the Higgs boson – which has a low SM cross section [57] – could become interesting in the case of an enhanced $H\gamma\gamma$ coupling. Last but not least, the two-photon exclusive production of muon pairs will provide an excellent calibration of luminosity monitors [58, 6].

Processes		σ (fb)	**Generator**
$\gamma\gamma \rightarrow$	$\mu^+\mu^-$ ($p_T^\mu > 2$ GeV/c, $\lvert\eta^\mu\rvert < 3.1$)	72 500	LPAIR [54]
	W^+W^-	108.5	MG/ME [52]
	F^+F^- (M = 100 GeV/c^2)	4.06	//
	F^+F^- (M = 200 GeV/c^2)	0.40	//
	S^+S^- (M = 100 GeV/c^2)	0.68	//
	S^+S^- (M = 200 GeV/c^2)	0.07	//
	$H \rightarrow b\bar{b}$ (M = 120 GeV/c^2)	0.15	MG/ME [52]

Table 1: Production cross sections for $pp \rightarrow ppX$ (via $\gamma\gamma$ exchange) for various processes (F for fermion, S for scalar) computed with various generators [12].

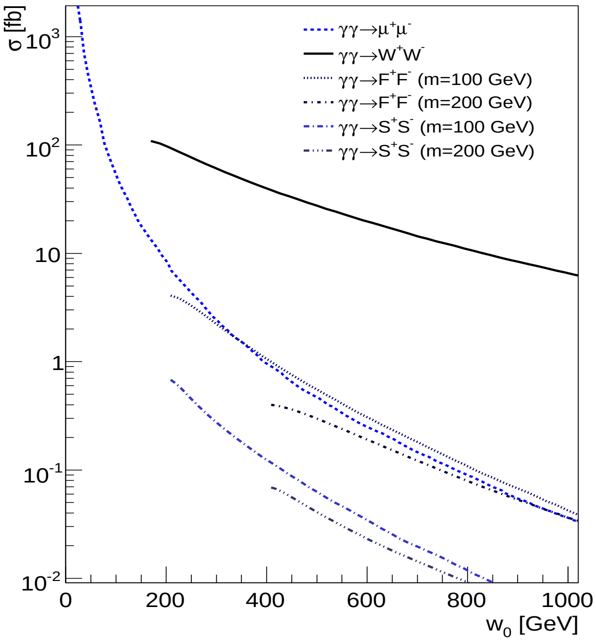

Fig. 9: Cross sections for various $\gamma\gamma$ processes at the LHC as a function of the minimal $\gamma\gamma$ centre-of-mass energy W_0 [12].

Lepton pairs

Two-photon exclusive production of muon pairs has a well known QED cross section, including very small hadronic corrections [59]. Small theoretical uncertainties and a large cross section at LHC energies ($\sigma = 72.5$ pb, Table 1) makes this process a perfect candidate for the measurement of the LHC absolute luminosity [6]. Thanks to its distinct signature the selection procedure is very simple: two muons within the central detector acceptance ($|\eta| < 2.5$), with transverse momenta above two possible thresholds ($p_T^\mu > 3$ or 10 GeV/c). As the forward protons have very low p_T, the muons have equal and opposite (in ϕ) momenta. The effective cross sections after the application of these acceptance cuts ($\sigma_{\rm acc}$), with or without the requirement of at least one FP420 tag, are presented in Table 2. About 800 muon pairs should be detected in 12 hour run at the average luminosity of 10^{33} cm^{-2}s^{-1}.

cross section [fb]	σ_{acc}	σ_{acc} (with forward proton tag)
$p_T^\mu > 3$ GeV/c, $\lvert\eta^\mu\rvert < 2.5$	21 600	1 340
$p_T^\mu > 10$ GeV/c, $\lvert\eta^\mu\rvert < 2.5$	7 260	1 270

Table 2: Cross sections for $pp(\gamma\gamma \to \mu\mu)pp$ after application of typical ATLAS/CMS muon acceptance cuts, and coincident requirement of a forward proton [12].

An important application of these exclusive events is the absolute calibration of the very forward proton detectors. As the energy of the produced muons is well measured in the central detector, the forward proton energy can be precisely predicted using the kinematics constrains. This allows for precise calibration of the proton taggers, both momentum scale and resolution, in case of e.g. misalignment of the LHC beam-line elements, and leads to a good control of the reconstructed energy of the exchanged photon [60]. The large cross sections could even allow for run-by-run calibration, as the requirement of at least one forward proton tag results in more than 300 events per run. As the momenta of both forward protons are known from the central leptons, it is only necessary to measure one of them. This is fortunate as it allows low mass ($\sim$10 GeV/c^2) forward pairs to be used, with rates much higher than in the FP420 double-arm acceptance. Finally, it is worth noting that the two-photon exclusive production of e^+e^- pairs can also be studied at the LHC, though triggering of such events is more difficult. Electron pair reconstruction, e.g. in the CMS CASTOR forward calorimeter, has been discussed in [8].

W and Z boson pairs

A large cross section of about 100 fb is expected for the exclusive two-photon production of W boson pairs at the LHC. The very clean event signatures offer the possibility to study the properties of the W gauge bosons and to make stringent tests of the Standard Model at average centre-of-mass energies of $\langle W_{\gamma\gamma\to WW} \rangle \approx 500$ GeV. The cross section for events where both W bosons decay into a muon and a neutrino – resulting in events with two muons with large transverse momentum within the typical $|\eta| < 2.5$ ATLAS/CMS muon acceptance range – are large and only slightly reduced after adding the requirement of at least one forward proton tag (Table 3).

cross section [fb]	σ_{acc}	σ_{acc} (with forward proton tag)
$p_T^\mu > 3$ GeV/c, $\lvert\eta^\mu\rvert < 2.5$	0.80	0.76
$p_T^\mu > 10$ GeV/c, $\lvert\eta^\mu\rvert < 2.5$	0.70	0.66

Table 3: Cross section σ_{acc} for $\gamma\gamma \to W^+W^- \to \mu^+\mu^-\overline{\nu_\mu}\nu_\mu$ after application of typical ATLAS/CMS muon acceptance cuts, and coincident requirement of a forward proton [12].

The unique signature of WW pairs in the fully leptonic final state, no additional tracks on the l^+l^- vertex, large lepton acoplanarity and large missing transverse momentum strongly reduces the backgrounds. The two-photon production of tau-lepton pairs, having in addition low cross-section at large invariant masses, can then be completely neglected. Moreover, the double diffractive production of the W boson pairs is also negligible, and the inclusive partonic production (about 1 pb, assuming fully leptonic decays, and both leptons passing the acceptance cuts) can be very efficiently suppressed too by applying either the double tagging in the forward proton detectors, or the double LRG signature. Similar conclusions can be reached for the exclusive two-photon production of Z boson pairs, assuming fully leptonic, or semi-leptonic decays. In the SM, $\gamma\gamma \to ZZ$ is negligible; this would be a test of anomalous γZZ couplings. The dominant SM source of exclusive ZZ is $H \to ZZ$ if the Higgs boson exists, so the background in this channel is very small.

Two-photon production of W pairs provides a unique opportunity to investigate anomalous gauge boson couplings, in particular the quartic gauge couplings (QGCs), $\gamma\gamma WW$ [61]. The sensitivity to the anomalous quartic vector boson couplings has been investigated [12] in the processes $\gamma\gamma \to W^+W^- \to l^+l^-\nu\overline{\nu}$ and $\gamma\gamma \to ZZ \to l^+l^- jj$ using the signature of two leptons (e or μ) within the acceptance cuts $|\eta| < 2.5$ and $p_T > 10$ GeV/c. The upper limits λ^{up} on the number of events at the 95% confidence level have been calculated assuming that the number of observed events equals that of the SM prediction (corresponding to all anomalous couplings equal to zero). The calculated cross section upper limits can then be converted to one-parameter limits (when the other anomalous coupling is set to zero) on the anomalous quartic couplings. The obtained limits (Table 4) are about 10000 times better than the best limits established at LEP2 [62] clearly showing the large and unique potential of such studies at the LHC. A corresponding study of the anomalous triple gauge couplings can also be performed [63]. However, in this case the expected sensitivities are not as favourable as for the anomalous QGCs.

Supersymmetric pairs

The interest in the two-photon exclusive production of pairs of new charged particles is three-fold: (i) it provides a new and very simple production mechanism for physics beyond the SM, complementary to the standard parton-parton processes; (ii) it can significantly constrain the masses of the

Coupling limits $[10^{-6}\ \mathrm{GeV}^{-2}]$	$\int \mathcal{L}\mathrm{d}t = 1\ \mathrm{fb}^{-1}$	$\int \mathcal{L}\mathrm{d}t = 10\ \mathrm{fb}^{-1}$
$\lvert a_0^Z/\Lambda^2 \rvert$	0.49	0.16
$\lvert a_C^Z/\Lambda^2 \rvert$	1.84	0.58
$\lvert a_0^W/\Lambda^2 \rvert$	0.54	0.27
$\lvert a_C^W/\Lambda^2 \rvert$	2.02	0.99

Table 4: Expected one-parameter limits for anomalous quartic vector boson couplings at 95% CL [12].

new particles, using double forward-proton tagging information; (iii) in the case of SUSY pairs, simple final states are usually produced without cascade decays, characterised by a fully leptonic final state composed of two charged leptons with large missing energy (and large lepton acoplanarity) with low backgrounds, and large high-level-trigger efficiencies.

The two-photon production of supersymmetric leptons or other heavy non-Standard Model leptons has been investigated in [56, 64, 65, 66]. The total cross-section at the LHC for the process $\gamma\gamma \rightarrow \tilde{l}^+\tilde{l}^-$ can be as large as ~ 20 fb ($\mathcal{O}(1\,fb)$ for the elastic case alone), while still being consistent with the model-dependent direct search limits from LEP [67, 68]. While sleptons are also produced in other processes (Drell-Yan or squark/gluino decays), $\gamma\gamma$ production has the advantage of being a direct QED process with minimal theoretical uncertainties.

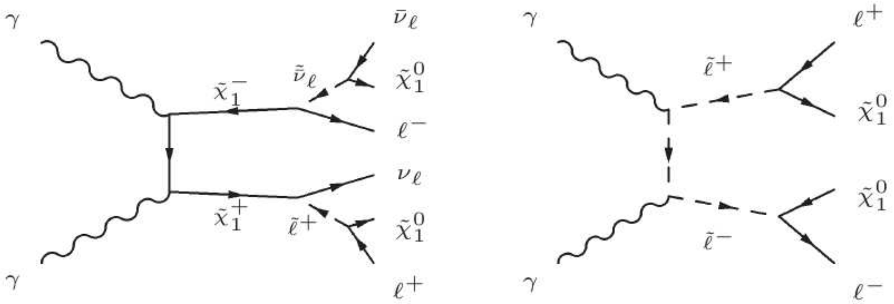

Fig. 10: Relevant Feynman diagrams for SUSY pair production with leptons in the final state: chargino disintegration in a charged/neutral scalar and a neutral/charged fermion (left); slepton disintegration (right) [12].

In [12], three benchmark points in mSUGRA/CMSSM parameter space constrained by the post-WMAP research [69] have been chosen:

- LM1: very light LSP, light $\tilde{\ell}$, light $\tilde{\chi}$ and $\tan\beta$=10;
- LM2: medium LSP, heavy $\tilde{\ell}$, heavy $\tilde{\chi}$ and $\tan\beta$=35;
- LM6: heaviest LSP, light right $\tilde{\ell}$, heavy left $\tilde{\ell}$, heavy $\tilde{\chi}$ and $\tan\beta$=10.

The masses of the corresponding supersymmetric particles are listed in Table 5.

m [GeV/c^2]	LM1	LM2	LM6
$\tilde{\chi}_1^0$	97	141	162
$\tilde{\ell}_R^+$	118	229	175
$\tilde{\ell}_L^+$	184	301	283
$\tilde{\tau}_1^+$	109	156	168
$\tilde{\tau}_2^+$	189	313	286
$\tilde{\chi}_1^+$	180	265	303
$\tilde{\chi}_2^+$	369	474	541
H^+	386	431	589

Table 5: Masses of SUSY particles, in GeV/c^2, for different benchmarks (here $\ell = e, \mu$)

The study concentrates on the fully leptonic SUSY case only. The corresponding Feynman diagrams are shown in Figure 10. Signal and background samples coming from SUSY and SM pairs were produced using a modified version of CALCHEP [53]. The following acceptance cuts have been applied: two leptons with $p_T > 3$ GeV/c or 10 GeV/c and $|\eta| < 2.5$. The only irreducible background for this type of processes is the exclusive W pair production since direct lepton pairs $pp(\gamma\gamma \to \ell^+\ell^-)pp$ can be suppressed by applying large acoplanarity cuts. Standard high-level-trigger (HLT) efficiencies are high for all these types of events. In typical mSUGRA/CMSSM scenarios, a light right-handed slepton will have a branching fraction of $B(\tilde{l}^\pm \to \chi_1^0 l^\pm) = 100\%$. This results in a final state with two same-flavor opposite-sign leptons, missing energy, and two off-energy forward protons. Assuming a trigger threshold of 7 GeV/c for two isolated muons, the efficiency would be $71-74\%$ for smuons in the range of typical light mSUGRA/CMSSM benchmark points (LM1 or SPS1a). With an integrated luminosity of 100 fb^{-1}, this would result in a sample of $15-30$ triggered elastic-elastic smuon pairs, plus a slightly smaller number of selectron pairs. Including the less clean singly-elastic events would increase these yields by roughly a factor of 5. The irreducible $\gamma\gamma \to WW$ background can be suppressed by a factor of two by selecting only same lepton-flavour (ee, $\mu\mu$) final states. The measured energy of the two scattered protons in forward proton taggers could allow for the distinction between various contributions to the signal by looking at the distribution of the photon-photon invariant mass $W_{\gamma\gamma}$. HECTOR [60] simulations of forward protons from slepton events consistent with LM1 benchmark point indicate that the TOTEM 220 m detectors will have both protons tagged for only 30% of events. Addition of detectors at 420 m increases that to 90% of events.

The expected cumulative $W_{\gamma\gamma}$ distributions for LM1 events with two centrally measured leptons and two forward detected protons are illustrated in Figure 11. With this technique and sufficient statistics, masses of supersymmetric particles could be measured with precision of a few

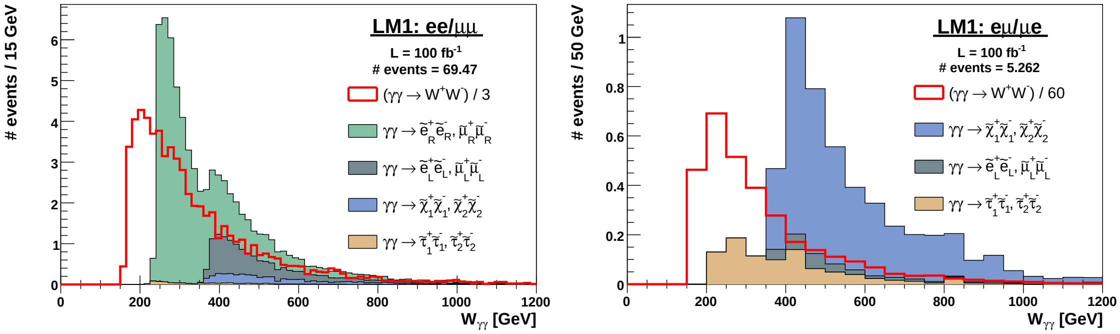

Fig. 11: Photon-photon invariant mass for benchmark point LM1 with $\int \mathcal{L}dt = 100$ fb^{-1}. Cumulative distributions for signal with two detected leptons ($p_T > 3$ GeV/c, $|\eta| < 2.5$), two detected protons, with same (left) or different flavour (right). The WW background has been down-scaled by the quoted factor [12].

GeV/c^2 by looking at the minimal centre-of-mass energy required to produce a pair of SUSY particles. In the same way, missing energy can be computed by subtracting the detected lepton energies from the measured two-photon centre-of-mass energy. For backgrounds missing energy distributions start at zero missing energy, while in SUSY cases they start only at two times the mass of the LSP.

2.8.3 Photon-proton processes

The high luminosity and the high centre-of-mass energies of photo-production processes at the LHC offer very interesting possibilities for the study of electroweak interaction and for searches Beyond the Standard Model (BSM) up to the TeV scale [12]. Differential cross sections for $pp(\gamma q/g \to X)pY$ reactions, as a function of the photon-proton centre-of-mass energy, are presented in Figure 12 together with the acceptance region of forward proton taggers. A large variety of processes have sizeable cross section up to the electroweak scale and could therefore be studied during the very low and low luminosity phases of the LHC. Interestingly, potential Standard Model background processes with hard leptons, missing energy and jets coming from the production of gauge bosons, have cross sections only one or two orders of magnitude higher than those involving top quarks. The large top quark photo-production cross sections, $\mathcal{O}$(pb), are particularly interesting for measuring top quark related SM parameters, such as the top quark mass and its electric charge. In addition, and in contrast to parton-parton top production, photo-production of top quark pairs and of single top in association with a W boson have similar cross sections. This will certainly be advantageous in analyses aiming at measuring the Cabibbo-Kobayashi-Maskawa (CKM) matrix element $|V_{tb}|$ in associated Wt production.

In order to illustrate the discovery potential of photon-proton interactions at the LHC, we discuss in the next two subsections the possibility to observe: (i) the SM Higgs boson produced in

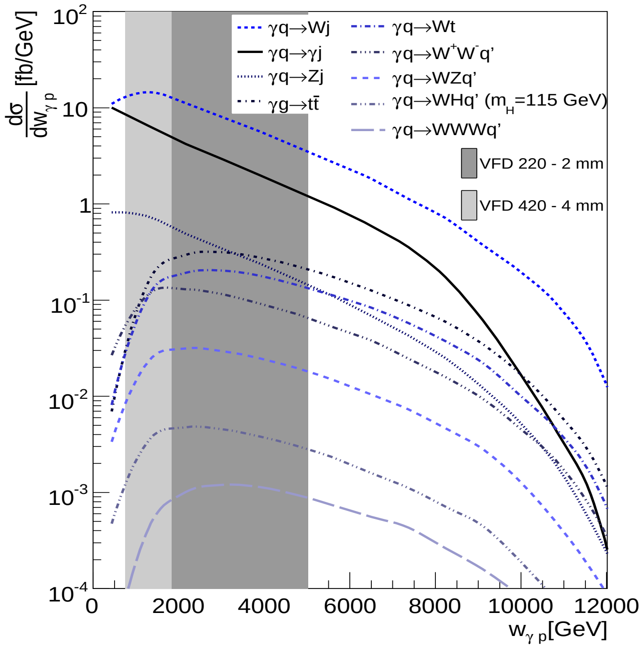

Fig. 12: Differential cross-sections for $pp(\gamma q/g \to X)pY$ processes as a function of the c.m.s. energy in photon-proton collisions, $W_{\gamma p}$. The acceptance of roman pots (220 m at 2 mm from the beam axis and 420 m at 4 mm from the beam axis) is also sketched [12].

association with a W ($\sigma_{WH} \approx 20$ fb for M_H = 115 GeV/c^2, representing more than 2% of the total inclusive WH production at the LHC), (ii) the anomalous production of single top, which could reveal BSM phenomena via Flavour Changing Neutral Currents (FCNC).

Associated WH production

The search for WH associate production at the LHC will be challenging due to the large W+jets, $t\bar{t}$ and WZ cross sections. Indeed, although Standard Model cross sections for the process $pp \to WHX$ range from 1.5 pb to 425 fb for Higgs boson masses of 115 GeV/c^2 and 170 GeV/c^2 respectively, this reaction is generally not considered as a Higgs discovery channel. This production mechanism however, is sensitive to WWH coupling which might be enhanced when considering fermiophobic models, and might also give valuable information on the $Hb\bar{b}$ coupling, which is particularly difficult to determine at the LHC. The possibility of using γp collisions to search for WH associate production was already considered at electron-proton colliders [70]. At the LHC the cross section for $pp(\gamma q \to WHq')pY$ reaction reaches 23 (17.5) fb for a Higgs boson mass of 115

GeV/c^2 (170 GeV/c^2). The dominant Feynman diagrams are shown in Figure 13. Although cross sections are smaller than the ones initiated by quarks, the signal-to-background ratio is improved by more than one order of magnitude [12].

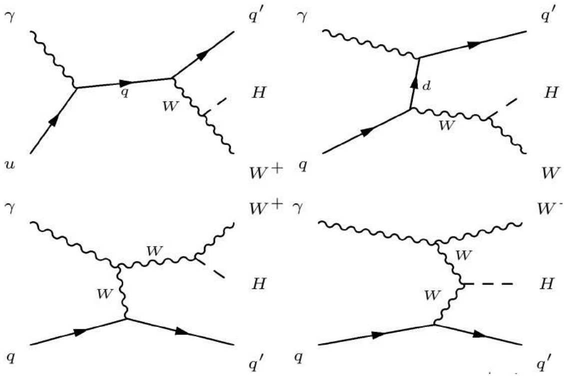

Fig. 13: The Feynman diagrams for $\gamma q \to HW^+q'$ associated production at LO [12].

Anomalous top production

In the Standard Model, exclusive single top photo-production at LHC energies is only possible for higher order electroweak interactions, since neutral currents preserve quarks flavour at tree level. The observation of a large number of single top events would hence be a sign of FCNC induced by processes beyond the Standard Model. FCNC appear in many extensions of the Standard Model, such as two Higgs-doublet models or R-parity violating supersymmetry. The dominant Feynman diagram contributing to photo-production of top quarks via FCNC, can be seen in Fig. 14. The effective Lagrangian for this anomalous coupling can be written as [71] :

$$L = iee_t\bar{t}\frac{\sigma_{\mu\nu}q^\nu}{\Lambda}k_{tu\gamma}uA^\mu + iee_t\bar{t}\frac{\sigma_{\mu\nu}q^\nu}{\Lambda}k_{tc\gamma}cA^\mu + h.c.,$$

where $\sigma_{\mu\nu}$ is defined as $(\gamma^\mu\gamma^\nu - \gamma^\nu\gamma^\mu)/2$, q^ν being the photon 4-vector and Λ an arbitrary scale, conventionally taken as the top mass. The couplings $k_{tu\gamma}$ and $k_{tc\gamma}$ are real and positive such that the cross section takes the form :

$$\sigma_{pp\to t} = \alpha_u\, k^2_{tu\gamma} + \alpha_c\, k^2_{tc\gamma}.$$

The computed α parameters using CALCHEP are $\alpha_u = 368$ pb$, \alpha_c = 122$ pb. The best limit on $k_{tu\gamma}$ is around 0.14, depending on the top mass [72] while the anomalous coupling $k_{tc\gamma}$ has not been probed yet.

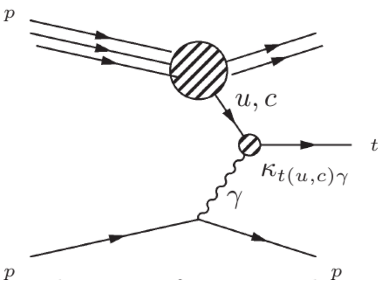

Fig. 14: Photo-production of top quarks at LHC through FCNC [12].

The single top final state is composed of a b-jet and a W boson. The main irreducible backgrounds for the considered topology, $\ell E_T^{miss} b$, come from γp interactions producing a W boson and a jet, especially c-jets which can be miss-tagged as a b-jets. Limits on the anomalous couplings $k_{tu\gamma}$ and $k_{tc\gamma}$ have been extracted after application of acceptance cuts in [12]. These results appear on Table 2.8.3 for two integrated luminosities.

Coupling limits	$\int \mathcal{L}\, dt$ = 1 fb^{-1}	$\int \mathcal{L}\, dt$ = 10 fb^{-1}
$k_{tu\gamma}$	0.043	0.024
$k_{tc\gamma}$	0.074	0.042

Table 6: Expected limits for anomalous couplings at 95% CL [12].

2.8.4 Photon-photon and photon-proton physics summary

A summary of various unique photon-photon and photon-proton interactions accessible to measurement at the LHC, and discussed in detail in [12], has been presented in this section. Interesting studies and searches can be performed for initial integrated luminosities of about 1 fb^{-1}, such as exclusive dimuon production in two-photon collisions tagged with forward large rapidity gaps. At higher luminosities, the efficient selection of photon-induced processes is greatly enhanced with dedicated forward proton taggers such as FP420. Photon induced reactions can provide much higher sensitivity than partonic reactions for various BSM signals such as e.g. anomalous quartic $\gamma\gamma WW$ gauge couplings. The associated photoproduction of a top quark or a W boson is also very large, offering a unique opportunity to measure the fundamental Standard Model parameters, such as the top quark charge or the V_{tb} element of the quark mixing matrix. Anomalous γqt couplings might also be uniquely revealed in single top photoproduction. Larger integrated luminosity, of about hundred inverse femtobarns, will open complementary ways to search for production of supersymmetric particles in photon-photon interactions. Even larger luminosities might help to access important information on the Higgs boson coupling to b quarks and W bosons. FP420 detectors are mandatory for the determination of the masses of the centrally produced particles, and to increase the sensitivity to new anomalous couplings contributions in two-photon interactions.

Last but not least, studying the photon-induced processes in the early LHC runs can provide valuable checks of the various components of the general formalism used to predict the cross sections of central exclusive reactions [36]. Thus, the photon-exchange dominated W-boson production with rapidity gaps on either side provides information on the gap survival factor S^2. As discussed in [36], such studies can be performed even without tagging of the forward proton. Another example is exclusive Υ photoproduction induced by the process $\gamma p \to \Upsilon p$ [73], now observed by CDF [48]. The study of such processes will not only reduce the theoretical uncertainties associated with the generalised, unintegrated gluon distributions f_g, e.g., by testing models based on diffusion in transverse momentum as incarnated in the Balitsky-Fadin-Kuraev-Lipatov (BFKL) equation [74], but will be of help to calibrate and align the forward proton detectors.

2.9 Diffractive physics

Proton tagging with FP420 will allow a continuation of the study of hard diffraction, expanding and extending the investigations carried out at CERN by UA8 [75], and more recently at HERA by H1 and ZEUS and at Fermilab by CDF and D0 (see, e.g., [76, 77, 8, 78] and references therein). The coverage of FP420, $0.002 < \xi < 0.02$, is centred on the diffractive-peak region where the contribution from mesonic exchanges (Reggeons) is negligible, and is thus complementary to that of TOTEM (or of any near-beam detectors at 220 m from the interaction point), which is $0.02 < \xi < 0.2$ with high-luminosity LHC optics (see Fig. 15).

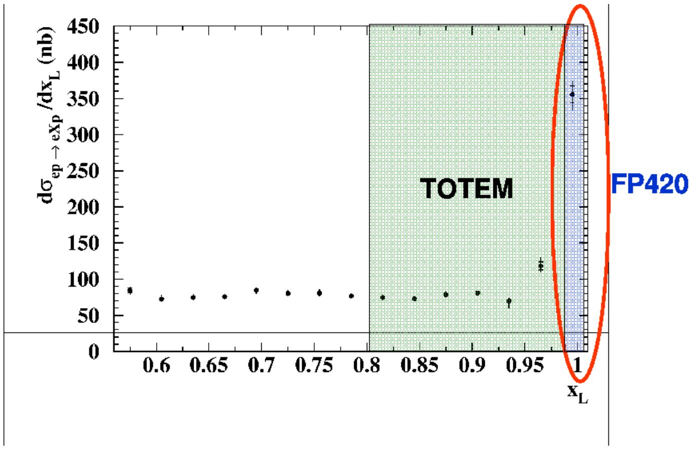

Fig. 15: $x_L = 1 - \xi$ coverage of FP420 and TOTEM (or any near-beam detectors at 220 m from the interaction point). The data points are for the reaction $ep \to eXp$ [79] and are only meant to illustrate the position of the diffractive peak at $x_L \approx 1$.

The following reactions can be studied:

1. at instantaneous luminosities where pile-up is negligible, single diffractive (SD) dissociation

of the proton, $pp \to Xp$, where one proton is measured in FP420 and the other dissociates into a state X which contains high-E_T jets, vector bosons or heavy flavours: the limitation to low luminosities is due to the fact that the timing constraint cannot be applied when only one proton is measured;

2. at all luminosities, double Pomeron exchange (DPE), $pp \to pXp$, where both protons are tagged by FP420, and again X includes high-E_T jets, vector bosons or heavy flavours;
3. also at all luminosities, central exclusive production of di-jets, $pp \to pjjp$.

Processes 1 and 2 are sensitive to the low-x structure of the proton and the diffractive parton distribution functions (dPDFs), which can be interpreted as conditional probabilities to find a parton in the proton when the final state of the process contains a fast proton of given four-momentum. Process 3 is sensitive to the generalised (skewed) parton distribution functions (GPD), which are crucial for the estimate of the cross section for central-exclusive Higgs production.

Inclusive jet and heavy quark production are mainly sensitive to the gluon component of the dPDFs, while vector boson production is sensitive to quarks. The kinematic region covered expands that explored at HERA and Tevatron, with values of β (the fractional momentum of the struck parton in the diffractive exchange) as low as 10^{-4} and of Q^2 up to tens of thousands of GeV^2.

The extraction of the dPDFs and the GPDs is complicated by the breakdown of QCD diffractive factorisation in hadron-hadron collisions: to determine the dPDFs and GPDs, it is necessary to establish by how much diffractive interactions are suppressed because of soft interactions of the spectator partons from the interacting hadrons [33, 80]. This is quantified by the so-called rapidity-gap survival probability, a critical ingredient for the calculation of the cross section for central-exclusive Higgs production. The rapidity-gap survival probability is interesting in its own right because of its relationship with multiple scattering effects and hence the structure of the underlying event in hard collisions. All three processes listed above can be used to determine the rapidity-gap survival probability. For example, as a consequence of the factorisation breakdown, the diffractive structure function extracted from SD jet production will differ from that obtained from DPE jet production. The ratio of these two structure functions is sensitive to the rapidity-gap survival probability. A rather unique additional possibility which arises with FP420 is to observe events with three (or more) large rapidity gaps; two gaps fixed by the forward protons and the third gap selected in the central detector. This may help shed further light on the dynamics behind the rapidity-gap survival probability.

Also of interest is the fact that good data on single diffractive dissociation at high energies could prove very important for a better understanding of the nature of ultra high-energy cosmic ray interactions, see e.g. Chapter 10 of ref. [8].

Finally, it is natural to expect that the secondaries produced by an ‘incoming’ pomeron ($I\!\!P$) will be enriched with glueballs (G). With tagged protons, one could look for the quasi-elastic diffractive $I\!\!Pp \to GX$ process. Similarly, tagging both protons allows one to observe $I\!\!P - I\!\!P$ interactions at much larger energies, $\sqrt{s_{I\!\!PI\!\!P}} \sim 100 - 200$ GeV, than have been explored so far.

Cross sections for hard-diffractive processes can be large, as shown in Table 7. In the following, we summarise some of the studies that have been performed.

Process	Cross section
$pp \to Xp$, with X including a W boson	70 pb
$pp \to Xp$, with X including a di-jet ($E_T > 50$ GeV)	30 nb
$pp \to pXp$, with X including a di-jet ($E_T > 50$ GeV)	1.5 nb

Table 7: Cross sections for a few hard-diffractive processes, as obtained with the POMWIG generator [81].

2.9.1 Single-diffractive production of W, Z bosons or di-jets

Selection efficiencies were studied in [8, 82] for $pp \to pX$, with X containing a W or a Z boson that decays to jets or to muons, as well as with X containing a di-jet system. Samples of 100,000 signal events each were generated with the POMWIG Monte Carlo generator [81] (version 1.3). For these studies, the CMS detector response was simulated using the OSCAR [83] package. The digitisation (simulation of the electronic response), the emulation of the Level-1 and High-Level Triggers (HLT), and the offline reconstruction of physics objects were performed with the CMS full-reconstruction ORCA package [84]. For four example processes, Fig. 16 shows the efficiency as a function of the L1 threshold value, normalised to the number of events (in the muon rate case to the number of events with a muon in the final state) with $0.001 < \xi < 0.2$. Three different trigger conditions are considered: (i) only central detector information, (ii) central detector information in conjunction with a single arm track at 220 m and (iii) central detector information in conjunction with a single arm track at 420 m. Also shown is the number of events expected to pass the L1 selection per pb^{-1} of LHC running. In [8, 82], a gap survival probability of unity was assumed. However, at the LHC this factor is expected to be $\mathcal{O}(0.1)$ [85].

2.9.2 Single-diffractive and double-Pomeron exchange production of B mesons

Inclusive SD and DPE production of B mesons, with $B \to J/\psi X$ and $J/\psi \to \mu^+\mu^-$, was studied in [8] using the generator DPEMC 2.4 [86] in conjunction with the fast CMS simulation code FAMOS, version 1.3.1 [87]. As discussed earlier, this process is sensitive to the dPDFs of the proton. Events were selected which had at least one pair of oppositely charged muons. If two pairs were found, the one with invariant mass closer to that of the J/ψ meson was taken to be the one originating from the J/ψ decay. Events were selected if $2.7 < M_{\mu\mu} < 3.5$ GeV/c^2, with $M_{\mu\mu}$ the invariant mass of the muon pair, $p_T^\mu > 3$ GeV/c (at L1) and $p_T^\mu > 7$ GeV/c (HLT). In addition, the detection of a proton on either side of the interaction point was required for the SD events and on both sides for the DPE events. The estimated event yield, after the cuts, for an integrated luminosity of 1 fb^{-1} is of hundreds of SD events and a few DPE events.

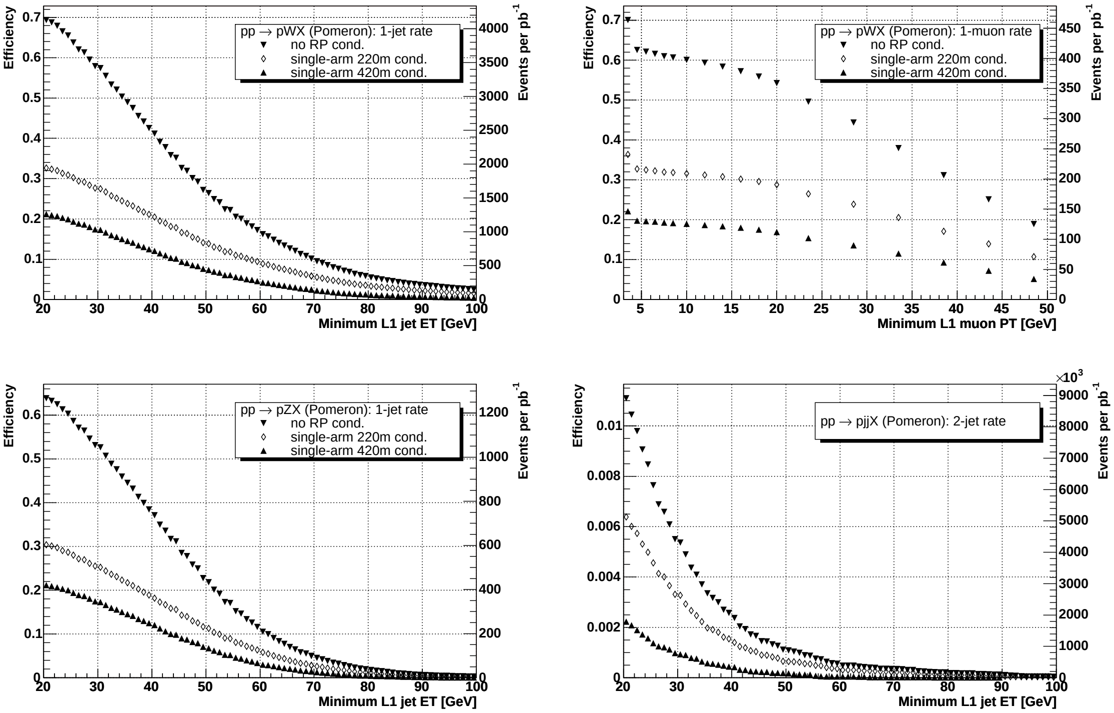

Fig. 16: Selection efficiency as function of the threshold value for $pp \to pWX$ (upper left and upper right), $pp \to pZX$ (lower left), $pp \to pjjX$ (lower right). At least one L1 jet with E_T above threshold is required (upper and lower left), at least two L1 jets with E_T above threshold are required (lower right), at least one L1 muon with p_T above threshold is required (upper right). The normalization of the efficiency curves (left y-axis) is explained in the text. The number of events expected to pass the L1 selection per pb^{-1} of LHC data (right y-axis) does not take into account the gap survival probability which at the LHC is expected to be $\mathcal{O}(0.1)$. All plots are for the non-pile-up case. From [8].

2.9.3 Double-Pomeron exchange production of W bosons

Also studied in [8] is inclusive DPE production of W bosons, $pp \to pXWp$, which probes the dPDFs of the proton. The reaction was simulated with the DPEMC generator v2.4 [86]. The generated events were passed through the fast simulation of the CMS detector, FAMOS version 1.2.0 [87]. Events in the electron channel, $W \to e\nu$, were selected by requiring an electron with $E_T > 30$ GeV and missing E_T larger than 20 GeV. These cuts are tighter than the CMS L1 trigger thresholds. Several thousand events are expected after the selection cuts, which include the demand of a tagged proton, for 1 fb^{-1}. Events in the muon channel, $W \to \mu\nu$, were selected by requiring a muon with $E_T > 20$ GeV and missing $E_T > 20$ GeV. Also these cuts are tighter than the CMS L1 trigger thresholds. The expected distributions of the W and muon variables for 1 fb^{-1} are shown in Fig. 17 for different choices of the diffractive PDFs. Here again, several thousand events are expected after the selection cuts.

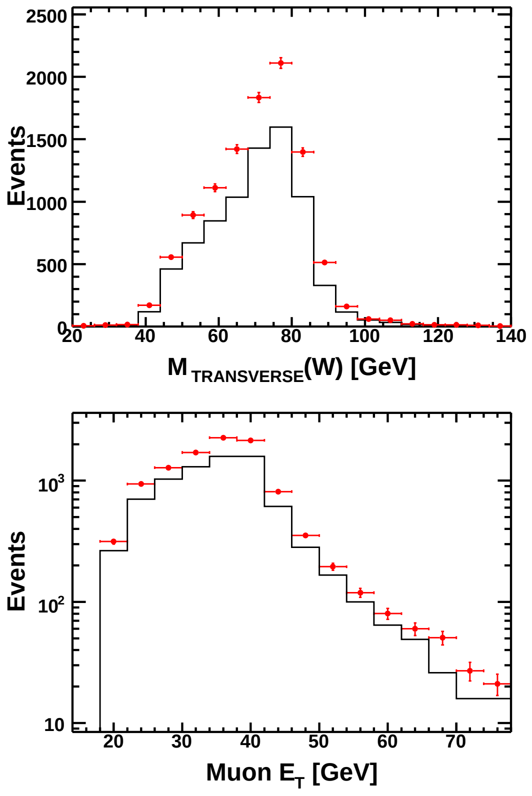

Fig. 17: Distributions, for $\int \mathcal{L} dt = 1$ fb^{-1}, of (a) transverse mass of the $W^{\pm}$ boson, (b) transverse momentum of the $W^{\pm}$, (c) transverse momentum of the muon, (d) pseudorapidity of the muon for $W \to \mu\nu$. Full points: approximately flat diffractive gluon density (H1 fit 2 [88]); histograms: more peaked diffractive gluon density (H1 fit 3 [88]). From [8].

2.10 Physics potential of p_T measurements in FP420

A study of the correlations between the proton transverse momenta p_{it} in the CEP processes will provide us with extra leverage in the the forward physics programme. First of all, such measurements are important for testing the underlying physics of diffraction [2]. The absorptive rescattering effects present in inelastic diffraction clearly violate Regge factorization and lead to non-trivial correlations between proton transverse momenta p_{1t} and p_{2t} in the process $pp \to p+M+p$. Measuring the transverse momenta and the azimuthal angle φ distribution for different values p_{it}, allows a detailed probe of the opacity of the incoming proton, and more generally, testing the dynamics of soft survival. One of the best examples to study such effects is exclusive high E_T dijet production [2, 37], where the cross section for the hard subprocess is large and well known.

Another important feature of the correlation study is that it offers a unique possibility for direct observation of a CP-violating signal in the Higgs sector by measuring the azimuthal asymmetry of the outgoing tagged protons [28, 89]. In some MSSM scenarios the azimuthal asymmetry

$$A = \frac{\sigma(\varphi < \pi) - \sigma(\varphi > \pi)}{\sigma(\varphi < \pi) + \sigma(\varphi > \pi)} \tag{3}$$

is expected [28] to be quite sizable. For instance, $A \simeq 0.07$, in a benchmark scenario of maximal CP-violation ([90]) or in the tri-mixing scenario of Ref. [26].

2.11 Other physics topics

2.11.1 Pomeron/Graviton duality in AdS/CFT

Another motivation for further study of central exclusive production is as testing ground of possible connections with string theory, through the so-called Anti-de-Sitter/Conformal-Field-Theory (AdS/CFT) or “gauge/string” correspondence [91]. The application of AdS/CFT correspondence between strongly coupled QCD and weakly coupled gravity has recently successfully applied to the computation of various observables in high-energy heavy-ion physics (see e.g. [92] and refs. therein). Diffractive scattering and the Pomeron represent another area where a connection with the string-theory-based techniques may well be ripe. Like heavy-ion physics, the physics of diffraction and the Pomeron lies largely outside the regime where perturbative field theory computations can be performed with confidence. Indeed they are known not to fully describe HERA data. Thus as in heavy-ion physics, there is much interest in approaching these phenomena with a tool which replaces non-perturbative field theory with perturbative string theory. The connection with the stringy aspects of the five-dimensional description is indeed very direct in the case of Regge phenomenology.

A number of papers by string theorists and recently even QCD/nuclear theorists have studied aspects of the Pomeron, which in the string theory description is related to the graviton and its higher spin partners on the leading (five-dimensional) Regge trajectory (see e.g. [93] and refs. therein). The physics of the Pomeron has been described with considerable technical success, allowing insights into various aspects of Regge phenomenology in the corresponding four-dimensional gauge theories. Few attempts have been made so far to connect these technical results with QCD data, and the question of whether this connection will be as suggestive as in the nucleus-nucleus case remains open at present. Also, important problems of relevance to the current proposal, such as central hadron production, rapidity gap suppression, and Higgs boson production are just now receiving some (as yet unpublished) technical consideration from theorists. But there is a real opportunity for growth of an interdisciplinary research area out of diffractive physics in general and central diffractive production in particular.

2.11.2 Exotic new physics scenarios in CEP

A.R. White has developed [94, 95] a theory of the pomeron which requires the existence of new particles in the LHC domain, and would give rise to dramatic effects in diffraction. If correct, exclusive processes such as $p+p \rightarrow p+W^+W^-+p$ and $p+p \rightarrow p+ZZ+p$ could be orders of magnitude higher than in the Standard Model. In the Standard Model, exclusive W^+W^- production occurs mainly through $\gamma\gamma \rightarrow W^+W^-$ and $h \rightarrow W^+W^-$, if the Higgs boson exists with $M_h \sim 135$ GeV/c^2. Exclusive ZZ production only proceeds, to a good approximation, through h decay. In White's theory the pomeron is approximately a reggeised gluon together with a sea of 'wee' gluons, with the unitary Critical Pomeron produced via reggeon field theory interactions. A special version of QCD, QCD_S, is required in which the asymptotic freedom constraint is saturated, a requirement naturally satisfied by QCD_S, which contains the known six colour triplet quarks plus a doublet, $[U,D]$, of heavy (hundreds of GeV) colour sextet quarks. The Higgs mechanism is provided, not by a fundamental scalar Higgs boson, but by sextet pion composites, i.e. $[U\bar{U}-D\bar{D}]$. This results in a relatively strong coupling between the pomeron and vector bosons, with large cross sections for $I\!\!P I\!\!P \rightarrow W^+W^-$ and $I\!\!P I\!\!P \rightarrow ZZ$. The enhancement in diffractive W^+W^- and ZZ production (but not WZ production) should be large enough to see without forward proton tagging, with or without requiring large rapidity gaps. However, determining that the pomeron - vector boson coupling is responsible and studying it in detail will require forward proton measurements. QCD_S provides a natural dark matter candidate, the sextet neutron, $N_6 = [UDD]$, which should be stable and have a mass in the TeV range. QCD_S also embeds uniquely in an underlying SU(5) theory, called QUD, which potentially describes the full Standard Model.

3 Simulated measurement of $h \to b\bar{b}$ in the MSSM

As a more detailed example of our proposed methodology, we describe in this section how we intend to study the production of the MSSM $h \to b\bar{b}$ channel. Full details can be found in [20]. Similar cuts to reduce the backgrounds are found in the analysis for the CMS-TOTEM document [8] and also in Ref. [19]. There are two properties of FP420 that are critical to the detection of Higgs bosons in any decay channel. The first is the acceptance, described in detail in Section 4, which for a fixed LHC optics depends primarily on the distance of approach of the active edge of the silicon detectors to the beam. We will focus on those events in which both protons are tagged at 420 m, although we comment on the inclusion of forward detectors at 220 m in Section 3.4. For 120 GeV/c^2 central systems, the acceptance is independent of the distance of approach out to approximately 7 mm (10σ is 2.5 mm at 420 m). Here we assume that the active edge of the 420 m detectors is 5 mm from the beam, which gives an acceptance of 28% for both protons to be detected.

The second important property of FP420 is its ability to measure the difference in arrival time of the forward protons on opposite sides of the central detector. This allows a measurement, from timing information alone, of the vertex position of the Higgs candidate event in the central detector, under the assumption that the detected protons are from the same proton-proton collision as the Higgs candidate. This vertex-matching requirement – between the vertex determined with the central detectors and that obtained with the fast-timing forward detectors – is vitally important at the high LHC luminosities, where the large number of proton-proton collisions per bunch crossing (often referred to as pile-up) leads to a high probability that forward protons from single diffractive or double pomeron (DPE) collisions not associated with the Higgs candidate event will enter the forward detectors during the same bunch crossing. The design goal is to achieve a timing resolution of 10 ps in the detectors with negligible jitter in the reference timing system. This corresponds to a vertex measurement accurate to 2.1 mm from the tagged protons. The FP420 fast timing system is described in detail in Section 10.

The central exclusive signal events were generated using the ExHuME Monte Carlo v1.3.4 [96], which contains a direct implementation of the calculation described in Section 2.2. Using CTEQ6M PDFs and soft survival factor $S^2 = 0.03$, the cross section $\times$ branching ratio to $b\bar{b}$ for the CEP of a Higgs boson of mass $M_h = 119.5$ GeV/c^2 in the M_h^{max} scenario of the MSSM is predicted to be 20 fb. There are three primary sources of background;

1. Central exclusive dijet backgrounds. Central exclusive $b\bar{b}$ production is suppressed by the $J_z = 0$ selection rule, but will still be present at a reduced rate and forms an irreducible continuum beneath the Higgs boson mass peak. Central exclusive glue-glue production is not suppressed, and contributes to the background when the gluon jets are mis-identified as b-jets. The mis-tag rate at ATLAS for gluon jets is 1.3%, leading to a mis-tag rate for di-gluons of 1.69×10^{-4}. These are the dominant central exclusive backgrounds; the other CEP background contributions, such as gHg and $b\bar{b}g$ discussed in [14, 97], are either small from the beginning or could be suppressed due to the experimental cuts outlined in Section 3.2.
2. Double pomeron backgrounds. Double pomeron exchange (DPE) is defined as the process

$pp \rightarrow p + X + p$ where X is a central system produced by pomeron-pomeron fusion. In this picture the pomeron has a partonic structure and the system X therefore always contains pomeron remnants in addition to the hard scatter. DPE events are simulated using the POMWIG v2.0 Monte Carlo [81] with the H1 2006 fit B diffractive PDFs [98] and $S^2 = 0.03$. With this choice of PDF, the DPE background is expected to be small [99]. The effect of different choices of diffractive PDFs is studied in [20] and found to make little difference to the overall conclusions.

3. Overlap backgrounds. Overlap events (as discussed in [8, 20]) are defined as a coincidence between an event that produces a Higgs boson candidate in the central detector and one or more single diffractive or DPE events which produce protons in the acceptance range of the forward detectors. Note that non-diffractive protons become important only for detectors at 220 m [20] and that protons from photon-induced processes are negligible in comparison to single diffraction. At a luminosity of 10^{33} cm^{-2} s^{-1} (low luminosity) there will be on average 3.5 interactions per bunch crossing including elastic scattering, and 35 interactions per bunch crossing at 10^{34} cm^{-2} s^{-1} (high luminosity). There are three possible types of overlap background, for which we use the following notation: [p][X][p] for events in which there is a coincidence of three overlapping events, the detected protons coming overwhelmingly from soft single diffractive events; [pp][X] where the detected protons come from a single double pomeron exchange event; [pX][p] for events in which a single diffractive event produces a hard central system which fakes a Higgs candidate, and a second event produces a proton on the opposite side.

   These backgrounds are approximately 10^7 times larger than the signal. The majority of the rejection is achieved through kinematic and topological variables as demonstrated in the following sections. However, the proton time-of-flight (TOF) information from FP420 provides an additional reduction. As described above, a 10 ps resolution in the proton time-of-flight gives a vertex measurement accurate to 2.1 mm. For the overlap backgrounds however, the protons tagged by FP420 do not come from the same interaction as the dijets and therefore the event vertex implied from proton TOF will not, in general, match the dijet vertex measured by the inner tracking detectors. A TOF measurement accurate to 10 ps gives a rejection factor of 18 at low luminosity and 14 at high luminosity[6] for [p][X][p] events, if we require that the two vertex measurements differ by no more than 4.2 mm (2σ) and the spread in interaction points is ∼4.5 cm. This rejection factor is used as a default in the following sections. Results are also presented in the scenario that the overlap background can be effectively removed, for example by improved efficiency of the kinematic and topological rejection variables (discussed in Section 3.2) and/or an improvement in the fast-timing system - i.e. a TOF measurement accurate to 2 ps results in a factor 5 increase in the overlap rejection factor (see Sec. 10)[7].

---

[6] The luminosity dependence arises due more than one proton occurring in an arm of FP420. In this case, the event is retained if any of the predicted vertices from ΔTOF matched the dijet vertex.

[7] While this is beyond present-day performance, it may be achievable on a few-years timescale and there is an active R&D programme. Note that the detectors have very small area ∼1 cm^2.

Background events are constructed using ExHuME for the exclusive events, POMWIG for the hard single diffractive and DPE events, and HERWIG + JIMMY [100, 101] for the hard dijet system [X] in [p][X][p] and [pp][X] events. The soft single diffractive protons are generated according to a parameterisation of the single diffractive cross section at LHC energies given in [85], which has been normalised to CDF data, and added into the event record. The forward proton momenta are smeared by the expected resolution of FP420 and the central particles are smeared to simulate the response of the ATLAS detectors. Full details are given in [20].

3.1 Trigger strategy for $h \to b\bar{b}$

FP420 is too far away from the central detector to be included in the current level 1 (L1) trigger systems of ATLAS and CMS, which have a latency of 2.5 μs and 3.5 μs respectively. However, for all CEP analyses, information from FP420 can be used at level 2 (L2) and/or high-level-trigger (HLT) to substantially reduce the rate. The requirement that there be two in-time protons detected at 420 m would reduce the rate at L2 by a factor of $\sim$20000 (140) at a luminosity of 10^{33} (10^{34}) cm^{-2} s^{-1}. In addition, cuts on basic topological variables, such as those outlined in Section 3.2, which compare the kinematics of the central system measured by ATLAS/CMS to that measured by FP420, would reduce the rate further.

The challenge therefore is to design a trigger strategy, based on central detector information, that is capable of retaining CEP events at L1. The situation for a light Higgs boson decaying to b-jets is especially difficult because the un-prescaled threshold for dijets at ATLAS is foreseen to be 180 GeV at low luminosity and 290 GeV at high luminosity due to the large rate for QCD $2 \to 2$ scatters at hadron colliders. In this analysis, we consider three possible L1 triggers. The first is a low p_T muon trigger of 6 GeV/c in addition to a 40 GeV jet, which is labeled MU6 in the analysis that follows. The jet requirement is required to reduce the rate for low p_T muons at high luminosity. We also consider a higher muon threshold of 10 GeV/c (MU10). The MU6 (MU10) trigger at ATLAS has an efficiency of 10% (6%) for a $b\bar{b}$ system. A similar trigger was considered in the CMS-TOTEM studies [8], that is, a 40 GeV jet with a 3 GeV/c muon, which was found to have an efficiency of 9%.

The second trigger is to require a rapidity gap in addition to the 40 GeV jet. Such a trigger requires a central jets with $E_T > 40$ GeV and a lack of hadronic activity in the forward region. The gap would be defined in the forward calorimeters of ATLAS/CMS, which approximately cover $3 < |\eta| < 5$. At ATLAS, an additional gap could be defined in the LUCID detectors, which cover $5.4 < |\eta| < 6.1$, and the Zero Degree Calorimeter (ZDC) [102], which covers $8.3 < |\eta| < 9.2$. At CMS IP, the gap could be extended to cover $3.1 < |\eta| < 4.7$ by the TOTEM T1 detector, $5.1 < |\eta| < 6.5$, by the CASTOR [103] and TOTEM T2 detectors, $5.2 \lesssim |\eta| \lesssim 6.6$, and $|\eta| > 8.1$ for neutral particles in the ZDC [104]. It was found in [8] that the L1 rate for the QCD production of jets was reduced by several orders of magnitude by requiring that the T1 and T2 detectors be devoid of activity. The CEP process, however, would have 90% efficiency in the absence of pile-up events in the same bunch crossing. This means that the rapidity gap trigger is self pre-scaling with luminosity; at 10^{33} cm^{-2} s^{-1} the probability for no pile-up events is 17%, which drops to 2% at 2×10^{33} cm^{-2} s^{-1}.

The final trigger is to allow a high, fixed L1 rate for 40 GeV jets, which is then substantially reduced at L2 by utilizing information from FP420 as outlined above. In this analysis, we consider a 25 kHz (J25) and a 10 kHz (J10) fixed L1 rate. The J25 trigger would not be pre-scaled at a luminosity of 10^{33} cm^{-2} s^{-1} and would be pre-scaled by a factor of 10 at 10^{34} cm^{-2} s^{-1}. At L2, requiring two in-time proton hits would reduce the J25 rate to less than 200 Hz at high luminosity and could be reduced further to a few Hz by using the basic topological requirements outlined in Section 3.2.

A complementary L1 trigger has been considered in [8] for the CMS-TOTEM system, which was not considered in the analysis presented here. The trigger strategy utilises the scalar sum, H_T, of all jets. The requirement that essentially all of the transverse energy be concentrated in two central jets, i.e that $(E_T^1+E_T^2)/H_T > 0.9$, reduces the QCD rate by a factor of two but barely affects the signal. Thus the J25 trigger, which is considered to be a fixed rate of 25 kHz, could in fact have a final L1 output rate of 12.5 kHz. Another way to tag events with protons in FP420 proposed in [8] makes use of a diffractive type of trigger sensitive to asymmetric events where one proton is detected in one FP420 detector and the other proton in the 220 m Roman Pot on the other side. This is briefly discussed in Section 3.4

3.2 Experimental cuts on the final state

The Monte Carlo samples are initially standardised by requiring that there are two jets, one with $E_T > 45$ GeV and one with $E_T > 30$ GeV; the jets are reconstructed using the cone algorithm with cone radius of 0.7. Furthermore, the outgoing protons are required to lie within the acceptance of FP420 as defined in Section 4. This corresponds approximately to the kinematic range $0.005 \leq \xi_1 \leq 0.018$, $0.004 \leq \xi_2 \leq 0.014$ and unrestricted in t, where ξ is the fractional longitudinal momentum loss of the outgoing proton and t is the squared 4-momentum transfer at the proton vertex. Full details are given in [20]. The following variables are then useful to characterise CEP events:

- The difference in rapidity, Δy, of the central system measured by FP420 to that measured from the average pseudo-rapidity of the dijets, i.e.

  $$\Delta y = \left| y - \left(\frac{\eta_1+\eta_2}{2} \right) \right| \tag{4}$$

  where y is the rapidity of the central system measured by FP420 and is given by

  $$y = \frac{1}{2}\ln\left(\frac{\xi_1}{\xi_2}\right). \tag{5}$$

- The dijet mass fraction, R_j, which is the fraction of the mass of the centrally produced system carried by the dijets. R_j is an improved definition [105] of the dijet mass fraction variable

R_{jj}, which has been used to identify exclusive events at CDF [37]. R_j is defined as

$$R_j = \frac{2E_T^1}{M}\cosh(\eta_1 - y), \tag{6}$$

where E_T^1 and η_1 are the transverse energy and pseudo-rapidity of the leading jet in the event and M is the mass of the central system measured by FP420, given by

$$M^2 \approx \xi_1 \xi_2 s \tag{7}$$

where $\sqrt{s}$ is the centre-of-mass energy of the proton-proton interaction. For a true CEP event with no out-of-cone and detector smearing effects, $R_j = 1$.

- The multiplicities of charged tracks, N_C and $N_C^{\perp}$, with $p_T \geq 0.5$ GeV/c and $|\eta| \leq 1.75$ that are associated with (i.e. within ±2.6 mm of) the dijet vertex. N_C is the number of charged particles in the event that are not associated with the hard scatter, i.e. not contained within the jet cones. It is of course dependent on the jet algorithm used to reconstruct the jets. $N_C^{\perp}$, defined as the number of charged tracks that are perpendicular in azimuth to the leading jet, provides a measure of the particle multiplicity associated with the underlying event. Both N_C and $N_C^{\perp}$ should vanish for CEP processes with negligible final-state radiation and underlying event. We use the definition adopted in [106], which assigns charged particles to the underlying event if they satisfy

$$\frac{\pi}{3} \leq |\phi_k - \phi_1| \leq \frac{2\pi}{3} \quad \text{and} \quad \frac{4\pi}{3} \leq |\phi_k - \phi_1| \leq \frac{5\pi}{3}, \tag{8}$$

  where ϕ_k is the azimuthal angle of a given charged particle and ϕ_1 is the azimuthal angle of the highest transverse energy jet. We also choose to not use the full inner detector tracking coverage ($|\eta| \leq 2.5$) to count charged tracks so that a small vertex window can be used; particles at large pseudo-rapidity have the poorest vertex reconstruction and would require a larger vertex window, which would increase the probability of tracks from pile-up events contaminating the signal (and background).

These variables are extremely efficient at separating the overlap and DPE backgrounds from the CEP events. For overlap events, the central system kinematics predicted by FP420 do not, in general, match the observed dijet kinematics. Figure 18(a) shows the R_j distribution for signal, DPE and overlap events and Fig. 18(b) shows the Δy distribution. To a good approximation, the overlap background is flat over a very large region of R_j and Δy, whereas the signal forms a well defined and narrow peak. Figures 19(a) and 19(b) show the N_C and $N_C^{\perp}$ distributions respectively. As expected, the central exclusive events have few charged particles outside of the jet cones. In contrast, the overlap events have many charged particles due to the break up of the protons and the underlying event activity associated with standard QCD events at the LHC. The final exclusive candidate sample is defined by the following cuts:

- The dijet mass fraction, $0.75 \leq R_j \leq 1.1$.

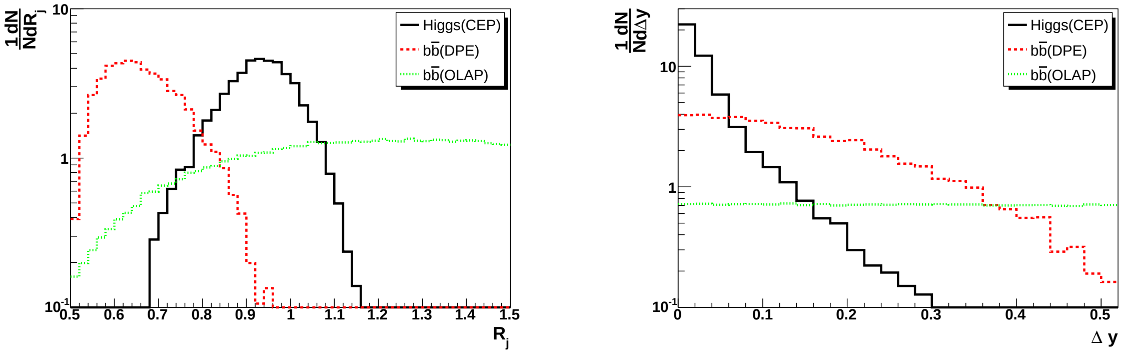

(a) (b)

Fig. 18: The R_j and Δy distributions are shown in (a) and (b) respectively for the signal, [p][$b\bar{b}$][p] and DPE [p $b\bar{b}$ p] backgrounds . The distributions were reconstructed using a cone radius of 0.7 after smearing the particles with detector resolution.

- The difference in rapidity of the central system measured by FP420 to that measured from the dijets, $\Delta y \leq 0.06$.
- The jets are back-to-back , i.e $\pi - |\Delta\phi| \leq 0.15$.
- The charged track multiplicity associated with the dijet vertex, $N_C \leq 3$ and $N_C^{\perp} \leq 1$.

3.3 Results and significances

The cross sections for the signal and the dominant backgrounds, excluding the trigger efficiency, are shown in Table 8. The final cross sections are defined in a mass window around the Higgs boson mass of $\Delta M = \pm 5.2$ GeV/c^2. This is significantly larger than the projected resolution of the forward detectors because the width of the Higgs boson with this choice of MSSM parameters (M_A = 120 GeV, $\tan\beta = 40$, μ = 200 GeV) is 3.3 GeV/c^2. The overlap backgrounds are defined at a luminosity of 10^{34} cm^{-2} s^{-1}, which is the worst-case scenario because even when the LHC is operating at peak design luminosity the average luminosity over a fill will be lower than 10^{34} cm^{-2} s^{-1}. Table 8 shows that the dominant background at high luminosity is the [p][X][p] overlap background.

In order to determine the significance of the signal, a pseudo-data sample was constructed using the generators described above and a full analysis was performed including various L1 trigger strategies and applying the aforementioned selection cuts. Figure 20(a) shows a simulated mass fit after 3 years of data taking at 2×10^{33} cm^{-2} s^{-1}, corresponding to an integrated luminosity of 60 fb^{-1}. The L1 trigger strategy is J25 + MU6 + rapidity gap trigger (see definitions in Sec 3.1). The peak is fitted with a Gaussian function, which represents the known mass resolution of FP420, convoluted with a Lorentzian function. The shape of the background is assumed to be well known,

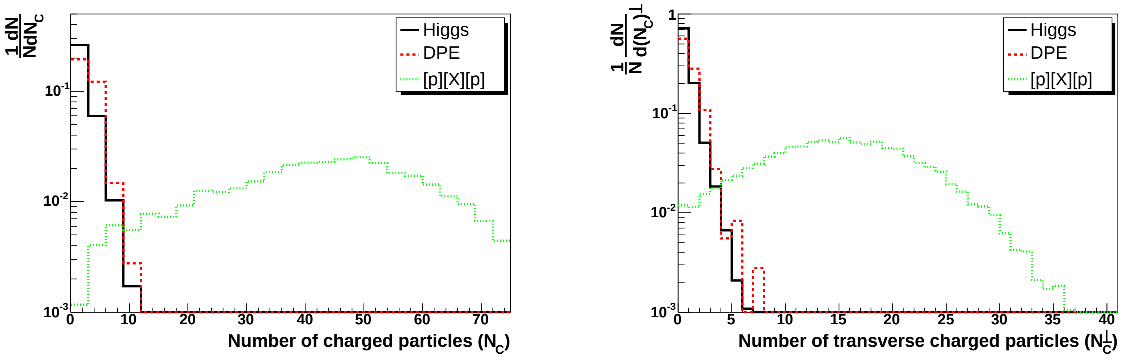

(a) (b)

Fig. 19: (a) The charged track multiplicity outside of the dijet system, N_C. (b) The number of charged particles that are transverse to the leading jet as defined by equation (8). In both cases the particles must satisfy $p_T > 0.5$ GeV/c and $|\eta| \leq 1.75$. Only 80% of the particles are used, which replicates ATLAS reconstruction efficiency for low p_T tracks.

as it can be measured with high statistics using the forward detectors; in our case, we use all the MC events (in the correct ratio) to determine the shape[8]. The significance of this fit is 3.5σ.

Figure 20(b) shows a mass fit for the same experimental conditions for 3 years of data taking at 10^{34} cm^{-2} s^{-1} (300 fb^{-1}). Because of the increase in overlap backgrounds, the significance falls slightly to 3σ and improvements in the overlap rejection are required to take full advantage of the high luminosity. This could be achieved through an upgrade to the fast-timing system, as discussed in Section 10, or an improvement in the background rejection variables. Figure 21(a) shows the same mass fit under the assumption that the overlap backgrounds can be effectively eliminated; the significance is now 5σ. Figure 21(b) shows the significance as a function of luminosity for two different L1 trigger strategies, J25 + MU6 and a more conservative J10 + MU10. The curves labelled OLAP are for the baseline rejection factors shown in Table 8. Curves are also shown for the improved overlap rejection and above luminosities of 5×10^{33} cm^{-2} s^{-1} it becomes valuable to push for additional rejection and improved timing. This suggests a possible upgrade strategy for the FP420 timing system.

The largest loss of events at high luminosity comes from the L1 trigger efficiency, which is at best around 20% at 10^{34} cm^{-2} s^{-1} for the L1 strategies considered here, although it is close to 100% at 10^{33} cm^{-2} s^{-1} . If, in a future upgrade to the central detectors, the L1 trigger latency were increased beyond 4 μs, a trigger efficiency of close to 100% could be achieved by requiring two forward protons tagged by FP420. Coupled with improved fast timing, a 5σ observation with a mass measurement better than 1 GeV/c^2 could be achieved for 100 fb^{-1} of data taken at 10^{34} cm^{-2} s^{-1}.

---

[8] We have also checked the possibility of using a quadratic background and reach the same results.

	Cross section (fb)						
Cut	CEP			DPE	[p][X][p]	[p][pX]	[pp][X]
	$h \to bb$	bb	gg	bb	bb	bb	bb
E_T, ξ_1, ξ_2, M	1.011	1.390	2.145	0.666	5.42×10^6	8.98×10^3	1.16×10^6
TOF (2σ,10 ps)	0.960	1.320	2.038	0.633	3.91×10^5	7.33×10^2	6.29×10^4
R_j	0.919	1.182	1.905	0.218	4.73×10^4	85.2	7.59×10^3
Δy	0.774	1.036	1.397	0.063	2.16×10^3	1.38	3.50×10^2
$\Delta\Phi$	0.724	0.996	1.229	0.058	6.66×10^2	0.77	1.07×10^2
N_C, $N_C^{\perp}$	0.652	0.923	0.932	0.044	6.49	0.45	1.35
ΔM	0.539	0.152	0.191	0.009	1.28	0.06	0.28

Table 8: Cross section (fb) for the CEP Higgs boson signal and associated backgrounds after applying each one of the cuts in the text. The first cut requires that both protons are tagged at 420 m, the mass measured by the forward detectors is between 80 and 160 GeV/c^2 and the transverse energy of the leading jet is greater than 40 GeV. The second cut is the requirement that the di-jet vertex is within ±4.2 mm of the vertex predicted by proton TOF. The overlap backgrounds are defined at high luminosity (10^{34} cm^{-2} s^{-1}).

For the benchmark scenario discussed above, the fits to the simulated data were relatively insensitive to the width of the Higgs state, which was 3.3 GeV/c^2. For Higgs bosons of decay width $\sim$ 5 GeV/c^2 and greater, a measurement of the width should be possible with the standard FP420 experimental configuration for those regions of MSSM parameter space in which the cross sections are 10 times larger than the Standard Model cross section.

3.4 Inclusion of forward detectors at 220 m

Adding forward detectors at 220 m, in addition to FP420, has a number of benefits for this analysis. Firstly, for a 120 GeV/c^2 central system, there can be a large acceptance for asymmetrically tagged protons, i.e. one tagged at 420 m and one at 220 m. The exact acceptance depends on the distance of the detectors from the beam (see Section 4) and is approximately 16% if the 220 m detectors are 2 mm from the beam and the FP420 detectors are 5 mm from the beam[9]. If the analysis is repeated for both symmetric and asymmetric tagged events, the significance increases to 4.4σ for the J25+MU6 trigger for 60 fb^{-1} collected at 2×10^{33} cm^{-2} s^{-1}. If improvements in fast-timing or rejection techniques result in the removal of the overlap backgrounds, the significance for 300 fb^{-1} of data collected at 10^{34} cm^{-2} s^{-1} increases to 5.5σ (3.6σ) for the J25+MU6 (J10+MU10) trigger strategy. The combined significances increases further if the detectors are moved closer to the beam.

It is also possible to devise a L1 trigger strategy for the asymmetric events incorporating information from the 220 m detectors. The trigger would require a proton hit, with a momentum

---

[9] The beam spot is smaller at 220 m and the detectors can be placed much closer to the beam

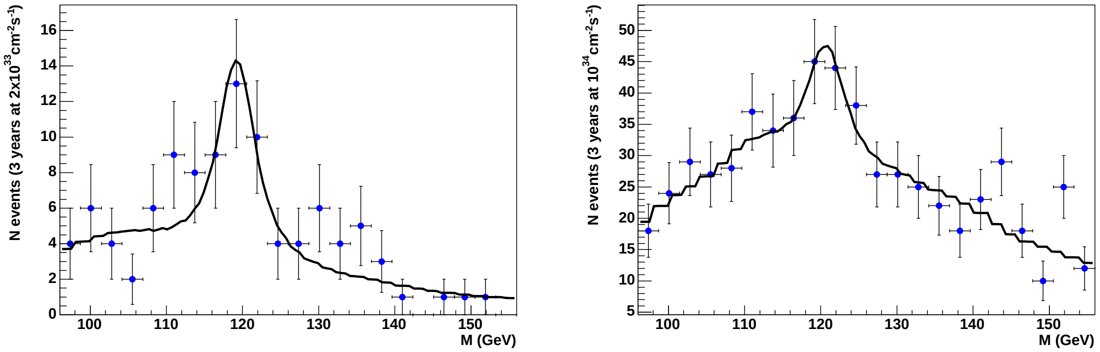

(a) (b)

Fig. 20: Typical mass fits for the 120 GeV/c^2 MSSM $h \to b\bar{b}$, with the L1 trigger and analysis cuts discussed in the text, for 3 years of data taking at 2×10^{33} cm^{-2} s^{-1} (60 fb^{-1} 3.5σ, left plot) and at 10^{34} cm^{-2} s^{-1} (300 fb^{-1}, 3σ, right plot).

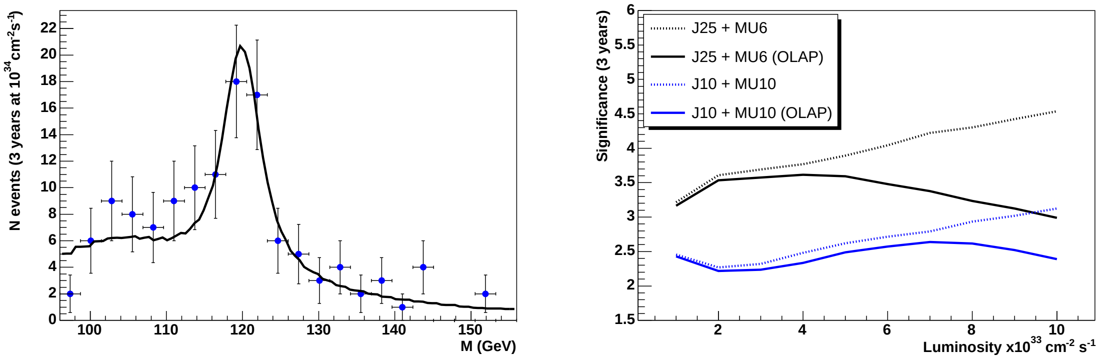

(a) (b)

Fig. 21: (a) Typical mass fit for the 120 GeV/c^2 MSSM $h \to b\bar{b}$ for 3 years of data taking at 10^{34} cm^{-2} s^{-1} after removing the overlap background contribution completely with improved timing detectors. The significance is 5σ for these data. (b) Significance of the measurement of the 120 GeV/c^2 MSSM Higgs boson versus luminosity, for two different combinations of muon – MU6, MU10 – and jet-rate – J25, J10 – triggers, see Sec. 3.1, and with an improved (baseline) FP420 timing design (OLAP labels).

loss measurement that is compatible with an opposite side proton hit at 420 m, and that the jet energies contained the majority of the energy deposited in the calorimeters. Such a trigger would have a rate below 1kHz up to an instantaneous luminosity of 2×10^{33} cm^{-2} s^{-1} [8]. Thus at low luminosities, all of the asymmetric tagged events could be retained for little bandwidth and at high luminosities this approach would act as another method to reduce the prescale for events with low E_T jets. It is demonstrated in [20] that the significance of the asymmetric events using this trigger strategy is 3.2σ for 60 fb^{-1} of data collected at 2×10^{33} cm^{-2} s^{-1}, if the forward detectors at 220 m (420 m) are placed at 2 mm (5 mm) from the beam. The significance increases to 5σ if the detectors are moved to 1.5 mm (3 mm) from the beam.

3.5 Comparison of the $h,H \to b\bar{b}$ analyses

In this section, we compare the results of Heinemeyer et al. [19] (Sec. 2.4) to the results of Cox et al. [20] (presented in Section 3.3) for a 120 GeV/c^2 Higgs boson. The overall signal efficiency, excluding the trigger, assumed by Heinemeyer et al. is 2.0% for protons tagged at 420 m. This efficiency is found using the fast simulation of CMS and is very similar to the analysis published in [8] for SM $h \to b\bar{b}$. The corresponding efficiency observed by Cox et al. is 2.7%. Note that Cox et al. use a larger mass window, which results in the a factor $\sim$1.3 more events. After normalizing to the larger mass window, the Heinemeyer et al. efficiency increases to 2.5%. There are two ongoing analysis using the ATLAS fast detector simulation that show similar experimental efficiencies.

The expected number of overlap events, for the combined 420/220 detector acceptance, is found to be 1.8 by Cox et al. for 30 fb^{-1} of data taken at 10^{33} cm^{-2} s^{-1}. This includes a mass window around the Higgs boson peak as outlined in Section 3.3. Very large rejection factors are obtained using the exclusivity variables, R_j, Δy, N_C and $N_C^{\perp}$, as shown in Table 8. These rejection factors are also being studied using the ATLAS fast detector simulation. Preliminary results are consistent with Cox et al. [20]. The effects of using different event generators for the inclusive QCD event background has also been studied. Using Pythia [107], with the ATLAS/DWT tunes to Tevatron data [106] predicts less underlying event activity at the LHC than HERWIG+JIMMY. The corresponding rejection factor of the N_C and $N_C^{\perp}$ cuts is at least a factor of two smaller when using Pythia [20]. The nature of the underlying event at the LHC will be determined with very early data. Despite this uncertainty due to the different underlying event models, it has been demonstrated that the overlap background rejection from the charged track multiplicity cut is largely unaffected by changes in luminosity.

Different trigger strategies are employed in the analyses presented in Secs. 2.4 and 3. Heinemeyer et al. do not consider a pre-scaled jet rate trigger - the majority of the events in the analysis are triggered at L1 by a proton tag at 220 m. The significance of the measurement, given a 120 GeV/c^2 Higgs boson at $\tan\beta = 40$, is slightly larger than 3σ given 60 fb^{-1} of data (Fig 4, 60 fb^{-1}). As discussed in Section 3.4, Cox et al. find that the asymmetric tagging alone achieves a significance in the region of 3.2σ to 5σ for 60 fb^{-1} of data collected at 2×10^{33} cm^{-2} s^{-1}; the exact value is dependent on the distance of the active detector edge to the beam. Furthermore, the jet-rate trigger could retain up to 50% of the symmetric events at this luminosity, with a significance of up to 3.5σ as shown in Fig. 21(b). Thus it is likely that, at low luminosity, the efficiency curves in Figs. 4 and 5 (labelled 60 fb^{-1}) are a conservative estimate. Heinemeyer et al. do not consider the contribution of the overlap backgrounds, however, which become the dominant background at high luminosity. Thus, the high luminosity curves in Figs 4 and 5 (600 fb^{-1}) are only valid if the overlap background can be effectively eliminated. This could be achieved through improved efficiency of the rejection variables, outlined in Sec. 3.2, or if the time-of-flight system is upgraded, as discussed in Sec. 10.

3.6 Recent improvements in background estimation

Recently, there have been a number of improvements in the calculations of the backgrounds in the $h \to b\bar{b}$ channel. Firstly, NLO calculations [108] indicate that the central exclusive production of $gg \to b\bar{b}$ is a factor of two (or more) smaller than the LO values assumed in the estimates in Sec. 3.3. Secondly, the overlap backgrounds presented in the previous sections were calculated assuming fixed instantaneous luminosity for a given integrated luminosity. This is a very conservative estimate as the luminosity decreases during a store and the largest overlap background cross section scales with $\mathcal{L}^2$. For 300 fb^{-1} of data, it is maybe more realistic to assume that half of the data was collected at a luminosity of 10^{34} cm^{-2} s^{-1} and half of the data was collected at 7.5×10^{33} cm^{-2} s^{-1}. Although crude, this approximates the luminosity profile typical of a LHC store. Such a choice would reduce the dominant [p][X][p] background by 25%.

Further improvements related to the experimental efficiency with respect to reducible backgrounds have been investigated. Firstly, recent studies suggest that an improvement in b-tagging efficiency could be obtained with respect to gluons, improving the rejection of the CEP $gg \to gg$ background. Secondly, it is expected that the [pp][X] background contribution is overestimated. The calculation of this background depends crucially on the fraction of events at the LHC that produce two forward protons, $f_{[pp]}$. The cross section presented in Sec. 3.3 uses the value of $f_{[pp]}$ predicted by the PHOJET event generator [109], but other theoretical predictions result in a value of $f_{[pp]}$ which is more than an order of magnitude smaller [18, 22]. In addition, the DPE central system must be about 100 GeV as the protons have to lose enough energy to produce a ‘missing mass’ that is approximately the same size as the signal. In the analysis presented above the charged tracks from the [p] and [pp] vertices were not simulated. However, after fast-timing constraints, the [pp] vertex will be within 4.2 mm of the di-jet vertex and it is likely that additional charged tracks will cause the whole event to fail the charged multiplicity cuts outlined in Sec. 3.2.

To estimate the effects of these improvements we have repeated the analysis detailed above, with the following modifications: (i) The CEP $b\bar{b}$ background is reduced by a factor of two, (ii) the gluon mis-tag probability is reduced from 1.3% to 0.5%, (iii) the [pp][X] background is assumed to be negligible, (iv) the luminosity profile is not fixed: For example for 300 fb^{-1}, half the data is assumed to be collected at 7.5×10^{33} cm^{-2} s^{-1} and half at 10^{34} cm^{-2} s^{-1}. Figure 22 (a) shows the effect of these improvements given the baseline 10 ps fast-timing resolution and Fig. 22 (b) shows the effects given a factor of two improvement in the fast-timing system (central timing or 5 ps forward timing resolution). The significance is increased to 3.7σ and 4.5σ respectively from

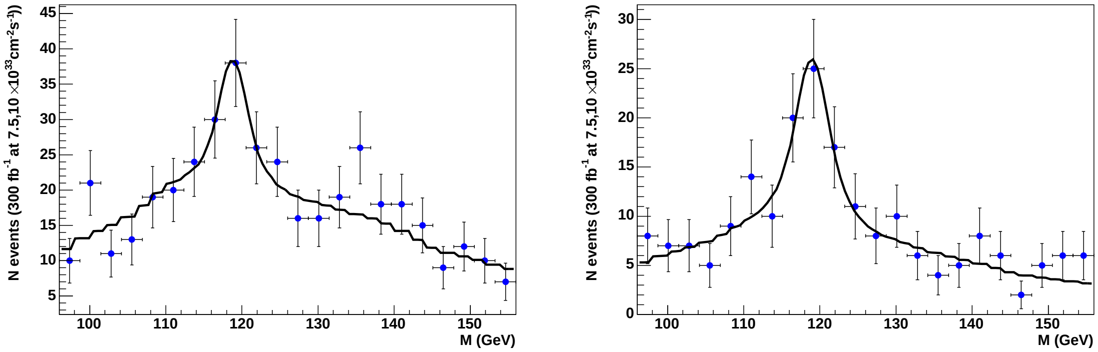

(a)

(b)

Fig. 22: Mass fit for 300 fb^{-1} of data for the improved background estimates described in the text (reduced CEP backgrounds, negligible [pp][X] and a luminosity profile consisting of half the data collected at 7.5×10^{33} cm^{-2} s^{-1} and half at 10^{34} cm^{-2} s^{-1}). The plots are made assuming (a) baseline timing of 10ps and (b) improved timing of 5 ps or central timing.

the 3σ significance of Fig. 20(b).

4 LHC Optics, acceptance, and resolution

4.1 Introduction

The configuration of the LHC beamline around the interaction points is shown schematically in Figure 23. The proposed forward detector stations are to be installed in the regions located at approximately 220 m and 420 m from the IP1 and IP5 interaction points in both beamlines downstream of the central detector. Here protons that have lost energy in the primary interaction are able to emerge from the beamline. The acceptance and the ultimately achievable experimental resolution of the forward detectors depends on the LHC beam optics and on the position of the detectors relative to the beam.

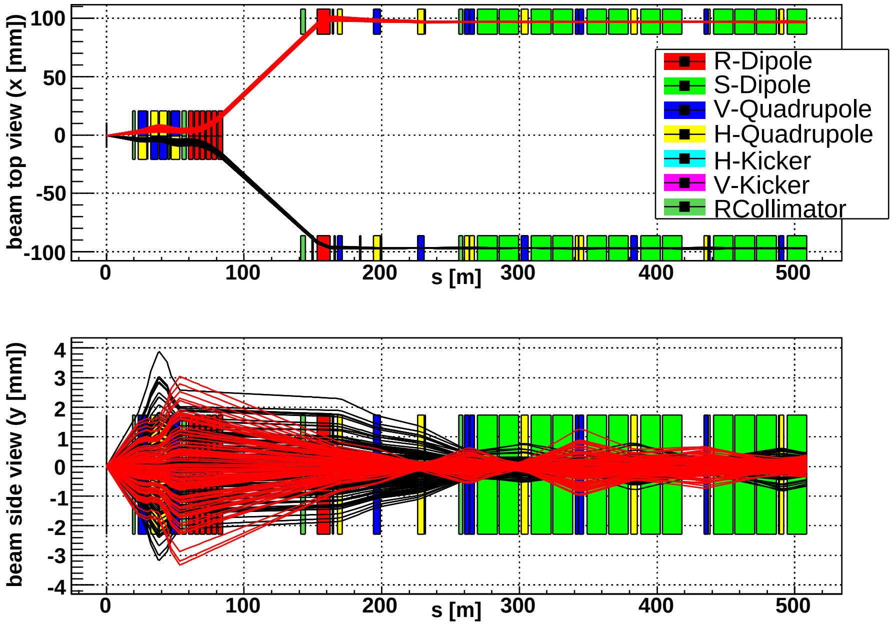

Fig. 23: Schematic plan view and side view of the beamline at IP5 (CMS); the IP1 configuration (ATLAS) is similar except that the kicker magnets are vertical (see also Fig. 125) [60]. The horizontal curvature of the beamline has been straighted out for purposes of simplification here.

The FP420 Collaboration has written two independent proton tracking programs, FPTrack [110] and HECTOR [60], and implemented a model of the LHC beamline into the package BDSIM [111] in order to simulate machine-induced backgrounds. The BDSIM model is described in detail in section 5.1. The three simulations, FPTrack, HECTOR and BDSIM are in good agreement with each other and with MAD-X, the standard LHC beam transport program used at CERN. Figure 24 shows the β functions for beams 1 and 2 as computed by HECTOR and compared to MAD-X. (Comparison with MAD-X strictly verifies the tracking programs only for 7 TeV protons.) HECTOR has also been verified for protons above 80% of the nominal beam energy (i.e. all protons within the acceptance of 220 m and 420 m detectors) by direct comparison to numerical calculations [60]. All the programs perform aperture checks through each of the LHC optical elements. Figure 25 illustratively shows the losses occurring for a set of protons with mean energy loss of 110 GeV in the MB.B9R5.B1 dipole at 338 m from IP5 using LHC beam 1 optics. It is aperture restrictions of this kind that chiefly limit the high-mass acceptance of FP420.

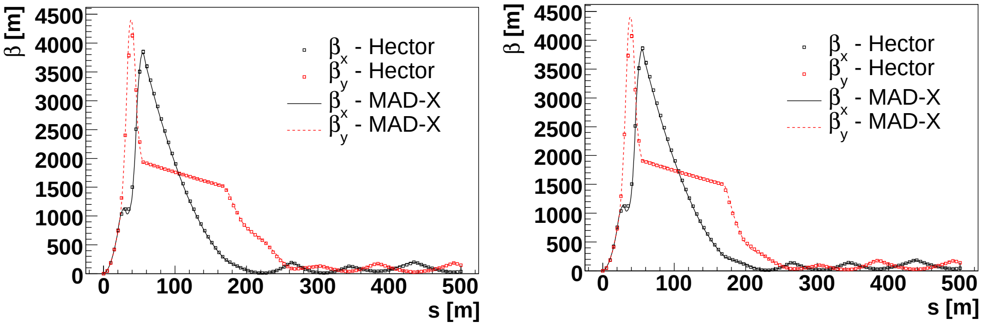

Fig. 24: Beta functions β_x (horizontal) and β_y (vertical) for LHC beam 1 (left) and beam 2 (right) calculated by MAD-X (lines) and HECTOR (squares).

Unless otherwise stated, we use the ExHuME Monte Carlo [96] to generate outgoing protons from the central exclusive production of a SM Higgs boson, although the results apply for any centrally-produced system of the same mass. Version 6.500 of the LHC optics files have been used with: $\beta^* = 0.55$ m; angular divergence $\sigma_\theta = 30.2$ μrad at the IP; crossing angle = 142.5 μrad in the vertical (horizontal) plane at IP1 (IP5); beam energy spread $\sigma_E = 0.77$ GeV. Full details can be found in [60]. The energy spread of the 7000 GeV beam is an irreducible limiting factor on the mass resolution that can be obtained by proton tagging detectors at the LHC. We show acceptances below for both 420 m alone and for 420 m and 220 m stations operating together.

4.2 Detector acceptance

The position and direction of a proton in the 220 m and 420 m detectors (for a given LHC optics) depend on the energy and scattering angle of the outgoing proton and the z-vertex position of the collision. The energy and scattering angle are directly related to the kinematic variables ξ, the fractional longitudinal momentum loss of the outgoing proton, and $-t$, the square of the four-momentum transfer. Figure 26 shows the acceptance in the ξ-t plane for the 220 m and 420 m regions for beam 1 and beam 2 respectively, around IP1 (ATLAS), as calculated by FPTrack. The mapping of the energy loss and outgoing angle of a proton at the IP to a position and angular measurement in the detector at 220 m or 420 m can be visualised using chromaticity grids. Figure 27 shows iso-energy and iso-angle curves for protons with energy loss ranging from 0 to 1000 GeV in steps of 200 GeV at 220 m (left), and from 0 to 100 GeV in steps of 20 GeV at 420 m (right). The

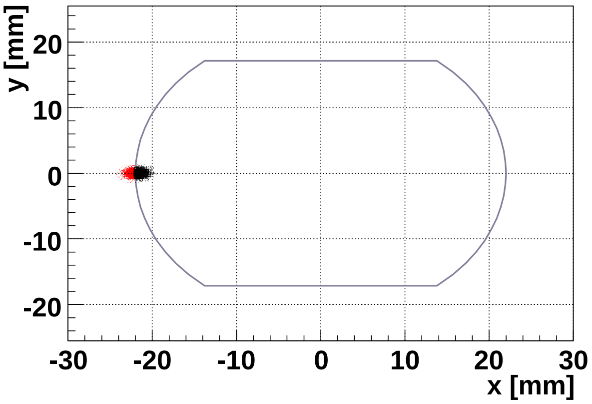

Fig. 25: Example of aperture check for a typical Main Bending dipole at 338m from IP5, for a set of protons with a mean energy loss of 110 GeV. The protons which exit the aperture are shown in black, and those which hit the walls are shown in red.

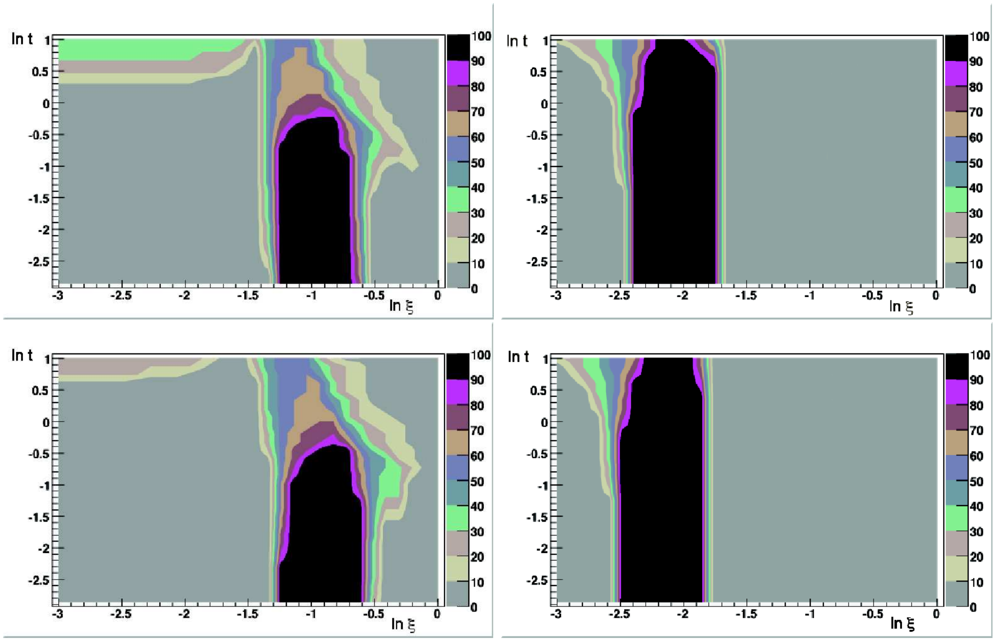

Fig. 26: Acceptances in the ξ, t plane for protons to reach planes at 220 m (left) and 420 m (right) for beam-1 (top) and beam-2 (bottom) around IP1 (ATLAS) computed with FPTrack. The variables plotted are t, the modulus of the squared momentum transfer to the proton at the IP, and ξ, its fractional energy loss. No detector effects are included here.

angle of the outgoing proton at the IP ranges from 0 to 500 μrad in steps of 100 μrad. The angle of the proton track measured at the detector θ_x is shown on the vertical axis, and the horizontal position from the beam, x, is shown on the horizontal axis. The non-linear nature of the grids is due to the energy dependence of the transfer matrices, without which the grid would be a parallelogram. The chromaticity grids show that the measurement of the energy of the outgoing proton requires good position and angle measurements in the detector stations. A measurement of the angle of the outgoing protons from the IP, and hence p_T, at 420 m requires a far better spatial resolution than the energy (ξ) measurement. This can be seen, for example, by noting that the separation in x_1 of the (10 GeV, 0 μrad) and (10 GeV, 500 μrad) fixed-energy points is much smaller than that of the (10,0) and (100,0) fixed-angle points. We return to this issue below when discussing the required measurement precision. We expect to achieve $\sim 1\mu$rad precision on θ_x.

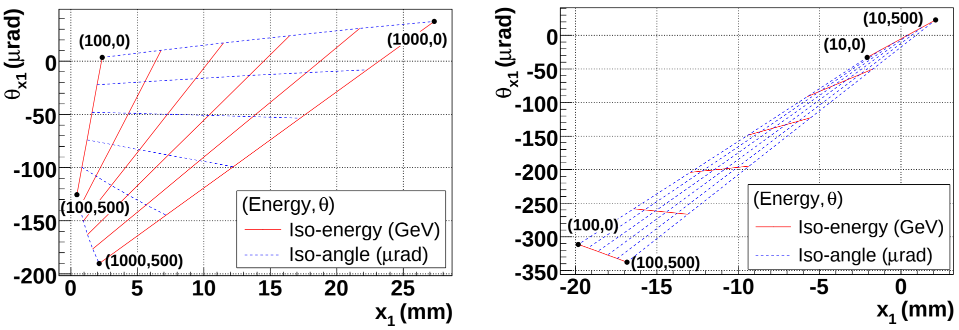

Fig. 27: Chromaticity grids: iso-energy and iso-angle lines for 220 m (left) and 420 m (right) detectors at IP5, beam 1 computed with HECTOR. The vertical axis θ_{x1} is the angle of the scattered proton relative to the beam at 220 or 420 m, and the horizontal axis x_1 is the horizontal displacement of the scattered proton relative to the beam. The solid lines are iso-energy lines, ranging from proton energy loss 0 GeV to 1000 GeV in steps of 200 GeV at 220 m, and from 0 GeV to 100 GeV in steps of 20 GeV at 420 m. The dotted lines are lines of constant proton emission angle at the interaction point, and range from 0 μrad to 500 μrad in steps of 100 μrad.

The low-ξ (and therefore low mass) acceptance depends critically on the distance of approach of the active area of the silicon sensors from the beam. This is shown in Fig. 28 for proton tags at 420 + 420 m and 420 + 220 m. It is clear from the left hand plot in Fig. 28 that operating as far away as 7.5 mm does not compromise the acceptance for central masses of 120 GeV/c^2 and above, for 420 + 420 m tagged events. Acceptance at higher masses requires the 420 m detectors to be used in conjunction with 220 m detectors. For this configuration, however, the acceptance becomes more sensitive to the distance of approach for masses in the 120 GeV/c^2 range (Fig. 28 right). This is because the 220 m detectors have acceptance only at relatively high ξ (Fig. 26), forcing the proton detected at 420 m to have low-ξ, and therefore to be closer to the beam. As we shall see in the following sections, the possible distance of approach depends on the beam conditions, machine-induced backgrounds and collimator positions, and the RF impact of the detector on the LHC beams. Such studies have been performed by us only for 420 m stations – for further details on the current and proposed 220 m designs see Refs. [10, 8]. It is envisaged that the 220 m detectors will be able to operate as close as 1.5 mm from the LHC beams [10]. At 420 m the nominal operating position is assumed to be between 5 mm and 7.5 mm, depending on beam conditions. This is discussed further in Sections 5 and 8. For central masses above 150 GeV/c^2 or so, the inclusion of 220 m detectors becomes increasingly important.

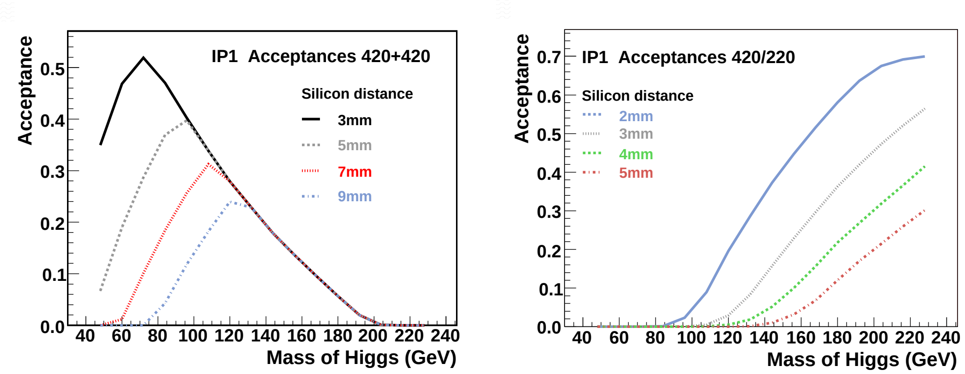

Fig. 28: Acceptance as a function of centrally produced mass for (left) 420 + 420 m proton tags for the silicon detector active edge positioned at different distances from the beam; (right) for 220 + 420 m proton tags with the 420 m silicon at 5 mm from the beam and the 220 m at different distances from the beam. The small upward deviation at high mass for the 2 mm silicon positions, show the additional acceptance from 220 + 220 m coincidences.

Figure 29 shows several interesting features of the acceptance, including differences between the IP1 (ATLAS) and IP5 (CMS) regions. The upper plots show that if the 220 m detectors are sufficiently far from the beam (3 mm in this case) then there is negligible difference in 420 +420 m acceptance between IP1 and IP5, and beam 1 and beam 2. The fact that the crossing angle is in the vertical plane at IP1 and the horizontal plane at IP5, however, results in a higher acceptance at IP1 than IP5 for 420 + 220 m event[10], as shown in Fig. 29. The bottom plots show that for closer insertions at 220 m (2 mm in this case), there is a decrease in the 420 +420 m acceptance for the IP1 region, due to the dead region (from the thin vacuum window) of the 220 m detectors intercepting protons that would otherwise be detected at 420 m. This dead region is taken as 0.7 mm in the acceptances shown in the figure, and has negligible affect for clearances of more than 2 mm from the beam line at 220 m. The accuracy of the proton momentum measurement (see next section) is higher at 420 m than at 220 m, so the operating conditions at 220 m must be chosen so as to achieve an optimum balance between the mass resolution and acceptance.

---

[10] Right now the different choice of crossing plane at the IPs leads to a reduced acceptance for IP5, but it would be possible to use the same crossing plane at both IPs with some minor modifications to the LHC around IP5.

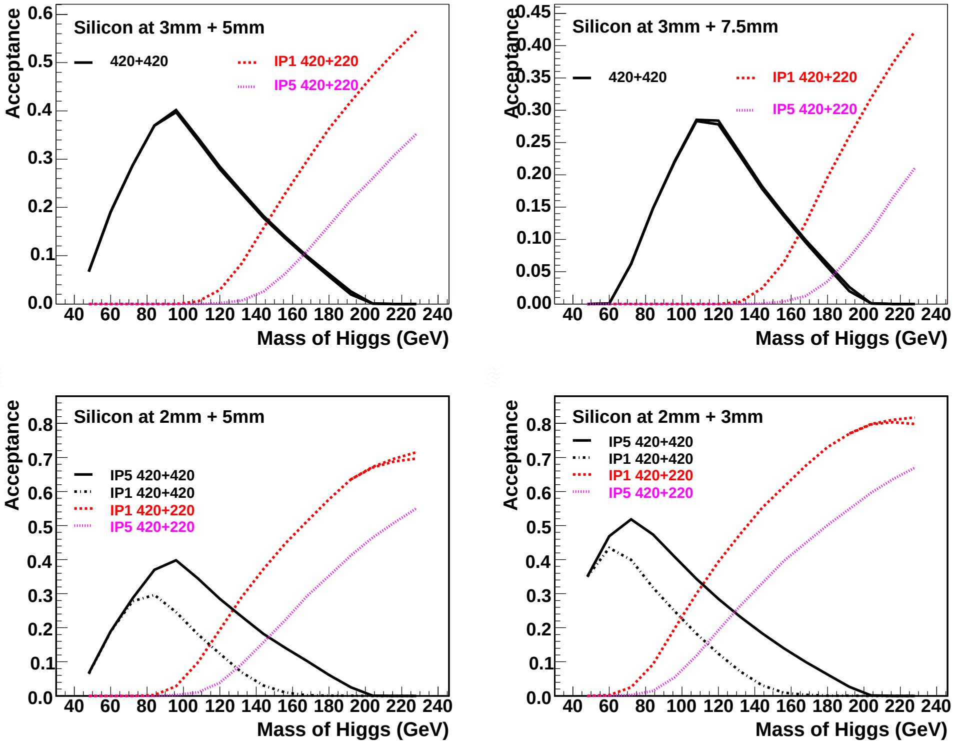

Fig. 29: Acceptances as a function of Higgs boson mass with detector active edge at various distances from the beam centre at 420 m for IP1 (dotted line) and IP5 (dashed line). Also shown is the acceptance for events with one proton detected at 220 m and one proton at 420 m (or also 220 m, upper branch) . The smaller distance in the legend is always the 220 m distance.

4.3 Mass resolution

Typical $x-y$ distributions of hits in a detector at 420 m are shown in Fig. 30. The distribution extends over the full horizontal width of the detector but is narrowly confined vertically. Note that the detector sensitive area need only be $\sim$2 mm (V) × 20 mm (H). In practice we will use a larger vertical area to allow for beam position variations. From measurements in a minimum of two stations in each region, the mean position and direction of the scattered protons can be determined. The position and angle in the x-y plane of a proton at any point along the beam-line can be used to measure its energy loss and p_T at the interaction point. A simple reconstruction method for the energy of the detected proton has been studied which takes account only of the dispersion; here a polynomial fit is performed for the proton energy as a function of the horizontal position at the detector (Fig. 31). As seen in Fig. 27, however, an angular measurement in the horizontal plane θ_x is required to give good momentum reconstruction accuracy; this must be particularly precise at 420 m because the iso-angle lines are highly compressed. A precision of at least ±1 μrad is necessary and appears attainable (see Section 9.7); the tracks are measured over an 8 m lever arm with <80 μm precision at front and back.

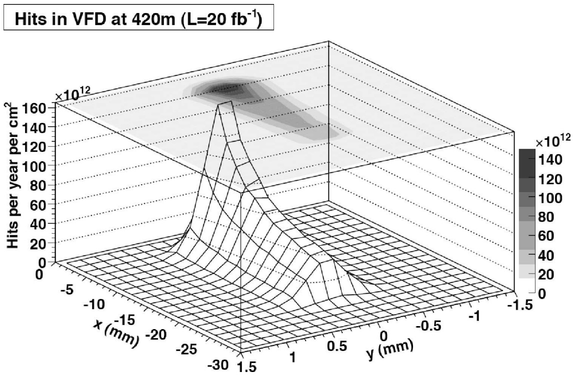

Fig. 30: Number of proton hits due to the process pp → pX for 20 fb^{-1} integrated luminosity. Protons were generated with PYTHIA 6.2.10 (single diffraction process 93) and tracked through the beam lattice with HECTOR.

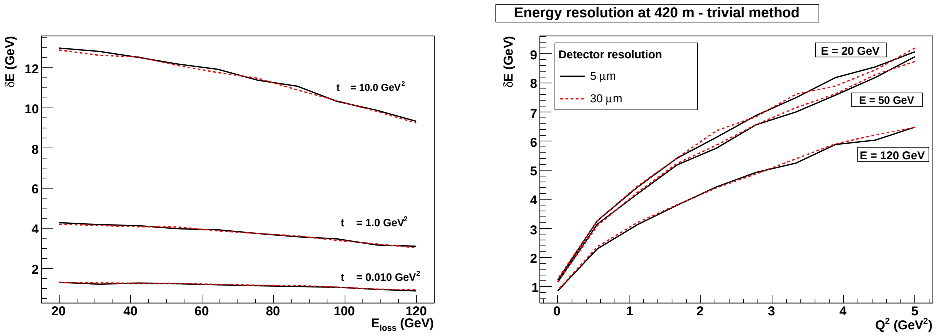

Fig. 31: Energy resolution for the simple reconstruction method described in the text for protons at 420 m. The resolution is shown as a function of energy loss (left) and $Q^2(=-t)$ (right). Also shown is the effect of varying the error on the positional measurement on the detectors from 5 μm to 30 μm.

For optimal results, polynomial-based parametrization formulae have been developed in order to evaluate the proton momenta from the measured parameters in the silicon detectors. The formulae are based on fits to the calculated positions and angles, using the generated values of the momentum and emission angle at the IP, and averaging over the width of the beam-beam interaction region. From the momenta of the pair of oppositely emerging protons in an event, the mass of the centrally produced system can then be calculated by a missing-mass formula [1]. Using these parametrizations we have evaluated the resolution achievable on the missing mass of a diffractively produced object. Minimizing this resolution is critical to the physics capabilities of the proposed new detectors. We present results for a vertex at $z = 0$, but there is no significant dependence on the z vertex within the interaction region. To allow for any dependence on x we note that this will be well measured by the central detector for every event, and is expected to be quite stable within a run. Thus offline corrections for these variations are easily applied. The residual event-by-event variation of the x position is taken into account below in the mass resolution calculation.

The following factors affect the measured resolution of a narrow object produced in the exclusive double diffraction process:

- The Gaussian width of the momentum distribution of the circulating proton beam. This is specified as 0.77 GeV/c.
- The lateral uncertainty of the position of the interaction point. This is taken to be 11.8 μm from the intrinsic beam width, but could be improved if the central silicon detector system provides a better measurement on an event-by-event basis.
- The position measurement uncertainty in the RP system
- The angular measurement uncertainty in the RP system.

Figure 32 shows the effect of each one of the above factors on the mass resolution. Full sets of curves are presented for 420 + 420 m measurements up to 180 GeV/c^2 (left) and 420 + 220 m measurements above 140 GeV/c^2 (right). The two top curves which are given in both figures indicate a combination of the two measurements. Resolutions were determined by applying a chosen combination of Gaussian smearings and fitting the resulting histograms of reconstructed minus true mass with a Gaussian function, whose width is plotted here. The sets of curves represent the resolutions obtained: (1) with no physical smearing applied, indicating the precision of the reconstruction algorithm, (2) applying smearing due to the 0.77 GeV/c Gaussian distribution of the primary proton beam momentum (3), also including a 10 μm lateral smearing of the interaction vertex within incident beam spot, (4) also including a 10 μm smearing of the measured position x in the silicon system, (5,6) also including 1, 2 μrad smearing, respectively, of the dx/dz measurement in the silicon system. The curves in (c) give the overall mass resolution under the conditions of (5) and (6) for all events in both regions combined. The effects of a small smearing of the x measurement in the silicon system are seen to be small in comparison with the other effects. The overall resolution is as low as 2 GeV/c^2 in the central mass range of interest, using the expected 1μrad angular uncertainty in the dx/dz measurement. It should be noted that the 2 μrad curve could be considered an upper limit to the resolution, as a comparable resolution can be obtained by simply constraining the angle of the emitted proton to be along the beam direction at the interaction point.

It is possible to measure the transverse momentum of the proton as it emerges from the interaction point, again by means of polynomial-based parametrization formulae using the measurements in the detector stations. Both x and y measurements are required to determine the full transverse momentum of the proton. The measurement is degraded by two factors. The angular beam spread at the interaction points is equivalent to a ± 0.21 GeV/c transverse momentum spread, both horizontally and vertically, and the poorer measurement uncertainty in the y direc-

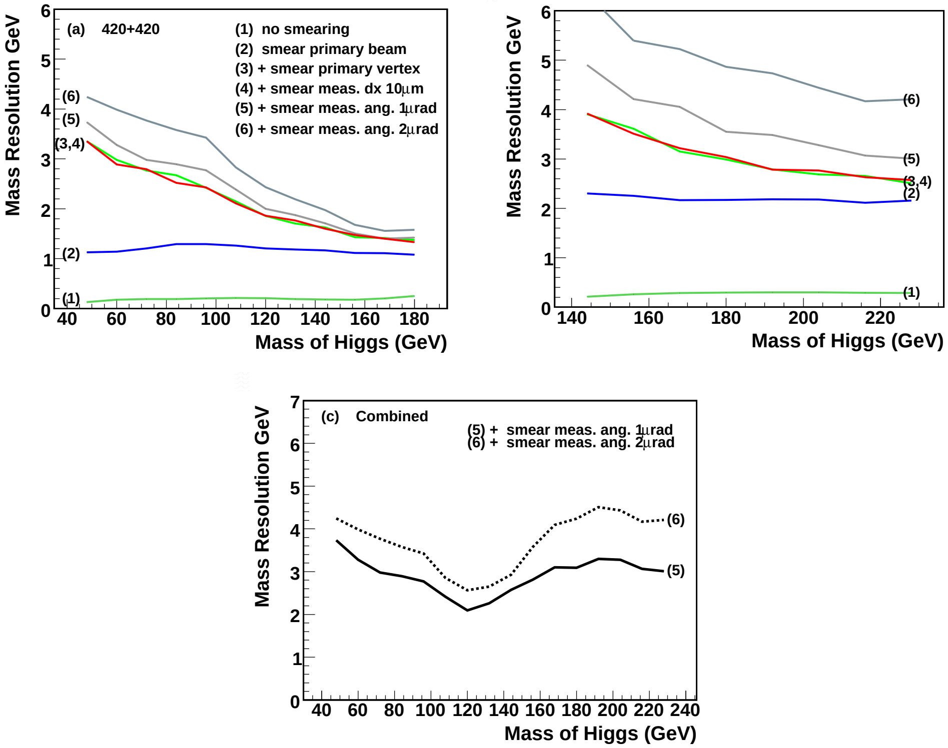

Fig. 32: Mass resolutions obtainable in ATLAS (a) for 420 + 420 m measurements, (b) for 420 + 220 m measurements, (c) combined. The curves have different amounts of smearing applied as explained in the text.

tion increases the overall uncertainty on p_T significantly. Studies are continuing to determine the requirements for particular physics studies and whether they can be achieved.

4.4 Optics summary

The beam optics at LHC allows protons that have lost momentum in a diffractive interaction to emerge from the beam envelope at regions 220 m and 420 m from the interaction point. By placing silicon detector arrays in these locations we can detect the protons and obtain good acceptance for diffractively produced objects with a wide range of masses above 60 GeV/c^2, the precise acceptances depending on how close it is possible to place the detectors relative to the beam. Even under cautious assumptions, the mass range above 100 GeV/c^2 is well covered, but to obtain good acceptance for masses above 150 GeV/c^2 the 220 m system is essential. The expected position and angle resolutions for the protons obtained in the silicon stations are expected to yield a mass resolution reaching values of 2 to 3 GeV/c^2 per event.

5 Machine Induced Backgrounds

5.1 Introduction

A precise evaluation of the particle flux environment at 420 m caused by machine operation provides critical input to the FP420 project in several areas. It is necessary for the determination of expected FP420 operating parameters such as the the minimum safe distance of approach to the beams, and also for assessment of the level of radiation exposure of the detectors and associated electronics. Moreover, machine-induced background entering the detectors may result in fake proton tracks, which will contribute to the pile-up background described in Section 3 and also result in increased occupancy in the silicon sensors, which must be considered in the tracking algorithm performance. The assessment of machine-induced backgrounds relies on detailed simulations of the machine geometry, the LHC collimation scheme and cleaning efficiency, the beam optics, the bunch structure and the residual gas density. In this section, the status of the estimates of all contributions to the background are presented, and preliminary conclusions discussed. Unless otherwise stated, all results are calculated for the case of full instantaneous luminosity of 10^{34} $\mathrm{cm}^2\mathrm{s}^{-1}$.

The background in the FP420 region is comprised of the following components:

- **interaction point (IP) particles**: generic proton-proton collisions at the interaction point produce a great number of particles dominantly in the forward direction, some of which reach the 420 m region. The control of this so-called overlap background is discussed in Section 10.1.
- **beam-gas particles**: elastic and inelastic proton-nucleus collisions between the beam protons and residual gas molecules produce shower particles, which represent a direct background when the collisions occur close to the FP420 detector stations. This is referred to as the *near beam-gas background*.
- **beam halo particles**: *distant* beam-gas interactions (occurring around the whole ring and not only in vicinity of the detectors), various beam instabilities and a limited dynamic aperture lead to beam protons leaving their design orbit and impact on the collimation system. This builds up beam halo particles circulating in the machine.
- **secondary interactions**: beam-halo particles or particles resulting from proton-proton or beam-gas collisions can interact with the machine elements creating **secondary showers** that can irradiate the detector region with a potentially large flux of charged and neutral particles. Showers can also originate in the detector structure itself.

The following sections consider each of these background sources.

5.2 Near beam-gas background

The beam-gas contribution arises from the interaction of beam particles with residual gas in the beam pipe region immediately before 420 m. These elastic and inelastic proton-nucleon collisions perturb the angular (large-angle scattering) and momentum phase space distribution of the primary protons, and cause secondary production in the vicinity of the detector. Study of this background requires a detailed model of the beam line, coupled with gas pressure profiles and computation of proton/gas interactions. The Protvino group have started performing simulations using [112] for the forward detectors at 220 m and 240 m from the IP1 (ATLAS) and IP5 (CMS and TOTEM) interaction points, based on estimated pressure profiles in the IR1 and IR5 straight sections. These calculations will be extended to 420 m, and normalised to beam lifetime. Furthermore, the beam-gas pressure profiles can be used within the BDSIM [111] (see Sec. 5.5) simulations of the beam-line, to complement and cross-check the Protvino calculations and also to assess the integrated beam-transport/beam-gas background spectrum at FP420.

Until these studies are completed, a rough estimate of the number of beam-gas interactions per bunch in the 420 m detector region can be extrapolated from the results obtained for the straight section regions [113]. Such simulations include protons that are lost after scattering with the gas nuclei and secondary particles produced due to proton losses upstream the considered scoring plane. In a scoring plane set at 240 m from IP1, the total number of charged hadrons assessed by the simulations is $\mathrm{np}_{240\ \mathrm{m}} = 2.4\,\mathrm{s}^{-1}$. This result is obtained considering an average residual gas density along IR1 [114, 113] $\rho_{240\ \mathrm{m}} = 3.4 \cdot 10^{11}\,\mathrm{molecules} \cdot \mathrm{m}^{-3}$ (converted in hydrogen-equivalent species). The dynamic residual pressure at 420 m is expected to be higher than the straight sections, due to synchrotron radiation. As a very conservative upper limit, we can consider a residual hydrogen density of about $\rho_{420\ \mathrm{m}} = 1 \cdot 10^{15}\,\mathrm{molecules} \cdot \mathrm{m}^{-3}$, which is compatible with a beam-gas lifetime of 100 hours. If the level were any higher than this the energy deposition per meter in the LHC arcs would exceed the cooling power needed to avoid magnet quenches [115]. With such a gas density, the total number of expected hadrons per bunch, due to near beam-gas events, is around

$$np_{420\ m} = \frac{np_{240\ m}}{N_{bs}} \cdot \frac{\rho_{420\ m}}{\rho_{240\ m}} = 1.8 \cdot 10^{-4} \tag{9}$$

where $\mathrm{N}_{\mathrm{bs}} = 4 \cdot 10^{7}$ is the number of bunches per second that will circulate in the LHC with nominal conditions.

This estimate predicts a very low background rate contribution, especially taking into account that it refers to the full mechanical beam pipe aperture and only a small fraction of those hadrons will hit the FP420 detectors. In addition, after the LHC startup phase, the residual gas density in the arcs is expected to correspond to a beam-gas lifetime larger than 100 hours. However, such an approximation has to be validated with dedicated simulations and eventually with real data.

5.3 Beam halo

During standard LHC operation a so-called *primary halo* will be filled continuously due to beam dynamics processes. These particles are lost by the limitations of the mechanical aperture at various places around the LHC ring, resulting in a finite beam lifetime. Given the high intensity of the LHC beam, it will be unacceptable to lose even a small amount of the particles populating the halo in the super-conducting magnets. The collimation system has been designed to clean the beam halo without inducing magnet quenches due to beam losses [116]. The system is based on a set of movable primary, secondary and tertiary collimators that can be adjusted during the different phases of a physics run. They are divided into two categories: *betatron cleaning collimators* (located at IR7) that clean particles performing large betatron oscillations, and *momentum cleaning collimators* (located at IR3) that clean particles with large momentum offset. The two systems will be always adjusted such that they comprise the limiting transverse and longitudinal machine apertures.

The collimation system is designed mainly to protect the machine, but it reduces also the experimental backgrounds related to the primary halo. However, the unavoidable cleaning inefficiency of the multi-stage collimation process generates *secondary* and *tertiary* halos populated by protons scattered at the collimators. Such particles can circulate for many turns before being removed by the cleaning/absorbing elements or in other locations depending on the phase advance of their betatron oscillation. Tertiary collimators are located in all experimental straight sections to protect super-conducting magnets from the tertiary halo. Additional devices (*absorbers*) are designed to protect from showers generated by the cleaning insertions and physics debris from the interaction points.

The fact that primary collimators are not distributed around the LHC ring, but are concentrated in IR7 and IR3 results in a beam secondary halo distribution that will be different for the four potential FP420 locations around ATLAS and CMS.

Although FP420 is in the shadow of the collimators, this will not be sufficient to completely avoid hits from beam halo particles. In particular conditions (linked to the betatron phase advance between the collimators and FP420, the dispersion functions, and the particles momenta), elements with apertures larger than the collimators may be hit by halo particles.

In the following sections, we review the LHC collimators settings and the expected beam parameters at FP420. We also address in more detail the beam halo generated at the two collimation systems elements (Sec. 5.3.2 and 5.3.3) and around the whole LHC ring due to small scattering angles beam-gas interactions (Sec. 5.4).

5.3.1 Collimator settings and beam parameters

During high luminosity running at 7 TeV, it is foreseen to set the collimator position as shown in Table 9.

Such values are expressed in terms of the radial distance from the beam envelope evaluated at one σ_β. It must be noted that at each location s in the ring, the actual transverse beam size is defined by the particle betatron oscillations and by the closed orbit offset due to the particle

System	Name	Location	Half Gap $[\sigma_\beta]$
Primary betatron cleaning	TCP	IR7	6
Secondary betatron cleaning	TCSG	IR7	7
Primary momentum cleaning	TCP	IR3	15
Secondary momentum cleaning	TCSG	IR3	18
Tertiary collimators	TCT	IR1,IR2,IR5,IR8	8.3
Absorbers	TCLA	IR3	20
(for showers in cleaning insertions)		IR7	10
Absorbers (for physics debris)	TCLP	IR1,IR5	10

Table 9: LHC collimator settings for nominal optics at 7 TeV. Details about the collimator exact number, materials, location and orientation (horizontal, vertical or skew) can be found in [117, 118].

momentum error. Considering the horizontal plane relevant for FP420:

$$\sigma_x(s) = \sqrt{\frac{\varepsilon_x^* \beta_x(s)}{(\beta\gamma)} + [D_x(s) \cdot \delta]^2} = \sqrt{\sigma^2_{\beta x}(s) + \sigma^2_{\delta_x}(s)}, \tag{10}$$

where β_x and D_x are the betatron and dispersion functions, ε_x^* the normalised emittance (at 1σ), $\delta = dp/p_0$ the particle's r.m.s momentum spread, $\gamma = E/E_0$ the Lorentz factor and $\beta = v/c$. As a baseline, in order to guarantee safe operation conditions, experimental insertions like FP420 will be allowed to approach the beam as close as $15\sigma_{x,y}$. Smaller distances will need to be discussed and approved by the concerned LHC committees.

The optics parameters at the entrance of FP420 are summarised in Table 10. Also shown is the horizontal beam size for the nominal values $\varepsilon_x^* = 3.75\,\mu$m and $\delta = 1.13 \cdot 10^{-4}$. The betatron functions and the horizontal dispersion in the dispersion suppressor region for one of these combinations (Beam 1 downstream IP5) are shown in Fig. 33.

	distance from IP [m]	β_x [m]	D_x [m]	$\sigma_x = \sigma_{\beta x} + \sigma_\delta$ [mm]	$15\sigma_x$ [mm]
IP1 Beam 1	418.5	127.1	1.51	0.305	4.573
IP1 Beam 2	418.8	106.9	2.02	0.325	4.873
IP5 Beam 1	418.5	127.1	1.47	0.302	4.534
IP5 Beam 2	418.2	106.9	1.96	0.321	4.808

Table 10: Beam parameters at the end of the last element before FP420 using LHC optics V5.0

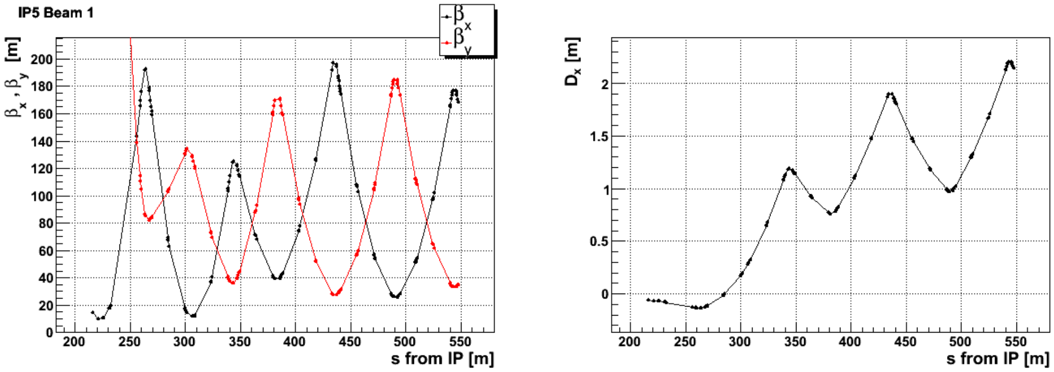

Fig. 33: The betatron functions and horizontal dispersion in the FP420 region for Beam 1 downstream of IP5.

5.3.2 Beam halo induced by momentum cleaning collimators

During the physics runs, the momentum cleaning system is designed mainly to protect the machine from protons leaving the RF bucket because of energy loss due to synchrotron radiation. Off-momentum protons can potentially perturb the operation of the FP420 detectors due to the closed orbit displacement caused by the high dispersion function (Table 10). For this reason, a series of simulations has been carried out in order to characterise the beam halo populated by such protons and the effect of the cleaning system settings on the FP420 background. The simulations have as input $2 \cdot 10^6$ protons belonging to the primary halo hitting the momentum cleaning primary collimators in IR3. A multi-turn tracking routine follows the protons emerging from the collimator surface until they are absorbed by the cleaning system or lost in other aperture limitations of the machine (not including the FP420 detectors). At each turn, the proton distribution is recorded at the 420 m locations. Two separate sets of simulations have been carried out for Beam 1 and Beam 2 using STRUCT [119].

The fraction of the initial protons reaching 420 m as function of the number of turns after their interaction with the collimators is shown in Fig. 34. The plots confirm the multi-turn nature of the cleaning process, as almost 100% of the

protons hitting the collimators reach 420 m at “turn 1” (when the particles have only traversed the distance from IR3 to 420 m) and almost 90 % of them survive the first full turn. Therefore, for background considerations, all the primary halo off-momentum protons that continuously hit the momentum cleaning collimators and fill the secondary and tertiary halos, must be considered at 420 m. Of course reasonable operating positions will be chosen to avoid the bulk of this halo.

If the collimators in IR3 are set at $x(s_c)$ and the dispersion function at that location is $D_x(s_c)$,

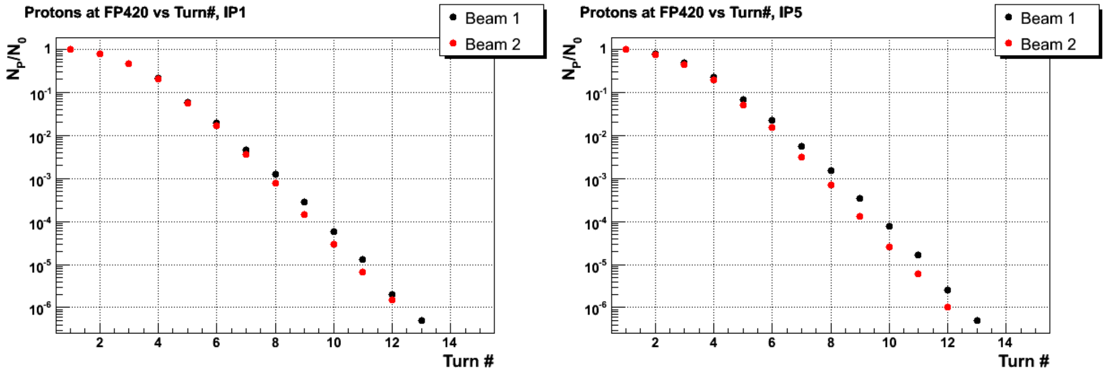

Fig. 34: Total number of particles at FP420 as a function of the turn number after scattering on the momentum cleaning collimators.

all particles with

$$\delta \equiv 1 - \frac{p}{p_0} \leq \frac{x(s_c)}{D_x(s_c)} \equiv \delta_c \tag{11}$$

hit the collimator at every turn. Given $D_x^{b1}(s_c) = 2.20$ m and $D_x^{b2}(s_c) = 2.46$ m for Beam 1 and Beam 2 respectively, and the collimator positioning at $15\sigma_\beta$, the cut in momenta for the two distributions is expected to be at $\delta_c^{b1} = 1.78 \cdot 10^{-3}$ and $\delta_c^{b2} = 1.57 \cdot 10^{-3}$. This is confirmed by Fig. 35. In addition, at the FP420 locations, the proton horizontal distribution is expected to be centred around

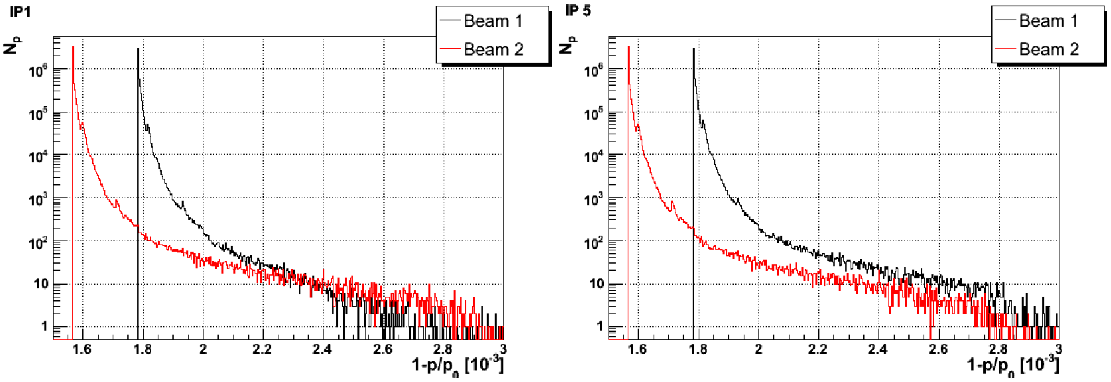

Fig. 35: Momentum distribution of the protons emerging from the momentum cleaning collimators.

$$x_{cut}^{FP420} = -D_x(s_{420}) \cdot \delta_c, \tag{12}$$

as confirmed by the simulation results in Fig. 36 which show the horizontal halo distributions with the expected peak values (dashed vertical lines). The shape of the distributions depends on the

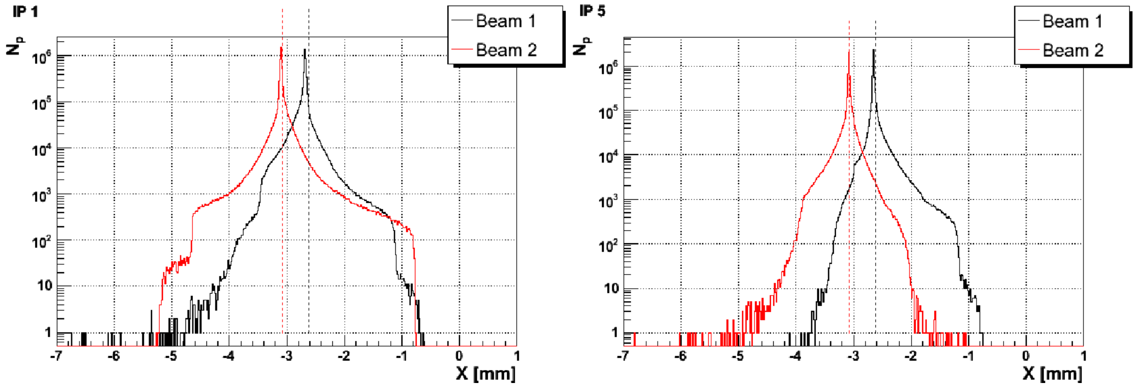

Fig. 36: Horizontal distribution of the protons emerging from the momentum cleaning collimators as observed at FP420 after the simulations of $2 \cdot 10^6$ proton interactions with the primary momentum cleaning collimators.

betatron phase advance between the collimators and the detectors.

In order to estimate the absolute background level, the distributions must be normalised for the number of protons that will interact with the momentum cleaning collimators during normal LHC operations. Assuming:

- the nominal LHC beam intensity for high luminosity runs $I_0 = 3.2 \cdot 10^{14}$ protons,
- an exponential decay of the beam current due to off-momentum proton losses

$$I(t) = I_0 \cdot e^{-t/\tau}$$

- a beam lifetime accounting for losses of off-momentum particles $\tau = 150$ hours,

then the corresponding maximum proton loss rate is:

$$r(t=0) = -\left.\frac{dI}{dt}\right|_{t=0} = \frac{I_0}{\tau} \approx 5.9 \cdot 10^8 \ [p/s]. \tag{13}$$

Hence, the loss rate at FP420 as a function of transverse position can be calculated by normalizing the histograms of Fig. 36 according to:

$$\begin{aligned} r(t, \Delta x) &= N_p \cdot \frac{r(t_0)}{N_0} [p \cdot s^{-1} \cdot (\Delta x)^{-1}] \qquad (14) \\ N_0 &= 2 \cdot 10^6 \ \text{(simulation input)} \\ \Delta x &= \text{bin-width.} \end{aligned}$$

The normalised distributions are shown in Section 5.4 together with the distributions generated by beam-gas interactions.

5.3.3 Beam halo induced by betatron cleaning collimators

The impact of the primary beam halo protons on the betatron cleaning collimators will also generate secondary and tertiary halos. Given the collimator settings shown in Table 9, however, it is clear that halo generated by these collimators will be negligible at reasonable 420 m detector positions ($x = 10$ to $15\sigma_x$). If this were not the case high luminosity LHC operation and the protection of superconducting magnets would be extremely problematic, so we can neglect this halo term in our considerations.

5.4 Halo from distant beam-gas interactions

The LHC beam halo will be populated also by protons that experience scattering with the residual gas nuclei. When the resulting proton momentum loss and scattering angle are small, the protons remain within the machine momentum and transverse acceptance and can circulate for several turns. Therefore the scattering is elastic or inelastic, provided the momentum loss is small enough for multi-turn survival.

A series of simulations was carried out by the Protvino group using STRUCT [119]. Ten million protons (for each LHC beam) were generated at the location of the collimator labelled as TCP.6L3 (at 177 m upstream of IP3), with momentum equal to 7 TeV and distributed according to the nominal transverse phase space. Each proton was tracked around the LHC ring model while assuming a uniform gas density in the LHC arcs and dispersion suppressor regions. After a proton-gas interaction, all protons that are scattered with a small angle and momentum loss are tracked around the machine until they are either lost in a machine aperture limitation or rescattered in a collimator. In the latter case, the scattering process proceeds as for the momentum halo simulations in Section 5.3.2. At each turn, all protons with transverse position $|x| > 7\sigma_x$ or $|y| > 7\sigma_y$ are recorded at the entrance of the FP420 regions[11].

The horizontal distribution of the beam halo protons at FP420, after the simulation of $1 \cdot 10^7$ proton-beam gas interactions per beam are shown in Fig. 37. These distributions are normalised for the expected beam lifetime τ_{bg} related to beam-gas interaction, as shown by Eq. 14.

During the LHC startup period, τ_{bg}, averaged over the all LHC ring, is expected to be around 100 hours. Later, during the LHC operation at high luminosity (after the so-called "beam pipe conditioning" by the beam itself), such value is expected to be higher and here we use $\tau_{bg} = 500$ hours. The normalised profiles are shown in Fig. 38, where the resulting number of protons per second and per millimeter is compared to the simulated distribution (and normalised to the relevant lifetime $\tau = 150$ hours) for the momentum cleaning collimators beam halo (Sec. 5.3.2).

Also here, it is instructive to apply another normalization factor $\mathrm{N_{bs}} = 4 \cdot 10^7$ (number of bunches per second), to obtain the beam halo distributions associated with each bunch crossing, as shown in Fig. 39. The same data can be used to calculate the total number of beam halo protons that will enter the 420 m regions, for different horizontal positioning of the detectors (i.e. the number

---

[11] As for the tracking simulations related to momentum cleaning collimators, the FP420 detectors are considered transparent for the beam.

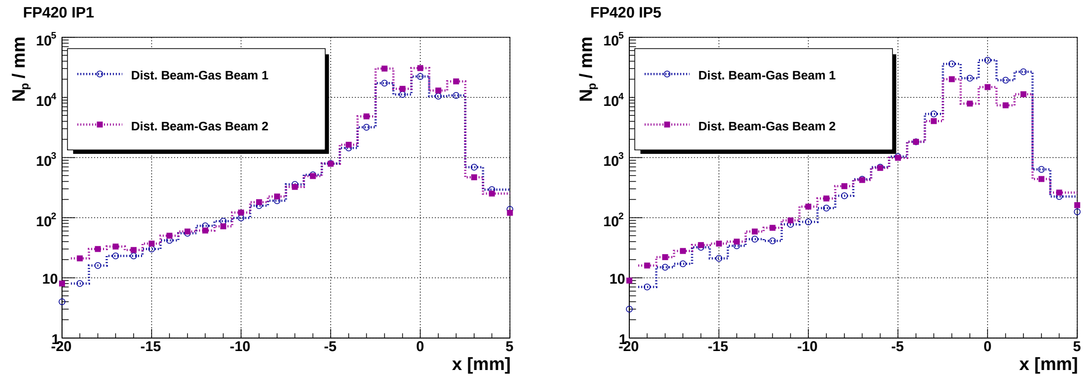

Fig. 37: Horizontal distribution of the protons scattered due to beam-gas interaction, as observed at FP420 after the simulation of $1 \cdot 10^7$ proton-gas nuclei events per LHC beam.

of protons integrated from the outer beam halo edge to the detectors inner edge.). This has been calculated in the plots of Fig. 40.

The peak of the beam-halo distribution (see Fig. 38 or Fig. 39) is determined by the LHC momentum cleaning collimator settings. For nominal collimator settings FP420 detectors located 5 mm from the beam would be well away from this peak. To operate closer than 5 mm an adjustment of the collimator positions would likely be required. Furthermore, for detector distances greater than 5 mm, this background is dominated by distant beam gas and the background rate is low.

5.5 Secondary interactions

The transport of a proton bunch with an energy distribution will result in proton losses when the protons interact with physical elements of the beamline. This process results in electromagnetic and hadronic showers, causing deposited energy and the production of background particle species. The assessment of the effects of these showers along the beam line and in the detector regions requires

- modelling of the beamline and detector regions, to correctly describe the type and distribution of matter;
- simulation of the proton transport through the beam line optics;
- simulation of the interaction of the beam particles with the beam line apertures and the detectors.

To obtain a full simulation of secondary production along the beam line the toolkit BDSIM [111] (Beam Delivery System Simulation) has been used. This code, developed to study this class of problem combines fast vacuum tracking of particles in the beampipe with GEANT4 [120], which models the interaction of beam particles with matter and is used whenever particles leave the beampipe and enter solid parts of the machine. Hence BDSIM allows a seamless integration of

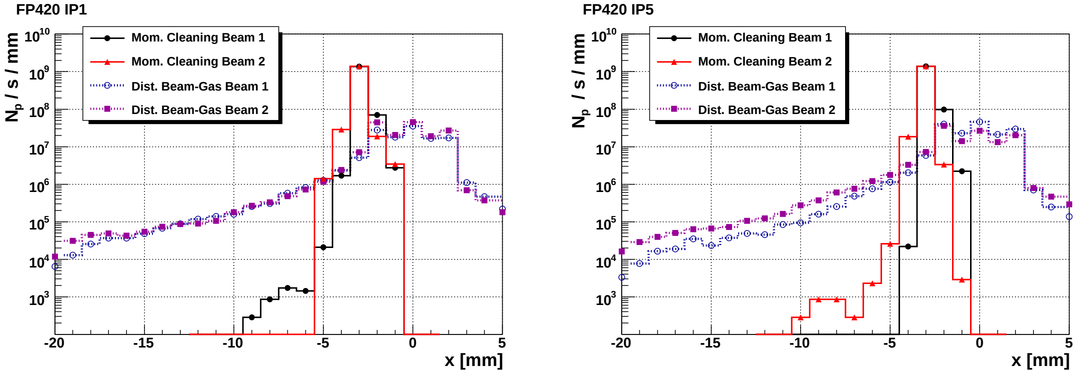

Fig. 38: Horizontal distribution of the protons emerging from the momentum cleaning collimators and scattered due to beam-gas interaction, as observed at 420 m, after normalization for the beam lifetime as described in text.

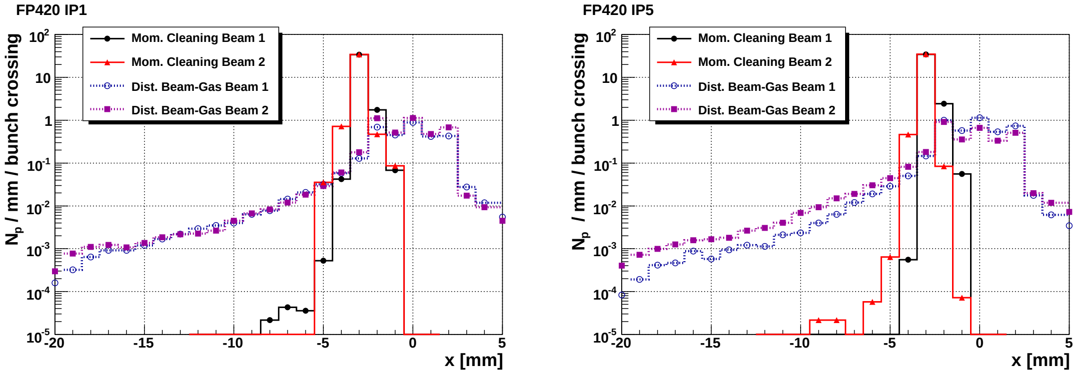

Fig. 39: Renormalised versions of Fig. 38 yielding the number of halo protons per bunch crossing.

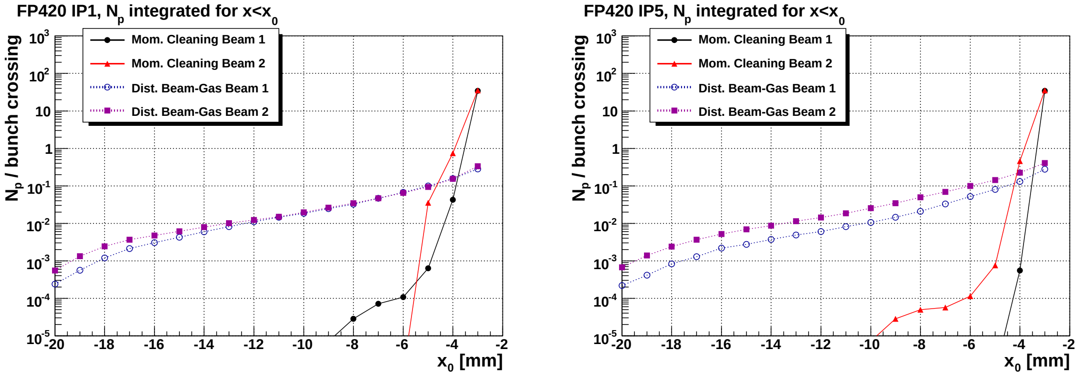

Fig. 40: Total amount of beam halo protons predicted at the 420 m regions for different FP420 detector horizontal positions.

the optical properties of the beamline with a full particle-matter interaction model. Figure 41 shows the 3D volumes included in the BDSIM model of the beamline from the ATLAS detector to FP420; red denotes a quadrupole element and blue denotes a bending element.

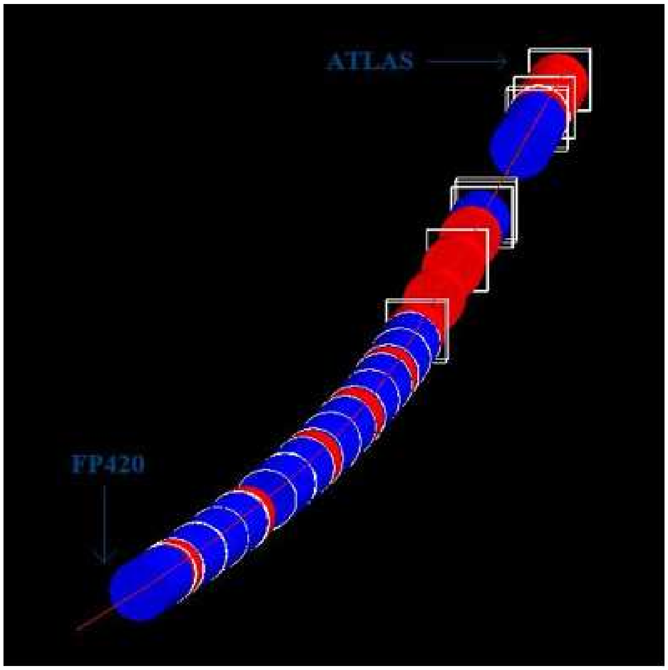

Fig. 41: Beam line model created with BDSIM, showing the beamline from Atlas to the position of the FP420 detector (red denotes a quadrupole element and blue donates a bending element).

The input particle phase space from proton-proton collisions at the interaction point was generated with the Monte Carlo program DPMJET [121]. DPMJET is the reference program for most of the background studies for the LHC, and was chosen to produce the final state proton spectra for this reason. Figure 42 shows a comparison between the leading proton spectrum as a function of fractional momentum loss ξ generated by DPMJET and used in this analysis compared to the ξ distribution measured by the ZEUS Collaboration at HERA [79].

The following simulations were performed to check the consistency of loss maps between BDSIM and the code MADX [122]. They were performed for the IP5 beamline, for the LHC Beam 1, starting from the same proton sample generated with DPMJET at IP5 and consisting of 50000 protons with $\mathrm{dp}/\mathrm{p} < 0.05$ with respect to the nominal momentum $\mathrm{p}_0 = 7\mathrm{TeV}$. The resulting number of protons lost as a function of the distance from the IP, in the region from 300 to 420 m is shown in Figure 43. The figure shows a very good consistency of found loss locations between the two codes. Studies aiming at understanding the differences are ongoing.

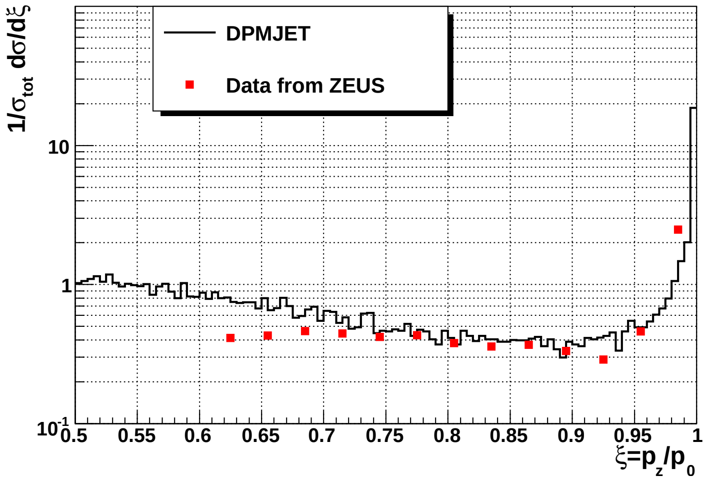

Fig. 42: The leading proton spectrum as a function of fractional momentum loss ξ predicted by DPMJET and measured by the ZEUS Collaboration [79].

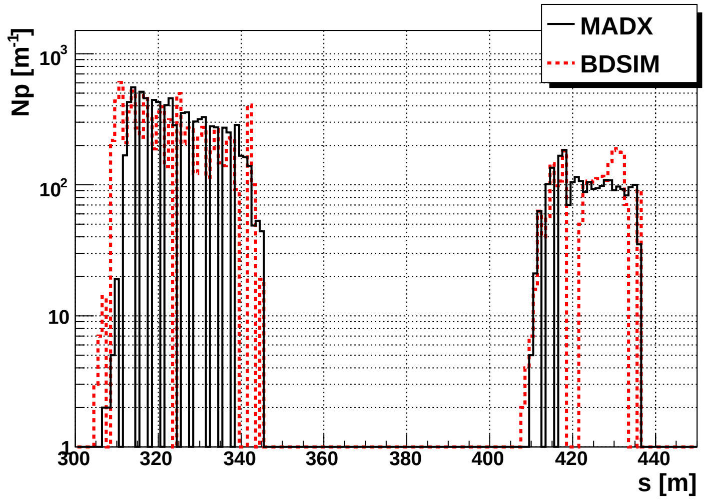

Fig. 43: Loss maps produced for the IP5 beamline with a DPMJET phase space sample using MADX and BDSIM.

5.5.1 *Background particle fluxes and detector modeling*

The loss of protons shown in Fig. 43 results in the production of secondaries and the subsequent irradiation of the FP420 detector region. The electromagnetic and hadronic showers resulting from the transport of the DPMJET phase space sample was calculated using BDSIM, and the number and properties of the particle spectra estimated at 420 m. These calculations were done using a subset of a DPMJET events with 565,000 final state protons on one forward side, which caused proton loss and showering in the beamline immediately preceding 420 m. The LHC total proton-proton cross section gives about 35 proton-proton collisions per bunch crossing, of which approximately 1/3 give forward protons, and BDSIM estimates the neutron rate to be 0.11 neutrons per bunch crossing at 420 m. This is equivalent to an integrated rate of $44.4{\cdot}10^3$ neutrons per $\mathrm{cm}^2{\cdot}\mathrm{s}$, with a time structure similar to the bunch structure with a slight smearing to later times. The distribution of in-time backgrounds is important for time-of-flight analysis. Hadronic models uncertainties in GEANT4 and uncertainties in the number of events per bunch crossing imply that the numbers quoted here are preliminary, and may result in a suppression of hadronic rates. These numbers are currently being used to estimate the effect on the detector signal-to-noise ratio and long-term damage, through equivalent neutrons, and the systematic errors are under study. In addition, the background contribution from charged secondary particles generated by proton losses in the accelerator elements immediately upstream of 420 m is under investigation. Preliminary results of the Protvino group simulations [113] (accounting for diffractive proton losses as source of secondary showers) are shown in Fig. 44. These results have to be confirmed and crosschecked with BDSIM.

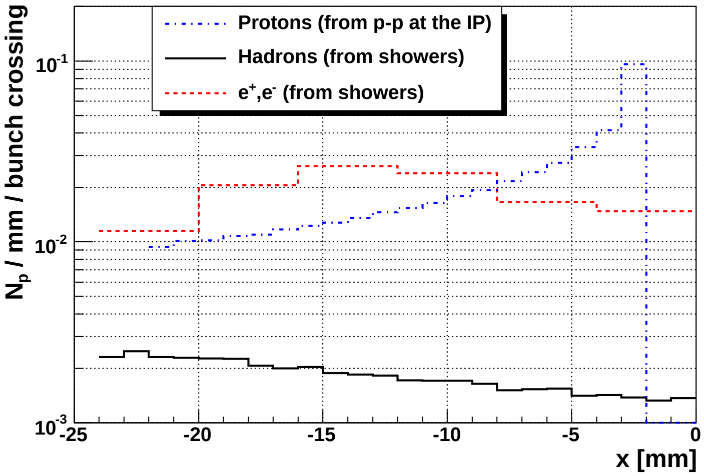

Fig. 44: Secondary particles flux at the entrance of the 420 m region downstream IP5 (preliminary results). The shower source is diffractive protons, generated with DPMJET, lost on the last bending magnet before FP420. The surviving diffractive protons are shown too.

The detector region has also been simulated with GEANT4 [120], and one aim of the background analysis is to integrate the BDSIM model of the beamline with the GEANT4 model of the detector. This simulation of the complete chain will allow studies beginning with proton interactions at the IP, and ending with the production and reconstruction of tracks in the detector stations.

The GEANT 4 geometry of the detector pockets is shown in Fig. 45. In the GEANT4 simulations to-date, different layout of the detector stations and surrounding pockets have been considered, along with different numbers of sensitive planes. In all cases the rate of secondary interactions of 7 TeV protons traversing the full detector region was studied as a function of the materials used and their thickness. The results of these studies are described in Section 9.7, where their impact on the design of the layout of the detector region is discussed.

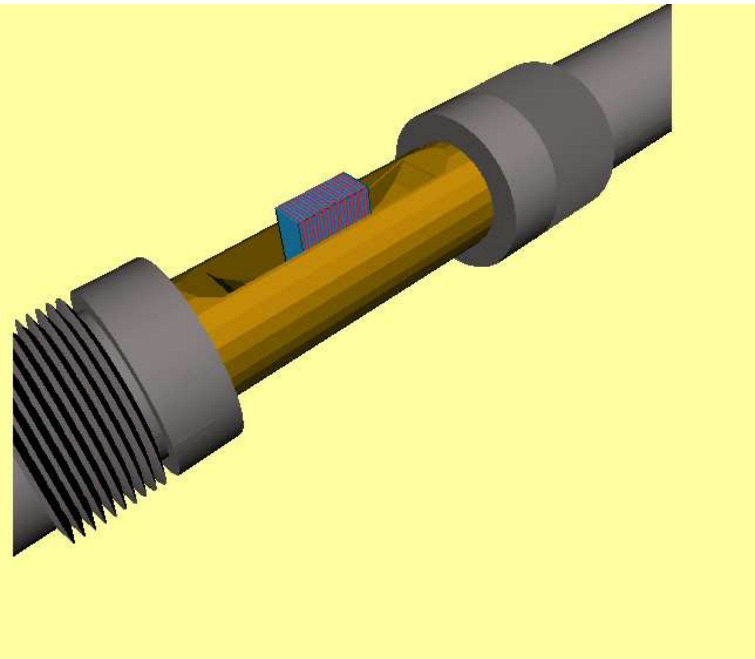

Fig. 45: An example of the GEANT 4 geometry of the pocket hosting the detectors. This model was used to study the interaction rate of 7 TeV protons, which is described in Section 9.7.

5.6 Machine background summary

The machine-induced background contribution at 420 m from near beam-gas and the betatron cleaning collimation is expected to be small, due to the arguments given in this chapter. However, there is a contribution to the background rate arising from far beam-gas, the momentum cleaning collimators and proton loss in the beamline. The first two of these contributions give a proton background which is described by a peak determined by the momentum cleaning collimator settings, and a tail dominated by far beam-gas halo protons. The combined distribution is shown in Fig. 40. At detectors transverse distance of 5 mm or greater, the expected integrated number of protons from beam halo is expected to be less than 1 per bunch crossing. The impact of a rate of less than 1 proton per bunch crossing on the FP420 physics signal in a pixel detector requires further study and comparison of the background and signal spatial, angular and temporal distributions. This may allow some degree of background rejection.

The proton loss background contribution is a mixture of charged and neutral particles produced immediately upstream of 420m. The BDSIM estimate of the neutron rate is 0.11 neutrons per bunch crossing at 420 m. The impact of these preliminary neutral background rates will be assessed in term of detector performance and survivability.

In summary, the preliminary proton and neutron background rates at 420 m have been estimated and need to be combined with detailed detector and signal studies to understand the impact on the FP420 experiment.

6 A new connection cryostat at 420 m

The LHC beamline layout downstream of an interaction point (IP) consists of a triplet of low-beta quadrupole magnets, two beam separation dipoles and a matching section of quadrupoles up to quadrupole Q7. This is followed by a dispersion suppressor region of standard dipoles and quadrupoles and finally the periodic lattice of the arc. In the dispersion suppressors there is a 14 m drift space, sometimes called the "missing magnet" drift space, which is approximately 420 m downstream of the IP. In the LHC it was decided, mainly for cost reasons, to place the dispersion suppressors and arc magnets in one continuous cryostat from Q7, all the way to the symmetric Q7 quadrupole upstream of the next IP [123]. At the position of the missing magnet, 420 m downstream of each IP, there is a 14 m long Connection Cryostat (CC) which contains cold beam-pipes, the 2K heat exchanger, or X-line, and various cryo-lines which run throughout the continuous cryostat, as well as the superconducting busbars and nearly 100 superconducting cables of the main bending magnets and corrector magnets. There are sixteen CCs in the LHC, each made to be as similar as possible to a standard arc cryostat, as far as interconnection and handling are concerned. At this 420 m point, the dispersion function D, with the standard high luminosity optics, is approximately 2 m and hence protons from the IP which have lost around 1% of their momentum are well separated from the circulating beam, as described in Sec. 4. Placing detectors directly inside the 1 m diameter cryostat at a temperature of 2K was considered, but ultimately dismissed, primarily because of the inevitable very high local heat load on the LHC cryogenic system. The alternative is to replace the existing connection cryostat with a warm beam-pipe section and a cryogenic bypass. At the end of each arc cryostat of the LHC there is a special short cryostat called an Arc Termination Module (ATM) which includes cold to warm transitions for the beampipes and connects cryo-lines and superconducting busbars and cables to the electrical feed boxes. A New Connection Cryostat (NCC) with approximately 8 m of room temperature beam-pipes has been designed using a modified ATM at each end.

In addition to the two modified ATMs and warm beam-pipes, the NCC shown in Fig. 46 has a small cross section cryostat below the beam-pipes carrying all the cryo-lines and superconducting circuits and a new specially designed cryostat for the X-line. All this is supported by two longitudinal beams to make a single unit which can be directly exchanged for an existing connection cryostat. The passage of the X-line through the ATM modules is the main modification needed to the standard ATMs, but the geometrical layout of this passage has been arranged to be as far away as possible from the downstream beam-pipe and hence leave adequate space for near-beam detectors and their associated equipment. The cross-section of the NCC, with the space around the beam-pipes available for detectors and associated mechanics, is shown in Fig. 47.

The existing connection cryostat contains a box structure of lead plates of 15 mm thickness enclosing the two beam-pipes to reduce the radiation field in the tunnel, essentially replacing the shielding provided by the cold mass in a standard arc dipole cryostat. The same thickness of lead shielding will be provided around the warm beam-pipes and detector stations of the NCC. A preliminary design, which provides a complete radiation shield while giving access to the detector stations and passages for services is shown in Fig. 48.

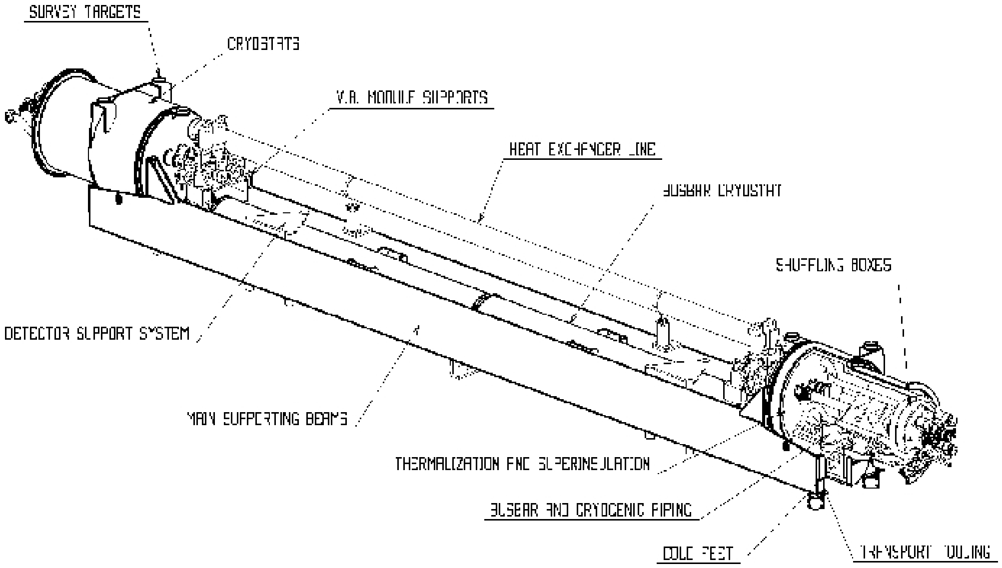

Fig. 46: The new connection cryostat for FP420

There are also short lengths of cylindrical shielding in the form of collars around the beampipes at each end of the existing connection cryostat to limit the risk of quenching adjacent superconducting magnets. These same collars will be incorporated into the modified ATM's at each end of the NCC in order to ensure that the performance of the NCC is also equal to the existing cryostat in terms of influence on the local radiation fields.

The engineering design of the new connection cryostat is in progress in the CERN central design office of the TS/MME group. The design aim is to meet or exceed the same specifications as the existing connection cryostat, whilst providing the maximum useable space for the FP420 detectors. The preliminary design offers acceptable solutions for all cryogenic and mechanical engineering aspects as well as integration into the LHC environment [124, 125]. The final cryogenic performance will depend on the detailed design, but it has already been established that the additional static heat load arising from the two additional cold to warm transitions will be tolerable for the LHC cryogenic system. In fact, simulations show that during LHC operation the NCC actually has a lower dynamic heat load than the existing connection cryostat, because in the 8 m long warm section synchrotron radiation will be absorbed at room temperature.

The detailed design of this second generation connection cryostat is in progress and will be followed by an Engineering Change Request (ECR) submitted to allow a detailed engineering

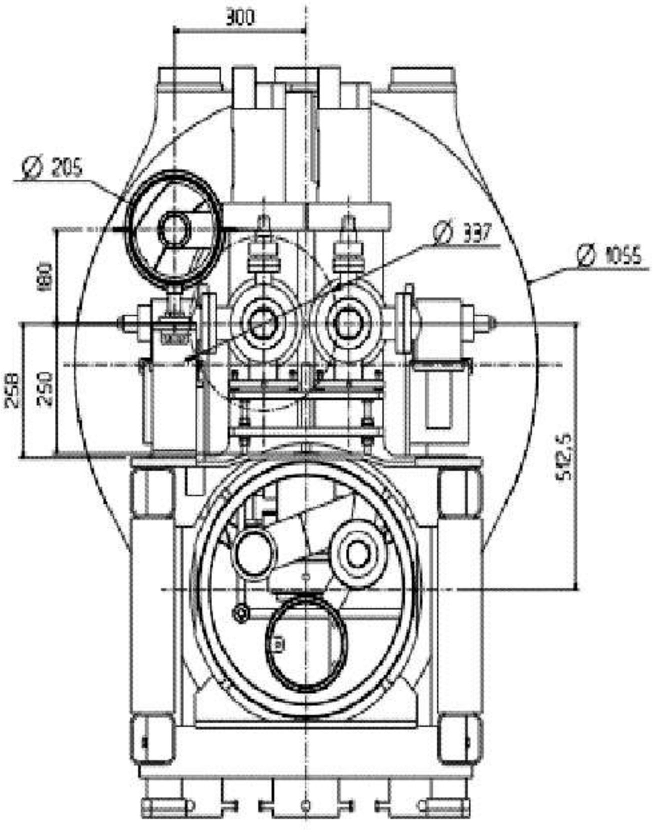

Fig. 47: Cross-section view of the new connection cryostat for FP420

review of all machine aspects to be performed. Following acceptance of the ECR it would in principle be possible to build two complete NCC's in about a year and have them tested and ready for installation in late 2009. Vittorio Parma of the AT Department's MCS group has accepted to take up responsibility for the cryostat. He will lead a working group which will verify the compatibility of the existing conceptual design and develop the detailed design for manufacture. As regards construction of the NCC's, the sixteen ATM modules of the LHC were assembled at CERN in a dedicated workshop in Building 110, under the responsibility of Ramon Folch (TS/MME). His team has prepared a preliminary construction schedule and cost estimate for the new cryostats [126].

The cutting and removal of the existing connection cryostat and its replacement by an NCC is very similar to the replacement of a standard LHC dipole and has been evaluated by the group responsible for all the LHC interconnections. As mentioned above this is the same group that took

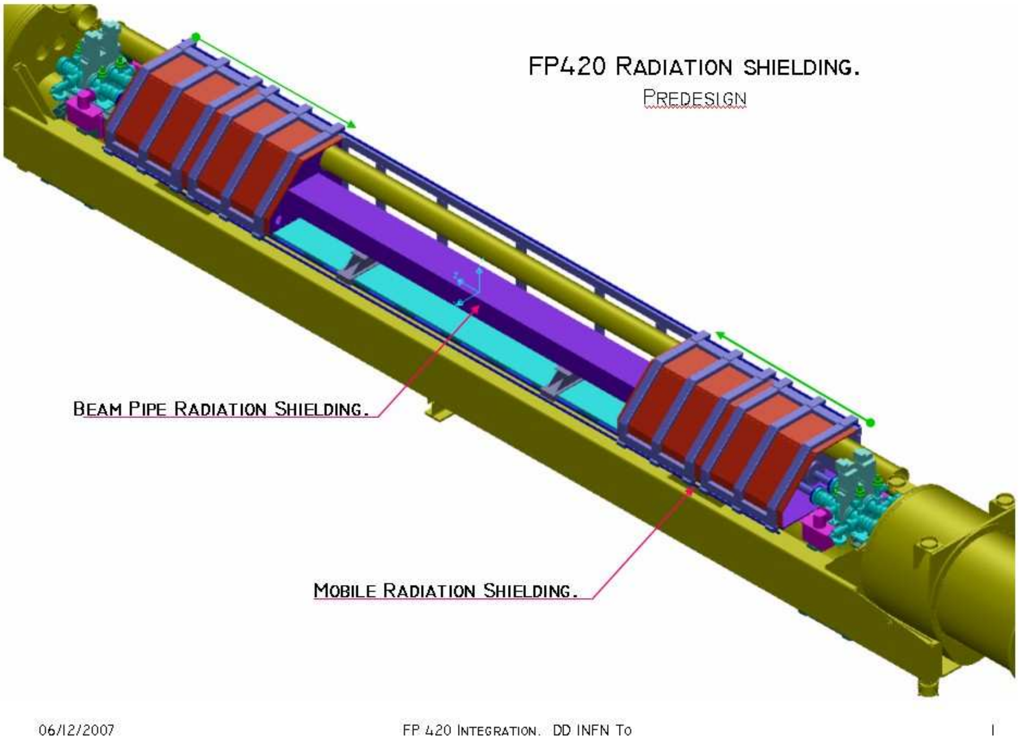

Fig. 48: Preliminary design for radiation shielding around the warm beampipes and detector stations. The mobile shielding can be rolled sideways on rails to give access to the detector stations.

responsibility for the design installation and performance of the existing connection cryostat.

Table 11 shows the sequence of operations and the estimated time needed in normal working days to complete the exchange of a connection cryostat from start of warm-up to being ready for beam. It is thus conceivable that the installation of FP420 modules consisting of an NCC cryostat and associated detectors could be completed in an annual long shutdown. A preliminary study of the transport aspects has shown that adequate tooling exists and it can be expected that the time needed will be in the shadow of other operations shown in Table 11. However, the number of connection cryostats that can be replaced in a standard annual shutdown will depend on the number of LHC magnets requiring replacement and the work load of the interconnection teams.

6.1 Cryostat summary

In summary, a preliminary design for a replacement connection cryostat that would allow detectors to be placed in the 420 m region has been completed, and a final design is in progress. This solution is expected to actually lower the dynamic heat load of the LHC and have similar radiation profiles. With the appropriate approvals and funding, two such cryostats could be built and installed in late

	Normal Days
Warmup from 1.9K to 4.5 K	1
Warmup from 4.5K to 300 K	15
Venting	2
Dismantling interconnection	10
Removal of the connection cryostat	2
Installation of the FP420 cryostat	5
Realization of the interconnections	15
Leak test and electrical test	4
Closing of the vacuum vessel	1
Evacuation/repump	10
Leak test	2
Pressure test	4
Cool-down from 300 K to 4.5 K	15
Cool-down from 4.5K to 1.9 K	3
Total [days]	89

Table 11: The estimated time in days required to install one NCC

2009, and in principle, two more in 2010 with negligible risk to LHC operations.

7 Hamburg beam-pipe

7.1 Introduction

Detection of diffractive protons at 420 m from the IP is particularly challenging since it requires detectors to be placed between the two LHC beam-pipes, the exteriors of which are separated by about 140 mm (the distance between the pipe axes is nominally 194 mm). In addition, the nearby cryogenic lines severely limit the available free space. Due to these space constraints the traditional Roman Pot (RP) technique cannot be used, and another concept for near beam detectors, pioneered at DESY is proposed. This technique of moving sections of beam-pipe with integrated detectors is known as “Hamburg pipes” and was developed within the ZEUS collaboration in 1994 to measure very forward-scattered electrons as a signature of photoproduction [127]. The concept was inspired by the moving pipes used in the PETRA wiggler line to allow for beam-line aperture changes. The ZEUS version involved small electromagnetic calorimeters attached to the moving pipe (44 m from the interaction point). The detectors were retracted during beam injection, but could be positioned close to the beam axis during stable beam conditions, and thus measure scattered electrons with reduced energy, which exited the pipe through special thin windows. Since the detectors were located outside of the machine vacuum, they could be easily maintained and were successfully and routinely used for six years, providing data essential for several publications [128]. The detectors were positioned remotely by the HERA shift crew, which inserted the detectors at the working position, typically about 15 mm from the coasting electron beam, using the HERA slow control system.

Prior to installation at HERA, the Hamburg pipe system was tested by making several thousand displacement operations. No significant radio-frequency (RF) effects on the electron beam were observed due to the modified beam-pipe geometry. It should be noted that no special RF screening was used; it was sufficient to have the so-called RF fingers providing good electrical contact across the connecting bellows.

The moving pipe technique has many advantages with respect to the RP design. It allows much simpler access to detectors and provides direct mechanical and optical control of the actual detector positions. In addition, unlike the Roman pot case which involves forces from pressure differences as the detectors are inserted into the vacuum, the Hamburg pipe maintains a fixed vacuum volume. This results in much less mechanical stress, consequently allowing a very simple and robust design.

7.2 FP420 moving pipe design

A modified connection cryostat (Section 6) has been designed with approximately eight meter long warm beam-pipes, providing adequate lateral space to install the FP420 detectors. Figure 49 shows the layout of the connection cryostat including two detector stations and the support table. The entire detector arm is fixed on the support table, which is attached to the tunnel floor, independent of the cryostat. Both ends of the detector arm are equipped with vacuum pumping and control stations and isolation valves. Figure 50 shows one of the two detector stations equipped with timing and silicon detectors, an LVDT (Linear Variable Differential Transformer) for position measurement and one moving and one fixed beam position monitor (BPM). The support table and motion system are shown in Fig. 51.

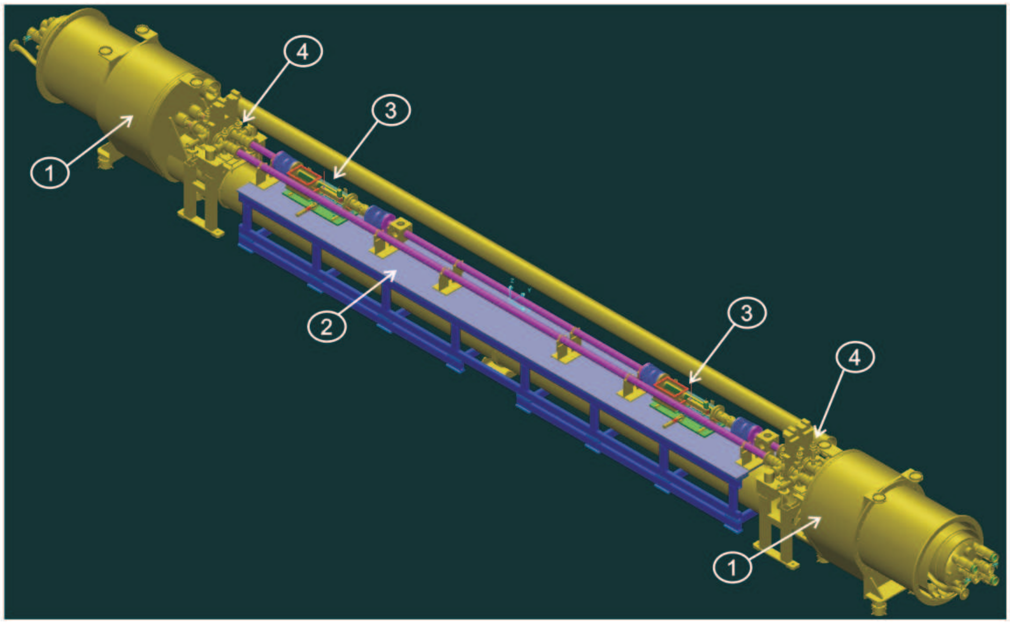

Fig. 49: Schematic view of the connection cryostat (1) and detector arm with support table (2), two detector sections (3) and vacuum pumping sections (4).

The basic dimensions of the stations are defined by the LHC standard beam-pipe diameter, the required lateral detector translation, and by the longitudinal dimensions of the FP420 detectors. Each station is composed of a beam-pipe with inner diameter of 68.9 mm, wall thickness of 3.6 mm and a length of about 1000 mm, fixed on a motorised drive. Rectangular thin-walled pockets are built into the pipe to house the different detectors that must be positioned close to the beam. The displacement between data taking position and the retracted or parked position is about 25 mm. The ends of the moving beam-pipes are connected to the fixed beam-pipes by a set of two bellows. Inside, these may be equipped with moving RF-contacts to assure electrical continuity. In general, this design allows significant flexibility in the configuration of the detectors stations, allowing optimization of the detector operation, scattered proton detection, kinematical reconstruction, and alignment.

7.3 Pocket Design and Tests

A key factor in the pocket design is the desire to maximise detector acceptance, which is achieved by minimizing the distance of the detector edge from the LHC beam. This in turn requires that

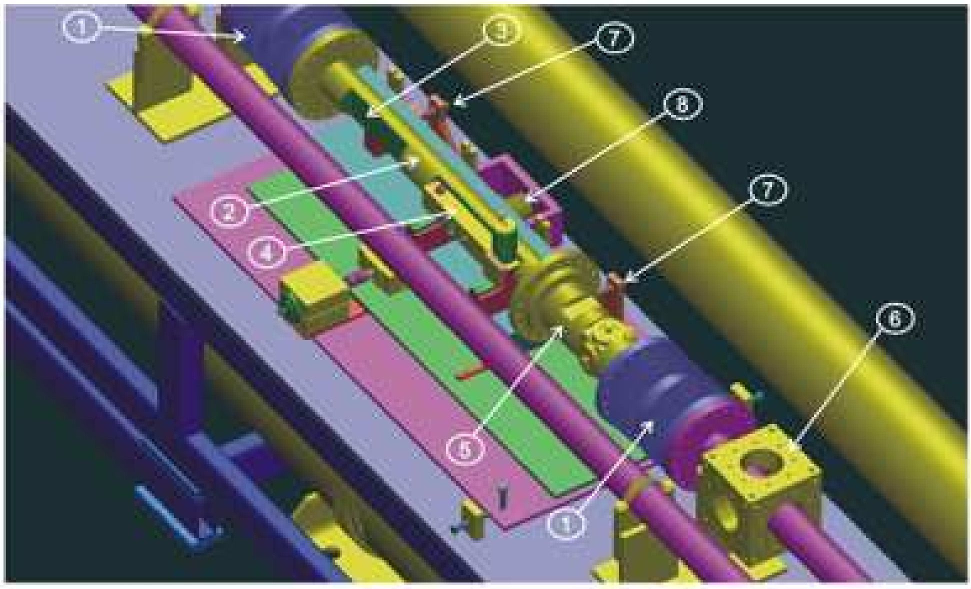

Fig. 50: Top view of one detector section: bellows (1), moving pipe (2), Si-detector pocket (3), timing detector (4), moving BPM (5), fixed BPM (6), LVDT position measurement system (7), emergency spring system (8).

the thickness of the detector pocket wall should be minimised to limit the dead area. Care must be taken to avoid significant window deformation which could also limit the detector-beam distance.

A rectangular shaped detector pocket is the simplest to construct, and minimises the thin window material perpendicular to the beam which can cause multiple scattering and degrade angular resolution of the proton track. RF studies of the rectangular pocket have shown (see Sec. 8) that the effects on the beam dynamics are minor. For reasons of mechanical stiffness, thermal stability and fabrication of the pockets, only stainless steel beam tubes are suitable. They will be copper coated for RF-shielding and Non-Evaporative Getter (NEG) coated for vacuum pumping. A rectangular slot of adequate height and length is machined in the beam tube. A thin window is then welded in this slot. Both welded and extruded pipes have been used in tests. Figure 52 shows the interior of the Hamburg pipe including the thin vacuum window as seen by the scattered protons.

First tests using welded pipes showed excessive deformation due to asymmetrical stresses appearing after the machining of the cylindrical pipes. Several welding techniques for different length pockets have been considered and two have been tested: Tungsten Inert Gas (TIG) welding and laser welding, the latter expected to produce somewhat smaller deformation. A first prototype used thin (0.2 and 0.3 mm) windows of 83 mm height and 200 mm length TIG welded in rectangular slots, machined in a tube of diameter 89 mm. The deformation for this setup under vacuum

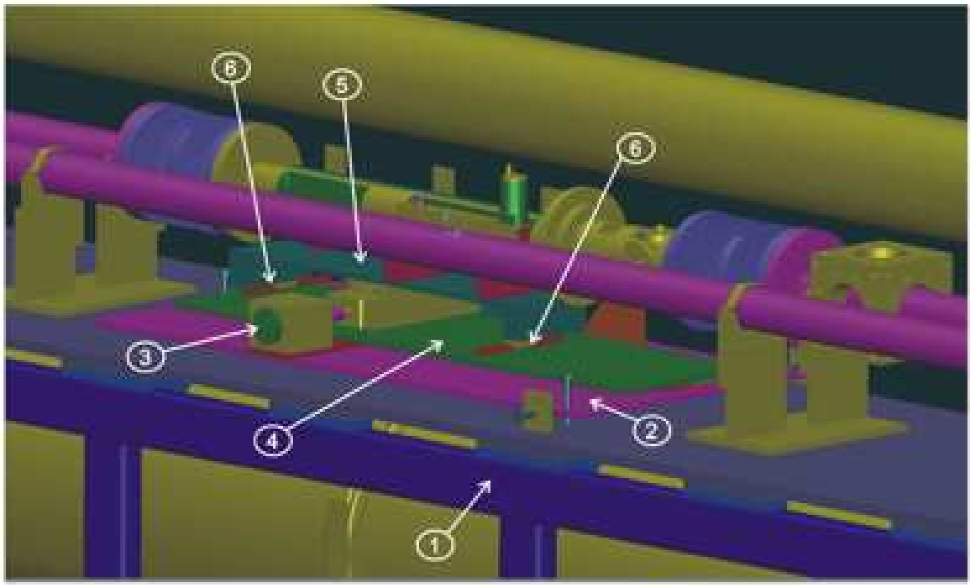

Fig. 51: Support table (1), drive support table with alignment system (2), drive motor (3), intermediate table for emergency withdrawal (4), moving support table (5), and linear guides (6).

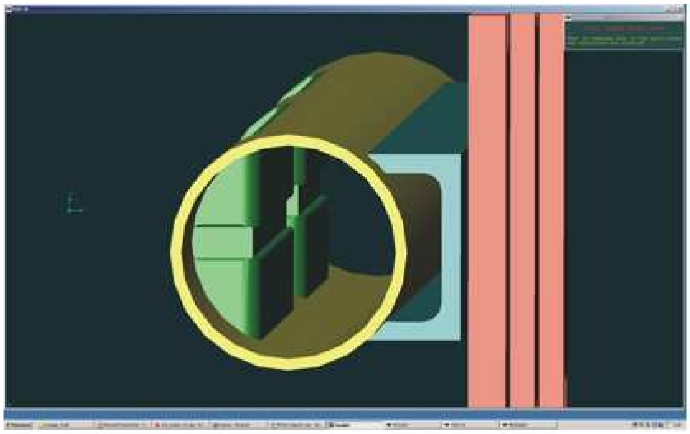

Fig. 52: Interior of the moving beam-pipe as seen by the particles.

were unacceptable, exceeding 5 mm in the centre. Pressure tests with this prototype have shown that the TIG weld is quite strong, as it supported pressures of up to 7 bar.

A first improvement was to use specially machined windows, which have a thin wall of 0.5 mm only over 10 mm height and uses thicker, solid walls for the remainder of the pipe (we note that the full scale range of the scattered protons of interest is only a few mm as shown in Sec. 4. Figure 53 shows this design with the machined window TIG welded onto a long tube.

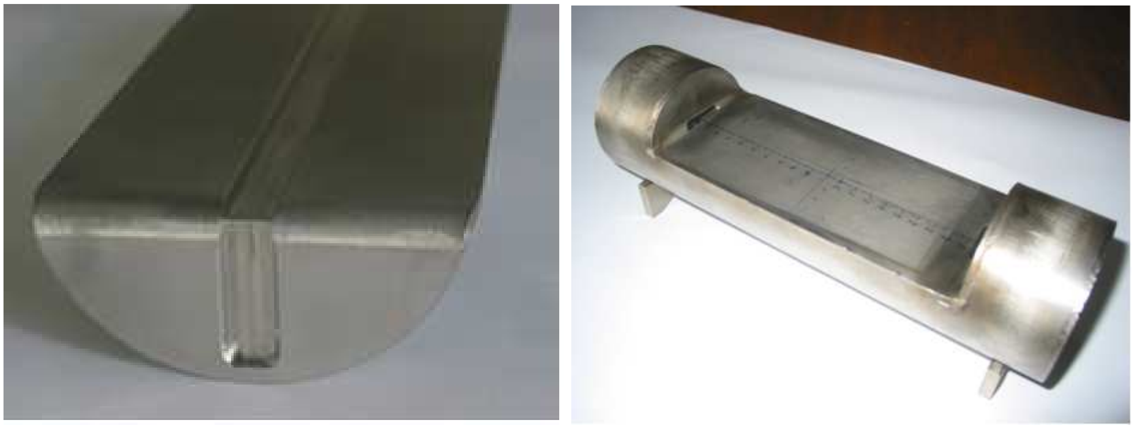

Fig. 53: Hamburg pipe prototypes: (left) an end view of a machined window before welding to the beam-pipe; (right) a 200 mm long pocket, TIG welded in a tube without reinforcement.

A second improvement to keep the cylindrical tube from deforming was to weld a U-shaped steel support to the back side of the pipe. Figure 54 shows the coordinate system used to measure the deformation (and the locations where the measurements are made) and the tube before and after the reinforcement is attached.

We measured the deformation of the 600 mm pocket at different stages. Figure 55(a) shows the deformation as a function of length at the "Side II" (as defined in previous figure) location before (blue) and after (pink) laser welding. Although the magnitude of the deformation increases after welding, but is still less than 100 μm, far superior than the TIG welding case. Figure 55(b) shows the deformation after welding but before vacuum pumping for three parallel lengths. The effect is similar, although it is a little worse in the middle (blue) than in the two sides, as expected, it is still less than 100 μm. Figure 56(a) shows that although the deformation at the sides (edges) is not much affected by vacuum pumping, it becomes much larger (> 300 μm) in the middle. After reinforcement, however, it is reduced to acceptable levels, as shown by the perpendicular height profile at the middle of the tube in Figure 56(b). We also note that the final design will have pockets of 1/3 to 1/2 the length, implying significantly less deformation.

A new 1 micron-precision 3D multisensor measuring device has been tested on a 200 mm long TIG welded window. The result is shown in Fig. 57. This device will help us fully evaluate the final prototypes.

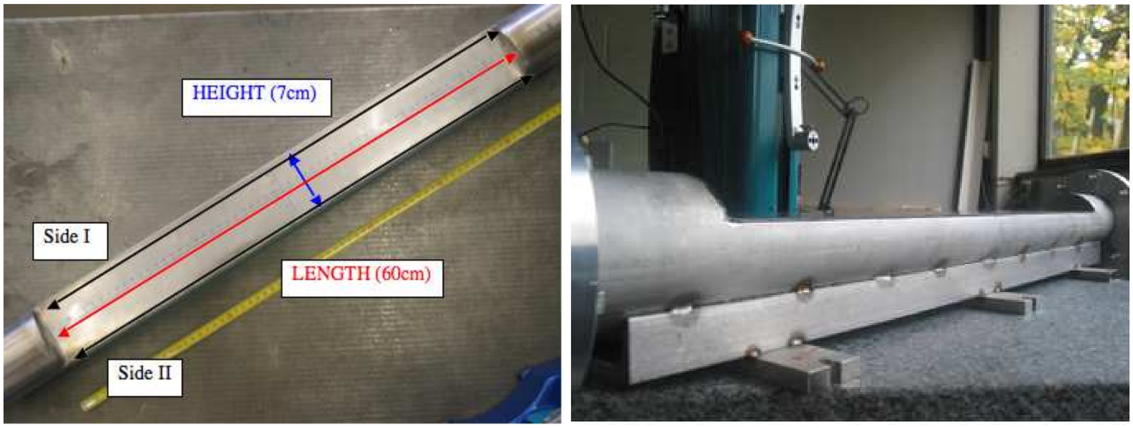

(a) (b)

Fig. 54: Hamburg pipe prototypes: (left) view of a 600 mm long pocket, laser welded in a tube without reinforcement; (right) picture of a 600 mm long pocket welded by laser in a reinforced tube.

Two prototype beam tubes equipped with 600 mm long pockets were used for RF measurements at the Cockcroft Lab. The results of these measurements are described in Sec. 8.

7.4 Test beam prototype

The baseline prototype of the moving beampipe was prepared for use in test beam at CERN in October 2007. Figure 58 shows the 1 m long beam-pipe equipped with two pockets, one of 200 mm length for the 3D pixel detector (Section 9) and the other of 360 mm length for the gas Čerenkov timing detector (Section 10) . The vacuum window thickness was 0.4 mm. A detector box for the 3D detectors was mounted in the first pocket. The moving pipe was fixed on a moving table, driven by a MAXON motor drive and guided by two high precision linear guides. The moving table was equipped with alignment adjustments in the horizontal, vertical, and axial (along the beam axis) directions, and was attached to a fixed structure in the test beam area. The relative position of the moving pipe was measured with two SOLARTRON LVDT displacement transducers, which have 0.3 μm resolution and 0.2% linearity.

7.5 Motorization and detector system positioning

In routine operation, detector stations will have two primary positions (1) the parked position during beam injection, acceleration and tuning, and (2) close to the beam for data taking. The positioning must be accurate and reproducible. Two options have been considered: equipping both ends of the detector section with a motor drive which are in principle moving synchronously but allowing for axial corrections with respect to the beam axis, or a single drive at the centre, complemented with a local manual axial alignment system. A two motor solution in principle allows perfect positioning of the detector station, both laterally and axially. However, it adds complexity to the

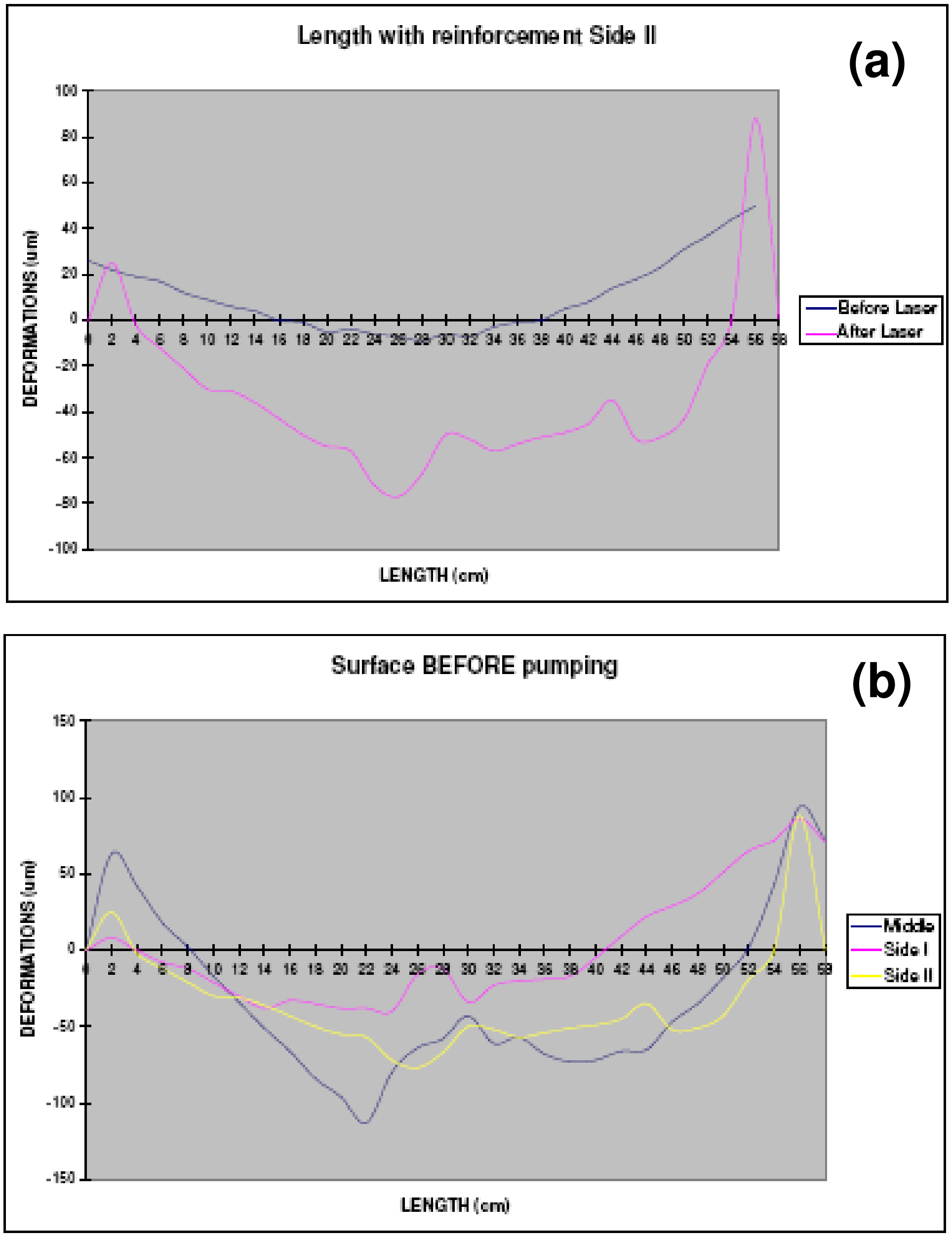

Fig. 55: (a) Deformation as a function of length at the "Side 2" location before (blue) and after (pink) laser welding. (b) Deformation after welding but before vacuum pumping for the three locations.

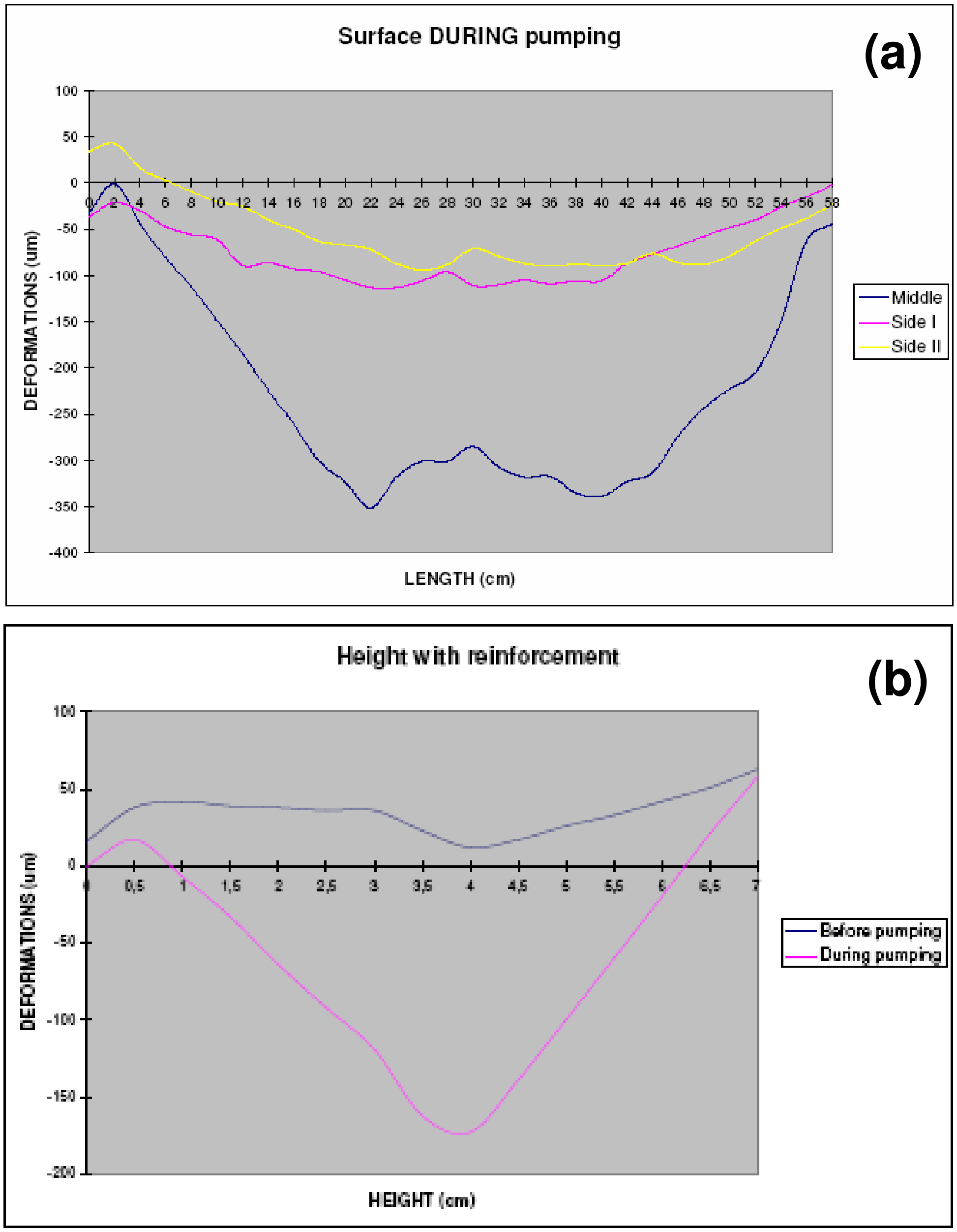

Fig. 56: (a) Deformation as a function of length after vacuum pumping. (b) Height profiles after reinforcement.

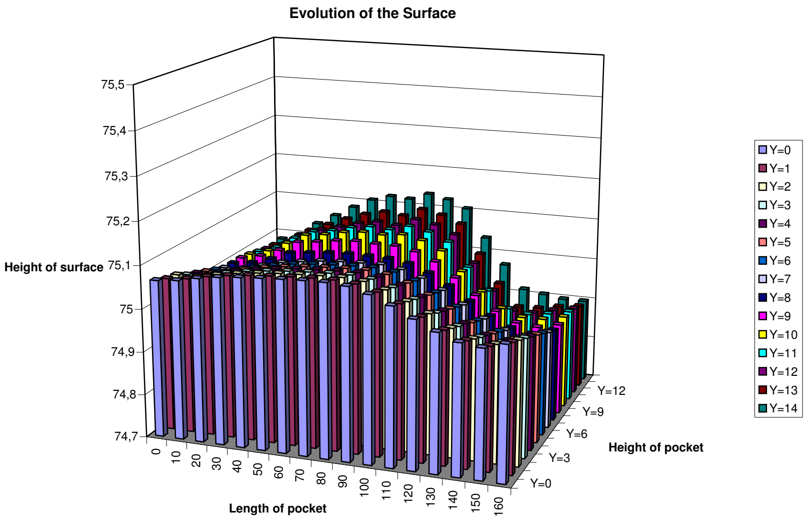

Fig. 57: Example of a 3D profile measurement run using the multi sensor equipment.

control system, reduces reliability, and increases cost. Positioning accuracy and reproducibility are also reduced because extremely high precision guiding systems can no longer be used, due to the necessary additional angular degree of freedom. Therefore, a single motor drive system has been chosen, accompanied by two precise LVDTs. As in the LHC collimator system, no electronics is foreseen in highly irradiated zones, close to the motors, to limit radiation damage. For ease in integration, we are planning to adopt the collimator stepping motor solution. As these have never been irradiated, the stepping motors will be tested in the high neutron flux test beamline at the Louvain-la-Neuve cyclotron centre CRC [129].

7.6 System operation and safeguards

Given the FP420 schedule, it will be possible to learn from the experience that will be gained during the LHC commissioning by the operation of machine elements with similar control and surveillance aspects, namely the TOTEM [130] and ATLAS ALFA Roman Pot [131] detectors and the LHC collimators [132]. Nevertheless a series of aspects specific to FP420 need to be addressed. The F420 detectors will operate at all times in the shadow of the LHC collimators in order to guarantee low background rates and to avoid detector damage from unwanted beam losses.

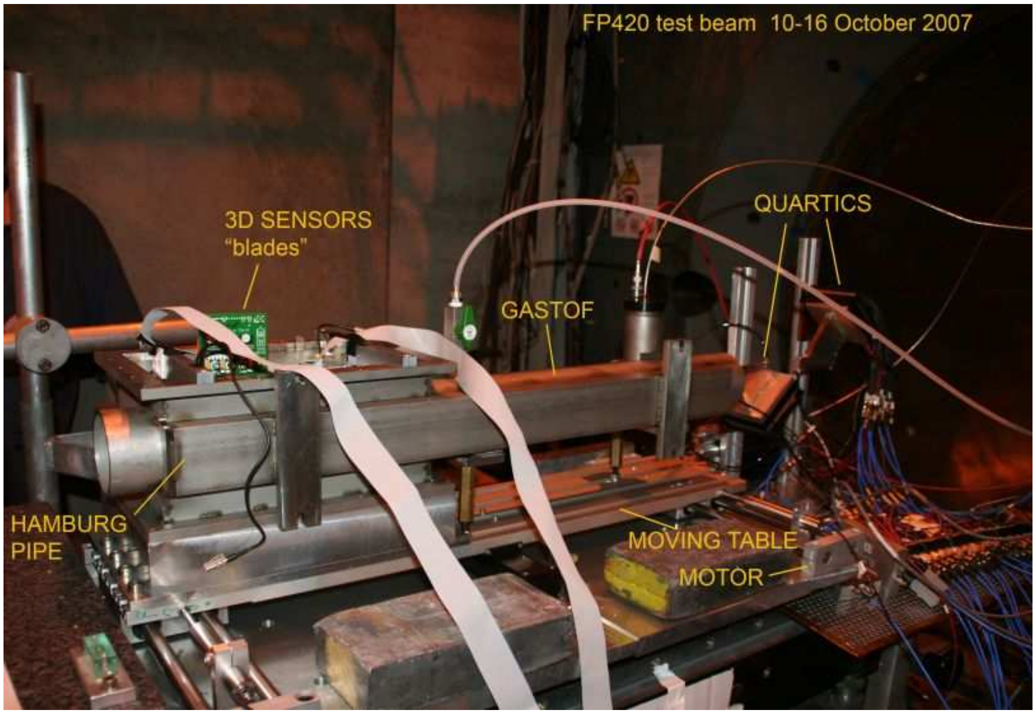

Fig. 58: Photograph of the prototype beam-pipe section used in the October 2007 CERN test beam.

In addition, for machine protection constraints, it will be unacceptable for FP420 to interfere with the beam cleaning system (e.g. to avoid magnet quenches downstream the 420 m region).
Therefore, the high-level Hamburg pipe control system will be integrated in the collimator controls. The interface between low- and high-level controls will be implemented with the CERN standard Front End Standard Architecture (FESA) [133].
The Main Control Room will position the detectors close to the beam after stable collisions are established. The precision movement system will be able to operate at moderate and very low speed for positioning the detectors near the beam. During insertion and while the detectors are in place, rates in the timing detectors will be monitored, as well as current in the silicon. The step motor and LVDT's will provide redundant readback of the position of the detectors and the fixed and moveable BPM's will provide information on the position of the detectors with respect to the beam. Separate mechanical alignment of the height and orientation with respect to the beam are discussed in Sec. 11.

7.7 Hamburg pipe summary and outlook

The Hamburg moving pipe concept provides the optimal solution for the FP420 detector system at the LHC. It ensures a simple and robust design and good access to the detectors. Moreover, it is compatible with the very limited space available in the modified connection cryostat and with the expected position of the scattered protons between the two LHC beampipes. Its reliability is linked to the inherent absence of compensation forces and the direct control of the actual position of the moving detectors. Finally, rather large detectors, such as the timing devices, can naturally be incorporated using pockets, rectangular indentations in the moving pipes. The prototype detector pockets show the desired flatness of the thin windows, and the first motorised moving section, with prototype detectors inserted, has been tested at the CERN test beam. This was a first step in the design of the full system, including assembling, positioning and alignment aspects. A full prototype test is planned in test beam in Fall 2008.

We want to stress that the moving pipe design development and prototyping has been done in direct contact with the LHC cryostat group. In particular, the Technical Integration Meetings (TIM), held regularly at CERN and chaired by K. Potter, provided an efficient and crucial framework for discussions and information exchanges.

8 RF impact of Hamburg pipe on LHC

8.1 Motivation and introduction

The electromagnetic interaction between the beam and its surroundings will be one of the phenomena limiting the ultimate performance of the LHC, because it can lead to single bunch and multi-bunch beam instabilities, beam emittance growth and beam losses. Usually such effects are expressed in terms of *wake fields* and beam *coupling impedance*. As discussed in the LHC design report [123], the LHC has an overall impedance budget that requires careful design of each element of the accelerator to minimise the total impedance. During the first years of operation, it is expected that the maximum intensity of the LHC colliding beams will be limited by collimation efficiency and impedance effects; consequently a series of studies designing upgraded configurations of the LHC was initiated many years ago. The primary focus of these studies is the collimation system, since it is the dominant component of the impedance budget.

In general, the electromagnetic effects are enhanced by the use of low electric conductivity materials, by small distances between the beam and the vacuum chamber and by any transverse cross section variation of the vacuum chamber. In particular, the transverse resistive wall impedance [134, 135] increases when the beam approaches the beam pipe wall, which will regularly occur during FP420 detector insertion. Both the real and imaginary part of the transverse impedance have to be controlled, in order to minimise the effect on beam instability growth rate and betatron tune shift.

Variation of the beam pipe cross-section in the 420 m region not only is a potential issue for LHC operations through increased impedance, but it can also affect the FP420 detectors. Trapped modes arising from the exchange of electromagnetic energy between the beam and its surroundings can cause heating of the detectors which increase their cooling requirements, since they must operate at low temperature. Moreover, the electromagnetic fields can penetrate through the beam pipe walls and be picked up by the detector electronics.

We have begun a series of studies to examine the different aspects of the FP420 impedance. Analytical calculations and numerical simulations are underway to assess the longitudinal and transverse impedance values. Laboratory measurements on an FP420 station prototype have been performed to validate the simulations and will serve to investigate the effect of electromagnetic disturbances on the detector electronics. These studies are also useful to suggest modifications to the final FP420 design to minimise RF effects.

During LHC operation, the real effect of wake fields on power losses and beam instability will be assessed by the convolution in the frequency domain between the beam spectrum and the coupling impedance. Therefore, the relevant upper limit on the frequency that must be considered is assessed by the nominal LHC beam bunch length, $\sigma_z = 0.25$ ns (r.m.s.). This permits us to limit our study up to a frequency of 3 GHz. The following sections describe the current status of the RF studies.

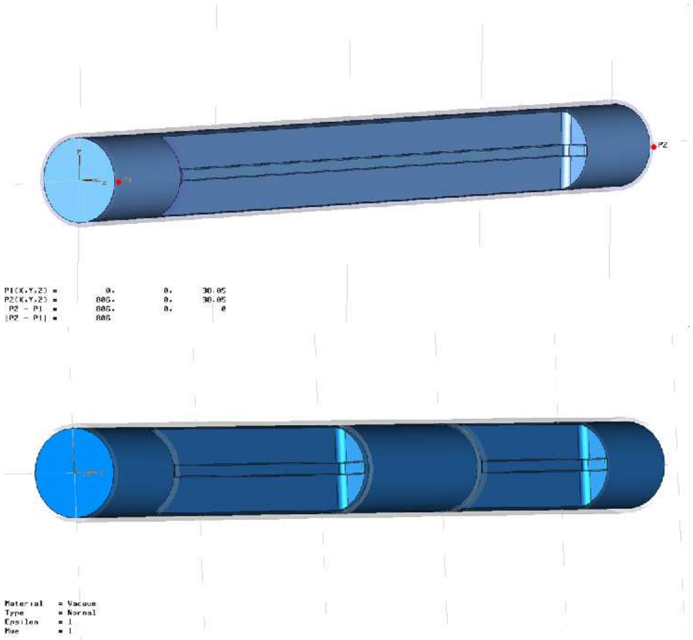

Fig. 59: The two benchmark FP420 pocket designs. The upper figure is a single pocket solution. The lower figure is a double pocket design, which will allow separate temperature and vacuum conditions for timing and silicon detectors

8.2 Longitudinal impedance

Most of the studies are based on the stretched wire method for evaluating the longitudinal coupling impedance Z_L through the measurement of the scattering parameters of the network composed by an RF source and the device under test (DUT) [136]. Usually, the RF source is a two ports Vector Network Analyzer that is used to send an electromagnetic wave through the wire stretched along the DUT. The measurement consists in determining the scattering parameter S_{21}, that is defined as the ratio of the output of the VNA port 2 to the incident wave on port 1. With such a method, the deviation of the impedance of the DUT from that of a reference vessel (REF) can be modeled with a loaded transmission line [137]. Solving the resulting non-linear equation to first order in impedance enables an explicit relation (as function of frequency f) between the longitudinal impedance Z_L and S_{21} to be obtained. This is referred to as the “log” formula:

$$\vec{Z}_L(f) = -2Z_c\, ln \frac{\vec{S}_{21}^{DUT}(f)}{\vec{S}_{21}^{REF}(f)}, \tag{15}$$

where Z_c is the characteristic line impedance.

The results will be expressed in terms of longitudinal impedance Z_L/n:

$$\left(\frac{Z_L}{n}\right) = \frac{Z_L(f)}{f/f_0}, \qquad (16)$$

where $n = f/f_0$ and f_0=11 kHz is the beam revolution frequency in the LHC. This quantity can be compared to predictions and measurements of other LHC elements, as reported in [123]. All the calculations and measurements refer to an FP420 pocket made of stainless steel.

8.2.1 Simulations

Figure 59 shows two beam pipe designs considered for the RF simulations, a single long pocket and an alternative design with two shorter pockets. The results of three different numerical simulation packages are presented. Ansoft HFSS© [138] was used to simulate the stretched wire setup and calculate the longitudinal impedance according to Eq. (15), while CST Particle Studio© (PST)[12] [139] and GDFIDL [140] provide a direct calculation of the electromagnetic field induced by a passing bunch on the surrounding structure.

Figure 60 shows, for all three simulations, the calculations of the real and imaginary parts of the longitudinal impedance. For the single pocket geometry, four narrow band impedance peaks are observed between 2.4 and 2.75 GHz for the HFSS and PST simulations. The frequency difference is attributed to the presence of the wire in the HFSS simulation. Two of the four resonances are significantly reduced for the double pocket simulation with GDFIDL. The wide band resonances that we observe (in both HFSS simulations and experiment) for $f < 2.4$ GHz are understood to be an artifact of the wire and do not represent a real beam impedance effect. Simulations of the double pocket geometry with HFSS are in progress and preliminary results confirm the laboratory experiments that are presented in the next section.

8.2.2 Laboratory measurements

The laboratory setup at the Cockcroft Institute comprises a sophisticated mechanical system equipped with micrometer screws, in order to stretch, move and monitor the relative position of the wire. A set of measurements in the time domain was used to determine the absolute position of the wire with respect to the pocket wall with an accuracy of about 100 μm [141].

Single pocket results

The real and imaginary part of the FP420 longitudinal impedance calculated from the measured S_{21} parameter (black solid line) and simulated by HFSS (blue dashed line) are shown in Fig. 61. This plot refers to a wire distance from the pocket wall of 3 mm, simulating a detector 3 mm ($10\sigma_x$) from the beam. Measurements and simulations have been carried out for several intermediate distances from this position of closest approach to a retracted position ($x > 50\sigma_x$ from the beam).

---

[12] In performing these simulations, a beta-version of PST has been used.

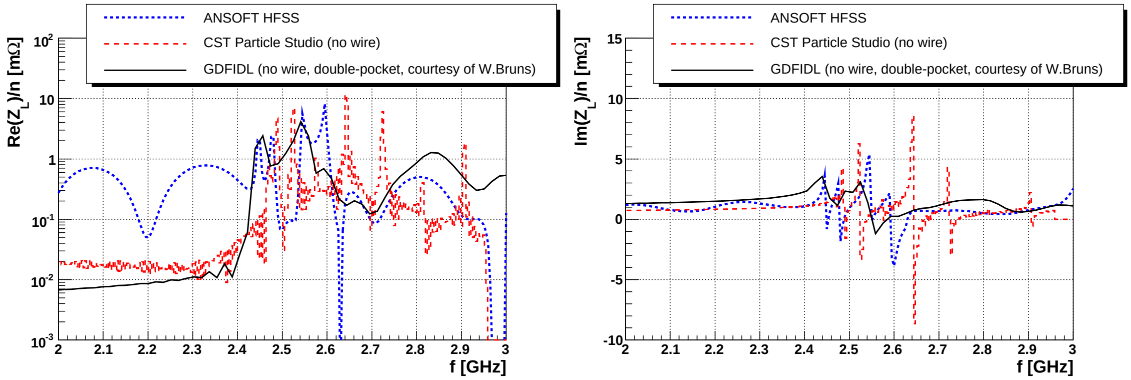

Fig. 60: Real (left) and imaginary part (right) of the longitudinal impedance for three different simulations of the single pocket prototype, effectively assuming the pocket wall is 3 mm away from the beam.

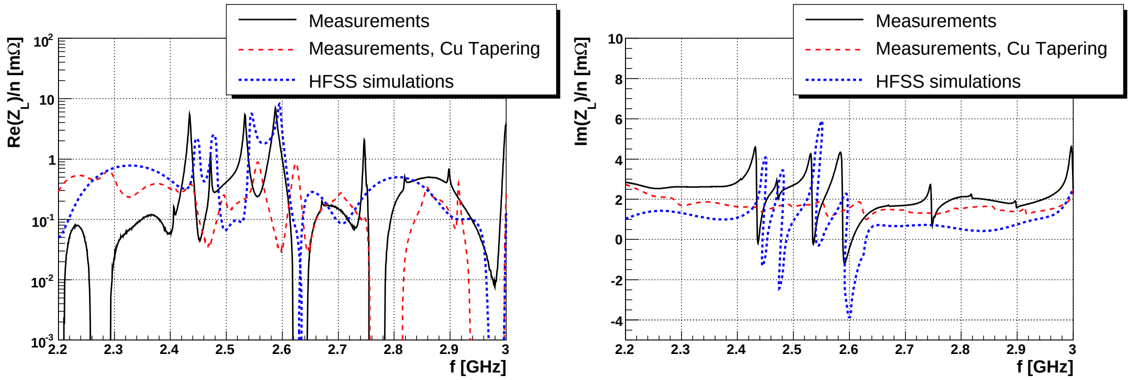

Fig. 61: Measurements of real (left) and imaginary part (right) of the longitudinal impedance with the beam 3 mm from the pocket wall for the single pocket prototype; also shown are the HFSS simulations.

The agreement between measurements and simulations, in terms of resonance peaks of the impedance is satisfactory as they lie within 3 $m\Omega$ in amplitude and a few MHz in frequency. At least one additional resonance appears in the measurements (e.g. at 2.75 GHz) and can be explained by a residual mismatch between the RF source and the DUT, not considered in the simulations.

The FP420 pocket was remeasured after applying a thin copper-plated tape at the indentation regions. The tape was placed outside the beam orbit region (i.e. above and below the 500 μm thin window), in order to provide a tapered transition of the beam pipe cross section variation. The result is shown by the red solid lines in Fig. 61. After tapering, the longitudinal impedance is reduced by an order of magnitude and thus the impedance is limited to no more than 1 $m\Omega$ over the measured frequency band.

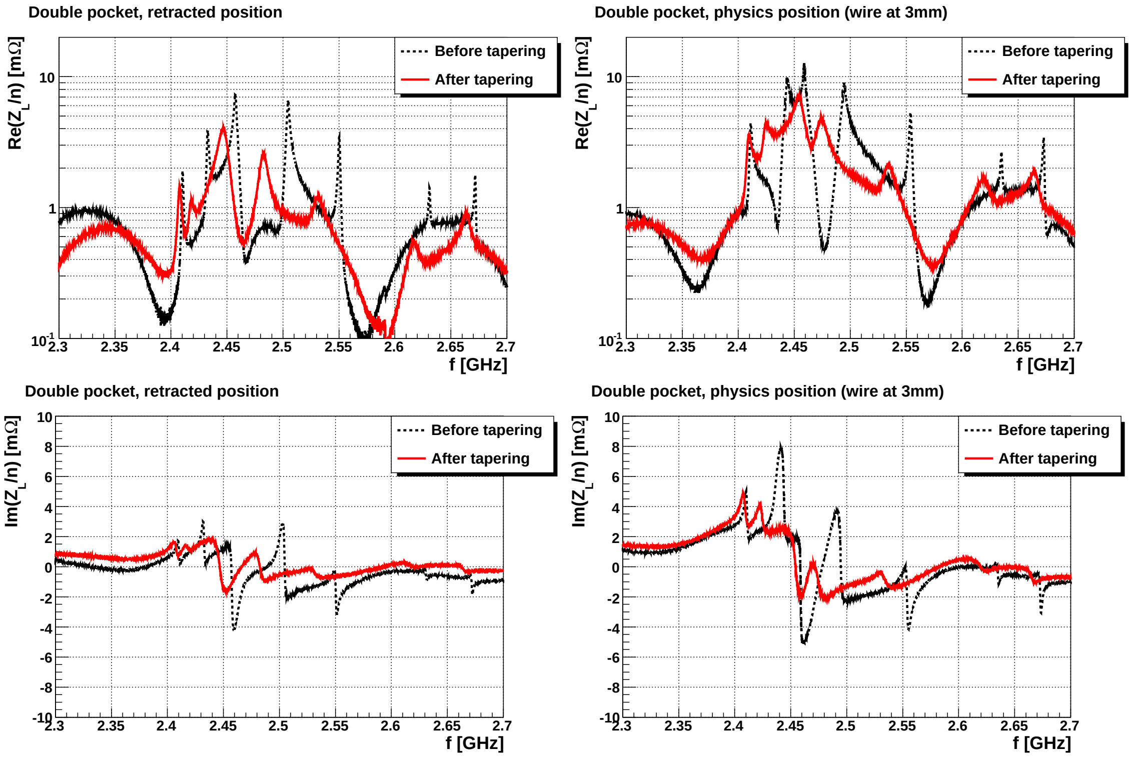

Fig. 62: Real and imaginary part of the longitudinal impedance for the FP420 physics (inserted) and parking positions, as measured for a double pocket prototype.

Double pocket results

A first set of laboratory measurements with an FP420 double pocket prototype has been completed. The results are shown in Fig. 62 in terms of the real and imaginary part of the longitudinal impedance and for parking and physics positions. The black dashed lines refer to the original beam pipe, whereas the solid red lines assess the measured impedance value after applying a copper tape at the accessible pockets indentations (i.e. for each pocket, the indentation at the beam pipe end). The two indentations in between the two pockets are not easily accessible after the beam pipe fabrication and could not be tapered or connected with an RF contact during these measurements. As for the single pocket prototype, there are no impedance peaks for frequencies below 2 GHz. After tapering, the real part of the longitudinal Z_L/n impedance remains above 5 $m\Omega$ at about 2.46 GHz, when the detectors are 3 mm from the beam. In all the rest of the frequency band of interest, both the real and imaginary parts of the longitudinal impedance are below 5 $m\Omega$.

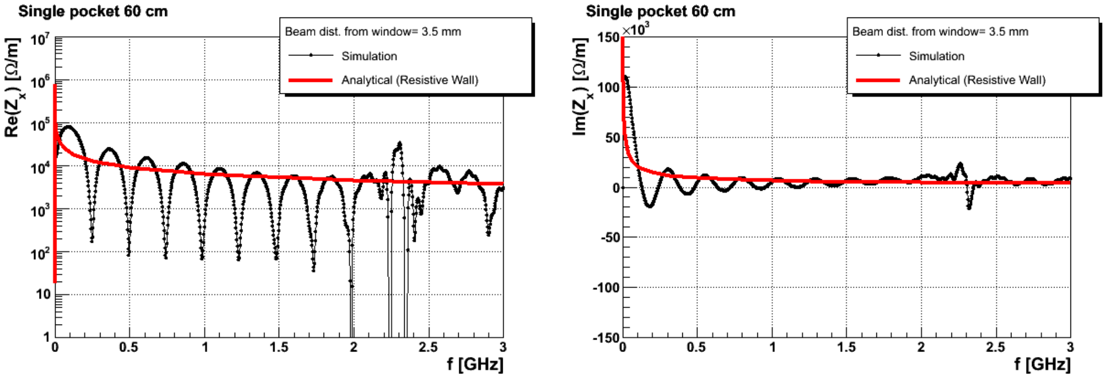

(a) Real part of Z_x (comparison with theory)

(b) Imaginary part of Z_x (comparison with theory).

Fig. 63: Single pocket transverse impedance vs. resistive wall theory.

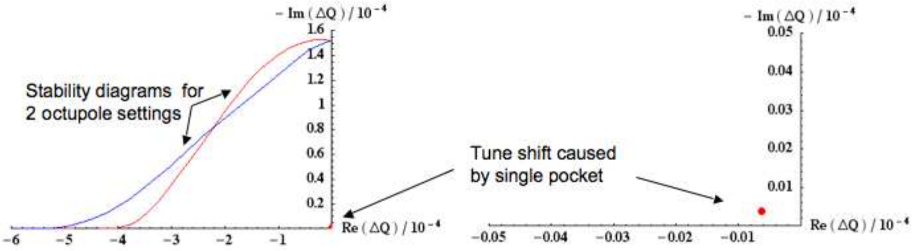

Fig. 64: Tune shift induced by FP420 single pocket at 3 mm, due to resistive wall transverse impedance (calculations based on B. Zotter and E. Metral's models). The effect is negligible when compared to the stability diagram that assesses how the LHC octupoles tuning can damp the instability.

8.3 Transverse impedance and beam instability

The transverse impedance can be inferred by the variation of the longitudinal impedance for different wire (beam) transverse positions. Figure 63 compares the simulated transverse impedance with an analytical prediction accounting for resistive wall effects only. The results are in good agreement since the oscillation at low frequencies given by the numerical simulations is attributed to the presence of the wire. The resonances between 2 and 3 GHz account for the geometric impact of the FP420 station on the beam pipe cross section not considered by the analytical formulas. Therefore, for frequencies below 2 GHz, the transverse impedance introduced by the FP420 insertion is dominated by the resistive wall effect. The impedance values calculated analytically can be used to predict the impact on the beam horizontal tune shift. The effect is very small, it results in $|\Delta Q_x| < 1 \cdot 10^{-6}$, well within the stability region defined by the available Landau damping octupoles at LHC [142], as shown in Fig. 64.

8.4 Coupling with detectors

The simulation of detector signal disturbances due to electromagnetic coupling between the beam and the surroundings is very difficult, due to the small amount of power that could be picked-up at the detector electronics level. A laboratory measurement using high power spike generators and a normalization to the real beam current is under consideration.

8.5 RF summary

The FP420 single pocket geometry has been characterised in terms of coupling impedance. Numerical simulations, analytical calculations and laboratory measurements showed consistent results, all indicating that this design will have a small impact on the total LHC impedance budget.

Tapering of the beam pipe indentations is recommended because it does reduce the impedance significantly, as measured both with the single pocket and double pocket designs. Since an effective tapering can be done outside the beam orbit region, this design modification can be implemented at no cost in terms of the forward proton signal to background ratio. With a double pocket station design, the beam pipe section between the two pockets can also be electrically connected outside the beam orbit region, in order to provide a good RF contact and minimise the effect of beam pipe cross section variation. This could not be tested in the laboratory, due to the difficulty of accessing the region after beam pipe fabrication. Simulations and laboratory measurements of a new prototype, modified according to the RF studies completed so far, will be continued.

The resultant effective longitudinal impedance follows from the convolution of the results presented here with the LHC beam spectrum. The beam harmonics at 2 GHz are expected to be below 10^{-2} of the main harmonic at 40 MHz and well below 10^{-3} at 2.5 GHz. This provides a further indication of the expected minimal impact of a FP420 station on the LHC impedance. One of the consequences is that, according to the available analytical models, the horizontal tune shift induced by a FP420 station is expected to be almost imperceptible when compared to the tune stability region defined by the available LHC octupoles magnets.

In addition, the worst case considered in these studies, refers to the positioning of a FP420 station at 3 mm from the circulating beam, whereas recent acceptance (Sec. 4) and background (Sec. 5) calculations indicate that 5 mm is a more likely distance of closest approach. This implies that the results are conservative in terms of disturbances to the beam. Further studies are ongoing in order to determine the characteristic loss factor, which will provide an estimate of the power dissipated due to electromagnetic coupling.

9 Silicon Tracking Detectors

9.1 Introduction

In order to detect protons from the production of central systems of masses $\sim$ 100 GeV/c^2, the detector edge has to approach the beam axis to a minimum distance of 5 mm (see Figure 28). This represents a challenge for the radiation hardness and radio-frequency pick-up in the detector and the nearby front-end electronics, as described in Sections 5 and 8. The detector system has to be robust, and for satisfactory control of systematic uncertainties its position has to be aligned and maintained to a positional accuracy of 10 μm in order to achieve the required track angular precision of 1μrad (see Section 4.3).

With a typical LHC beam size at 420 m of $\sigma_{beam} \approx 300$ μm, the window surface of the Hamburg pipe can theoretically safely approach the beam to $15 \times \sigma_{beam} \approx 4.5$ mm. As discussed in Section 5 however, this distance will ultimately be determined by the LHC collimator settings, since for beam 2 in particular the halo can extend to $\sim$ 5 mm with the nominal collimator positions. The window itself adds another 0.2 mm to the minimum possible distance of the detectors from the beam. To maximise the acceptance for low momentum-loss protons, the detectors should therefore be active as close to their physical edge as possible. In general, planar silicon detectors have a wide (0.25 mm – 1 mm) insensitive border region around the sensitive area that is occupied by a sequence of guard rings. This ring structure controls the potential distribution between the detectors sensitive area and the cut edge to remove leakage current. Planar silicon detectors designed for a heavy radiation environment or generally for operation at high bias voltages, contain multi-ring structures with typically about $\sim$20 rings.

The key requirements for the FP420 tracking system are

- To track efficiently as close as possible to the sensor's physical edge.
- To have extreme radiation hardness. A design figure equivalent to or better than the vertex systems used for ATLAS or CMS will be required, i.e. better than 10^{15} 1-MeV equivalent neutrons per cm^2.
- To operate at the highest LHC luminosity and be robust and reliable.
- Individual detectors should have a spatial precision of $\sim$10 microns. The tracking system angular precision should be 1 μrad. These requirements are discussed in detail in Section 4.
- At 420 m the tracking detector needs to cover an area of 25 mm x 5 mm.

3D silicon technology has been chosen as the baseline detector technology best equipped to meet the above requirements, although the tracking system has been designed such that any silicon technology compatible with the ATLAS pixel readout can be used. The 3D silicon sensor R&D is described in Section 9.2. Section 9.3 discusses the mechanical design of the tracking detector, Sec. 9.4 discusses solutions for the required high voltage and low voltage, and Sec. 9.5 discusses the infrastructure and readout. The thermal performance of the system is described in Section 9.6. The performance of the proposed tracking system is described in Section 9.7.

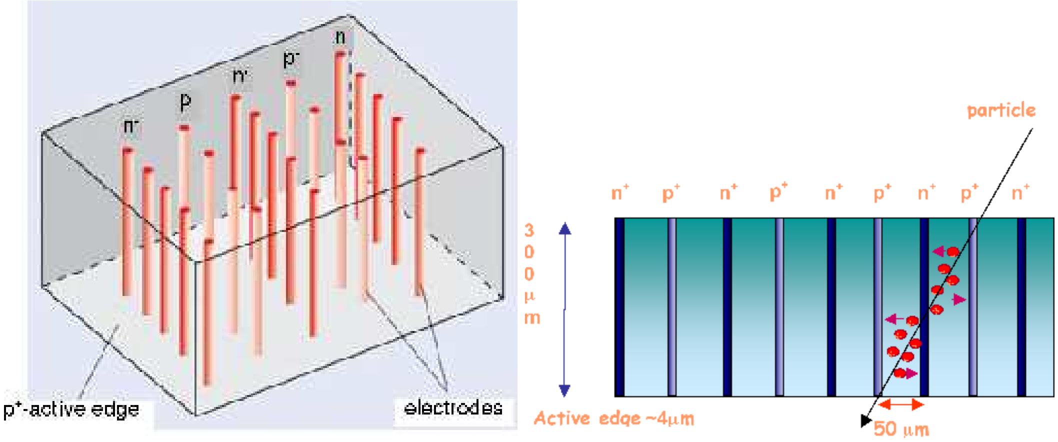

Fig. 65: Isometric and lateral view sketches of a 3D detector where the p+ and n+ electrodes are processed inside the silicon bulk. The edges are trench electrodes (active edges) and surround the sides of the 3D device making the active volume sensitive to within a few microns of the physical edge.

9.2 3D silicon detector development

3D detectors are a new generation of semiconductor devices [130, 143, 144, 145, 146, 147, 148, 149, 150, 151, 152, 153, 154, 155]. Using micro-machining techniques, electrodes penetrate the entire thickness of the detector perpendicular to the surface. This results in smaller collection distances, very fast signals, and substantially improved radiation tolerance. Figure 65 sketches the main features of this novel detector design. In addition, similar micro-machining techniques allow one to produce "active edges" where the amount of dead silicon at the edge of the detector is greatly reduced.

Full-3D silicon sensors have been successfully fabricated at CIS-STANFORD by J. Hasi (Manchester University) and C. Kenney (Molecular Biology Consortium) since 2001, following the original design of Sherwood Parker, University of Hawaii and C. Kenney who developed active edges. The Manchester/MBC/Hawaii Collaboration has been working since 1999 to develop this technology for applications in particle physics. Important results are summarised below.

The first 3D detector used 16 rows of 38 p+ electrodes spaced by 100 μm. n+ electrodes were placed 100 mm from the p+ electrodes. The total active area was 3.2 mm by 3.9 mm. The p+ electrodes were connected as strips to ATLAS SCTA readout chips. After tests in the X5 beam at the CERN SPS in 2003, the efficiency was found to be around 98% and particles were detected to within 5 μm of the physical edge, as can be seen in Figure 66. The full results of this beam test can be found in the TOTEM TDR [130] and Ref. [155]. A hybrid technology (planar/3D) detector was manufactured at Stanford and was successfully tested by TOTEM in a prototype Roman Pot at the CERN SPS in 2004. This uses planar technology but has a 3D active edge. This worked well, but is a factor 100 less tolerant to irradiation than full 3D technology.

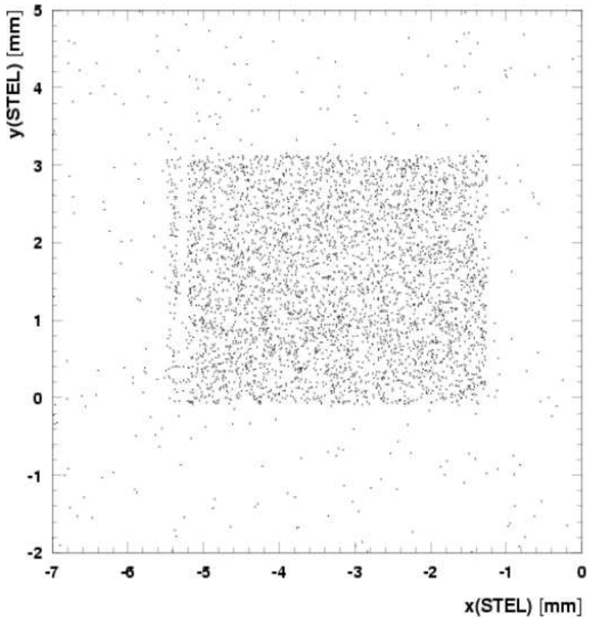

Fig. 66: Two-dimensional efficiency map of a fully operational 3D detector. A point is plotted with respect to the position (x, y) predicted by a telescope, with a precision of 4 μm as a valid track and a hit was recorded by a 3D detector. The inefficient band near the lower x-edge was caused by the detector's bonding pads. The upper and lower y edges were used for active edge measurements and showed a device sensitivity up to 4 microns of the physical edge.

Initial tests on irradiated 3D samples were made in 2001 [147]. The first results on the signal efficiency were obtained in 2006 using signal generated by an infrared laser. The 3D devices were irradiated with neutrons in Prague with an equivalent fluence of 10^{16} protons/cm^2 [154]. As expected, 3D devices can operate at much higher fluences than conventional silicon devices. For a minimum ionising particle, the signal size depends on the thickness. However, the signal collection distance is determined by the inter-electrode spacing, which can be as short as 50 microns. The measurement is shown in Figure 67 for a 3E device with an inter-electrode distance of 71 microns. This has three n-type collection electrodes in a pixel size of 50 micron by 400 microns. Figure 68 shows the signal efficiency versus fluence for the 3D detector. It is compared to the best that has been achieved using strip and pixel detectors for the LHC experiments. 3D technology is about a factor five more radiation tolerant.

For the FP420 application the ATLAS Pixel Readout chip was chosen. The total active area is 7.2 mm by 8 mm. The pixel structure is shown in Fig. 69. The 3D detectors were bump-bonded to the readout chip. To cover the full area, a minimum of three detectors are required. The details of the mechanical/electronic layout required to make a single layer with full area coverage is described in Section 9.2. Figure 70 shows that the 4E device can operate at the lowest voltage.

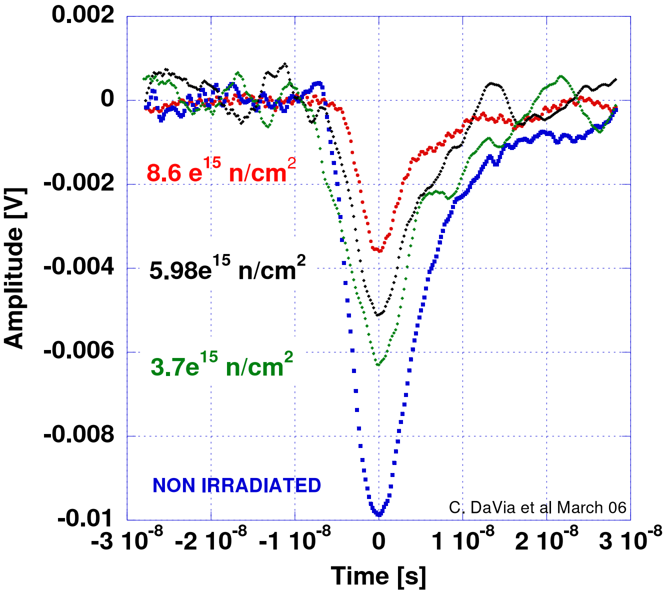

Fig. 67: Response of a 3 electrodes/pixel (3E) 3D device to a 1060 nm laser pulse after 3.7×10^{15}, 5.98×10^{15} and 8.6×10^{15} neutrons/cm^2.

Charge sharing only occurs very close to the pixel edge. Operating voltages are a factor ten less than for a standard planar device. Figure 71 shows a processed 3D wafer. The device yield was around 80%.

2E, 3E and 4E devices, bump-bonded to ATLAS Pixel readout chip were tested in the H8 beam at CERN in Autumn 2006 with support from LBL and Bonn. Individual detectors were placed between planes of a silicon microstrip tracking system. The beam was 100 GeV/c pions. Figure 72 shows a hit map for a 12 mm × 12 mm and 3 mm × 3 mm scintillator trigger. There were no dead or hot pixels.

Figure 73 shows the pulse height spectrum for a 3E detector for minimum ionising particles incident at zero (top) and fifteen degrees. The low pulse height at an ADC count of 10 is due to particles traversing the electrode. The tracking efficiency has been measured to be 95.9% and 99.9% respectively using a reference telescope. In the proposed FP420 tracking system, several planes will be used to form a track-segment. Half of the plans will be shifted by 25μm to improve the spatial resolution in one dimension. This guarantees that the efficiency will not suffer from electrode inefficiency. Figure 74 shows tracking residuals. This is consistent with the pixel dimen-

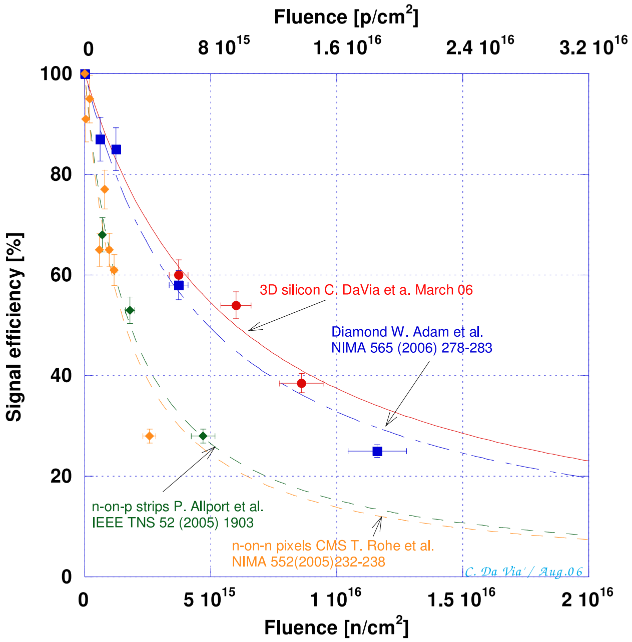

Fig. 68: Signal efficiency of 3D detector versus fluence of 1 MeV equivalent neutrons/cm^2. Data for n on p silicon strips and n-side readout pixel detectors are shown for comparison. Diamond detector results are also shown. Note that diamond gives a factor three less signal for a minimum ionising particle.

sions. The pulse height spectrum indicates that the efficiency is very high and is consistent with previous results. Millions of tracks have been recorded for incident angles between 0^o and 90^o for 2E, 3E and 4E devices.

An extended collaboration (3DC) has been formed between Manchester, Hawaii, Oslo, SINTEF and the Technical University of Prague, to transfer this technology to industry and guarantee large scale production. Variations on the full 3D detector design are also being studied by IRST and CNM. Further developments ar discussed in [156].

In order to understand the signal-to-noise performance for the various geometry detectors, the noise performance of the 2E, 3E and 4E 3D sensors was measured after bump bonding with the FE-I3 ATLAS pixel readout chip (Fig. 75). The equivalent noise charge (ENC) of the entire pixel matrix was measured, for each configuration, by injecting a variable amount of charge into each pixel front end and looking at the threshold dispersion over the entire matrix. This operation is possible since each front end electronics chip is equipped with a test input capacitance. Figure 76 shows a snapshot of the online display of the ATLAS pixel TurboDaq test system. The top of

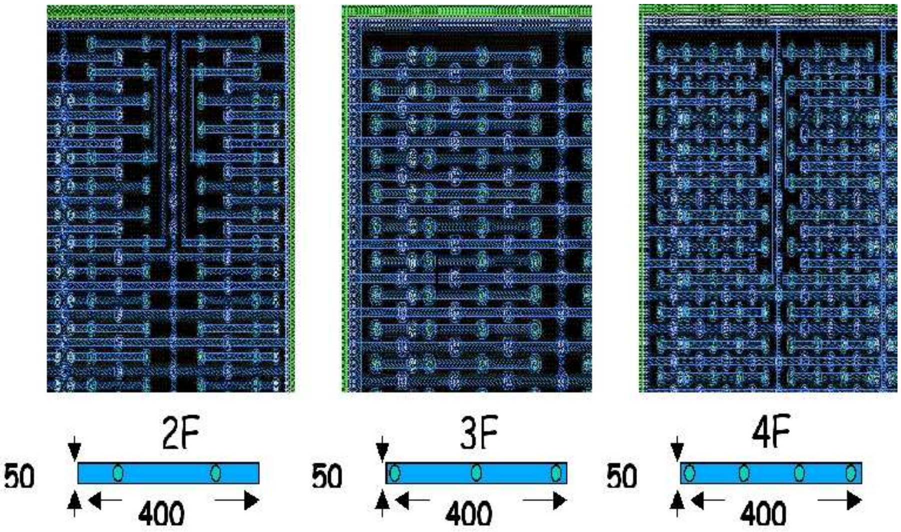

Fig. 69: Different 3D cell structures designed to be compatible with the ATLAS Pixel detector readout chip. The pixel size is 50 μm by 400 μm. The devices have either 2, 3 or 4 electrodes per pixel and are named 2E, 3E and 4E respectively. The electrodes cover 4%, 6% and 8% of the total area for 2E, 3E and 4E devices respectively.

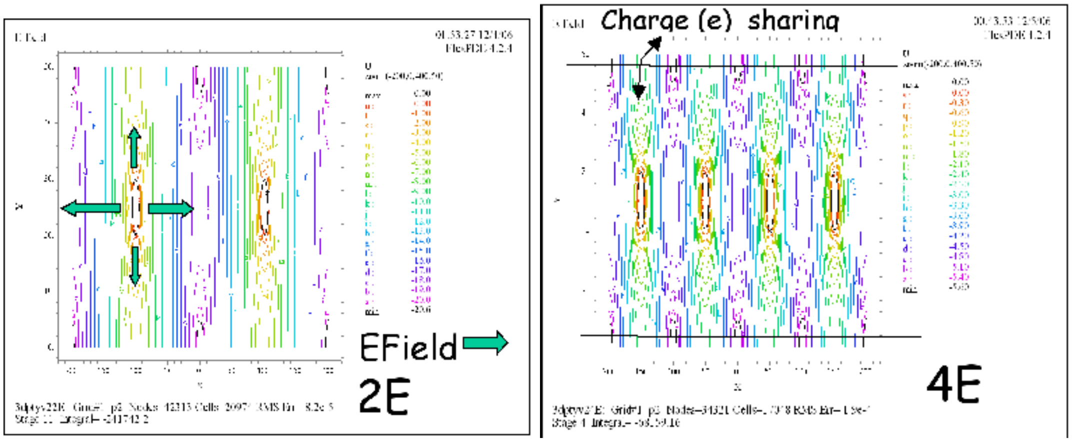

Fig. 70: Equipotentials in a 2E and 4E 3D detector. Pixel size is 50 μm (Y) by 400 μm (X). The bias is 20 V and 5 V for the 2E and 4E devices respectively. The direction of the electric field is indicated. The n-electrodes are at the centre. A maximum field of 1 V/μm occurs at 24 V and 14 V in a 2E and 4E device respectively.

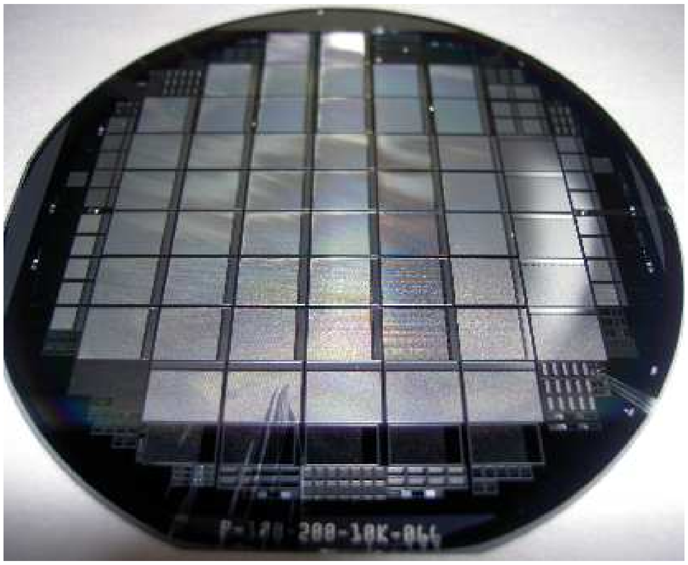

Fig. 71: Four-inch wafer processed for the FP420 project. This has 32 3E, 6 4E and 6 2E ATLAS pixel readout compatible devices and several test structures. The 250 micron substrate is 12 kΩ cm p-type.

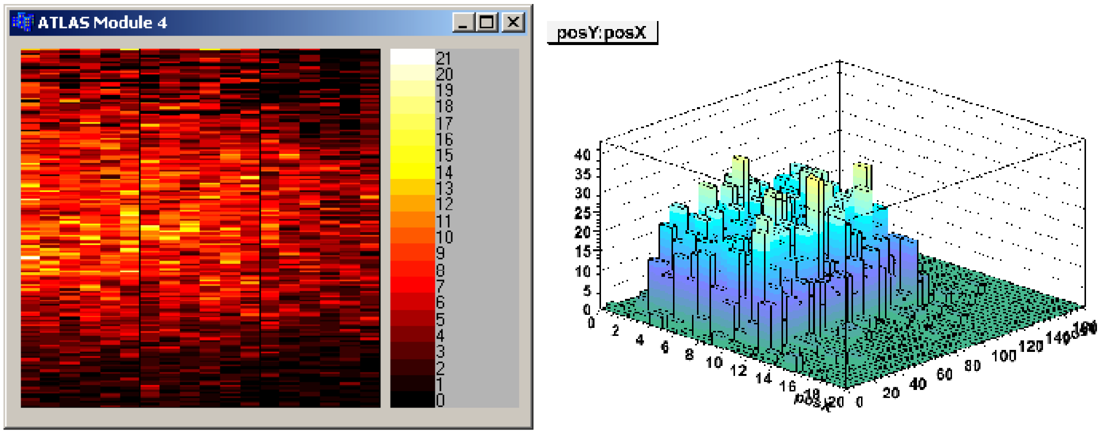

Fig. 72: Hit-map for a 12 × 12 mm^2 (left) and legoplot for a 3 × 3 mm^2 (right) scintillator trigger. Device 3D-2E-A operated at 30 V.

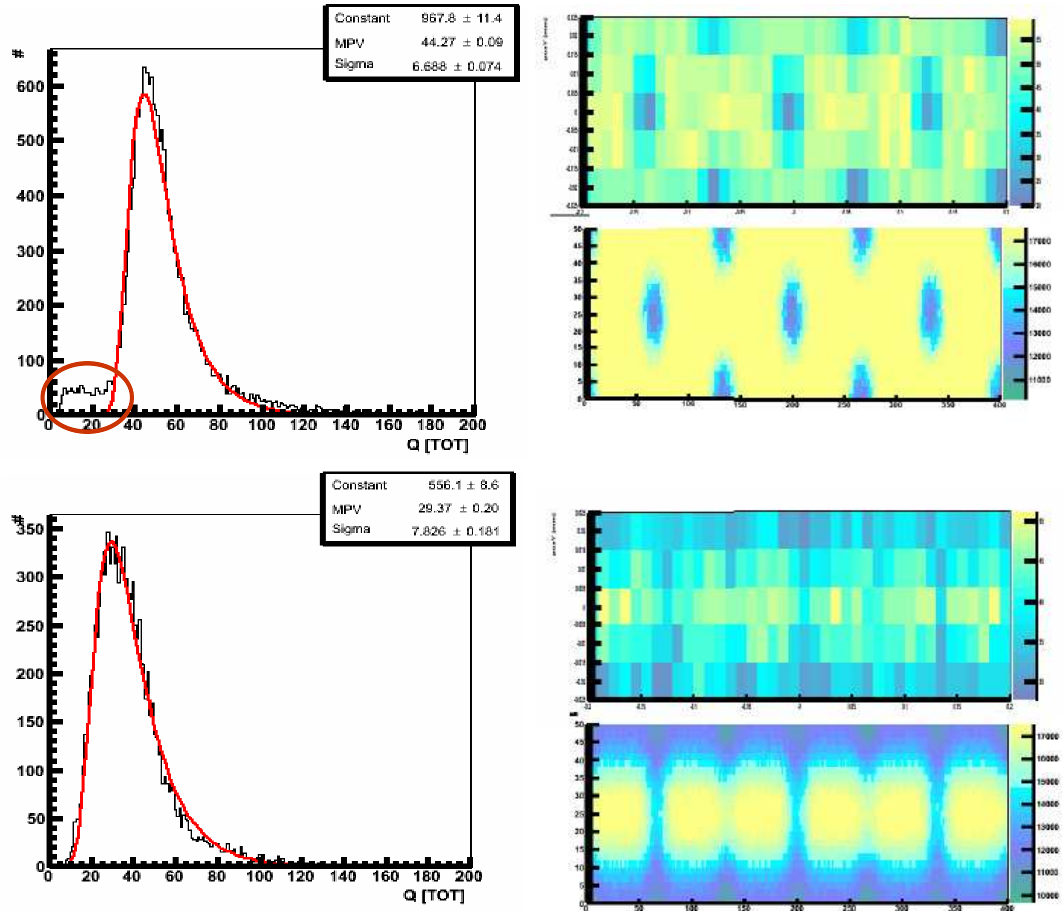

Fig. 73: Left: Pulse height spectrum for 100 GeV/c pions incident perpendicularly (top) and at a 15^o angle on a 3E-3D detector biased at 20 V. One Q[TOT] ADC count is 600 electrons. The threshold was 3200 electrons. The tracking efficiencies are 95.9% and 99.9% respectively. This takes into account the partial response of the central part of the electrodes. Right: Simulations (bottom) are in good agreement with the experimental results (top) [M. Mathes, Bonn].

the figure shows the response of the entire pixel matrix while the bottom shows the threshold distribution before and after tuning. The noise versus bias voltage for all the 3D pixel configurations can be seen in Figure 77.

The extrapolated signal-to-noise of the three configurations after irradiation is shown in Figure 78. The plot shows the S/N after a fluence of 3.5×10^{15} n cm^{-2} and 8.8×10^{15} n cm^{-2} respectively. The first set of values corresponds to the integrated fluence expected at 4 cm from the ATLAS interaction point (i.e. the ATLAS central tracker) after ∼10 years of operation of the LHC at nominal luminosity. The second set corresponds to the values expected after ∼5 years of opera-

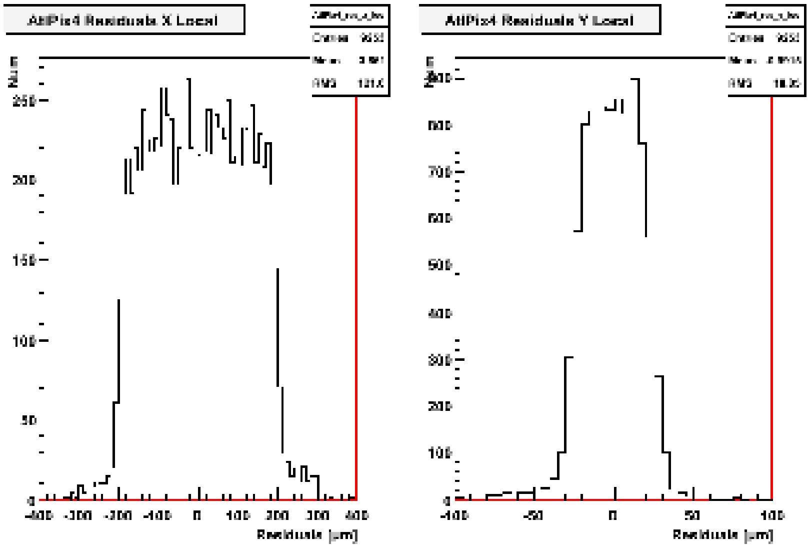

Fig. 74: Tracking residuals for 3D pixel detector [M. Mathes,Bonn].

Fig. 75: Picture of the 3D-ATLAS pixel assemblies mounted on one of a pcb testboard with a protective cover.

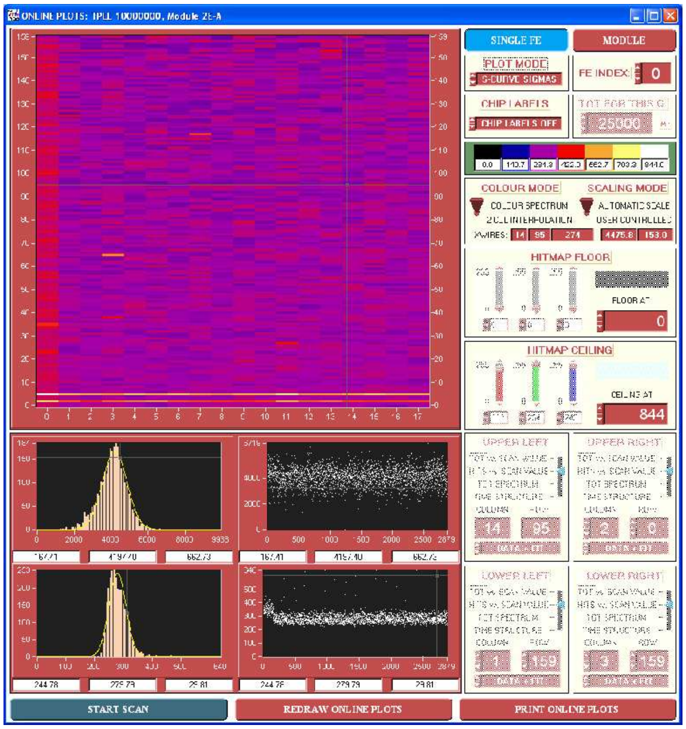

Fig. 76: Snapshot of the online display of the TurboDaq ATLAS pixel test setup. On the top the entire pixel matrix response to a test pulse. At the bottom the ENC (Equivalent Noise Charge) is measured as the sigma of the threshold distribution.

tion at the same distance at the SLHC. These S/N results indicate that the lower fluences expected at the FP420 location should not compromise the performance of the 3D pixel tracking detectors.

In conclusion, 3D detectors readout out using the ATLAS Pixel Chip fulfill all the requirements for use in the FP420 experiment

9.3 Tracking detector mechanical support system

The space available for the detectors is extremely limited. The baseline design is to have two independently moving pockets, one at each end of the 420 m region. The pockets may be subdivided to allow different cooling and vacuum conditions for the silicon and timing detectors. The optimal configuration may change depending on the pile-up conditions and the machine-induced background environment at the time of operation. A key design goal has therefore been to allow changes in the detector configuration to provide the optimal balance of detection points versus traversed material, and to allow simple replacement of failing detectors during permitted tunnel access. To achieve an active area of 5 mm $\times$ 25 mm requires a minimum of three silicon sensors. The basic detector unit, referred to as a superlayer, tiles the sensors to cover the required area.

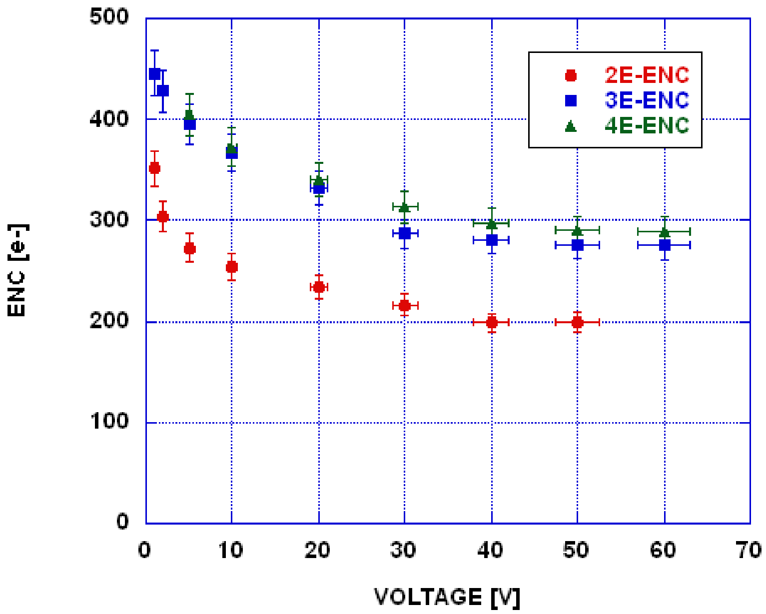

Fig. 77: The equivalent noise charge (ENC) of the 2E, 3E and 4E 3D detectors after bump-bonding with the FE-I3 ATLAS pixel readout chip.

A superlayer is made of two "blades". Figure 80 shows a schematic of the superlayer layout to illustrate the basic geometry and nomenclature. A single tracking station will consist of a number of superlayers. Schematic drawings of a superlayer and a modular tracking station consisting of five superlayers are shown in Figs. 81 and 82 respectively.

Since the 3D silicon sensors have rectangular pixels of 50 microns by 400 microns, they have better position resolution along one axis. This means that superlayers can be designed to position the sensors to give superior resolution in the horizontal (x) or vertical (y) plane. In the initial phase of FP420 operations, the horizontal (x) deflection of the protons from the beam is of prime importance, since this corresponds to a measurement of the energy loss and hence the missing mass. The vertical (y) position becomes important primarily when the p_T of the outgoing protons is required. Whilst there is a strong physics case for measuring the p_T of the outgoing protons the initial priority of FP420 is the missing mass measurement. Phase 1 will therefore be optimised for a high-precision x measurement, with y measurements considered as a potential future upgrade. Because of the modular design of the tracking stations, superlayers optimised for enhanced p_T resolution can easily be inserted in a short tunnel access.

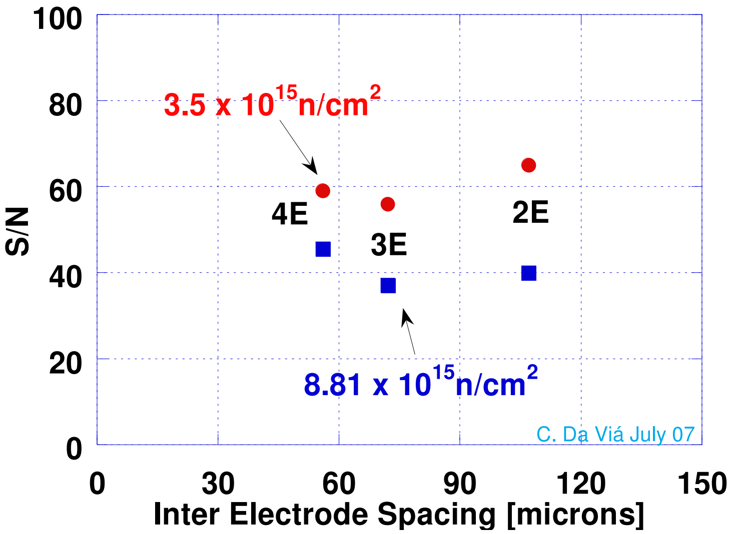

Fig. 78: Extrapolated Signal to Noise (S/N) ratios of three 3D pixel configurations at two different irradiation fluences.

9.3.1 Superlayer and blade design

A superlayer consists of two blades, each carrying two sensors. The two sensors closest to the beam overlap but are offset with respect to each other by half a pixel (25 micron) to improve track resolution for low ξ particles – see Section 9.2. A superlayer control card is positioned between the blades and connected by four flex circuits. Although the 3D silicon sensor technology is edgeless, tabs required for readout connections to the front-end ASIC, bias connections to the sensor and edge effects imply that it is impossible to tile the detectors in certain orientations. Even in the specific orientation unaffected by these tabs there are residual edge effects introduced by the front-end chip design. These constraints require detectors to be positioned over a number of overlapping layers to provide the required coverage. This is achieved by using both sides of the blade.

The choice of material for the blades is critical if the design goal of an internal mechanical alignment of 10 microns is to be achieved. The material must be stiff but machinable, have a high thermal conductivity and low coefficient of thermal expansion, similar to that of the attached silicon dies. The thermal conductivity must be optimised relative to the density to allow for extraction of heat from the detectors without too high a thermal gradient, whilst minimising the amount of material (radiation length) and hence multiple scattering.

Beryllium oxide and Beryllium metal although possessing good thermal and low mass parameters were rejected at this stage because of difficulties due to their toxicity, which makes pro-

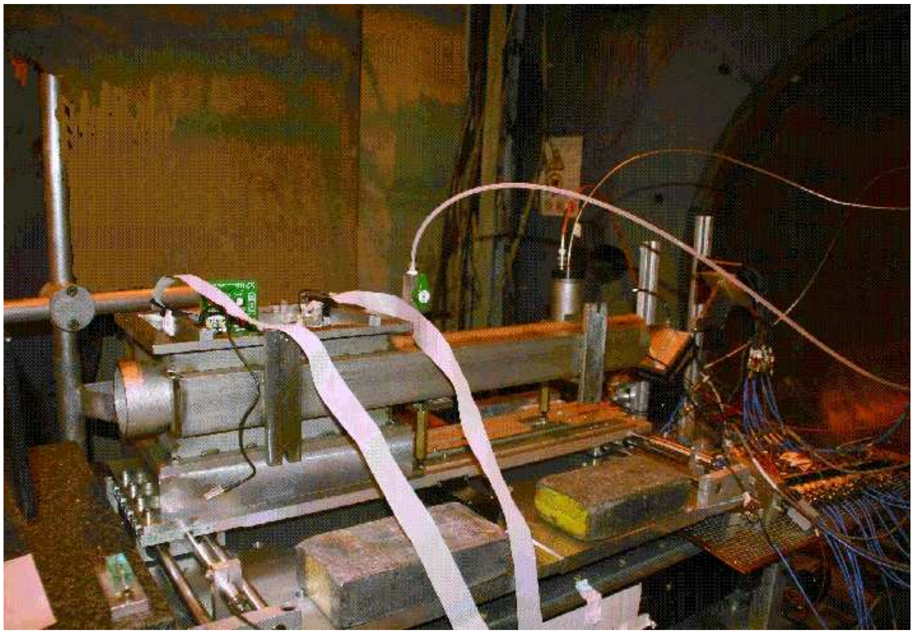

Fig. 79: FP420 2007 test beam setup including one movable station, two blades, and two timing detectors (one GASTOF and two QUARTICS).

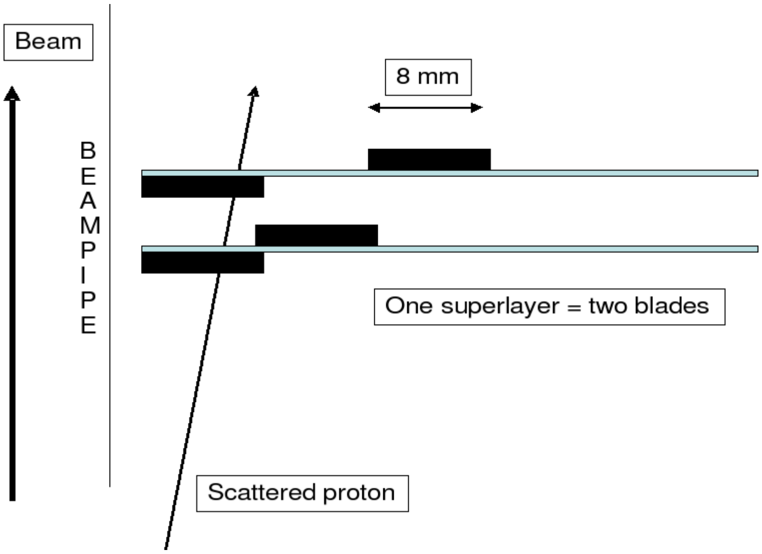

Fig. 80: Schematic of a superlayer consisting of four sensors.

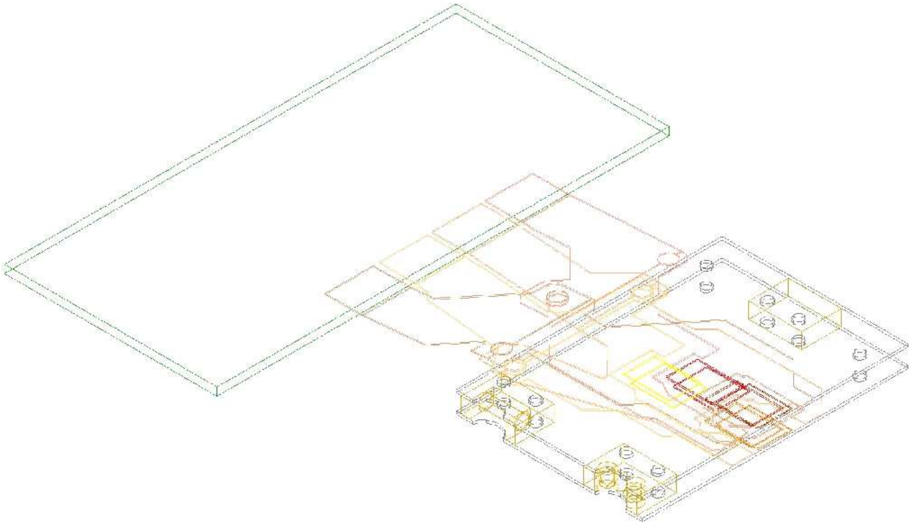

Fig. 81: A schematic drawing of a superlayer, consisting of two blades. The flexible circuits connect the four sensors to a common control card.

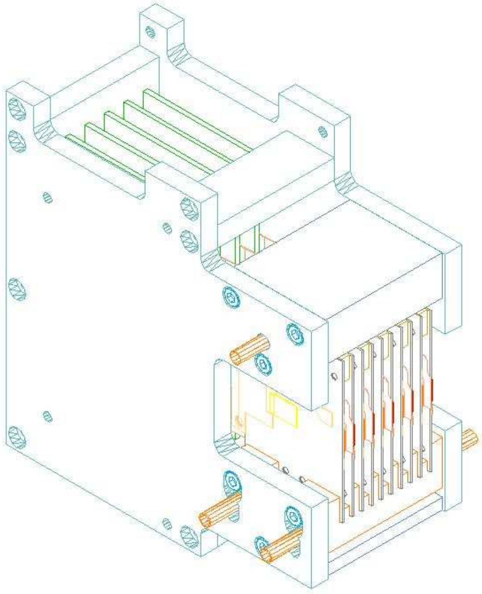

Fig. 82: A five superlayer tracking station. The mechanics supports the superlayers and also provides cooling blocks.

Material	Thermal conductivity K ($Wm^{-1}K^{-1}$)	Relative Density ρ	K/ρ	CTE (10^{-6} K^{-1})
CE7 (70/30 Si/Al)	125	2.4	52	7.4
Aluminum Nitride	180	3.26	55	5.2
Silicon	156-200	2.33	67-86	2.6

Table 12: Possible blade materials.

totyping difficult, time consuming and expensive.

Several blade design variants have been prototyped. We were initially attracted to the possibilities of CE7, a hypereutectic alloy of 70/30 silicon and aluminum because its aluminum component makes it machinable with conventional tooling, making it possible to construct a blade as one single component. Its K/ρ value of 52 compares well with more conventional materials such as aluminum nitride. The prototype blades used in the Sept 07 CERN test beam runs were of this design with the centre sector machined down to 500 microns. However material scattering considerations are pushing the design to be even thinner – 300 microns. It has proved difficult to machine CE7 to this tolerance due to its granular structure. Hence we have investigated an alternate design using a CE7 frame and a decoupled planar thin front section supporting the detector. This allows the use of hard materials such as silicon or Al N whose thicknesses can be lapped down to 300 micron with high surface finish. The superplane shown in Figure 81 has such a design. In a planar geometry the requisite shapes can be laser cut.

9.3.2 Thermal tests of the blades

Test blades have been built to investigate heat flow and thermal gradients and the resulting mechanical displacements using a thermal camera and a "smartscope" to measure the displacement. A realistic chip/glue/support interface structure was constructed using custom silicon resistors that match the size and power of the front end chip and have a similar bond pad layout. The model used for thermal testing is shown in Fig. 83. Also shown is the finite element analysis of the blades performed at Mullard Space Science Laboratory. The preliminary thermal tests indicate that the blade design meets the required criteria of thermal and mechanical stability at the 10 micron level.

9.3.3 Assembly and alignment

The silicon sensors will be positioned on the blades using an adaptation of the automated assembly stages and jigs used to construct silicon modules for the ATLAS SCT at Manchester. The system uses automatic pattern recognition of fiducials on the readout chip to provide coordinates to x, y, θ motion stages which position the detector on precision jigs. Components are glued using a Sony CastPro dispensing robot under software control. The system allows silicon sensors to be reliably positioned on opposite sides of a blade with an absolute position accuracy of 5 microns. Detector blades are independently surveyed using a Smartscope optical coordinate measuring machine

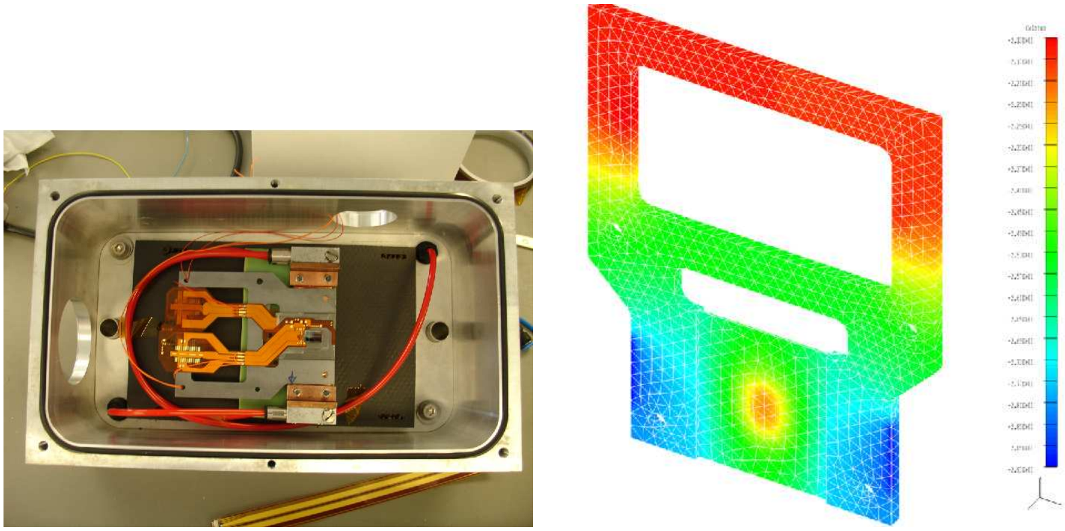

Fig. 83: Left: A thermal model blade with the silicon resistors as described in the text. Right: Finite element analysis of the thermal properties of a blade.

capable of one micron precision. Figs. 84 and 85 show the build sequence for a blade and then a superplane. Once the superplanes have been manufactured, the station needs to be assembled.

Linking individual blades together, in pairs as superlayers, and then into an entire station has some complexities. Several approaches have been prototyped. The simplest idea is to use linking dowel rods and precision wire cut washers stuck to each blade following the ATLAS SCT experience. These can be manufactured to 5 micron tolerance. However, the alignment of a stack of 10 is limited by sliding tolerances and difficulties in maintaining dowel angular tolerances. This led us to touch bearing designs. A touch bearing consists of a bar perpendicular to the dowel rod, pushed against it by a spring force such that there is a unique point contact between the two. These are arranged in a kinematic manner, providing a V and a flat. The kinematic single point contacts provide high reproducibility, whilst the spring force allows easy movement to position along the dowel. The challenge is to make such a bearing design small enough for this application. One of the restrictions imposed by through dowels is that it is difficult to remove an individual superplane without dismantling the entire system. This leads us to our current baseline design: open-sided touch bearings, one V, one flat are sandwiched between two blades as part of the superplane assembly process. These are located against two external dowel rods, held by a small ball spring. Figure 86 shows several superplanes and their bearings without the support structure and also the miniature touch bearings.

Figure 87 shows results of repeatedly repositioning a superplane – reproducibility at the 5 microns level or better is clearly demonstrated using the touch bearings. Measurements were taken

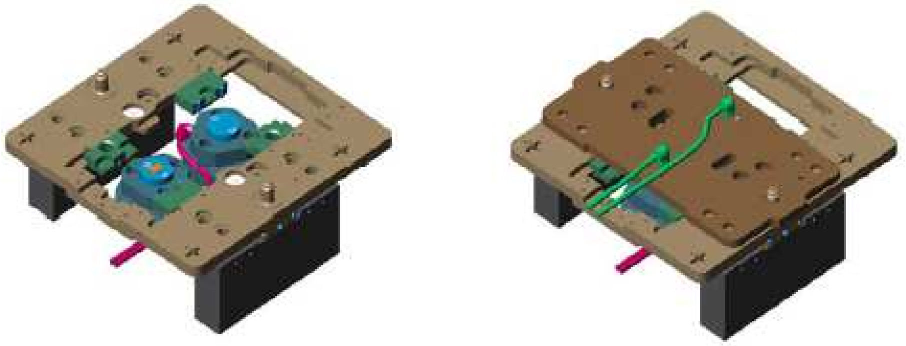

1. Transfer chuck aligned turnplate 2. Transfer chuck aligned turnplate

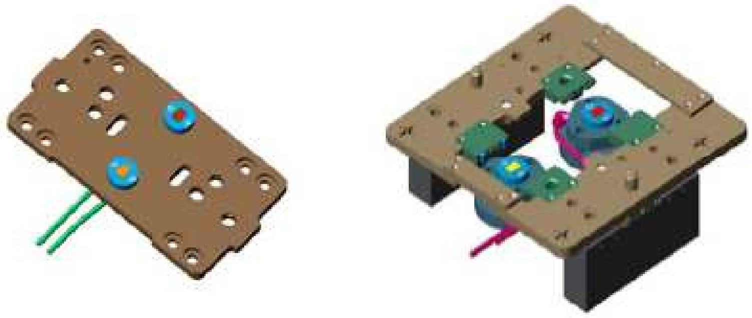

3. Chips transferred and held by vacuum 4. Invert turnplate. Repeat for chips 3&4

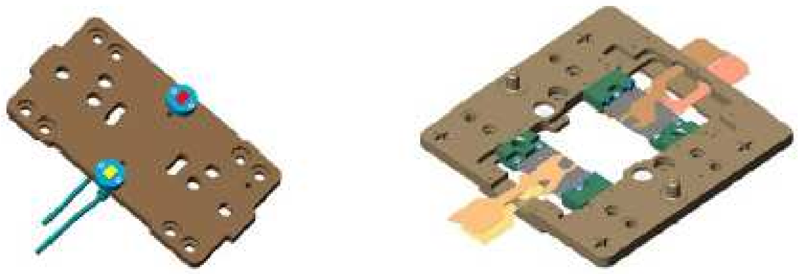

5. Chips 3&4 on second transfer chuck 6. Blade A (with Bearings) & Blade B (without inserted) in turnplate

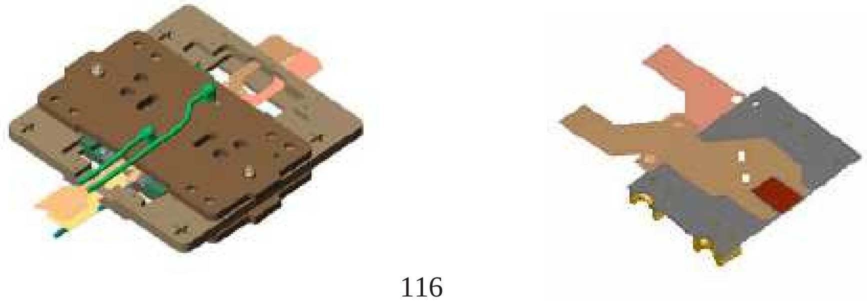

7. Transfer chucks replaced on turnplate 7. Blade A with chips on both sides

Fig. 84: Blade assembly – Positioning of chips 1 to 4 on Blades A and B.

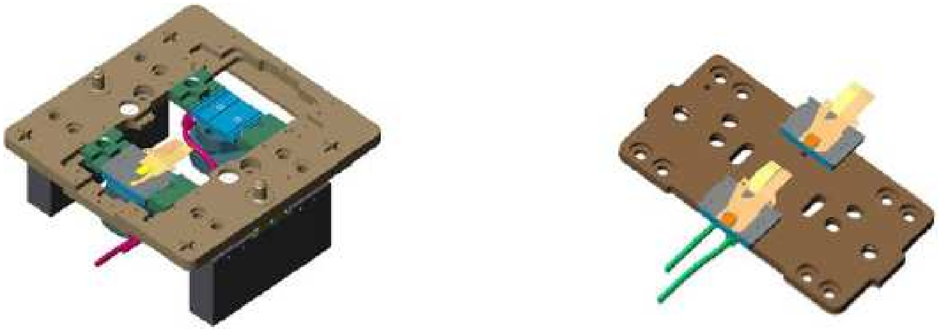

1. Two Blade B's aligned by stages

2. Blades transferred to transfer chuck.

3. Two Blade B's inserted in turnplate aligned by small touch bearings

4. Glue dispensed and Transfer chuck reunited.

5. Blades A&B assembled to form a superplane

6. Flex connections bonded to the MCC PCB

Fig. 85: Superplane assembly.

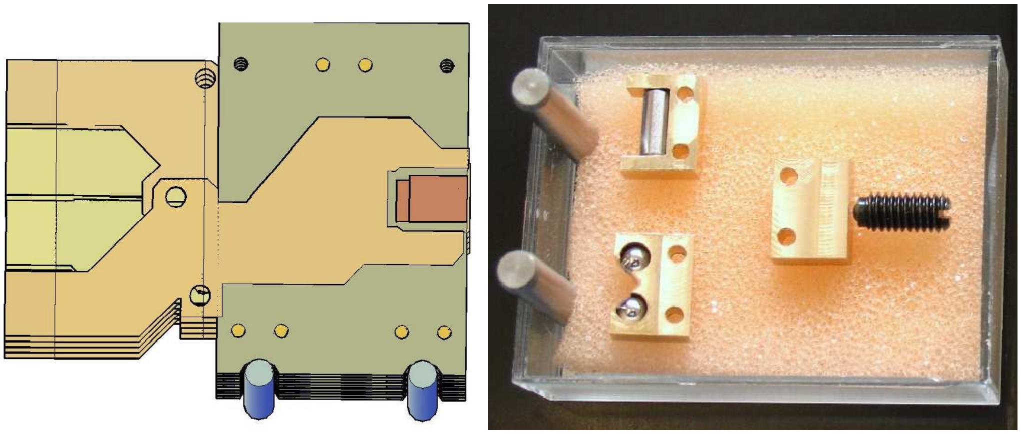

Fig. 86: Left: Several superplanes showing the bearings without the support structure. Right: Miniature touch bearing. The ball bearings are 3mm diameter.

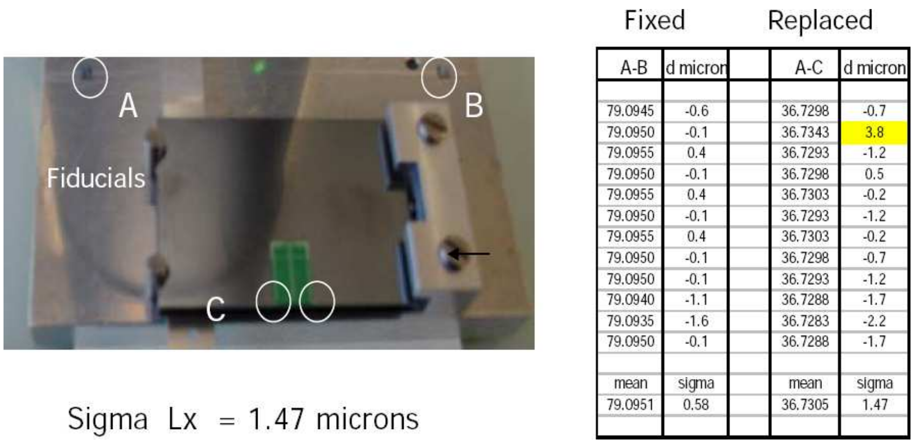

Fixed			Replaced	
A-B	d micron		A-C	d micron
79.0945	-0.6		36.7298	-0.7
79.0950	-0.1		36.7343	3.8
79.0955	0.4		36.7293	-1.2
79.0950	-0.1		36.7298	0.5
79.0955	0.4		36.7303	-0.2
79.0950	-0.1		36.7293	-1.2
79.0955	0.4		36.7303	-0.2
79.0950	-0.1		36.7298	-0.7
79.0950	-0.1		36.7293	-1.2
79.0940	-1.1		36.7288	-1.7
79.0935	-1.6		36.7283	-2.2
79.0950	-0.1		36.7288	-1.7
mean	sigma		mean	sigma
79.0951	0.58		36.7305	1.47

Fig. 87: Superplane positioning accuracy measurement.

using a Smartscope optical coordinate measuring machine of fiducials on a superplane front end compared with fixed fiducials on a base. The superplane was repeatedly removed and repositioned against the end bars.

To summarise: sensor to sensor positioning on a blade element can be achieved with an accuracy of 5 microns, and within a superplane to 10 microns.

The position of any sensor in the station once built can be surveyed by the Smartscope with a single measurement accuracy of 1 micron (several measurements may be required to link all sensors).

9.3.4 Electrical details of the superplane

A flex circuit situated behind and bonded to the sensor is used to connect the FEC chips to the power supply and data lines via wire bonds. The flex circuit is fitted with a control chip (the MCC) which services the FEC chips, distributing clock, control and trigger information and collecting data for onward transmission. Aside from some slow single-ended signals, the connection between the FEC and MCC chips are implemented using LVDS-style differential signaling, with lower current than LVDS terminated into 600Ω. The two-layer flex circuit is built on a 50 micron polyimide core with a nominal track/spacing of 100 microns falling to 60 microns in the bond region, 100 micron laser drilled vias, and a Ni/Au finish suitable for Al wire bonding. The flex is pre-assembled (passive decoupling components soldered) then glued to the blade. Positioning is visual with respect to the chip and performed with a manual placement workstation with a typical accuracy of around 20 microns. The positioning is not critical, the bonding process can cope with many tens of microns misplacement between flex and front end assembly. 25 micron Al wire with (99% Al, 1% Si) is used. Wedge-wedge bonding has been undertaken with a manual (semi-automatic) wire bonder during the prototyping phase; an automatic bonder will be used in production. We plan to investigate the benefits of plasma cleaning the flex, although our experience thus far has shown no difficulties bonding to the flex using a slightly elevated bonding power setting to overcome any surface contaminants. The individual blades need to be tested before final assembly as both the sensor assembly and their connections on the internal faces of the blades are not accessible after the blades have been combined into a superlayer, and it would not be practical to split and repair after assembly. The flex circuits have sacrificial tails that bring the signals to diagnostic headers. These connect to adapter boards allowing connection to the ATLAS Pixel TurboDAQ system which can be used for single chip testing. We foresee the option of potting the bonds after successful testing. Once both sides of the blade have been processed and all tests have been successfully completed the sacrificial tails are cut away. Two blades are combined with a control card and fixed together to form a superlayer. The flex circuits are glued to the control card with solder connections between the underside of the flex and the card for power, and data connections made by wire bond between pads on the topside of both. The bond pitch is much more generous and the alignment is not critical. The flex tension does not have any impact on the sensor positioning. The control card is a hybrid based on conventional PCB construction expected to have microvia breakout of the high density wire-bond connections to the MCC chip. Because of a shortage of MCC chips in this prototyping phase it will be necessary to mount the chip in a ceramic carrier which is placed into a socket on the board, but final production boards will be true hybrids. The power planes of this card provide the thermal path for the heat generated by the MCC chip. The connection from the superlayer has not been finalised. The prototypes use a SAMTEC QTE connector that straddles the board edge and mates to a custom made cable assembly.

Differential (LVDS like) data paths from each superlayer, together with power supply connections, span the detector box assembly to the support crate positioned either inside one of the support legs of the NCC or in an overhead gantry nearby. At the support crate, data links are merged and passed to the optoboard. Each superlayer has one inward link that provides

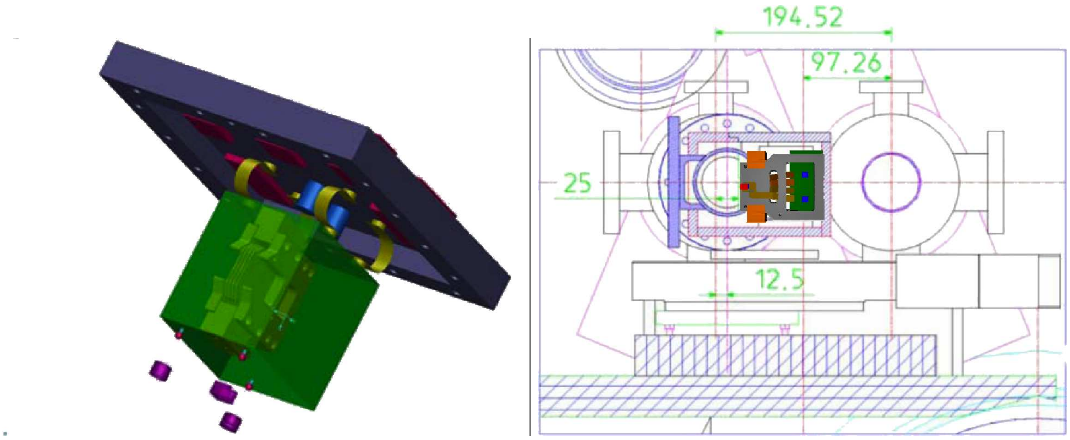

Fig. 88: Left: A complete tracking station attached to the lid. Also shown are the positioning studs. Right: Schematic view of the box in position around the beam pipe.

clock/trigger/control, and one outward link for data. The MCC support chips offer dual output links, but because of the low occupancy and small number of FE chips associated to each MCC (1/4 of density of the Pixel detector) only one link is required. We hope to be able to adopt the opto-components used at ATLAS, however the multimode fibre is susceptible to radiation which over these long distances may cause excessive attenuation, so it may be necessary to periodically replace the fibre. Alternatively, a rad-hard monomode based connection, as used at CMS, may need to be developed.

9.3.5 Station positioning

From an electrical point of view, a station is simply a collection of superlayers. It is worth noting however that the station is positioned inside a box that is welded to the beampipe and fitted with substantial lid, and so is a good Faraday cage. The blade carrier material is itself conductive; one point to be established therefore is whether this should be actively tied to the ground reference (the box/ beam pipe) or left to float. RF modeling studies together with practical testing on the RF test rig at the Cockcroft institute will help to determine the optimum strategy.

The tracking station will be loosely mounted from the lid of the vacuum vessel by flexible supports. Services , cables and cooling feedthroughs will be on the lid.

Precision alignment with respect to the beam pipe is achieved by location with kinematic ruby ball mounts on the base of the box. Figure 88 shows a station and lid, and relates these to the LHC beam pipes. Figure 89 defines key distances that will determine how closely the active silicon will be to the beam.

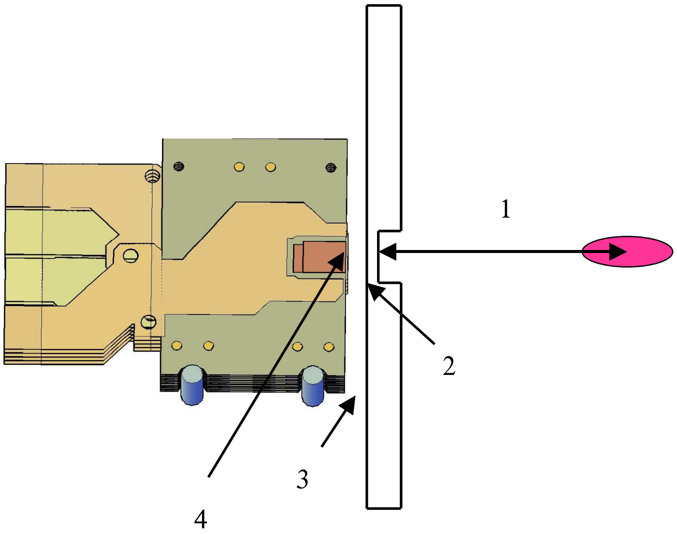

Fig. 89: Key dimensions from the beam to the edge of the first chip. 1 – beam to window, 2- window thickness, 3 - standoff of detector from window depends on thermal considerations and assembly tolerances , 4- distance of first pixel from from edge of blade defined by dicing considerations.

9.4 High-voltage and low-voltage power supplies

This section outlines some of the solutions envisaged for the bias and low-voltage supplies. Emphasis is on the supplies for the 3D sensors and their front-end chips. For more details, the reader is referred to Ref. [157].

9.4.1 Low-voltage power supplies specifications

Each superlayer requires two low-voltage supplies, preferably floating with minimum 1 V compliance range relative to each other, see Table 13. The low-voltage supply for a superlayer should be floating relative to that of any other superlayer. There will be decoupling capacitors close to the load.

One Pixel FE-I3 chip	Voltage range	Nominal voltage	Current	Current limit
Analog AVDD	1.6-2.0 V	1.6 V	5-70 mA	100 mA
Digital VDD	1.5-2.5 V	2.0 V	40-50 mA (1% occ.) 60-70 mA (10% occ.)	100 mA

Table 13: Low-voltage requirements for one ATLAS FE-I3 front-end chip. Currents are given for both 1% and 10% occupancy.

The required digital supply current depends on the detector occupancy. High occupancy results in higher current. The supply and its cables should take this into account. In Table 14 the requirements for one readout controller chip MCC are listed.

One MCC	Voltage	Current	Current limit
Digital VDD	1.8-2.5 V	120-150 mA	170 mA

Table 14: Supply requirement for one ATLAS MCC chip.

As each superlayer has 4 detectors and 4 FE-I3 chips plus one MCC chip sharing the digital supply with the front-end, we can sum up the total requirement per superlayer as shown in Table 15.

4 FE-I3 + 1 MCC Read-out driver	Voltage range	Nominal voltage	Current	Current limit
Analog (AVDD)	1.6-2.0 V	1.6 V	20-280 mA	310 mA
Digital (VDD)	1.8-2.5 V	2.0 V	280-350 mA (1% occ.) 360-430 mA (10% occ.)	480 mA
Monitor resolution	< 20 mV		< 10 mA	

Table 15: Overall specification for a low-voltage supply segment for one superlayer consisting of 4 PixelChips FE-I3 and one MCC chip. Remote monitor should enable observation of the voltage and current.

A few comments are in order. The voltages may need adjustments in the course of the lifetime of the system due to radiation effects. The low-voltage supply may need to have remote-sense feedback to compensate for the voltage drop. There must be a current limit which can be set either locally or remotely; it would be an advantage if its value can be set remotely as this will allow a more flexible system, capable of dealing with changes due to, for instance, radiation damage. The current limiting can be either of a saturating type or a fold-back with latching action. The latter requires some means of remote reset. Currents and voltages must be monitored and results provided remotely with the accuracy given in Table 15. A sample rate of the order of 1 Hz is sufficient. It is important that each superlayer low-voltage supply can be switched on/off individually (and remotely).

9.4.2 High-voltage power supplies specifications

A superlayer requires two high-voltage bias supplies, Vb1 and Vb2, with remotely controlled voltage in the range 0 to -120 V. Vb1 and Vb2 should be floating relative to each other within a superlayer with a compliance range on the zero terminal of at least 2 V. The high voltage bias supplies to a superlayer should be floating relative to any other superlayer with a similar compliance range. As the bias voltage for depleting the detector increases with radiation damage, it is an advantage to segment the supply into two: one for the detector pair closest to the beam (Vb1) and one for the pair away from the beam (Vb2). It is not necessary to separate the ground between Vb1 and Vb2 at the superlayer. The Vb zero line will be tied to the AVDD line. There will be passive RC low-pass filtering close to the load. Table 16 summarises the requirements.

4 detectors/2 voltages	Voltage	Current	Current limit
Vb1	0 to -120 GeV	<1 mA	1 mA
Vb2	0 to -120 GeV	<1 mA	1 mA
Monitor accuracy	<1 V	1 μA $\sim$ 12 bit res.	
Setting accuracy	<3 V $\sim$ 6 bit res.		

Table 16: Specifications for the high voltage bias supplies for one superlayer consisting of four detectors powered by two independent voltages. The voltage and current should be monitored remotely with at least the specified accuracy. The voltage should be controllable from remote with a resolution of better than 3 V.

There must be a current-limit at the indicated value. To increase flexibility, it would be an advantage if its value can be remotely adjusted. The limiting can be a simple saturating current-source type. Currents and voltages must be monitored and results provided remotely. Sample rate of the order of 1 Hz is sufficient. The high-voltage supply has to be remotely controllable. Remote-sense feedback on the wires to the load is not required as the current-induced voltage drop is negligible with respect to the required accuracy.

9.4.3 Power budget

Table 17 gives the power dissipated in the front-end for a worst case scenario where the occupancy is 10% and the voltages are at a maximum. For cooling design, the power from the radiation and the thermal flux from the ambient will have to be added to this list.

9.4.4 Low- and high-voltage channel count

Table 18 gives the number of channels assumed. The final count may differ from this.

9.4.5 Temperature monitoring

The temperature in the front-ends needs to be monitored. It will probably be necessary to have a probe on each superlayer. Temperature sensors of NTC type are known to be radiation tolerant and are used in other detectors at LHC. For instance LHCb (VELO repeater board, Low Voltage Card) uses NTC 103KT1608-1P from Semitec. The selection of the most appropriate device will require a later study. It is however sure that both excitation circuitry and an ADC to read the temperature values will be needed. It is an advantage if this excitation and measurement system can be integrated into the power supply crates.

One superlayer	Voltage (V)	Current (A)	Power (W)
AVDD	2.0	0.28	0.56
VDD	2.5	0.43	1.08
Vbias1	120	0.001	0.12
Vbias2	120	0.001	0.12
Total per Superlayer			1.88
		no of superlayers	
Total per pocket		5	9.38
		no of pockets	
Total per cryostat		3	28.13

Table 17: Power dissipated in the front-end electronics assuming 5 superlayers per pocket. Numbers are worst case values with 10% occupancy and maximum voltages and currents.

no. of channels	One superlayer	One pocket	One cryostat	FP420
	4 det.+ FE+1MCC	with 5 superlayers	with 3 pockets	with 4 cryostats
Low voltage	2	10	30	120
High voltage	2	10	30	120

Table 18: Number of low- and high-voltage supplies channels.

9.4.6 QUARTIC/GASTOF high- and low-voltage supplies

The QUARTIC/GASTOF modules have different requirements than the 3D detectors. The specifications per cryostat are for the moment rather loosely set as described in Table 19.

9.4.7 Discussion of the solutions considered

All solutions discussed in the following are based on commercially available modules. Three conceptually different approaches have been studied.

1. Power supplies located in the tunnel next to the FP420 cryostats and stowed underneath the adjacent magnets. The advantage is the low cable cost combined with options for extensive remote control and monitoring. The major drawback is the sensitivity to radiation, combined with difficult access for maintenance. A study of the radiation tolerance [158] of a solution based on CAEN supplies (see below) concludes that there may be 0.1 SEU (Single Event Upsets)/module/day if the modules are placed in the tunnel close to the cryostat. This will be the case from day-one of operation. This means that there will be several SEUs per day, in addition to the damage due to dose gradually accumulating over time (tens of Grays per

Table 19: Preliminary specifications for the QUARTIC/GASTOF power supplies for one cryostat.

	Number of channels	Nominal voltage	Current	Current limit
High voltage	4	-3.5 kV	TBD	TBD
AVp12	1	12 V	TBD	TBD
AVm12	1	-12 V	TBD	TBD
DVp5	1	5 V	TBD	TBD
DVp3.3	1	3.3 V	TBD	TBD

year).

2. Power supplies in the alcove areas RR17/13 for ATLAS and RR57/53 for CMS. The expected level of radiation here is 0.05-0.36 Gy/year at full LHC luminosity. This solution is similar to that adopted for the TOTEM Roman Pots.
3. All critical power supply electronics in the counting room and only very simple linear, radiation-hard regulators in the tunnel next to the cryostat.

Except for the CAEN version of solution 1. (see below), the high-voltage supplies are always assumed to be in the counting room, which is advantageous because radiation is thus no more a concern. The wires for high voltage can have a small cross section due to the small current ($<$ 1 mA) and need no remote sense. The high-voltage cables must be well shielded and with a noise filter at the detector.

Solutions 2. and 3. with 200 m long (or longer) low-voltage cables require local regulators next to the load. Without them it will not be possible to maintain a stable load voltage. Cables with a length of 200-500 m would have to have large cross section in order to limit the voltage drop to the level required (roughly $<$ 200 mV). Remote sensing, the classical way of overcoming this, is not effective due to the long delay in the cable. Linear regulators, albeit with much shorter cables, are used in many LHC detector systems, such as the TOTEM Roman Pots and the LHCb Vertex Locator (VELO). A pair of radiation-hard linear regulators have been developed in the framework of RD-49. The regulators are LHC4913 for positive voltages (SCEM: 08.57.56.011.7; 1.23 V to 9 V at 3 A) and for negative voltages LHC7913-4 (SCEM: 08.57.56.111.4; -1.2 V to -7 V at 3 A). In other LHC experiments using a linear regulator, a separate monitoring system for the voltage is exploited, which has to be radiation hard. For instance, in the CMS central tracker a system of FEC, DOHM and CCUs is used. The main issue with this solution is that it is highly specialised for these applications and not easily adapted to the FP420 requirements. Added to this is the difficulty of finding the components. As an alternative solution we suggest the following setup, which allows remote monitoring of the load voltage (see Fig. 90). The voltage at the load is fed back to the location of the power source via pairs in the same cable as the power source. We propose to put isolation resistors in series with the sense wires. As long as the ADCs at the acquisition end have high impedance and low leakage and bias current, the average current and thus the voltage drop across the sense resistors will be small. This means that the average voltage measured at the acquisition end will equal the average voltage at the load.

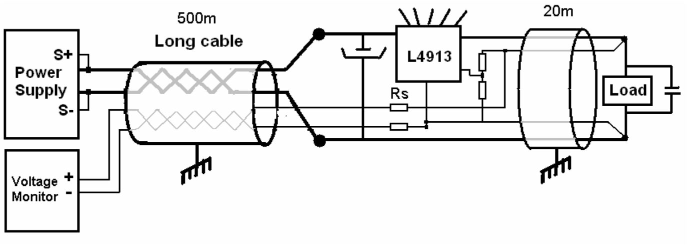

Fig. 90: Block diagram showing the principle of using a local radiation-hard linear regulator. Here for a positive voltage and the option of remote monitor of the load voltage via isolation resistors R_S.

Solution 1: supplies next to the cryostat

For this configuration we have one proposal from CAEN and two (A and B) from Wiener; all solutions still need refinements. The CAEN solution envisages putting both the low- and the high-voltage supplies in the tunnel; the Wiener solutions foresee only the low-voltage supplies in the tunnel.

CAEN

The schematic layout is shown in Figs. 91-93.

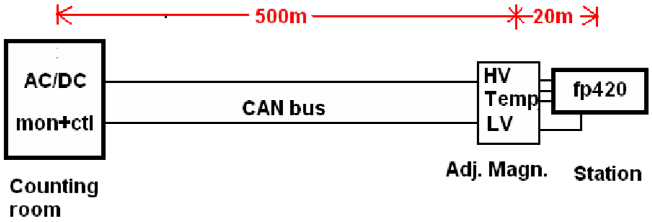

Fig. 91: Solution with all supplies in the tunnel, adjacent to the cryostat. “Station" indicates the FP420 cryostat and “Adj. Magn." the magnets adjacent to the FP420 cryostat.

The A3006 low-voltage supply is adjustable in the 4 to 16V range and may thus not be able to cover all the way down to 3.3 V, necessary for QUARTIC and GASTOF, without additional modifications.

Details of the degree of radiation tolerance of the CAEN modules are given in [157]. Modules A3009, A3486, A3540, A3801 have been tested to work up to doses of about 140-150 Gy. The

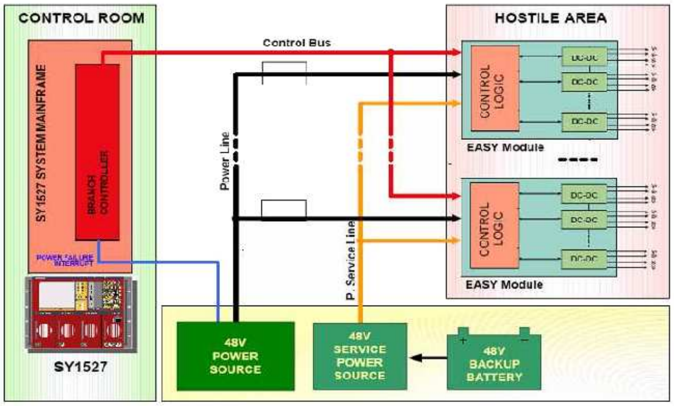

Fig. 92: Block diagram of the CAEN setup.

first three are radiation-certified for ATLAS. Module A3501 has never been tested, but its radiation behaviour should be the same as that of A3540, which has been radiation-certified for ATLAS.

The CAEN standard-module communication is not guaranteed to work over a 500 m cable. The CAEN CAN bus is operated at 250 kbit/s. A speed of 250 kbit/s has been verified to work over cable SCEM 04.21.52.140.4, without affecting signal integrity, but, due to the cable delay, the timing requirements of the CAN bus arbitration protocol are violated. Lowering the bit rate to 125 kbit/s would make the 500 m cable meet the specifications of signal integrity and arbitration protocol. CAEN has offered, at an additional cost, to modify the modules such that they operate at 125 kbit/s, but the modules will then become non-standard and will no longer be exchangeable with those used elsewhere at CERN.

In addition, the CAEN module A3501 is designed for 0 to -100 V, whereas -120 V may be necessary, as specified above. CAEN is able to modify the modules at an additional cost.

WIENER

Wiener, Solution A, MPOD LV next to cryostat, MPOD HV in counting room

Figures 94-95 show the schematic layout of the proposed system. This solution, based on Wiener MPOD modules, has only the low-voltage part in the tunnel. One crate at each location will be needed for the 3D supplies. The high voltage is supplied from MPOD modules in the counting room via a 500 m cable. No auxiliary power crate is needed in the tunnel, different from the CAEN solution. The MPOD modules have never been radiation tested. According to the company they are made in a way which is likely to qualify them to the level we require. It will however be necessary to test the modules in both proton and gamma fields.

Wiener, Solution B, Maraton LV crates next to cryostat, MPOD HV in counting room

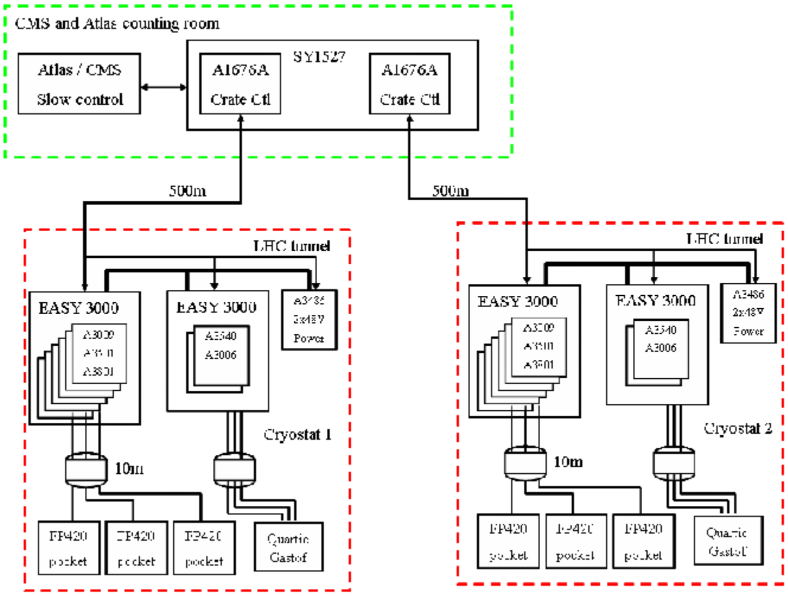

Fig. 93: Diagram of the solution suggested by CAEN. The number of pockets assumed is 3 per cryostat. Shown are also the system for temperature monitoring (A3801) and the supplies for QUARTIC/GASTOF detectors (A3540 and A3006).

Figures 96-97 show the schematic layout of the proposed system.

This solution has the low-voltage supplies housed in Wiener Maraton crates in the tunnel next to the cryostat. One crate will be needed per pocket. The high voltage is supplied over a 500 m long cable by an MPOD module in the counting room. This solution requires a customization of Wiener Maraton low-voltage modules in order to optimise it for low currents. The monitoring of the Wiener Maraton is with individual twisted pairs from each channel. The ADCs for this will need to be in a radiation-free environment, i.e. in the counting room. The length of the monitor and control cable of 500 m is beyond the specification in the data sheet, so this length of cable needs further testing.

The Wiener Maraton modules have been radiation qualified to 722 Gy, and 8×10^{12} n/cm^2. Their good radiation tolerance is partly obtained by moving the digital part of the control and monitoring circuitry away from the radiation zone. This results however in less flexibility compared to the CAEN and the Wiener MPOD solutions. So in the Wiener Maraton system the output voltage and current limit cannot be adjusted from remote, and monitoring is via analogue differential wires. One pair is required per measurement value (voltage and current) resulting in a large amount of monitor wires. The ADCs for this will need to be in a low-radiation environment, i.e. in the counting room. For improved radiation tolerance, mains supply AC to DC conversion is also done

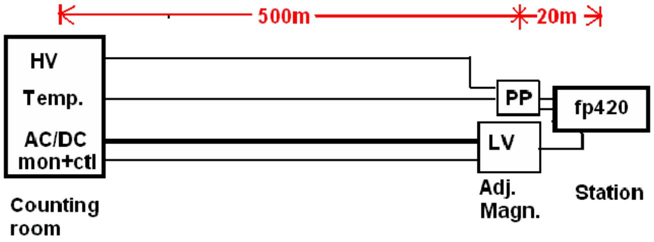

Fig. 94: Overview of the Wiener Solution 1, with MPOD LV next to cryostat, MPOD HV in the counting room. “Station" indicates the FP420 cryostat and “Adj. Magn." the magnets adjacent to the FP420 cryostat. “PP" is a patch panel.

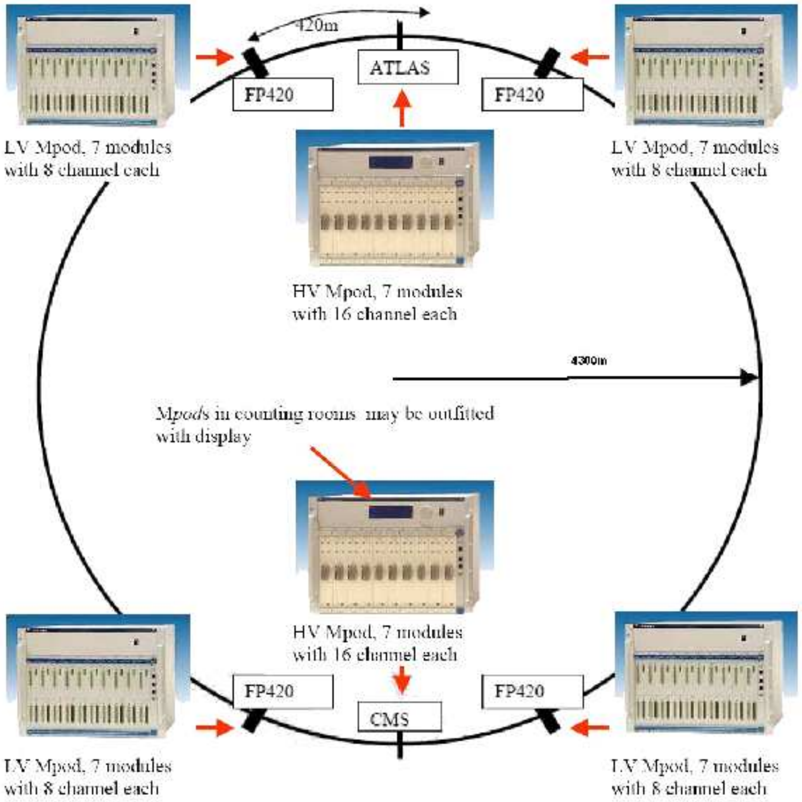

Fig. 95: Wiener solution with LV supplies in the tunnel and HV supplies in the counting room, delivering the bias via 500 m cables. The MPOD will require custom −120 V modules.

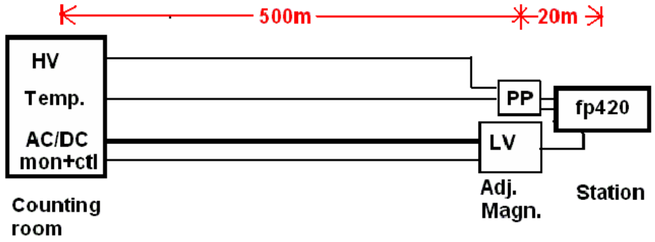

Fig. 96: Overview of the Wiener Solution 2, based on the Maraton modules next to the cryostat. “Station" indicates the FP420 cryostat and “Adj. Magn." the magnets adjacent to the FP420 cryostat. “PP" is a patch panel.

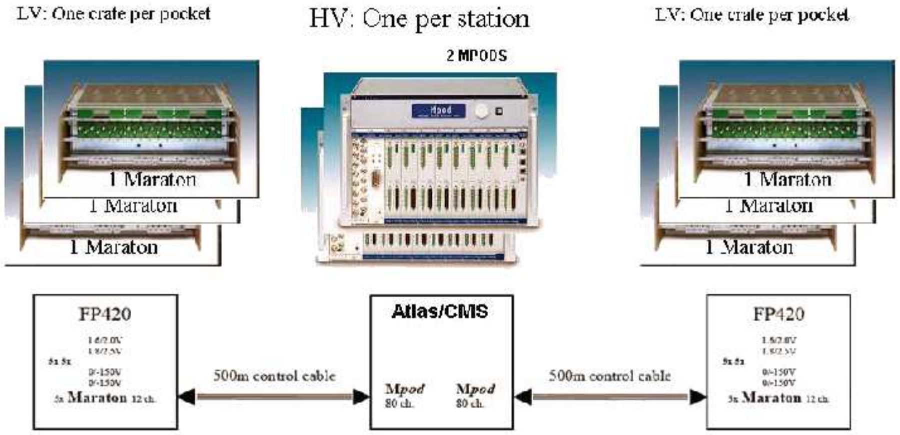

Fig. 97: Low-voltage Wiener Maraton supplies in the tunnel. High-voltage MPOD type supplies are located in the counting room. The Wiener Maraton system is qualified for the radiation environment expected in the tunnel under the magnets near the FP420 cryostat. The illustration shows the setup for either ATLAS or CMS. “Station" indicates the FP420 cryostat.

in the counting room.

The advantage of this solution is that it will fit the QUARTIC/GASTOF requirements without much modification. The disadvantages are the exposure to radiation and difficult access for maintenance. In addition, the Wiener Maraton only allows the voltage setting and current limits to be adjusted manually using potentiometers on the modules. No remote tuning is possible.

Solution 2: low-voltage supplies in alcoves, high-voltage supplies and temperature monitor in counting room, local regulators at load

This solution (Figs. 98-99) is based on the use of Wiener Maraton low-voltage supplies placed in the alcoves. CAEN also has radiation-tolerant power supplies, which could be considered. The Wiener Maraton modules are used for the TOTEM Roman Pot detectors and are also placed in the alcoves.

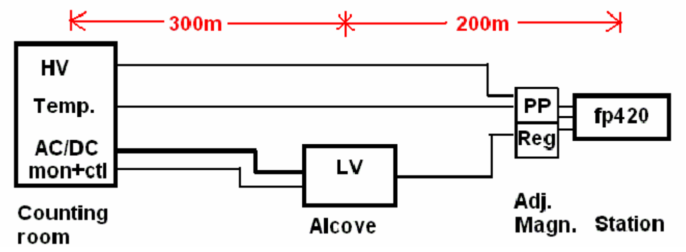

Fig. 98: Low voltage in alcoves, rest in counting room using 200 m cables from alcove to cryostat. “Station" indicates the FP420 cryostat and “Adj. Magn." the magnets adjacent to the FP420 cryostat. “PP" is a patch panel. “Reg" are linear regulators next to the load.

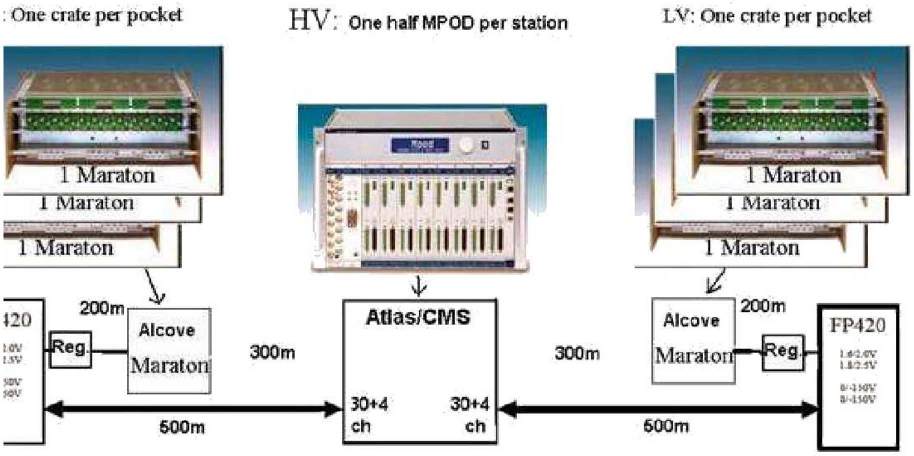

Fig. 99: Low-voltage Wiener Maraton supplies in the alcoves. High-voltage MPOD supplies in the counting room. The Wiener Maraton system is qualified for the expected radiation environment within a large margin. “Station" indicates cryostat.

This solution requires a customization of Wiener Maraton low-voltage modules in order to optimise it for low currents. The length of the monitor cable of 300 m is beyond the specification in the data sheet, so this length of cable also needs further testing, as already discussed. A linear voltage regulator is placed next to the front-end to ensure the voltage stability at the load.

Solution 3: low- and high-voltage supplies and temperature monitor in counting room, local regulators at load

This solution is illustrated in Fig. 100. The advantage is that the power supplies are not exposed to radiation. This widens the number of power supply candidates significantly, lowers their cost and makes the system simpler to maintain. The major drawback is the cable cost and the need for local regulators.

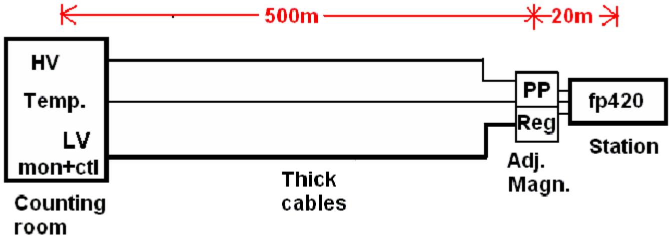

Fig. 100: Low- and high-voltage supplies in counting room using 500 m long cables to a patch panel with regulators next to the cryostat. “Station" indicates the FP420 cryostat and “Adj. Magn." the magnets adjacent to the FP420 cryostat. “PP" is a patch panel. “Reg" indicates linear regulators next to the load.

The low voltage needs to be regulated at the load as discussed earlier. The absolute maximum cable drop in the low-voltage long cables is 5.7 V. At this limit, 6 LV cables per cryostat will be necessary. Hardware tests will have to be done in order to determine if a voltage drop of 5.7 V is tolerable.

9.4.8 Summary of solutions

Figure 101 summarises the solutions outlined in this section.

9.5 Readout and infrastructure at the host experiment

9.5.1 CMS and ATLAS Specific issues

Readout installations at ATLAS and CMS necessarily differ, but will be based on the same parts, which are essentially single-crate versions of the ATLAS silicon readout. Refer to Figure 102. Fibre connections from the tunnel arrive at optomodules fitted to a back of crate BOC card. The BOC provides timing adjustments and passes the data to the ROD where event segments are combined and DSPs can perform monitoring. Event data are passed back through the BOC to an SLINK transmitter and onward to the ATLAS standard ROS. Integration into CMS will require some modification of the ROD firmware so that the output format can be interpreted as a CMS format event

Description of solution				Cable cost	Module cost	Notes
LV		HV				
Near station	CAEN Easy3000	Near station	CAEN Easy3000	27k€	180k€+ 10k€	• Maintenance access, radiation and SEU issues
	Wiener MPOD	Counting room	TBD	60k€	TBD	• Maintenance access, radiation and SEU issues. • Need further radiation tolerance qualifications
	Wiener Maraton		TBD	95k€	TBD	• Maintenance access issues • No voltage tuning from remote.
Alcove	Wiener Maraton		TBD	100k€	TBD	• Maintenance access issues. • Need linear regulator. • No voltage tuning from remote. • Radiation field is unclear. • QUARTIC/GASTOF's +-12V issues
Counting room	TBD		TBD	144k€	TBD	• Lowest module cost. • High cable cost. • Need linear regulator. • No voltage tuning from remote. • Little or no radiation or access issue. • QUARTIC/GASTOF's +-12V issues

Fig. 101: Summary of cable and module cost for various solutions covering both ATLAS and CMS. Custom modules with linear regulator are estimated to cost a total of 6 kEU. The cost of cable pulling and connector mounting is not included. “TBD" means that no particular manufacturer stands out as the best choice based on the investigations done so far. “QUARTIC/GASTOF +-12V issues" refers to the problem that the LHC4713/ LHC7913 regulators will not be suitable to regulate ±12 V presumably required for QUARTIC/GASTOF. Other solutions will have to be found for that case. “Station" indicates the FP420 cryostat.

stream. CMS experts describe this as “relatively straightforward”. DCS and DSS requirements have not been studied, but again it is anticipated that these will follow the example of the existing experiments.

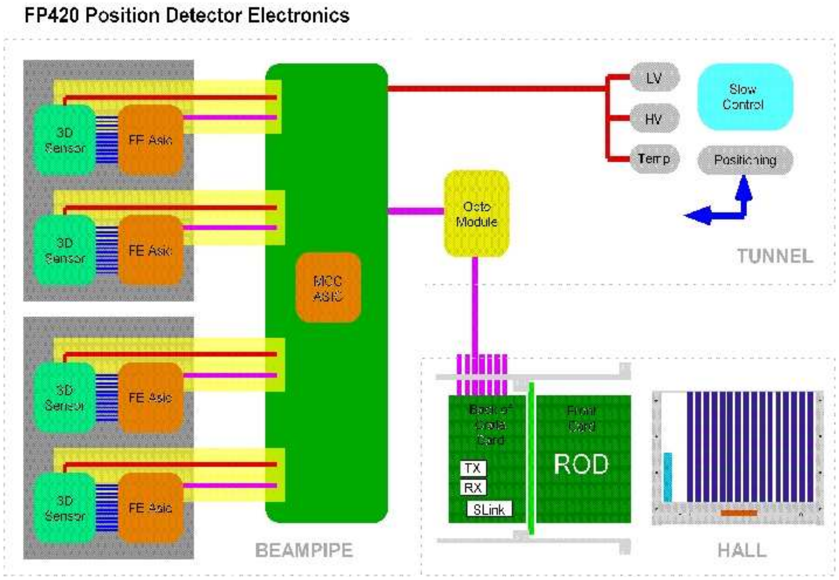

Fig. 102: Layout of the readout and DAQ system.

9.5.2 Tracker readout and downstream data acquisition

The 3D silicon assemblies and their readout take advantage of the significant design investment made by the ATLAS pixel groups. The bump-bonded detector assembly mimics an ATLAS pixel element and the downstream readout of FP420 can therefore be based very closely on the equivalent parts of the ATLAS pixel system. Each superlayer has independent connections to a support card situated within the support structure. LV and HV are supplied from commercial units positioned nearby, as described in Section 9.4. Fibre optic data links to and from the central detector areas terminate on the support cards. Each station has its own link back to a ROD card that drives each arm of FP420. The ROD crates are easily integrated into the ATLAS readout. Integration into CMS should require minimal work.

9.6 Thermal Design

9.6.1 Overview

Running detectors at -20ºC implies that if they are not shielded from the tunnel environment they will ice-up. In order to prevent this from happening it is crucial to isolate these detectors from the LHC tunnel environment. This can be achieved in various ways. One possibility is to use a foam insulation surrounding the detectors, another is to purge dry-nitrogen gas within the detectors to isolate them from the air in the tunnel. A third option is to enclose the detector block within a box. Then there are again two options, either purge the box with dry nitrogen or keep the detector box under vacuum.

1. Foam insulation is not practical within the limited available space. It would render the detectors themselves inaccessible (foam will have to be applied between and around the detector planes) and would not absolutely guarantee that no icing will take place at any point. This method is considered to be cumbersome and potentially harmful to the detectors with no guarantee it will work.
2. Purging dry nitrogen gas during operation is a viable option from an engineering point of view. However purging nitrogen gas continuously into the LHC tunnel is not allowed by CERN.
3. Maintaining a water vapour free environment around the detectors by enclosing them in a box, filled with dry nitrogen is an option. It would however compromise the cooling of the detectors themselves due to natural convection inside the box. It would require more heat to be pumped away compared to cooling the detectors in vacuum, which in itself is not directly considered to be a show-stopper. There is however a potential for icing-up of the enclosure due to the internal convection, which could be solved by applying heaters to the outside of the enclosure. The box would have to be gas tight, in order not to leak nitrogen into the tunnel. The convection of the nitrogen gas will yield larger thermal gradients over the detector plane compared to vacuum and potentially cause an asymmetric temperature distribution that could affect the measurements.
4. If the enclosure is kept under vacuum all drawbacks of option 3 disappear. Maintaining a vacuum around cold detectors is standard practice in laboratories and the technology required to maintain this vacuum is bulk-standard, off the shelf. It will minimise the cooling requirements and it will minimise the thermal gradients. Maintaining a gas-tight enclosure around the detectors (option 3) has the same level of complexity as a vacuum environment.

Option 1 is not considered to be viable and option 2 is not allowed. Because of the advantages attached to maintaining a vacuum around the cold detectors, compared to option 3, it was decided to go for option 4.

9.6.2 Thermal Requirements

The thermal requirements for the detectors are as follows;

- Lowest allowed operating temperature is -22ºC.
- Nominal operating temperature is -20ºC.
- Highest allowed operating temperature is -18ºC.
- Required thermal stability during operation is better than 0.5ºC per 24 hours.

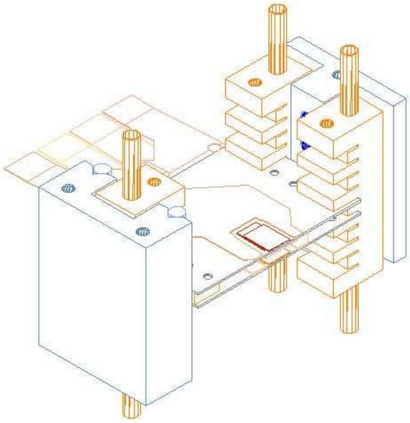

Fig. 103: Front-end of a superlayer showing the cooling block arrangement.

- The maximum allowed thermal gradient over an individual detector (chip) is 0.5ºC.
- All detectors within a test setup will be operating within 2ºC of each other. That is, the temperature of the hottest detector at any given time is no more than 2ºC higher than that of the coldest detector.
- The vacuum pipe, enclosing the LHC beam, will be at 30°C ± 5°C.
- The extreme temperatures to which the detectors will be exposed when non operating will be the ambient temperature in the LHC tunnel and that during transport. These are expected to be in the range of 10°C to 40°C. FP420 will not be part of the overall beam line tube bake out.

Figure 103 illustrates how heat will be transferred from the superplanes to copper blocks in the station support.

9.6.3 Heat Loads

Heat is dissipated inside the tracker cell (mostly in the ASIC underneath) and the control card. Other than that, heat enters the detector block via thermal radiation (enclosure is sitting at 30°C) and parasitic conductive heat loads via the harness and the supports. Analyses have been carried out to size these heat loads. The results are listed in the table 104.

The dissipated heat loads are conservative estimates and make up 75% of all dissipated heat. The parasitic heat loads are best estimates at the time of writing this document. It would be prudent

	Unit [W]	Number #	Total [W]	Type
ASIC/Tracker Cell	0.50	20	10.00	Dissipated
Control Electronics	1.00	5	5.00	Dissipated
Detector Support	0.02	6	0.10	Parasitic
Harness	0.50	5	2.50	Parasitic
Radiated Heat	2.25	1	2.25	Parasitic
LHC fluence	1.00	1	1.00	Beamline
Total			20.85	W

Fig. 104: The heat loads.

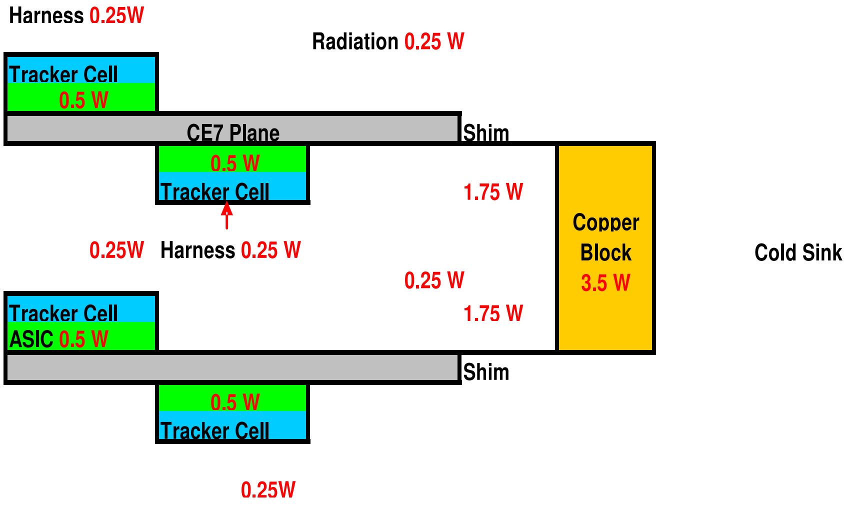

Fig. 105: Heat flow surrounding the tracker cells (local thermal network).

to put a safety factor of 2 on these numbers to quantify the required cooling power. Therefore the recommended cooling power for the cold sink should be better than 42 W. In the next sections the temperature of the cold sink is determined.

9.6.4 Heat Flow

The heat flow/gradient is determined by the dissipated heat together with the thermal resistance between the source and the cold sink. The heat flow has been pictured schematically below in Figure 105. When the overall heat flow is known, together with the thermal resistance of the network, gradients and overall temperature differences can be determined.

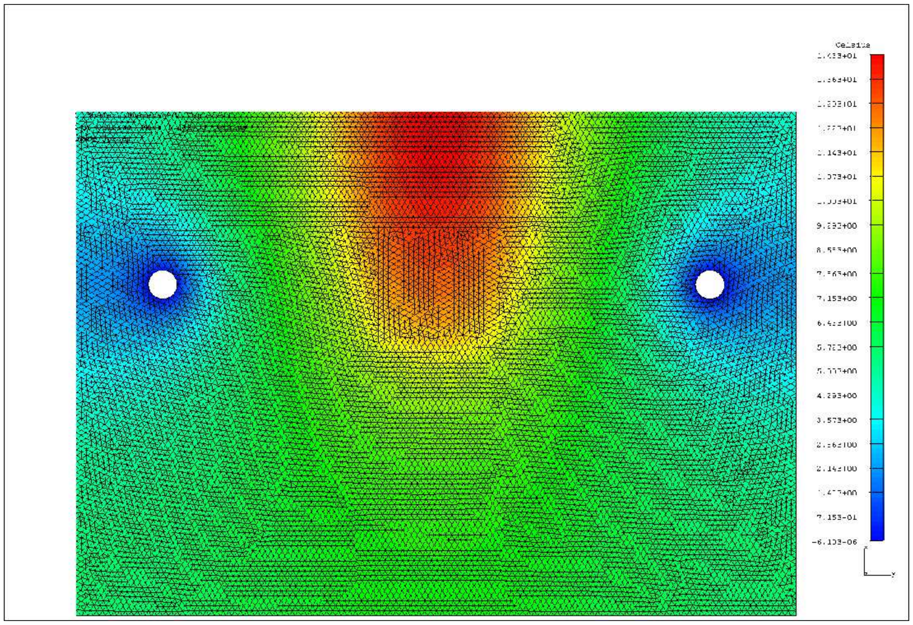

Fig. 106: CE7 detector plane gradient (worst-case configuration).

The CE7 (70/30 Si/Al) plane with two tracker cells has been analysed in some detail. Simplified thermal models were used to assess the effective thermal conductance between the edge and the tracker cell. In Figs. 105 and 106 the overall temperature distribution for an artificial load (1 W, with boundary at 0°C) is given. The resulting thermal resistance towards the edges is 1/14.3 = 0.07 W/K, which assumes heat sinks on either side of the tracker planes.

Figure 107 shows the gradient between the location of the tracker cells and two cold sinks on either side (represented by two holes). One has to assume that not the whole edge of the CE7 plane is available for a thermal load path (sink), hence this worst-case approach. There are some obvious improvements that can be made, but not many will yield a significant smaller gradient. The thermal “choke” as it were is the limited thickness of the CE7 plate, assumed here to be 300 microns.

Of interest to the sensors themselves is the gradient, in the CE7 support. This gradient is shown in Figure 107.

The various thermal resistances between the actual tracker cell and the cold plate next to the detector block have been analysed and the results are listed in the Table 108.

As can be seen from Table 108, the accumulated gradient between the tracker cell and the cold sink is 65.4°C. In order to gain some extra margin with respect to temperature, the recommended cooler temperature (at the heat sink) is -90°C, which gives 5°C margin on top of the 100% margin on the pumping capacity.

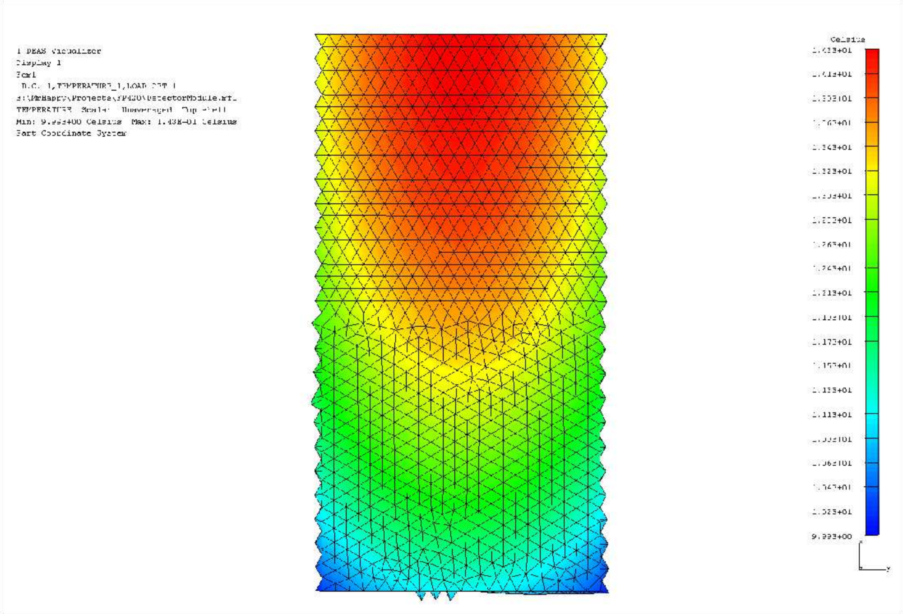

Fig. 107: Gradient in the CE7 plane underneath the tracker cell (4.3°C).

Conductive Path	Heat [W]	W/K	delta-°C
Tracker Cell to CE7 plane	0.75	0.10	7.5
CE7 plane across	1.50	0.07	21.4
Pressure contact between CE7 and copper shim	1.75	0.25	7.0
Bulk conductance copper shim (0.50 x 15 x 30 mm^3)	1.75	1.02	1.7
Pressure contact between copper shim and copper block	1.75	0.25	7.0
Bulk conductance copper block	3.50	10.00	0.4
Pressure contact between block and busbar (cooling plate)	3.50	0.25	14.0
Cold Sink	3.50	0.55	6.4
Total Jump			65.4

Fig. 108: Table: Heat flow for various conductive paths.

9.6.5 Cold Sink

The cold sink as shown in the table above needs to sit at -90°C since the tracker cell operates at -20°C nominally with a gradient of 65°C down to the cold sink (and 5°C extra margin). As mentioned in the heat load section, the cold sink needs to absorb 42 W (including a safety factor of 2). This amount of heat and the gradient excludes the use of Peltier cooling devices. Peltier cooling devices are not practical when they need to bridge gradients exceeding 50°C at sub-zero temperatures. At these temperatures, Peltier devices have trouble pumping heat and they are not efficient at all ($<$ 5%). Using Peltier coolers in stacks to bridge the gap between -90°C (cold sink) and +30°C (ambient) with an efficiency of less than 5% would yield the need to dump at least 10kW of heat into the LHC tunnel and we would still struggle to reach the required temperatures. The alternative would be to use some kind of fluid/vapour cooling stage; however the environment directly surrounding the beam line is extremely limiting. Not many cooling agents can survive the extremely intense radiation environment.

Within CERN several cooling methods have been developed. The cooling system developed for the TOTEM project seems appropriate to cool the FP420 detectors as it has been designed and is acceptable for use in the LHC tunnel. It can reach the required cold-sink temperature with margin and has sufficient cooling power. Other options we looked into required cooling fluids with a heat exchanger but none of the cooling fluids could be guaranteed to be radiation hard. Due to symmetry conditions and in order to have at least partial redundancy in the cooling system, it would be good to operate two coolers in parallel per detector block. Envelope restrictions or cost may however exclude this option.

Conclusions

The cooling system should be able to run for 2 years next to the LHC beam line, without servicing. It is strongly recommended to operate the tracker cells in vacuum. The required cooling for operation in vacuum is specified as follows: 42 W pumping power at -90°C. There are significant thermal gradients predicted across the CE7 plane and underneath the tracker cell.

Recommendations

Maintain a symmetrical cooling system, following the symmetry in each detector plane. It will minimise gradients and provide redundancy. A cooling system by CERN as for the TOTEM detector is recommended. The selected cooling system needs to be subjected to significant radiation levels during sub-system testing in preparation for the final design to prove performance and stability. When the tracker cell design and the flexible links have matured, together with the overall geometry, the analysis needs to be repeated at a slightly more detailed level. If gradients between the different super planes have to be minimised it would be prudent to introduce “dummy” planes at either end of the stack, sitting at the same temperature as the other planes. The extra planes would provide for a more uniform thermal radiative background.

9.7 Performance of the tracking system

The performance of the tracker has been evaluated using a simple Monte Carlo program and also by a full GEANT4 simulation. In the GEANT 4 simulation, the energy deposits within the sensitive detector volumes are translated into elementary charges and their collection on the electrodes is simulated. Capacitative coupling between closely placed channels as well as noise contribution are taken into account. The signal collected channel by channel is corrected by a gain factor, converted into an integer number and fed into a cluster-finding algorithm, if above a threshold. Clusters

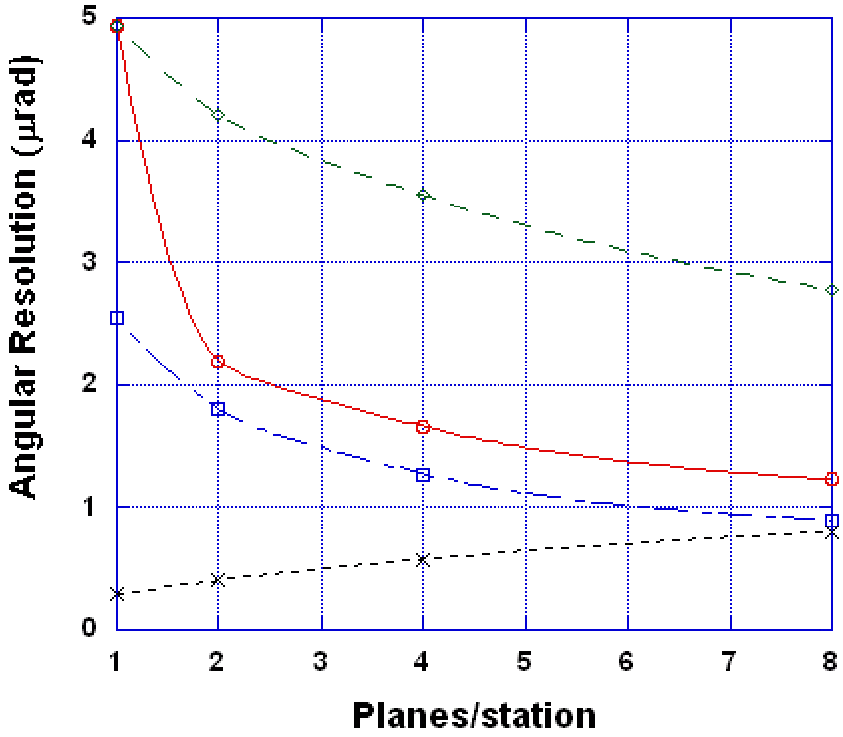

Fig. 109: Angular resolution for a tracker consisting of two stations separated by 8 metres. Each layer has a detector with a pitch of 50 microns. The curves from top to bottom are: aligned tracking layers, alternate layers shifted by 25 microns, theoretical best result, and multiple scattering contribution. The design goal is one μrad.

typically (∼90% of the cases) include just one channel. The efficiency to find at least one cluster per plane is 99.7%. A resolution on the simulated hit position close to 10μm has been measured for each plane. A track finding/fit algorithm based on a χ^2 fit loops over the available clusters.

One feature of forward tracking that does not occur in central trackers is that the tracks have a very small angle. This means that hits in each tracking layer are highly correlated and one does not improve the resolution by $1/\sqrt{N}$, where N is the number of layers. To improve matters, alternate layers will need to be shifted by half a pixel width to improve the tracking precision.

This is shown using a simple Monte Carlo model in Figure 109. The multiple scattering angle is roughly 2 μrad $\times\sqrt{\mathrm{thickness}/\mathrm{X}_0}$) per layer at 7 TeV. If each layer corresponds to about 1% of a radiation length, then one has a multiple scattering contribution of 0.2 μrad per layer. For the materials in this model tracker, roughly 0.2% of the protons will interact per layer. Figure 109 shows calculations for a tracker consisting of N planes per station, with two stations placed 8 metres apart. The spatial precision per layer is 50 microns/ sqrt(12) = 14 micron. Shifting alternate layers by 25 micron significantly improves the tracking performance. Multiple scattering degrades the tracking resolution if the number of planes per station is increased beyond ten layers. However, ten layers will give the design figure of one μrad.

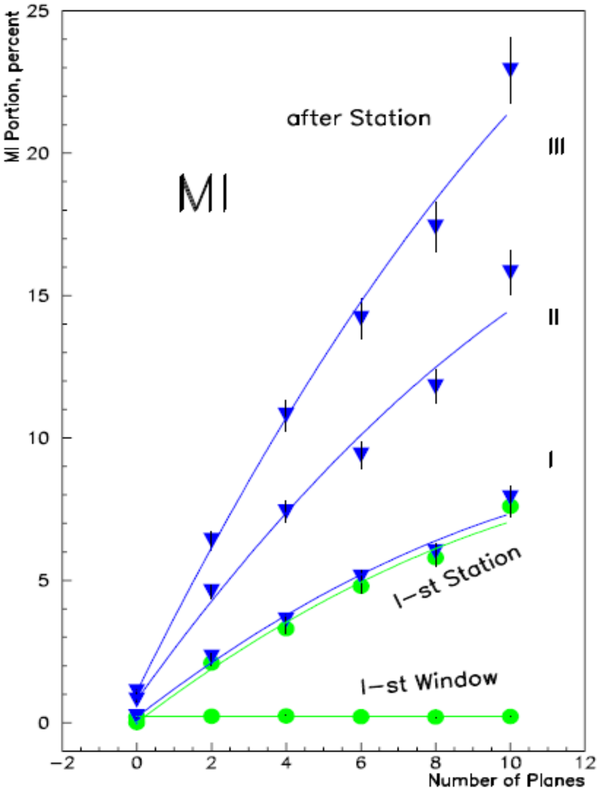

Fig. 110: Percentage of secondary interactions (MI) as a function of the number of planes and tracking stations. A revised design improves the performance – the two-station tracker has a 6.8% secondary interaction rate. See text.

In a full GEANT4 simulation, different layouts of the detector stations with different numbers of planes were simulated and their impact in terms of secondary interactions of 7 TeV protons was assessed. Moreover, the impact of a middle (3^{rd}) station was evaluated.

The secondary interaction rate (Multiple Interaction, or MI in the figures) was evaluated as the fraction of proton tracks which have an inelastic interaction anywhere along the spectrometer before the last plane of the last station. It was found that in 1 mm of stainless steel, ceramic, and silicon the secondary interaction rates are 1%, 0.5% and 0.4%, respectively. Figure 110 shows the rate of secondary interactions as a function of the number of planes per station for a three-station layout. Contributions to the 20% rate resulting after the third station come mainly (~15%) from the 1 mm ceramic support structure of the silicon detectors. Note that this is much larger than the model

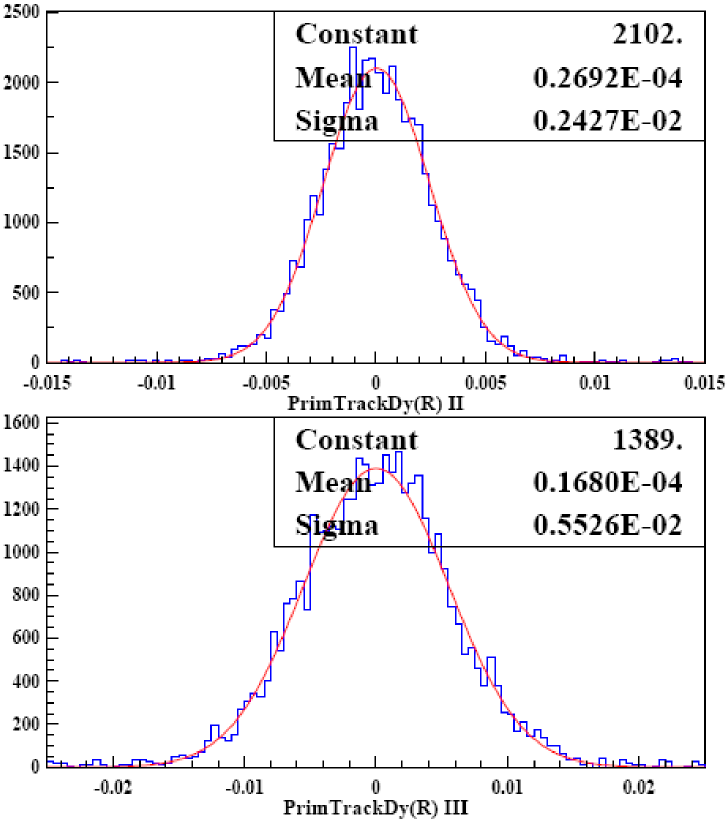

Fig. 111: GEANT4 estimate of the multiple scattering (in mrads) in the middle (top) and at the end (bottom) of the three-station tracker.

tracker discussed above. The GEANT4 results led us to consider CE7, a 70%/30% Si-Al compound support as an alternative. The contribution of a 250 μm stainless steel window, one for each station, turned out to be negligible. Consequently a more reliable secondary interaction estimate, based on an analysis of hits in the detector using realistic materials and a three-station layout is 10.1%. For a two-station layout, this drops to 6.8%. It should be noted that if an interaction takes place in the third station some tracks can nevertheless be well reconstructed with a χ^2/NDF less than 1.5. With this cut, the contamination of events with secondary interactions in the signal sample is negligible – around 0.5%. Losses of events are comparable to the secondary interaction rates, and are 10.4% and 7.1% for the three- and two-station layouts respectively.

An estimate of the multiple scattering for the two- and three-station layouts is shown in Figure 111. Figures 112 and 113 show the χ^2/NDF and angular resolution for the two-station (0.85 μrad) and three-station (0.91 μrad) layouts. These are both within the design specification. Finally,

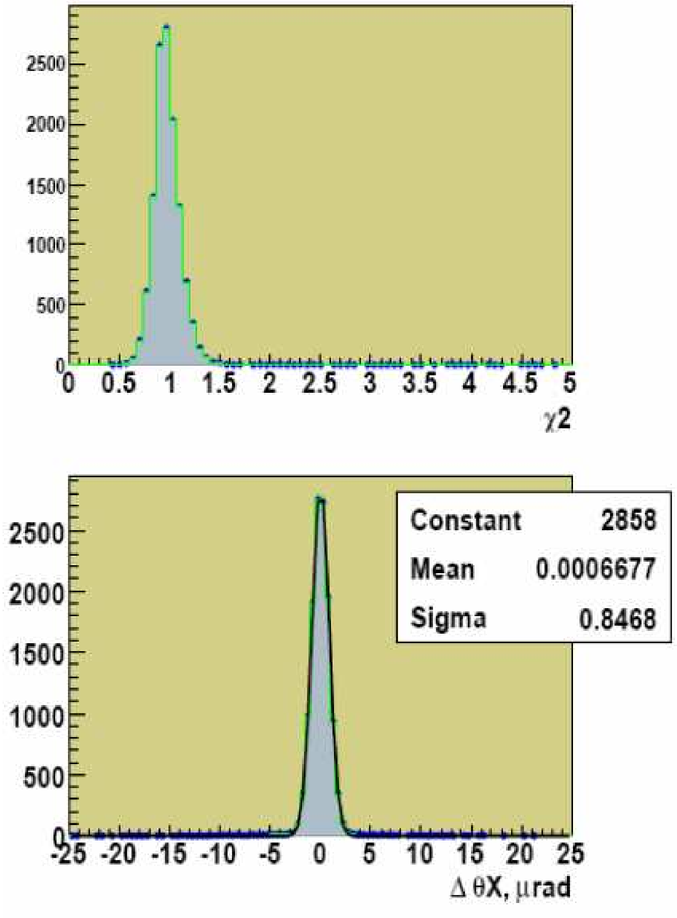

Fig. 112: Track χ^2/NDF (top) and angular resolution (bottom) for a two-station tracker. The angular resolution is 0.85 μrad if the χ^2/NDF is selected to be less than 1.5.

the efficiency of two-track reconstruction has been found to be 86% and 80% respectively for the two- and three-station layouts.

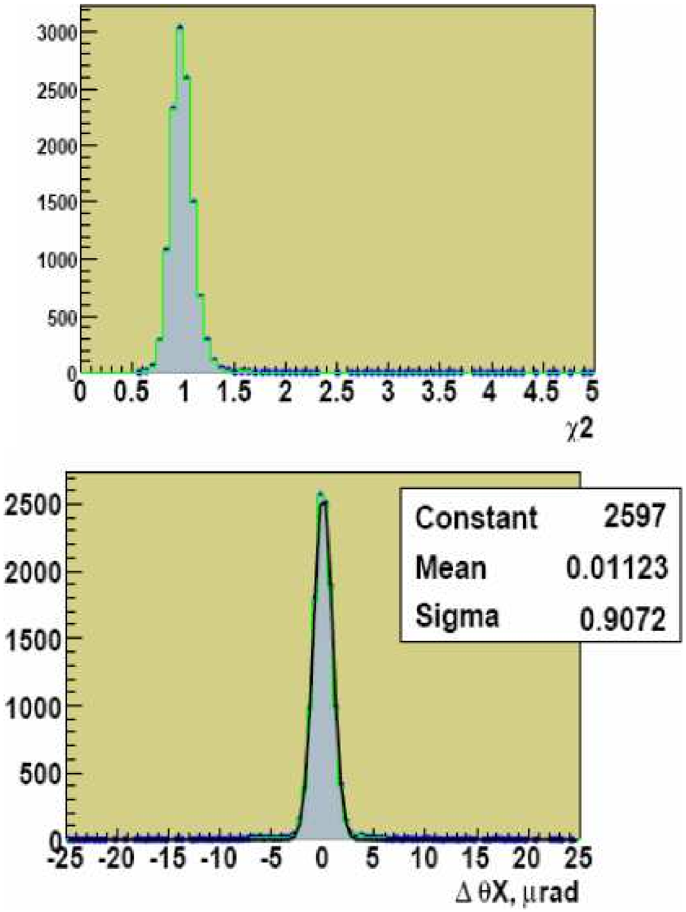

Fig. 113: Track χ^2/NDF (top) and angular resolution (bottom) for a three-station tracker. The angular resolution is 0.91 μrad if the χ^2/NDF is selected to be less than 1.5.

10 Fast Timing Detectors

10.1 Overlap background and kinematic constraints

The FP420 detectors must be capable of operating at the LHC design luminosity $\mathcal{L} \approx 10^{34}$ cm^{-2}s^{-1} in order to be sensitive to femtobarn-level cross sections in the central exclusive channel [pXp]. At these luminosities overlap background from two single diffractive events superimposed with a central hard scatter ([p][X][p]), as shown in Fig. 114(a), becomes a significant concern, especially in dijet final states. The 2-fold overlap coincidence backgrounds, shown in Fig. 114(b) and (c), also must be considered, however; as they scale with $\mathcal{L}^2$ instead of $\mathcal{L}^3$ they are less of a concern in the high luminosity limit. Fortunately, there are a number of techniques we can employ to reduce this overlap background. It can be substantially reduced at the high level trigger stage, or offline, by employing kinematic constraints. These factors, discussed in detail in the physics overlap discussion (Section 3), include consistency between the central system and the protons in rapidity and mass, and also use the fact that the number of particle tracks associated with the event vertex is much smaller for exclusive than generic collisions. Even after the significant background rejection afforded by these constraints, overlap backgrounds are still expected to dominate the signals without the additional rejection provided by precision timing of the protons, as detailed below.

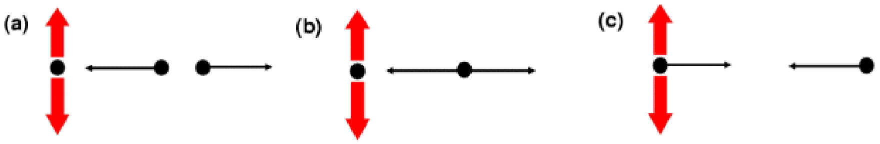

Fig. 114: A schematic diagram of overlap backgrounds to central exclusive production: (a) [p][X][p]: three interactions, one with a central system, and two with opposite direction single diffractive protons (b) [pp][X]: two interactions, one with a central system, and the second with two opposite direction protons (c) [p][pX]: two interactions, one with a central system and a proton, the second with a proton in the opposite direction.

10.2 Timing

High-precision time of flight (ToF) detectors at 420 m can be used to obtain a large reduction in overlap (or pile-up) backgrounds [1]. We need only measure the *relative* arrival time of the two protons, $\Delta t = t_L - t_R$. Under the assumption that they originate from the same event, the z-position of that event can be calculated as $z_{pp} = \frac{1}{2}\Delta t \times c$. The uncertainty on z_{pp} is $\delta z_{pp} = \frac{c}{\sqrt{2}}\delta t$, where δt is the (r.m.s.) time resolution of the proton measurement. For example, δt = 10 ps implies δz_{pp} = 2.1 mm. We then require a match between z_{pp} and the vertex position from the central detector, z_{vertex}, which is known with extremely good precision ($\approx$ 50 μm) [159].

In the case of the overlap backgrounds, the protons do not originate from the same event as the hard scatter and so the vertex reconstructed from time-of-flight information will, in general, not match the vertex observed in the central detector, which implies that a large rejection factor can be obtained. This rejection factor depends on four parameters; the timing resolution δt, the spread in interaction points σ_z, the vertex window size (i.e. the degree to which the vertices are required to match) and the luminosity. As the luminosity increases, the probability of there being more than one proton in an arm of FP420 increases. If any of the subsequent timing measurements results in a vertex that coincides with the central vertex, then these protons would be chosen as the 'correct' protons. Hence the rejection factor degrades slightly with increasing luminosity. The vertex window size is a trade-off between high signal efficiency and high background rejection. Clearly a smaller vertex window results in a higher background rejection but will also lead to more signal events failing the vertex matching requirement. Common choices are that the vertices must coincide to within 1, 1.5 or $2\times\delta z_{pp}$, which corresponds to a signal efficiency of 68%, 87% and 95% respectively. Finally, the rejection factor increases if the spread in vertices increases and is also approximately linear with δt.

The prototype detectors described below have a timing resolution of $\delta t \approx 20$ ps. As the luminosity grows, better timing resolution is required. We envisage a program of detector upgrades to match this requirement, eventually attaining resolutions smaller than 10 ps, as discussed in Section 10.9. The relatively small and inexpensive precision ToF detectors discussed here make this approach viable.

We have calculated the background rejection for the three overlap cases shown in Fig. 114 (a) [p][p][X] (b) [pp][X] and (c) [pX][p]. For example, if δt = 20 ps ($\delta z_{pp} = 4.2$ mm) and the spread in interaction points is $\sigma_z \approx 50$ mm [159], we obtain a rejection factor of 21 for the first two cases and 15 for the third if the vertex measurement from proton time-of-flight is required to fall within ± 4.2 mm ($\pm 1 \times \delta z_{pp}$) of the vertex measured by the central detector. Case (a) dominates at high luminosity and consequently for δt = 10 ps, we would be able to obtain a rejection factor of greater than 40 (for a $\pm 1 \times \delta z_{pp}$ vertex window), enabling FP420 to effectively cope with the large overlap backgrounds at the design luminosity. Note that the rejection factors presented in Table 8 in Sec. 3.3 are smaller than those presented here due to a larger vertex window ($\pm 2\delta z_{pp}$), which maximises the signal efficiency, and also a narrower spread in interaction points of 4.45 cm. This pessimistic vertex distribution is based on a large crossing angle scenario and results in a reduced background suppression power using the ToF detectors. For the nominal crossing angle of 250 μrad, the vertex spread exceeds 5 cm, and in addition, the expected growth in σ_z would result in an improved rejection. The final choice of vertex window will be optimised based on the analysis goals and instantaneous luminosity. For example, a discovery measurement might maximise signal to background, while a measurement of a state's properties might require very low background at the expense of signal efficiency.

A couple of other factors could impact the overall timing precision. If the path length of protons detected in FP420 were to vary significantly, this could degrade the vertex measurement accuracy. We have determined that even for the largest energy loss for protons in our acceptance compared to the beam protons, the path difference amounts to less than 30 μm, corresponding to a 100 fs time difference (even a smaller effect is expected from proton velocity differences). A precise measurement of the arrival time difference between deflected protons in the ToF detectors requires a reference timing signal at each detector with a $t_L - t_R$ jitter that is small enough not to contribute significantly to the overall time resolution. The large ToF detector separation of about 850 m makes this a challenging requirement. Our reference timing system, designed to yield an r.m.s. jitter of $\sigma_{LR} \approx 5$ ps, is described in Sec. 10.7.

The absolute calibration of the ToF detectors z-coordinate measurement will be determined and monitored with double pomeron exchange (DPE) physics events to correlate the vertex position measured with the central trackers with the vertex measured by the FP420 timing detectors. Since it is not possible to trigger on the protons at Level-1, it will be necessary to add a double Pomeron filter at the High-Level-Trigger to the highest cross section candidate DPE processes that pass the Level-1 trigger, dijets and dileptons for example, to select an adequate sample of events. Given the high cross section for DPE dijets (1.2 nb for $E_T > 50$ GeV, see Tab. 7), it will be possible to collect hundreds of such events each store.

10.3 Timing detectors

For quite a while the standard for time of flight detectors has been in the 100 ps range. Recently, there has been an explosion of interest in fast timing for medical purposes in addition to high energy physics detectors, and the idea of a detector with a few ps resolution is no longer considered unreasonable [160]. The ALICE collaboration has developed a time of flight system that has achieved a time resolution of about 20 ps [161]. A time resolution of $\sigma = 6.2$ ps (with $\sigma \approx 30$ ps for a single photoelectron) was recently achieved by a group from Nagoya [162] utilizing prompt Čerenkov radiation. A beam of 3 GeV/c pions was passed through a quartz radiator in line with a micro-channel plate photomultiplier tube (MCP-PMT). MCP-PMTs consist of a quartz faceplate and a photocathode followed by two back-to-back chevroned microchannel plates read out by a single anode or multi-anode pads. They are compact (only about 3 cm in depth) and provide a gain of about 10^6 for a typical operating voltage of 2.5 to 3.0 kV. Our requirements of an edgeless detector to measure particles within several mm of the beam combined with the very high beam energy renders the Nagoya geometry unusable, but alternate detector concepts described below are likely capable of 10 ps or better resolution.

Three main factors affect the time resolution of Čerenkov detectors: (1) the spread in arrival time of photons at the photocathode, (2) the time resolution of the MCP-PMT, dominated by the transit time spread (TTS) of the electrons from emission at the photocathode to arrival at the anodes, and (3) the downstream electronics, including signal dispersion in cables. The first factor is minimised using Čerenkov light and optimised geometrical designs. The MCP-PMTs we are considering have a small TTS, about 30 ps for a single photoelectron, leading to a resolution of 30 ps/$\sqrt{n_{pe}}$. The two major manufacturers of MCP-PMTs are Burle [163] and Hamamatsu [164]. Hamamatsu has concentrated on small active area (11 mm diameter) tubes with a single channel, for which the TTS is approximately 15 ps. Burle's tubes are larger (48 mm × 48 mm) and include a 64 pixel version that is well matched to one of our detector concepts.

We are developing two types of ToF counters for FP420, GASTOF (Gas Time Of Flight) and QUARTIC (QUARtz TIming Čerenkov). Prototypes of both types of detector have been built and tested.

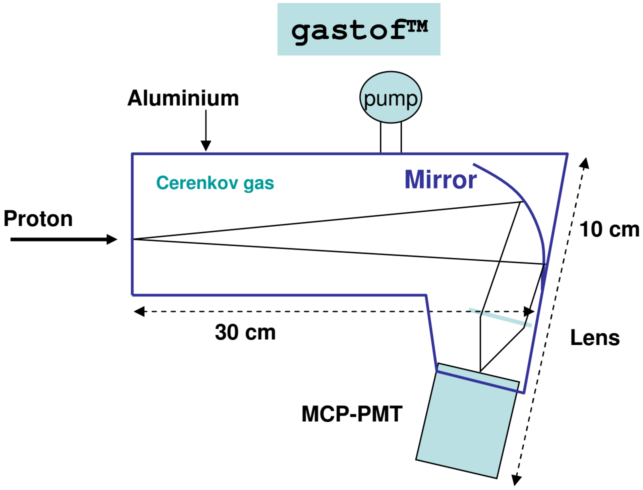

Fig. 115: Schematic of GASTOF, a gas-based Čerenkov counter proposed by Louvain, as described in the text.

A schematic diagram of the GASTOF detector developed at UC Louvain is shown in Fig. 115. It has a gas radiator at 1.3 bar in a rectangular box of 30 cm length, with a very thin wall adjacent to a specially designed flat pocket in the Hamburg beam pipe (Section 7). The protons are all essentially parallel to the axis. A thin 45° concave mirror at the back reflects the light to a MCP-PMT. The gas used in the tests, and which we propose to use in FP420, is C_4F_8O, which is non-toxic and non-flammable, and has a refractive index $n = 1.0014$ between 400 nm and 650 nm, giving a Čerenkov angle ($\beta = 1$) of 3.0°. C_4F_8O was first successfully used in a prototype RICH counter for BTeV [165].

The in-line material in a GASTOF (thin windows, mirror and gas) is minimal and does not cause significant multiple scattering. It can therefore be placed before the final tracking detectors. The GASTOF is intrinsically radiation hard, the only sensitive element being the MCP-PMT. Lifetime tests on gain, transit time spread, and quantum efficiency under laser light irradiation were carried out on Hamamatsu and Budker Institute tubes by the Nagoya group [166]. At 2.8×10^{14} photons/cm^2 some gain decrease occurred, recoverable by increasing the HV, but the TTS was not affected. For a 30 cm GASTOF, the mean number of photoelectrons is approximately 10.

The QUARTIC detector, which utilises fused silica (artificial quartz) bars as radiators, is a joint development effort of University of Alberta, Fermilab, and University of Texas, Arlington.

Figure 116(a) shows the concept: a proton passing through the silica bars radiates photons which are measured by the MCP-PMT. Figure 116(b) shows the QUARTIC detector baseline design, a 4 $\times$ 8 array of bars 15 mm in length with a 6 mm $\times$ 6 mm cross section is mounted at the Čerenkov angle, $\theta_c \approx 48^\circ$, minimizing the number of reflections as the light propagates to the MCP-PMT through an air-filled aluminised light guide. Air light guides are used rather than long silica bars to avoid the time dispersion from the wavelength dependence of the index of refraction. Figure 116(c) shows a third generation single row prototype used in the October 2007 CERN test-beam. The final four-row version will have a very thin wall adjacent to the beam-pipe, matching the dead area of the silicon detectors, to ensure full acceptance for all measured tracks.

The GASTOF and QUARTIC detectors have complementary features and we are proposing to use both in FP420. One GASTOF detector will be located in its own beam pipe pocket after the first silicon detector pocket. The two QUARTIC detectors, providing 16 independent measurements of the ToF of the detected proton, will be positioned in another pocket after the final silicon tracking detector. With this arrangement multiple scattering and interactions in the quartz bars are unimportant.

10.4 Detector simulations

GEANT4 simulations of the propagation, absorption, reflection, and arrival time (at the MCP-PMT face) of Čerenkov photons have been performed using the GASTOF and QUARTIC detector designs. These simulations provide an important aid to our understanding of the proposed detectors.

Figure 117 shows the simulation results for the distribution of arrival time and position of photons at the MCP-PMT face for a 30 cm long GASTOF. Due to the optimised geometry and small Čerenkov angle all the photons arrive within a few picoseconds, and consequently the time resolution is dominated by transit-time jitter in the MCP-PMT and the subsequent electronics.

Figure 118 shows some simulated light paths from the QUARTIC GEANT simulation. Figure 119 shows the distribution of the number of photoelectrons for one bar ($\langle n_{p.e.} \rangle \approx 3$) and the distribution of photon arrival times, including the measured quantum and collection efficiency of the Burle tube. Most of the photons arrive within the first 15 ps. Although the time spread is larger than the GASTOF and the number of photoelectrons is smaller, the philosophy of the QUARTIC detector is to compensate for the inferior resolution of a single channel with two detectors and multiple measurements. A proton traverses eight bars in each of the two QUARTIC detectors, giving 16 measurements with up to a 4-fold improvement in resolution over that of a single bar. The QUARTIC detector also has x-segmentation that could be useful to time multiple protons in the same bunch crossing.

10.5 Performance in test-beam measurements

Measurements of prototype GASTOFs and QUARTICs have been performed over the past year and a half using a 120 GeV proton beam at Fermilab. The results given here were obtained at the March 2007 test-beam. We tested two GASTOFs, G1 and G2, and two QUARTICs, QA and QB.

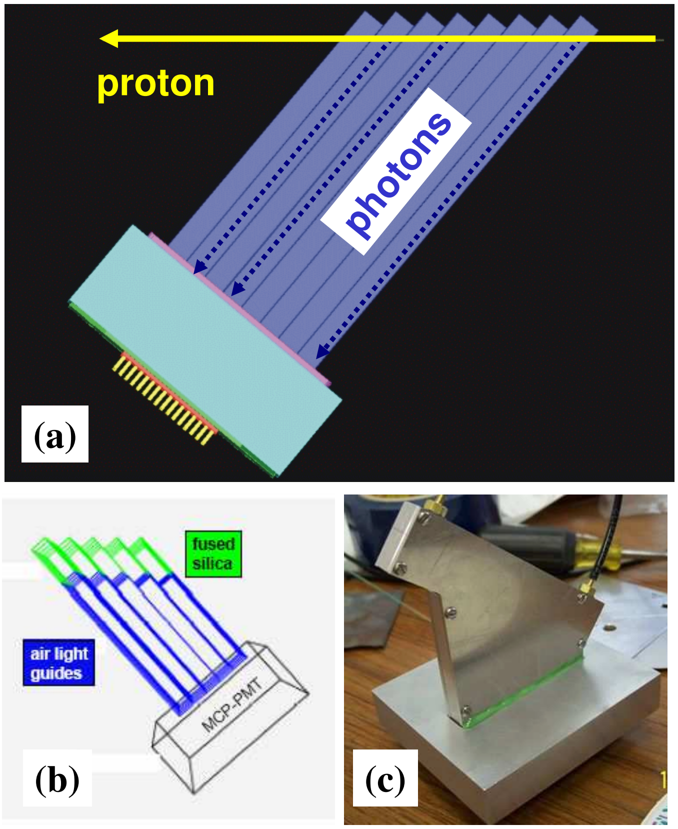

Fig. 116: (a), (b) Conceptual drawings of a QUARTIC detector, with four rows of eight 15 mm long bars, followed by air light guides to the MCP-PMT. (c) A photograph of the prototype detector used in the October 2007 CERN test-beam.

G1 was an initial prototype which ganged together four central channels of the (8×8 array of 6 mm $\times$ 6 mm pixels) Burle 85011-501 MCP-PMT with 25 μm pores. G2 was a second-generation prototype using an 11 mm diameter single channel Hamamatsu R3809U-50 MCP-PMT with 6 μm pores. QA and QB used the Burle 85011-501 with 10 and 25 μm pores, respectively.

The signal for the MCP-PMT's was amplified using a GHz amplifier, passed through a constant fraction discriminator (CFD), and read out by a Phillips 7186 TDC. Several types of amplifiers were tested: ORTEC 9306, Phillips BGA2712, Hamamatsu C5594, and Mini-Circuits ZX60-14012L. Several different CFD's were also used: ORTEC 934, ORTEC 9307, and a Louvain-made CFD circuit. We used a CAMAC-based data-acquisition system triggered by scintillator tiles located on either end of the detector setup. Multiwire proportional chambers provided track position information.

While the data-acquisition system provided a wealth of data allowing us to compare the per-

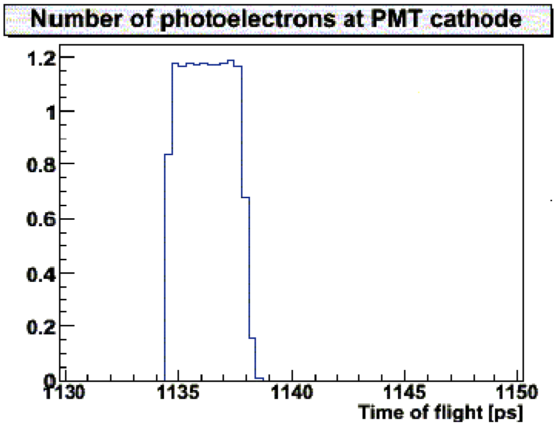

Fig. 117: Time of arrival of Čerenkov photons at the MCP-PMT photocathode in the GASTOF simulation.

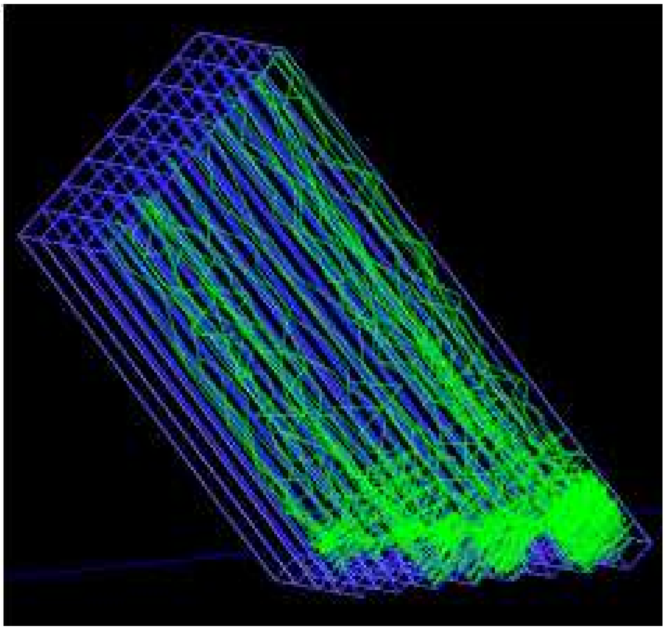

Fig. 118: Simulated Čerenkov light paths in a QUARTIC detector.

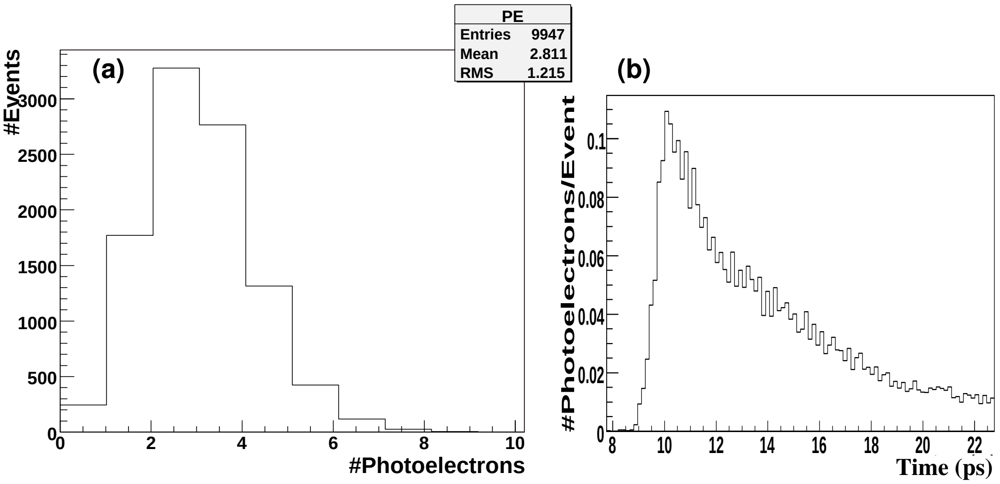

Fig. 119: (a) Simulated distribution in the number of photoelectrons from one bar of a QUARTIC detector. (b) Distribution in arrival times (ps) in one QUARTIC bar.

formance of the different components and multiple channels, the most useful results for evaluating the detector performance were derived from an analysis of waveforms recorded from four channels (G1, G2, QA-1 and QA-4) using a Tektronix DPO70404 4 GHz digital oscilloscope. Offline we applied fixed threshold discrimination and constant fraction discrimination algorithms. From the time differences between all pairs of channels we infer the individual resolutions. With an optimised CFD algorithm we achieved $\delta t(G1-G2)$ = 35±1 ps (r.m.s.) as shown in Fig. 120; from all combinations we inferred $\delta t(G1)$ = 32 ps and $\delta t(G2)$ = 13 ps. The G2 detector is expected to be superior due to a better mirror and a faster MCP-PMT. Unfolding the resolutions of QUARTIC bars, we find $\delta t \approx 60$ ps. The G1 efficiency is very high $\sim$ 98%, while the G2 efficiency is about 80% - probably due to improper alignment of the spherical mirror (this will be addressed in the next prototype). QUARTIC bar efficiencies are about 80%. The overall performance of the QUARTIC bars including electronics improved from 110 ps/bar in the first run to 82 ps/bar in the second run, due to improvements in the air light-guides and better tuned CFDs. The detector/MCP-PMT and the CFD/TDC electronics chain contribute comparable amounts to the overall resolution. Given an 80% efficiency we would expect about 13 measurements for two 8-bar QUARTIC detectors, implying an overall resolution of about 23 ps for the QUARTIC detectors alone. A full test demonstrating this resolution improvement is planned for CERN test-beams in Summer/Fall 2008.

The single-channel GASTOF detector has an intrinsic detector/MCP-PMT resolution on the order of 10 ps, so requires a different electronics strategy to maintain this superior resolution. As discussed in the next section, we envisage using a single photon counter with fast oscilloscope technology to maintain an overall timing resolution of 15 ps or better, even without further improvements, such as offline corrections to position of the tracks through the detector (which will be known to $\sigma(x,y) \approx 5\ \mu$m).

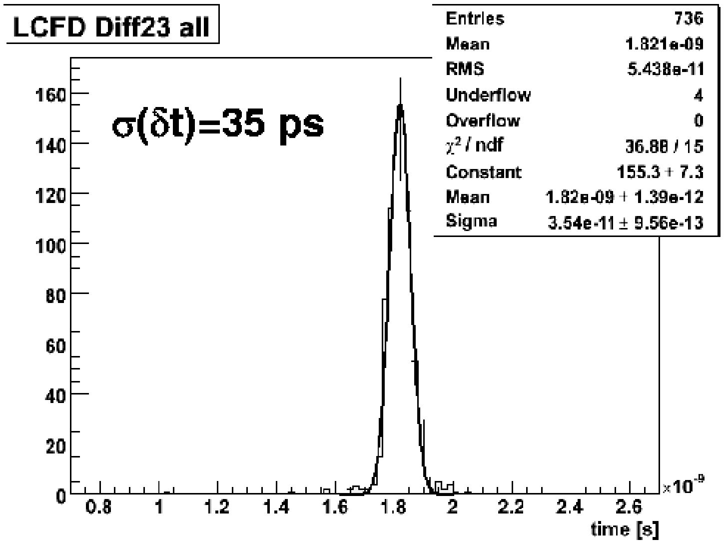

Fig. 120: The time difference between the first (G1) and second generation (G2) GASTOF prototype detectors.

We participated in the CERN test-beam in October 2007 and recorded oscilloscope data using many different combinations of voltage, attenuation, CFD threshold, bar length, etc. This data is currently being analyzed in parallel with developing laser test stands at UTA and Louvain for detailed MCP-PMT and electronics tests prior to the next test-beam at CERN in Summer 2008.

10.6 Electronics and data acquisition

The fast readout electronics must provide a timing resolution compatible with the baseline design of the ToF detectors. The Alberta and Louvain groups have extensive experience in this area and are responsible for the design and prototyping of the readout electronics. Both groups have developed fast amplifier boards and CFD boards for use in the beam tests. Independent tests with a fast laser have verified that the performance of these boards is comparable to commercial units, but the custom boards have the advantages of being much more compact and less expensive.

The largest single contribution to the timing resolution in our first test-beam run in Summer 2006 was the ORTEC 934 constant fraction discriminator. For the March 2007 test-beam run we employed a CFD board designed by the Louvain group. This new unit was designed to work with rise times as short as 150 ps, and to be insensitive to the non-linearity and saturation of the amplifier. Based on the results of the waveform analysis, we are producing an updated version for further beam tests in 2008.

The Alberta board consists of an integrated amplifier and CFD, providing an alternative approach to the separate amplifiers and CFD's developed at Louvain. The amplifier uses the Phillips BGA2717 chip, while the CFD is based on one developed by Alberta for the GlueX Experiment. It has also recently been adopted by the ATLAS LUCID detector. The circuit has been upgraded to use the most recent comparators and logic. Laser tests at SLAC gave a preliminary measured resolution of 19 ps for the Alberta CFD (ACFD) board.

For beam tests we used the Phillips 7186 25 ps TDC. The final readout for QUARTIC will probably use the HPTDC (High Precision Time to Digital Converter) chip which forms the basis of the CAEN V1290A TDC VME board and is employed in the ALICE ToF detector readout system. In addition, the HPTDC chip is radiation hard and has been designed for use at the LHC, including a 40 MHz clock and appropriate buffering. We have begun testing CAEN 1290 VME boards that will be used in our next test-beam run. The Alberta group is, in parallel, designing a custom readout system, comprised of ACFD and HPTDC boards, that will interface with the ATLAS ROD readout system. We plan to test a vertical slice of the FP420 readout chain in the fall of 2008.

We are also exploring other TDC options for when the TDC performance becomes a limiting factor. The development of a sub-10 ps TDC now seems to be possible, and is somewhat simplified by the limited dynamic range of ≈ 500 ps required for our application. New ideas such as sampling the waveform to replace the CFD/TDC functionality are also being pursued [160].

The amplifier/CFD combination ideally would be located close to the detector to minimise time dispersion in the cables. We are exploring the possibility of locating this front-end electronics in a shielded compartment at the base of the cryostat support connected to the detector via SMA 18 GHz cable. The length of the cable run to the TDC is not critical, so a mini-VME crate can be located nearby in a shielded area. If the radiation hardness of the CFD comparator becomes an issue, we may use the Louvain amplifier solution near the detector with a longer cable run to the Louvain CFD, which would be located near the TDC. We will be testing these options and radiation effects in the 2008 test-beams. Low-voltage and high-voltage power supplies are standard units (described in Sec. 12) and will follow the same specifications as the silicon detector power supplies.

For the GASTOF detectors a single photon counter, such as Boston Electronics SPC-134, can be used to replace the amplifier, CFD and TDC. This device has a timing resolution of 5 ps r.m.s., but is extremely expensive ($10K per channel), making it impractical for use with the 32-channel QUARTIC detectors.

The distance from the interaction region does not allow the FP420 detectors to be part of the Level 1 trigger for normal operation, but the timing signals can be used to provide a Level 1 trigger under certain conditions.

10.7 Reference time system

A reference time signal without significant jitter between the (L) and (R) ToF detectors is an essential component of our ToF system and will be provided by the LHC Timing Trigger and Control

(TTC) system [167]. A block diagram depicting the various elements of this system is shown in Fig. 121. A signal is derived from the 400 MHz LHC RF, converted to an optical pulse which is split and sent along optical fibres as a mono-mode pulse to both (L) and (R) detector stations, for each bunch crossing. In addition, we will use optical fibres (also enclosed in protective tubes) for clock and orbit transmission. The pulse-to-pulse jitter between the arrival of these optical pulses is negligible. There can be differences between the two arms due to temperature differences, for example. Any differences can be controlled by splitting the optical signal at the detectors and returning it to the source, where they are converted to electrical pulses in a receiver and compared. At the detector stations the optical pulses are converted to electrical pulses that are recorded in the detector TDCs. Only jitter in this conversion affects the Δt measurement; any jitter in generation of the optical pulse cancels. An r.m.s. (L-R) jitter of 4 ps can be expected [167], which is a negligible contribution to our resolution. The two path lengths to the (L) and (R) detectors do not have to be precisely equal, as we will use collision data (events of type [pXp]) to calibrate both the $z_{pp} = 0$ point and the conversion (TDC count difference)$\leftrightarrow$(z_{pp}) scale.

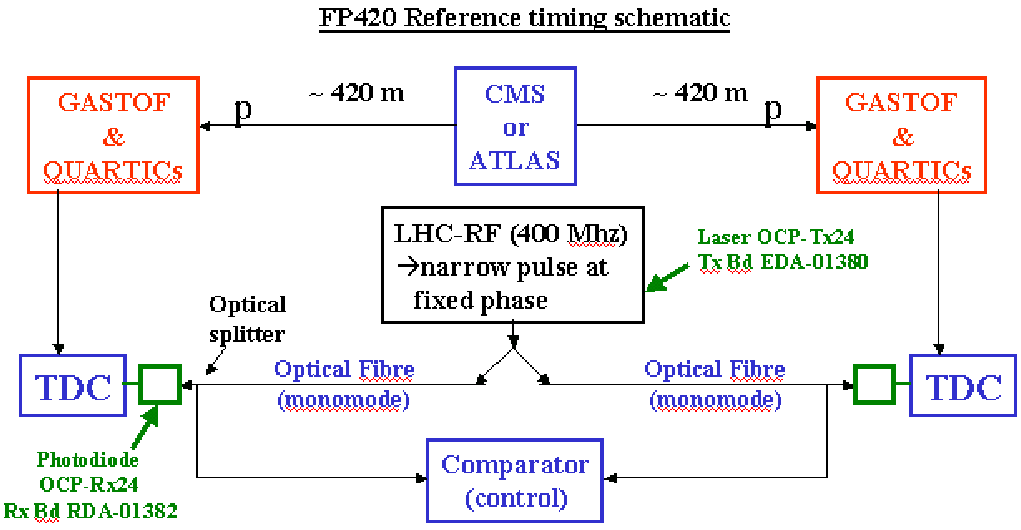

Fig. 121: A schematic of the reference time system.

10.8 Central detector timing

To this point, we have been focussing on relative timing of the forward protons to provide a vertex position measurement for comparison with the position of the central vertex. In Ref. [168] the space-time distribution of the luminosity profile for design beam parameters was calculated, and it was found that the position and time distributions of the vertex factorise. This implies that an absolute timing of the central detector portion of the event (two 60 GeV b-quark jets, for example) to much better than 170 ps would in principle provide a further overlap reduction factor for [p][X][p] events discussed earlier.

From test-beam results the ATLAS Electromagnetic Calorimeter (ECAL) was found to have a noise term of 500 ps/E(GeV) and a constant term of 70 ps. Reductions in the clock jitter could result in a smaller constant term during standard data taking. We have begun simulations to determine what central detector time resolution is possible for ATLAS and CMS. A 70 ps event resolution already would provide an additional factor of two in overlap rejection, and if it is eventually possible to reduce this to 10 ps this factor grows to 12.

10.9 Timing summary and future plans

We are in the process of developing an ultra-fast TOF detector system which will have a key role in the FP420 project by helping to reject overlap background that can fake our signal. Tests of the current prototype detector design imply an initial detector resolution of $\delta t \approx 20$ ps, including the full electronics chain, with an upgrade path to resolutions better than 10 ps matching the need for improved rejection as the luminosity increases. For a luminosity of $\mathcal{L} \approx 2\,10^{33}$ cm^{-2}s^{-1}, a 30 ps detector would be sufficient to keep the overlap background to the level of other backgrounds for the dijet channels, and render it negligible for other final states. For $\mathcal{L} \approx 5\,10^{33}$ cm^{-2}s^{-1}, a 10 ps detector (still with loose vertex cuts to maximise signal efficiency) would be desirable to keep overlap backgrounds totally under control, without any loss in signal efficiency. For $\mathcal{L} \approx 7\,10^{33}$ cm^{-2}s^{-1} to the design luminosity, we would control the background by (i) developing timing detectors in the 5 ps range, or (ii) adding extra rejection from central timing, or (iii) tightening the vertex window or other background cuts (a factor of several in rejection is possible with modest lost of efficiency), or more likely a combination of all of the above.

In addition to further analysis and beam tests to fully evaluate the current prototypes, we are continuing a program of simulation, development and testing of the detector concepts and electronics to provide a fully optimised robust timing solution. We are constructing new GASTOF prototypes with improved light collection efficiency using new 3 μm pore MCP-PMTs from Photek. We expect these detectors to have high efficiency and a resolution better than 10 ps. We are also developing a new Čerenkov concept using conical quartz radiators that promises to give an order of magnitude more prompt ($<$5 ps spread at the photocathode) photons than QUARTIC. Full simulations are being done and prototypes will also be beam-tested this year.

The radiation environment of the detectors remains a concern that has not been fully evaluated. Simulations are in progress to determine the radiation levels at the detector location and the composition of the radiation, especially with respect to soft particles that could cause background in the timing detectors. The issue of radiation hardness of certain electronics components is also a concern and different options are being explored depending on these levels as discussed above. Radiation exposure tests of the electronics are planned. The new ‘conical quartz’ concept allows the MCP-PMTs and electronics to be located far from the beam.

The detectors are small with relatively few channels and can be upgraded or replaced on a one-year time scale if significant technological improvements are made or if radiation damage is an issue. Since the intrinsic Čerenkov detector resolution is only a couple of picoseconds, eventual timing detector performance at the 2 ps level is conceivable with improvements in the electronics. The development of central detector timing also provides a path towards better background rejection and is being pursued in parallel.

Another upgrade desirable for high luminosity is the ability to measure multiple protons per bunch. Currently the GASTOF detector can only measure one proton per bunch (the first one), while the QUARTIC detector can measure two protons if they pass through different rows (about 2/3 of the time for 6 mm width bars). At design luminosity this will result in about a 10% efficiency loss. An upgrade to better determine the time of more than one proton per bunch is conceivable, either by making a segmented GASTOF detector, or by reducing the pixel size in the x-direction for the QUARTIC detectors. These are, in principle, straightforward upgrades, only requiring an increase in the number of electronics channels.

As the reference timing is also an important component of the timing resolution, we are also exploring other options for this, including interferometrically stabilised fibre optic links, where the standard is in the 10 femtosecond range.

In parallel with the development of GASTOFs and QUARTICs, we are studying the possibility of using fast streak cameras - sub-picosecond resolution photodetectors. We are also collaborating with other groups [169] who have long-term plans to develop large-area timing detectors with ps-level resolution.

11 Alignment and calibration

Precise measurement of the momentum loss of the outgoing protons will be achieved in FP420 by measuring the proton-beam displacement and relative direction (slope) as accurately as possible. To avoid significant degradation of the intrinsic uncertainty arising from physics processes and beam optics, FP420 must be aligned internally and relative to the beam to an accuracy of at most a few tens of microns.

In this section we discuss (1) internal alignment of the track detectors within the 420 m arm; (2) determination of the displacement of the detectors with respect to the passing beam, and their relative angle; (3) calculation of the proton momentum vector using the known LHC field elements (transfer matrices); (4) "on-line", real-time checks of the beam-track separation from data and (5) measurement of the M_X scale *and its resolution* from a known physics process, in particular exclusive $\mu^+\mu^-$ production.

11.1 Alignment requirements

"Internal alignment" is the issue of knowing the *relative* positions of all the tracking elements, with respect to a fiducial entrance point $[x_{in}, y_{in}, z_{in}]$ at 420 m and an exit point $[x_{out}, y_{out}, z_{out}]$ at about 428 m. The mechanical construction of the detector mountings on the moving pipe, and precision control of the motions (described below) will give us these relative positions to an accuracy $\sim$ 10μm. Any fine corrections can be obtained from the straight-track fits, as the high energy protons are not significantly affected by remnant magnetic fields. It remains to measure the entrance and exit points $x_{in}, y_{in}, x_{out}, y_{out}$ with respect to the beam (z_{in} and z_{out} do not need to be very precisely known).

For this we plan to build an independent real-time alignment system into the detector, for on-line knowledge of positions and also as it will be needed for safety while moving FP420 into its working position. Two options, both based on Beam Position Monitors (BPMs), are being considered: a 'local' system consisting of a large-aperture BPM mounted directly on the moving beampipe and related to the position of the silicon detectors by knowledge of the mechanical structure of the assembly, and an 'overall' system consisting of BPMs mounted on the (fixed) LHC beampipe at both ends of FP420, with their position and the moving silicon detectors' positions referenced to an alignment wire using a Wire Positioning Sensor (WPS) system. Figure 122 shows a schematic diagram of the proposed 'overall' alignment subsystem. To simplify the illustration only one moving beam pipe section is shown, although there may actually be more than one. Note that the larger aperture BPMs for the 'local' alignment system are not shown (one would be mounted on each moving beam pipe section), although it is likely that both the local and overall BPM alignment schemes will be implemented.

Sources of uncertainty in such a system include the intrinsic resolution of the WPS system, the intrinsic resolution (and calibration) of the BPMs, and the mechanical tolerances between the components. The mechanical uncertainties are expected to be affected by temperature fluctuations and vibrations in the LHC tunnel, and measurement is complicated by the fact that the detectors

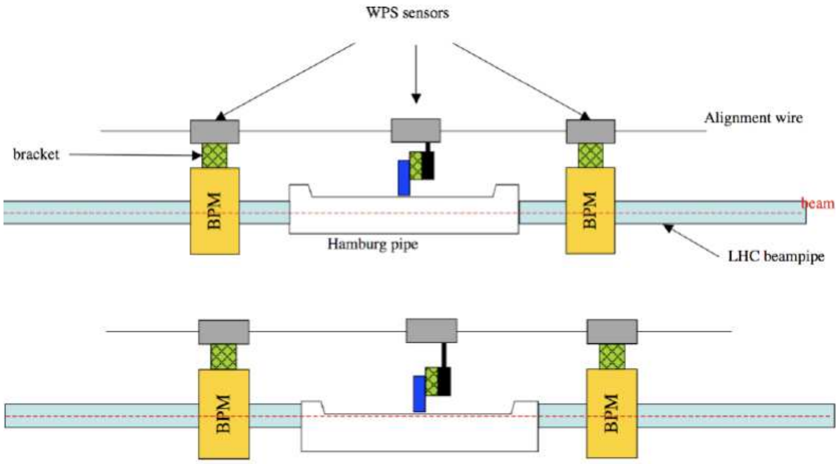

Fig. 122: The proposed overall alignment system, shown with detectors in garage position (top picture) and in operating position (bottom picture).

move with respect to the beam. The individual components of the system, with comments on their expected accuracy, are described in the following sections.

11.1.1 Beam Position Monitors (BPMs)

A direct measurement of the beam position at FP420 can be obtained with beam position monitors (BPMs). Although there are several pickup techniques available, an obvious choice would be the type used in large numbers in the LHC accelerator itself. The precision and accuracy of these electrostatic button pickups [170] can be optimised through the choice of electrode geometry and readout electronics (for a description of the LHC electronics, see [171].) While BPMs can be made with precision geometry, an important issue is balancing the gain of the right and left (or up and down) electronics; one can have a time-duplexed system such that the signals from opposing electrodes are sent through the same path on a time-shared basis, thus cancelling any gain differences. Multiplexing of the readout chain will avoid systematic errors due to different electrical parameters when using separate channels and detuning through time and temperature drift. Preliminary tests with electrostatic BPMs designed for the CLIC injection line have shown promising behavior on the test bench, even when read out with general purpose test equipment.

The LHC button-electrode pickups have been designed for best integration within the accelerator and its environment. Specially designed semi-rigid cables allow the front-end electronics to be moved to locations with lower radioactive exposure. However, less specific cables providing a sufficient bandwidth can be envisaged for FP420 since the BPM will be at room-temperature and therefore not subject to large temperature variations.

Although the requirements are not as demanding for the LHC as for FP420, it has been estimated that the necessary level of precision, resolution and acquisition speed can be obtained. It should be emphasised that the precision will depend to a large extent on the mechanical tolerances which can be achieved. Tests of these BPMs will begin soon on an alignment bench. Several strategies and optimizations have been proposed to reach precision and resolution of a few microns, and to achieve bunch-by-bunch measurement. The effect of the intrinsic non-linearity of button electrodes can be reduced if the particle beam passes close to the centre of the pickup in the operating position. In the case where only two electrodes are required the linearity of the signal could possibly be further improved by larger electrodes. While the detectors are in the parking position, away from the beam, the beam position measurement is also less critical.

Multi-turn integration will improve the resolution at least by a factor 10. This should still allow bunch/bunch measurements since the bunches in LHC can be tagged. In this case measurements of each bunch will be integrated over a number of turns. The variation of one specific bunch between turns is expected to be small. The estimated maximum orbit offset among bunches is 0.2σ and only subject to “slow” orbit drifts [172].

Wide band amplifiers could be envisaged to obtain single shot measurements, whereas narrow band amplifiers should allow a better resolution and signal-to-noise ratio.

Shortly before the installation of each complete 420 m section (with trackers and BPMs) a test-bench survey using a pulsed wire to simulate the LHC beam will provide an initial calibration of the BPMs. Further, in-situ calibration could be done by moving each BPM in turn and comparing its measured beam position with that expected from the measurements in the other BPMs in the system; the potential for success of such an online BPM calibration scheme has been demonstrated with cavity-style BPMs intended for use in linear colliders [173, 174]. Such calibration may even be possible at the beginning and end of data-taking runs when the BPMs are being moved between garage and operating positions, and therefore may not require dedicated calibration runs.

11.1.2 Wire Positioning Sensors (WPSs)

Wire Positioning Sensor systems use a capacitive measurement technique to measure the sensors’ positions, along two perpendicular axes, relative to a carbon-fibre alignment wire. Such systems have been shown to have sub-micron resolution capability in accelerator alignment applications [175] and will be used in LHC alignment. The principle of operation is shown in Fig. 123. Photographs of a sensor (with cover removed) and of two end-to-end sensors are shown in Fig. 124.

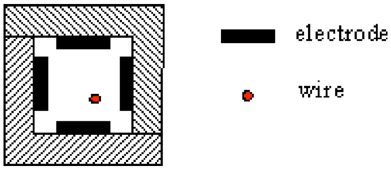

Fig. 123: A cross-sectional schematic of a WPS sensor and alignment wire.

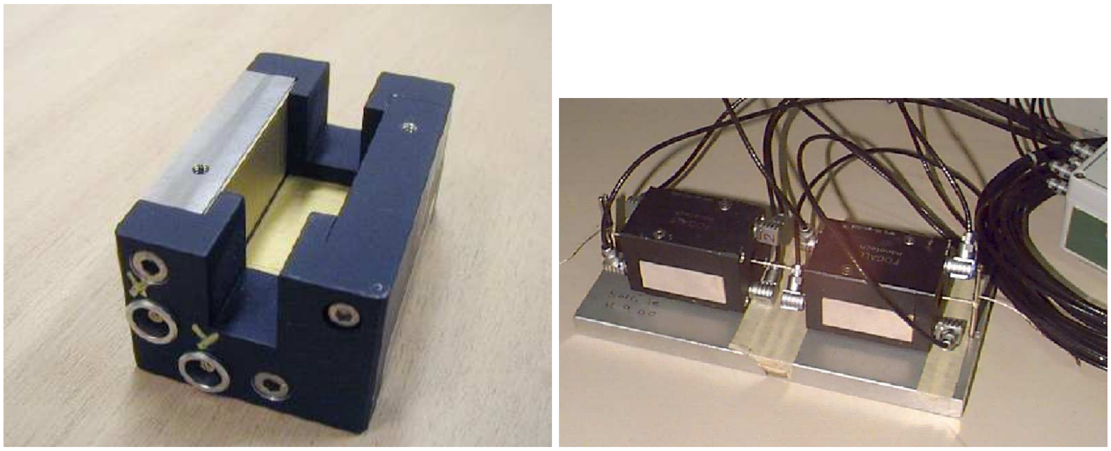

Fig. 124: A WPS sensor with lid removed (left), showing the electrodes. The aperture is 1cm square. Also shown are two WPS sensors on the test bench (right).

11.1.3 The moving detectors

FP420's silicon detectors will be mounted on moving beampipes. The detectors however must be referenced to the fixed WPS sensors. One way to achieve this is to use an LVDT or similar mechanical displacement-measurement device. However, "off-the-shelf" examples with long enough stroke length to accommodate the motion of the moving beampipe tend not to have sufficient accuracy, and they (particularly their readout electronics) are not generally guaranteed to be radiation-hard at the level needed by FP420. However Schaevitz® have made special LVDTs for aligning the LHC collimators [176]. These devices are by design sufficiently radiation-hard for our purposes, and although they are longer and less accurate than required for FP420, initial discussions with the company have resulted in the expectation that a similar device to meet FP420's needs can be manufactured; currently prototypes are being designed. In the event that this fails, there are potential fallback solutions, including a combination of a long stroke-length LVDT for the garage position with a shorter, more accurate device for the operating system; or an optical positioning (e.g. laser-based) system.

11.2 Beam and proton transfer calculations

There are several simulations of proton transport through the LHC machine elements. We have developed a fast simulator, HECTOR [60]. Each generated proton is represented by a phase space vector (x, x', y, y', E) at its point of origin. This vector is rotated in phase space by a product $M_{beamline}$ of matrices, each corresponding to a machine element (drifts, quadrupoles, dipoles, etc.). Aperture limitations are included. HECTOR has been validated by comparison with MAD-X [177] and found to be very accurate, providing the lateral positions of particles with inelastic protons with a precision at the few micron level. Figure 125 shows top and side views, in CMS and ATLAS (which are quite different due to the orthogonal crossing planes) of the beam protons. The bending of the dipoles has been switched off for display purposes, straightening the beam line after 250 m.

Figure 126 (top) shows the close correlation between scattered protons at x_1 ($z = 420$ m) and x_2 ($z = 428$ m). Numbers in parentheses are the energy loss (in GeV) and the production angle (in μrad). The bottom plot of θ_{x1} vs x_1 opens up the angular dependence and demonstrates that for good resolution it is not enough to measure the displacement of the proton from the beam; the angle is also crucial.

11.3 Machine alignment

Primarily because of the quadrupoles, the spectrometer performance is degraded by small misalignments of the LHC elements. We have studied these with HECTOR. One example in Figure 127 shows reconstructed 115 GeV/c^2 Higgs boson masses with no misalignment (central value 114.6 GeV/c^2 $\sigma(M)$ = 1.6 GeV/c^2), and with 500 μm misalignment of the MQXA1R5 quadrupole at 29 m [60]. The resolution is little changed but the central value shifts to 108.6 GeV/c^2. A partial correction can be applied using BPM information, and a full correction using exclusive dimuon calibration, see below. This assumes stability on a week- or month-time scale; it will be difficult to correct more frequent shifts in alignment, especially of the quadrupoles.

11.4 Mass scale and resolution measurement with physics processes

The study of exclusive Higgs boson production in FP420 demands not only good missing mass resolution, but also a means of calibrating the mass scale and measuring the mass resolution $\sigma(M)$. The width of a state can only be determined from an observed width by unfolding the resolution $\sigma(M)$. While a perfect knowledge of the machine, the central vertex and the FP420 tracking tells us this, in principle, a verification using data is very important. The production of *exclusive dileptons*, $p+p \rightarrow p+e^+e^-+p$ and $p+p \rightarrow p+\mu^+\mu^-+p$ is almost an ideal calibration reaction: a measurement of the central dilepton gives both forward proton momenta with very high precision. (One does not need to detect both protons.) The exclusive $\mu^+\mu^-$ will be easier to trigger on and will have less background. There are two contributing processes. Two photon production $\gamma\gamma \rightarrow \mu^+\mu^-$ is a purely QED reaction with a precisely known cross section, such that it has been proposed as a means of calibrating the LHC luminosity. The dimuon mass $M(\mu^+\mu^-)$ is a continuum; there are no significant resonances in the mass region considered here. While two-photon production of lepton pairs is well known at e^+e^- and ep colliders, it has only recently been observed (by CDF [178, 179]) at a hadron collider. The other important process is vector meson V photoproduction: $\gamma I\!\!P \rightarrow \Upsilon \rightarrow \mu^+\mu^-$ (muons from the $J/\psi, \psi'$ family have too low p_T). The Υ photoproduction cross section ($\times$ branching ratio) is larger in the mass region 9 – 11 GeV/c^2 than the two-photon continuum, so a trigger that includes this region is desirable, and achievable. In the FP420 detectors, protons with energy loss as low as 20 GeV, $\xi = 20/7000 = 0.0029$ are accepted. For a pair of exclusive muons each with transverse momentum p_T (in these processes the muons' p_T are ap-

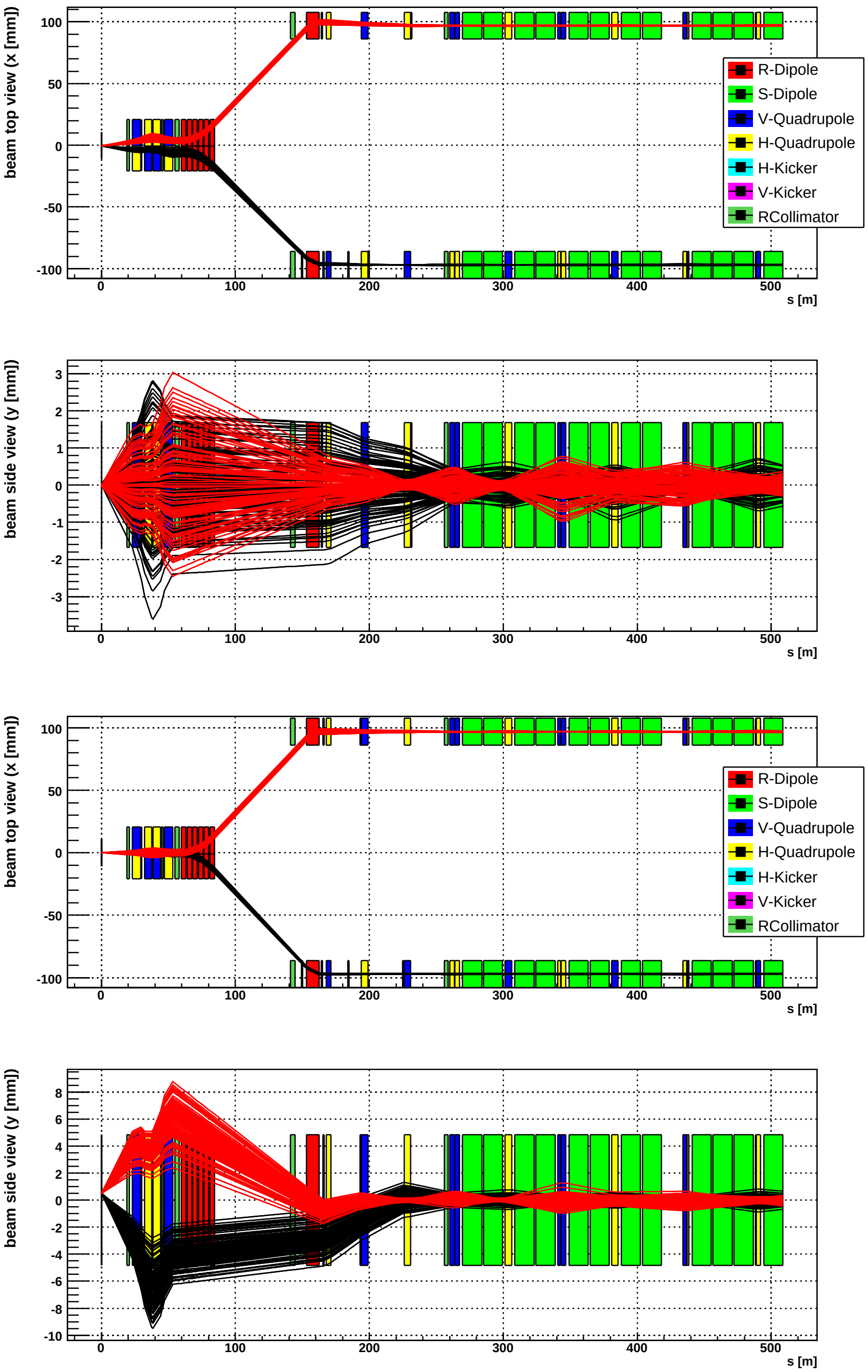

Fig. 125: Beam particle paths calculated by HECTOR [60], around CMS (top two figures) and ATLAS (bottom two figures). The beam line has been artificially straightened through the dipole region $z > 250$ m.

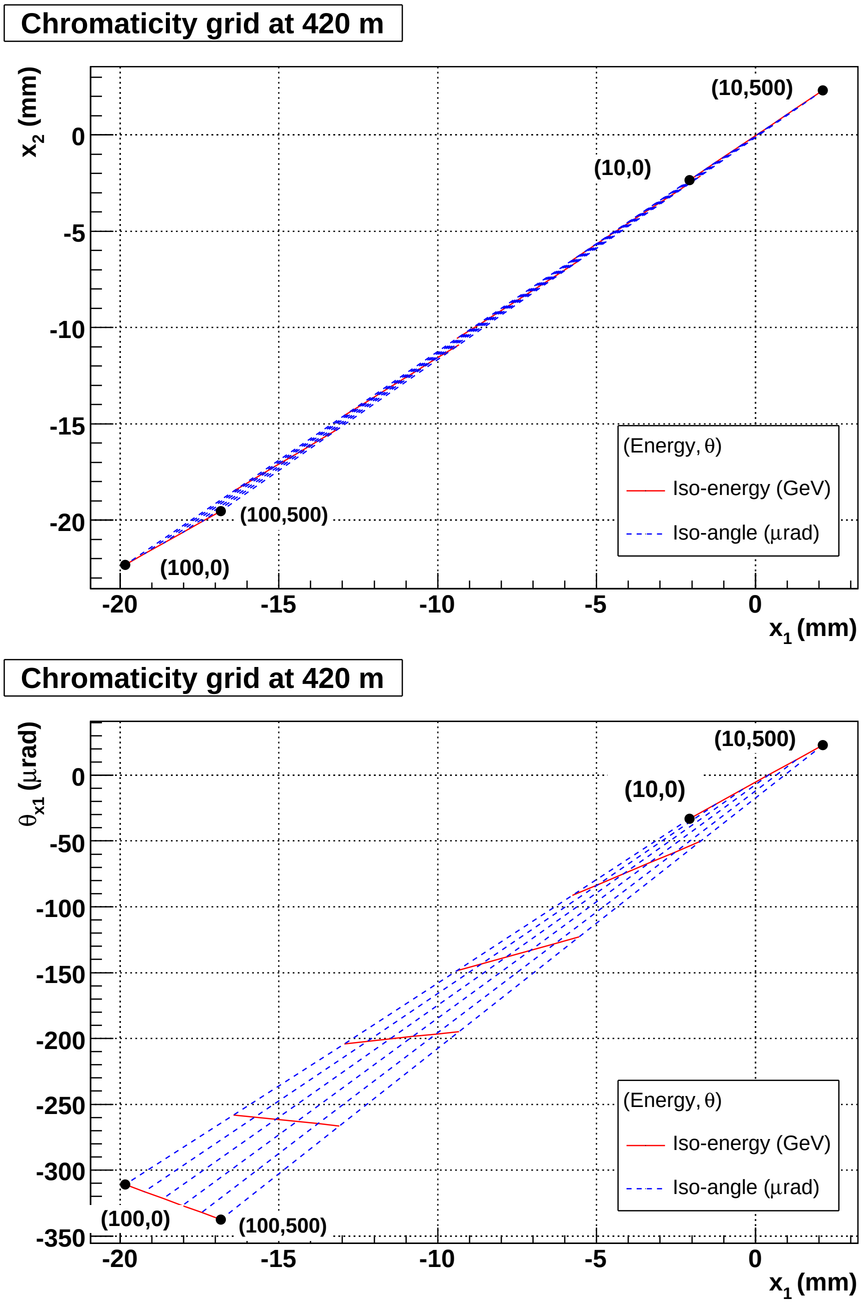

Fig. 126: Chromaticity grids: iso-energy loss and iso-production angle lines, from 10 GeV to 100 GeV and 0 to 500 μrad [60].

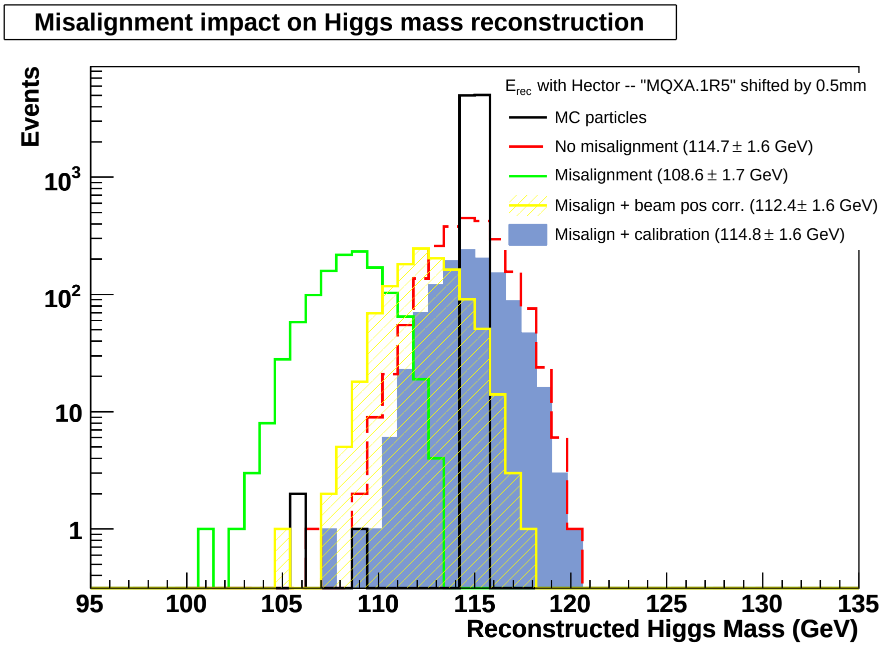

Fig. 127: Illustration of the effect on the missing mass reconstruction due to a misalignment of LHC quadrupoles. In this example a quadrupole (MQXA1R5) has been misaligned by 500 μm. Data from BPMs cannot fully recover the mass shift, while the exclusive dimuon calibration recovers it fully, and the resolution is not affected as long as the misalignment is stable [60].

proximately equal) and equal pseudorapidity η, we have $\xi_{1(2)} = \frac{2}{\sqrt{s}} p_T e^{+(-)\eta}$. So for $p_T = 4$ GeV/c and η = 2.0 (2.5), $\xi_1 = 0.0042(0.0070)$, inside the acceptance. The other proton is at much lower ξ. The exclusive events can be selected in the presence of pile-up, by requiring no other tracks on the dimuon vertex, and $\Delta\phi_{\mu\mu} \approx \pi$ with $p_T(\mu^+) \approx p_T(\mu^-)$, or $p_T(\mu^+\mu^-) \lesssim 1$ GeV/c, with a coincident consistent track in FP420. The dominant uncertainty of the forward proton momentum comes from the incoming beam spread, as the central dimuons are measured with a better resolution [7]. The two-photon cross section for central “large”-p_T muons is small; we expect about 300 events/fb^{-1} with $p_T(\mu) \geq 5$ GeV/c and $|\eta(\mu)| < 2.5$. If the threshold can be as low as 4 GeV/c, to include the Υ, the number of events is approximately doubled. With such good resolution on the predicted proton momentum, combinatorial background can be tolerated and a momentum scale calibration is achieved with very few (tens of) events, i.e. on a daily basis. However a good measurement of the resolution will require more events. A potentially important use of the dimuon events is not only to measure the spectrometer performance, but to optimise it, e.g. different tracking procedures can be tried and their resolution measured. While this reaction calibrates the missing mass scale in FP420, it cannot be used to check the angular reconstruction, or to calibrate detectors at 220 m as the exclusive $\mu^+\mu^-$ cross section is too small at such high ξ. A potentially important use of the dimuon events is not only to measure the spectrometer performance, but to optimise it. For example, different tracking procedures can be tried and their resolution measured. While the two-photon dimuon events calibrate the missing mass scale in FP420, it cannot be used for frequent re-calibrations of detectors at 220 m as the process cross section is much smaller at such high ξ. The upsilon photoproduction is important not only for improvement of calibration statistics but also for checking the resolution and bias of the muon p_T reconstruction in the central detectors. In addition, the Υ events can be used to check the forward proton angular reconstruction.

Other reactions and forward instrumentation can provide information that can be used to calibrate the forward detectors, not as well as exclusive muon pairs but in almost real time. One can make use for example of the Zero Degree Calorimeter, ZDC, installed at 140 m from both the ATLAS [102] and CMS [104] IPs. The bremsstrahlung process $p+p \rightarrow p+p+\gamma$ with the photons emitted into a very forward cone has a cross section of about 10 nb for $E_\gamma > 100$ GeV. The photon is detected in the ZDCs at 140 m, and the proton at 420 m. This allows a cross-calibration; the proton spectrometer is only calibrated as well as the ZDC. The background level (e.g. from forward π° production) remains to be seen. The angular distribution of bremsstrahlung photons is very forward peaked (typically with $\theta(\gamma) \lesssim 150\ \mu$rad) which helps with background reduction. The flow of neutral particles measured at the ZDC is huge and will allow the monitoring of the beam direction (tilt) at the IP with high precision. The LHC luminosity monitors (BRAN) [180] will also be capable of fast online tilt measurement (also bunch-by-bunch) with a resolution better than 10 μrad. This information together with the precise control of the lateral position of the proton collisions at the IP, provides very good and independent on-line monitoring of the actual proton-beam trajectory.

A measurement of the relative positions of the beam and the track detectors can also come from the distributions of single diffractive protons. The less critical vertical (y) distribution peaks at $y = y_{beam}$. (This allows a bunch-by-bunch monitor with time of y_{beam}.) Suppose the horizontal position to have a poorly known offset δx. Most of the tracks of protons from the intersection region will be from single diffraction, $p+p \rightarrow p+X$, which has an exponential t-distribution (at least in the low $|t|$-range), $\frac{d\sigma}{dt} \approx e^{bt}$. The intercept of the distribution at t=0 has a maximum when the beam-detector distance is correct, so by applying offsets offline one can find the actual distance. One can also vary the offset to find the maximum slope $\frac{d\sigma}{dt}$. This has been successfully applied in CDF [181, 182]; the accuracy on the offset was (at the Tevatron) approximately $\pm 30\mu$m in x and y.

Note that protons with $t = 0$ (more strictly $\theta = 0$) are inside our acceptance; this is where the diffractive cross section has a maximum. An improvement on the method could come from a measurement of the diffractive mass from the central detector, which would allow this technique to be used selecting bands of ξ; however that can not be done in the presence of pile-up[13].

---

[13] One or two bunch crossings with deliberately low luminosity, such that $< n > \approx 1$, could be useful for this and many other reasons.

11.5 Alignment summary

While alignment and calibration issues are crucially important for FP420 tracking, we have viable solutions to all the issues: within the FP420 arm, over its motion towards the beam, with respect to the passing beam, and through the 420 m spectrometer. We have on-line checks of the proton energy using bremsstrahlung and displacement from the beam using diffractively scattered protons. Finally, and very important, we will use the $p+p \to p+\mu^+\mu^- + p$ reaction to calibrate, offline, both the mass scale and its resolution, and to optimise the latter. We hope to continue to push the mass resolution towards the limit given by the incoming beam momentum spread. It is important to miminise instabilities (bunch-to-bunch, store-to-store, week-to-week etc.) of LHC elements (especially quadrupole alignments), and to monitor any residual instabilities to allow for off-line corrections to be applied.

12 Near detector infrastructure and detector services

The tunnel region at the location of the FP420 detectors presents a number of constraints for the installation of instrumentation such as FEE, HV and LV power supplies, cooling and detector gas supplies. A plan view of the tunnel area around FP420, showing the available space for services and electronics, is shown in figure 128.

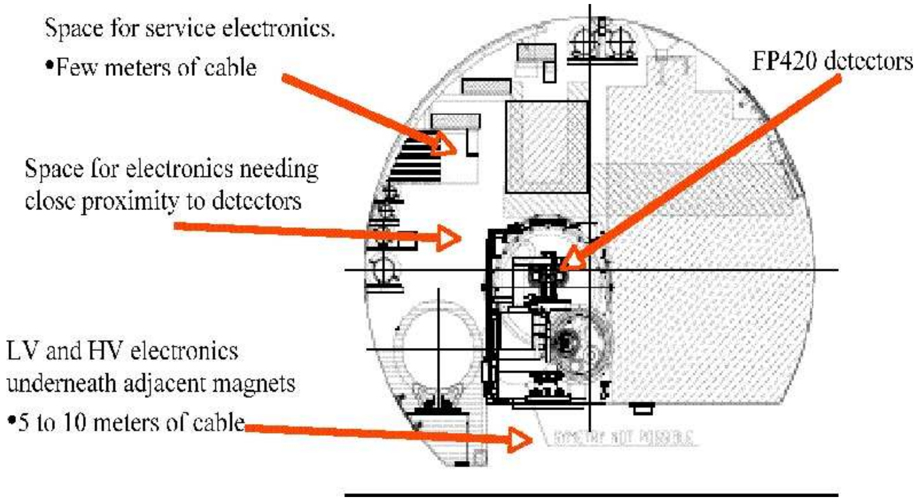

Fig. 128: Plan view of the tunnel area around FP420 and the available space for equipment and services, as detailed in table 20.

Simulations have shown [152] that the zone will be exposed to a reasonably high radiation dose. A careful assessment of the possible locations and type of instrumentation is therefore required. Provisionally space has already been reserved underneath adjacent magnets upstream and downstream from the NCC where the LV and HV supplies can be placed [*yy* = L0762023PL, L0762024PL, L0762045PL, L0762046PL, L0722023PL, L0722024PL, L0722045PL, L0722046PL]. Most of the machine electronics is already placed in this volume and such reducing the available space. The dose in this position under the arc magnets is expected to be between 10 and 20 Gy/year. FEE like trigger electronics, alignment and detector positioning control can be installed in cavities of the support beams of the NCC. In order to limit the radiation load on the environment at most to the level estimated with the present configuration, an envelop of adequate shielding (Pb plates) will be placed around the beam pipes and detectors as described in section 6. It will also be feasible to place some equipment along the LHC tunnel wall underneath the cable trays which run above the QRL line but the radiation level will be somewhat higher than under the dipole magnets.

Currently, active radiation monitoring instrumentation is being installed in the 420m region of the LHC tunnel. These monitors will be operational at LHC startup and thus provide valuable data to assess the real radiation levels in the area. At present no general services are provided in the LHC tunnel at the FP420 region. Power- and controls- cables as well as tubes for fibre-optic (FO) will therefore need to be pulled from the corresponding experimental area to this location. It is therefore proposed to install additional cable trays next to the overhead rail of the monorail. This strategy has already been used for the routing of the services for LHCf to both sides of point 1. FP420 can reuse these trays which will have to be extended from the present 150m to 420m. The FP420 power supplies and detector controls instrumentation could be connected to the LHC machine power. This would assure the electricity supply as long as the LHC machine power is available and reduce the cabling impact in the tunnel since additional power cables would only need to be routed from the nearest RR alcoves at a distance of about 200m. Space has also been reserved in the RR13, RR17, RR53, RR57 alcoves on the 2nd floor level above the LHC power converters (Figure 129). At this location the expected annual fluence of hadrons ($E > 20$ MeV) is in the order of 10^8, corresponding to a dose rate in the order of 0.3 Gy per annum, and considered suitable for installation of detector power supplies and electronics for the alignment monitoring system.

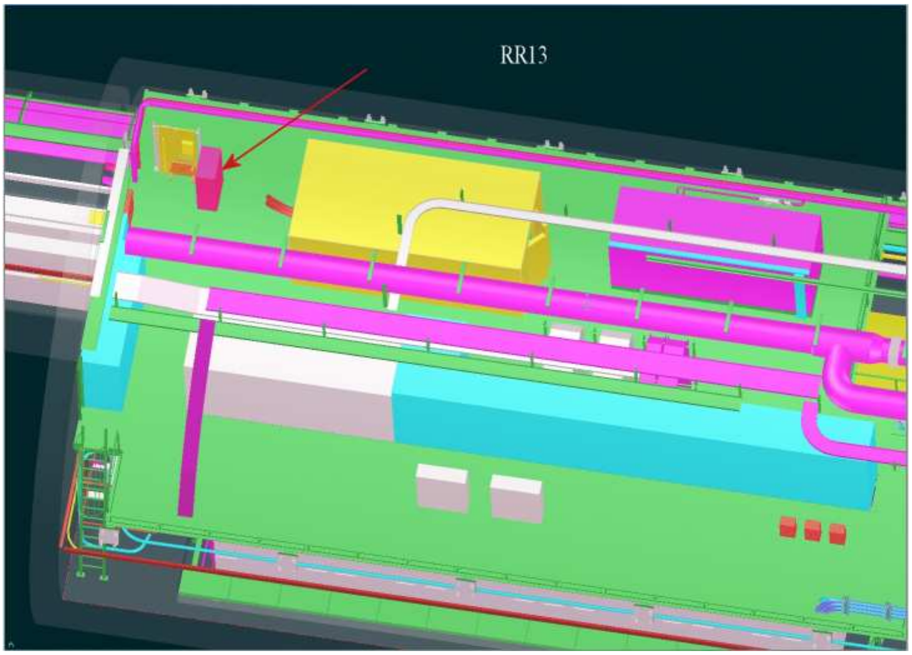

Fig. 129: Reserved rack space in the LHC alcove areas (RRs).

The assessment of types and quantities of services needed for the FP420 detectors is still rather difficult at this stage of the project. Those requirements which correspond to the present estimation for each sub-system are summarised in Table 20.

Sub-system	Requirements	Location	Comment
GasTOF	gas FEE, DAQ elec. power	Detector station Cryostat support beams see Fig. 94	Secondary vacuum
Quartic	FEE, DAQ elec. power	Cryostat support beams see Fig. 94	
3D (Silicon)	Cooling FEE, DAQ elec. power	Detector station Cryostat support beams see Fig. 94	
General Cooling	power, control		
Alignment	BPM, BLM, WPS, other	Detector station, Detector support table RRs	
Positioning	Movement drive, control	Detector support table see Fig. 94	
Timing	TTC, BST	Counting rooms	
Interlocks	Injection, Dump	Machine IF rack in exp. counting room	
Electrical power	400 V AC 230 V AC 48 V DC	RE alcoves	UPS for controlled shutdown ?
HV	16 ch. HV 4kV (timing) 36 ch. HV (tracking)	see Fig. 94	Control from IP (CAN bus ?)
LV	6 ch. LV (timing) 36 ch. LV (tracking)	see Fig. 94	Control from IP (CAN bus ?)
Communication, RH-diodes:	FO, Field bus RH-diodes: MITSUBISHI FU-427SLD-F1	ECR ←→ FP420	Space available for $\geq 2 \times 24$ fibres to each station Use BLM / BPM FEE ?
Miscellaneous	Cameras, lights	FP420	
Instrumentation space	VME crate equivalent each (5);	Cell 12L/R at IP1 & IP5 each (5); 13.8m tunnel wall; Call 11 L/R (5)	

Table 20: Summary of detector services required for FP420. Abbreviations: BPM - Beam Position Monitors, BLM - Beam Loss Monitors, FEE - Front End Electronics, FO - Fibre optics, WPS - Wire Positioning System.

13 Conclusions

The FP420 project proposes to install silicon tracker and fast timing detectors in the LHC tunnel at 420 m from the interaction points of the ATLAS and CMS experiments for the detection of very forward protons as a means to study Standard Model (SM) and New Physics signals. The FP420 detector system is a magnetic spectrometer consisting of a moveable silicon tracking system which measures the spatial position of protons scattered by a few hundreds μrads relative to the LHC beam line and their arrival times at several points in a 12 m region around 420 m. The measurement of the displacement and angle of the outgoing protons relative to the beam allows the reconstruction of their momentum loss and transverse momentum. The combined detection of both outgoing protons and the associated centrally produced system using the current ATLAS and/or CMS detectors gives access to a rich programme of studies in QCD, electroweak, Higgs and Beyond the Standard Model physics. The addition of such detectors will add the capability to make measurements which are currently unique at the LHC, and difficult even at a future linear collider.

A prime process of interest for FP420 is Central Exclusive Production (CEP), $pp \rightarrow p+\phi+p$, in which the outgoing protons remain intact and the central system ϕ may be a single particle such as a Higgs boson. Observation of new particle production in the CEP channel benefits from (i) enhanced signal over backgrounds (giving access to the difficult Higgs fermionic decay channels for example), and allows one to directly measure (ii) its quantum numbers (the central system has an approximate $J^{PC} = 0^{++}$ selection rule) as well as (iii) its mass with very good resolution, $\mathcal{O}$(2 GeV/c^2) irrespective of the decay channel of the particle. In some beyond-SM scenarios, the FP420 detectors may be the primary means of discovering new particles at the LHC. Section 2 of this document has presented an overview of the physics case for FP420 including the current theoretical status of CEP predictions. The state-of-the-art calculations of the production cross section for a 120 GeV/c^2 Standard Model Higgs boson via the CEP process at the LHC yields a central value of 3 fb, with a factor of 4 uncertainty. Supersymmetric extensions of the SM, yield Higgs boson cross sections 10 or 100 times larger and would allow the 5σ discovery of all CP-even scalar bosons in practically the whole $M_A - \tan\beta$ plane with $\mathcal{O}$(100 fb^{-1}). Section 3 has presented a detailed study of the trigger strategy, expected acceptance, reconstruction efficiencies, signal over backgrounds and final mass resolutions and yields for a particular $pp \rightarrow pHp$ measurement with Higgs boson decay in the $b\bar{b}$ mode. The Higgs boson line shape in this channel can be reconstructed with a 3σ or better significance with an integrated luminosity of 60 fb^{-1}.

A summary of various interesting photon-photon and photon-proton processes accessible to FP420 is presented (Section 2.8). Photon-induced reactions tagged with forward protons can provide a very clean environment for the study of various signals such as anomalous top or associated WH production in γp interactions; as well as anomalous gauge boson couplings, exclusive dileptons or supersymmetric pair production in $\gamma\gamma$ interactions. Hard diffraction studies (single-diffractive and double-Pomeron production of B-mesons, W, Z bosons or di-jets), sensitive to generalised parton distributions, are discussed in Section 2.9.

The beam optics at LHC (Section 4) allows protons that have lost momentum in a diffractive interaction to emerge from the beam envelope at regions 220 m and 420 m from the interaction point. The acceptance of silicon detector arrays in these locations placed at distances 3 – 9 mm from the beam centre allows for the detection of both outgoing protons from centrally produced objects with a wide range of masses above 60 GeV/c^2. However, to obtain good acceptance for masses above 150 GeV/c^2, the 220 m system is essential. The expected position and angle resolutions for the protons obtained in the silicon stations yield a mass resolution reaching values of 2 to 3 GeV/c^2.

The expected machine-induced backgrounds at 420 m such as beam-halo and beam-gas backgrounds are discussed in Section 5. Contributions at 420 m from *near* beam-gas and the betatron cleaning collimation are found to be small. For transverse separations between the detectors and the beam centre above 5 mm, the integrated number of protons, photons and neutrons from beam halo is expected to be less than 1, 0.16 and 0.003 per bunch crossing respectively. The impact of these estimated background rates needs to be assessed in term of detector performance and survivability.

Section 6 describes the new 420 m connection cryostat which will allow moving near-beam detectors with no effects on LHC operations. A preliminary design for a replacement connection cryostat that would allow detectors to be placed in the 420 m region has been completed, and a final design is in progress. Such a solution is expected to actually lower the dynamic heat load of the LHC and have similar radiation profiles. With the appropriate approvals and funding, two such cryostats could be built and installed in late 2009 (installation time is around 90 days), and in principle, two more in 2010 with negligible impact on LHC operations.

The design of the beam pipe in the FP420 region and the movement mechanism are discussed in Section 7. The Hamburg moving-pipe concept provides the optimal solution for the FP420 detector system as it ensures a simple and robust design and good access to the detectors. Moreover, it is compatible with the very limited space available in the modified connection cryostat and with the expected position of the scattered protons between the two LHC beampipes, and it permits the incorporation of rather large detectors, such as the timing devices, using pockets, i.e. rectangular indentations in the moving pipes. The prototype detector pockets show the desired flatness of the thin windows, and the first motorised moving section, with prototype detectors inserted, has been tested at the CERN test beam. A full prototype test, including assembling, positioning and alignment aspects, is planned in test beam in Fall 2008.

The studies of the radio-frequency impact of the design on the LHC are described in Section 8. Numerical simulations, analytical calculations and laboratory measurements have showed consistently that the proposed FP420 design will have a small impact on the total LHC impedance budget, even for transverse distances of the stations from the beam centre as small as 3 mm. Tapering of the beam pipe indentations is recommended because it reduces the impedance significantly, as measured both with the single pocket and double pocket designs. The beam harmonics at 2 GHz are expected to be below 10^{-2} of the main harmonic at 40 MHz and well below 10^{-3} at 2.5 GHz, and the horizontal tune shift induced by a FP420 station is expected to be almost imperceptible when compared to the tune stability region defined by the available LHC octupoles magnets.

In Section 9 we present a detailed description of the design of the FP420 3D silicon sensors including mechanical support system, superlayer and blade design and thermal tests, assembly and alignment, high- and low- voltages, tracker readout, downstream data acquisition and infrastructure at the host experiment. The performance of the tracker has been evaluated using a simple Monte Carlo program as well as a full GEANT4 simulation. Estimates of the multiple scattering for the three (two) station layouts indicate that the expected angular resolution is 0.85 μrad (0.91 μrad), well within design specifications. The efficiency of two track reconstruction has been found to be 86% and 80% respectively for the two and three station layouts.

Since the cross sections for CEP of the SM Higgs boson and other new physics scenarios are relatively small (few fb), FP420 must therefore be designed to operate at the highest LHC instantaneous luminosities of $10^{34}\mathrm{cm}^{-2}\mathrm{s}^{-1}$. A measurement of the relative time of arrival of the protons at FP420 in the 10 picosecond range is required for matching of the detected protons with a central vertex within $\sim$2 mm, which will enable the rejection of a large fraction of the pile-up overlap background. Section 10 describes two complementary fast timing detector designs: GASTOF (GAS Time Of Flight) and QUARTIC (QUARtz TIming Čerenkov). The *prototype* detector design is approaching a resolution of 20 ps. An upgrade to determine the time of more than one proton per bunch is conceivable, either by reading out individual pixels in the GASTOF MCP-PMT to resolve separate, but overlapping, Čerenkov discs, or by reducing the pixel size in the x-direction for the QUARTIC detectors. We are also developing a promising new type of focusing quartz Čerenkov detector. As the reference timing is also an important component of the timing resolution, we are also exploring interferometrically stabilised fibre optic links, where the standard is in the 10 femtosecond range.

In Section 11 we describe the alignment and calibration strategy, using both physics and beam position monitor techniques. Alignment and calibration is guaranteed for all experimental conditions: within the FP420 arm, over its motion towards the beam, with respect to the passing beam, and through the 420 m spectrometer. We have on-line checks of the proton energy using bremsstrahlung and of displacement from the beam using diffractively scattered protons. We will use the $p+p \to p+\mu^+\mu^- + p$ reaction to calibrate, offline, both the mass scale and its resolution, and to optimise the latter. It is important to miminise instabilities (bunch-to-bunch, store-to-store, week-to-week etc.) of LHC elements (especially quadrupole alignments), and to monitor any residual instabilities to allow for off-line corrections to be applied. Chapter 12 outlines the near detector infrastructure and detector services required for the FP420 project.

The studies presented in this document have shown that it is possible to install detectors in the 420 m region with no impact on the operation or luminosity of the LHC. These detectors can be aligned and calibrated to the accuracy required to measure the mass of the centrally produced system to between 2 and 3 GeV/c^2. This would allow an observation of new particles in the $60-180$ GeV/c^2 mass range in certain physics scenarios during 3 years of LHC running at instantaneous luminosities of 2×10^{33} cm^{-2} s^{-1}, and in many more scenarios at instantaneous luminosities of up to 10^{34} cm^{-2} s^{-1}. Events can be triggered using the central detectors alone at Level 1, using information from the 420 m detectors at higher trigger levels to reduce the event rate. Observation of new particle production in the CEP channel would allow a direct measurement of the quantum numbers of the particle and an accurate determination of the mass, irrespective of the decay channel of the particle. In some scenarios, these detectors may be the primary means of discovering new particles at the LHC, with unique ability to measure their quantum numbers. The FP420 opens, moreover, the possibility to develop an extensive, high-rate $\gamma\gamma$ and γp physics program. The addition of the FP420 detectors will thus, for a relatively small cost, significantly enhance the discovery and physics potential of the ATLAS and CMS experiments.

14 Costing

A preliminary estimate of the costing of the major components of FP420 detectors is given here as an indication. A detailed costing evaluation is still being performed.

- Two new cryostats per experiment, amounting to a total of 1.5 MCHF/experiment
- The silicon tracker including the electronics and mechanical parts: 0.7 to 1.0 MCHF/ experiment, depending on the purchasing of equipment
- Quartic timing detectors, including electronics, 100 kCHF/experiment for 4 detectors.
- GASTOF timing detectors, including electronics, DAQ, slow controls and cables: 145 kCHF
- BPMs and beampipe mechanics: 380 kCHF/experiment
- High voltage/Low Voltage: 160 kCHF/experiment

This leads to a approximate grand total of 3.5 MCHF/experiment for equipping both sides with FP420 detectors.

Acknowledgments

We thank many people in the accelerator (AB and AT) and technical (TS) Departments of CERN for their valuable help and continuing support in the FP420 design study (beam vacuum, electrical specifications, RF effects ...). In particular, we want to thank Thierry Renaglia, Sebastien Marques, Thierry Colombet, Alain Poncet and Vittorio Parma for their expertise and generous help with the cryostat studies. This work was supported in the UK by grants from the STFC and the Royal Society; in the USA by the Department of Energy (including Fermilab and Brookhaven National Lab funding, UT-Arlington base funding and the Advanced Detector Research program), and the Texas Advanced Research Program; in Belgium by FNRS and its associated fund (IISN), by FWO-Vlaanderen, IIKW, and by the Inter-University Attraction Poles Programme subsidised by the Belgian Federal Science Policy; in Italy by the Italian Istituto Nazionale di Fisica Nucleare (INFN) and by the Italian Ministry for Education, University and Scientific Research under the programme “Incentivazione alla mobilità di studiosi stranieri e italiani residenti all’estero".

References

[1] M. G. Albrow and A. Rostovtsev, hep-ph/0009336.

[2] V. A. Khoze, A.D. Martin and M.G. Ryskin, Eur. Phys. J. **C23** (2002) 311.

[3] B. E. Cox, AIP Conf. Proc. **753** (2005) 103.

[4] A. B. Kaidalov *et al.*, in the Proceeds Gribov-75 Memorial Workshop, Budapest, 2005, arXiv:hep-ph/0507040.

[5] J. R. Forshaw, contributed to “HERA and the LHC: A Workshop on the Implications of HERA and LHC Physics”, arXiv:hep-ph/0508274.

[6] K. Piotrzkowski, Phys. Rev. **D63** (2001) 071502.

[7] M. Albrow *et al.* [FP-420], CERN-LHCC-2005-025, LHCC-I-015.

[8] M. Albrow *et al.* [CMS and TOTEM Collaborations], “Prospects for diffractive and forward physics at the LHC”, CERN-LHCC-2006-039.

[9] S. Ask, Proceeds. DIS’07 arXiv:0706.0644 [hep-ex].

[10] C. Royon [RP220 Collaboration], arXiv:0706.1796 [physics.ins-det].

[11] P. J. Bussey, T. D. Coughlin, J. R. Forshaw and A. D. Pilkington, JHEP **0611** (2006) 027.

[12] J. Favereau de Jeneret, V. Lemaître, Y. Liu, S. Ovyn, T. Pierzchala, K. Piotrzkowski, X. Rouby, N. Schul, and M. Vander Donckt, CP3-08-04 (June 2008), to be submitted to Eur. Phys. J. C.

[13] V. A. Khoze, A.D. Martin and M.G. Ryskin, Eur. Phys. J. **C19** (2001) 477, erratum **C20** (2001) 599.

[14] A. De Roeck, V. A. Khoze, A.D. Martin, R. Orava and M.G. Ryskin, Eur. Phys. J. **C25** (2002) 391.

[15] A.B. Kaidalov, V.A. Khoze, A.D. Martin and M.G. Ryskin, Eur. Phys. J. C **33** (2004) 261.

[16] B. Cox *et al.*, Eur. Phys. J. **C 45** (2006) 401.

[17] V. A. Khoze, M. G. Ryskin and W. J. Stirling, Eur. Phys. J. C **48** (2006) 477.

[18] V. A. Khoze, A.D. Martin and M.G. Ryskin, Phys. Lett. B **650** (2007) 41.

[19] S. Heinemeyer, V. A. Khoze, M. G. Ryskin, W. J. Stirling, M. Tasevsky and G. Weiglein, Eur. Phys. J. C **53** (2008) 231.

[20] B. E. Cox, F. K. Loebinger and A. D. Pilkington, JHEP **0710** (2007) 090.

[21] V. A. Khoze, A.D. Martin and M.G. Ryskin, Eur. Phys. J. **C24** (2002) 459.

[22] M. G. Ryskin, A. D. Martin and V. A. Khoze, arXiv:0710.2494 [hep-ph].

[23] V. A. Khoze, A.D. Martin and M.G. Ryskin, Eur. Phys. J. **C18** (2000) 167.

[24] E. Gotsman, E. Levin and U. Maor, arXiv:0708.1506 [hep-ph].

[25] G. Weiglein, arXiv:0709.4408 [hep-ph].

[26] J.R. Ellis, J.S. Lee and A. Pilaftsis, Phys. Rev. **D71** (2005) 075007.

[27] J. R. Forshaw, J. F. Gunion, L. Hodgkinson, A. Papaefstathiou and A. D. Pilkington, arXiv:0712.3510 [hep-ph].

[28] V. A. Khoze, A. D. Martin and M. G. Ryskin, Eur. Phys. J. C **34** (2004) 327.
[29] V. A. Khoze, A.D. Martin and M.G. Ryskin, Eur. Phys. J. **C14** (2000) 525.
[30] V. A. Khoze, A. D. Martin and M. G. Ryskin, Eur. Phys. J. C **24** (2002) 581.
[31] X. D. Ji, Phys. Rev. D **55** (1997) 7114.
[32] A. V. Radyushkin, Phys. Lett. B **385** (1996) 333.
[33] J. D. Bjorken, Phys. Rev. D **47** (1993) 101.
[34] S. Alekhin *et al.*, in p. 221, "HERA and the LHC - A workshop on the implications of HERA for LHC physics: Proceeds. Part A", arXiv:hep-ph/0601012.
[35] L. Frankfurt, C. E. Hyde-Wright, M. Strikman and C. Weiss, Phys. Rev. D **75** (2007) 054009.
[36] V. A. Khoze, A. D. Martin and M. G. Ryskin, arXiv:0802.0177 [hep-ph].
[37] T. Aaltonen *et al.* [CDF Run II Collaboration], Phys. Rev. D **77** (2008) 052004.
[38] T. Aaltonen *et al.* [CDF Collaboration], Phys. Rev. Lett. **99** (2007) 242002.
[39] A. Vilela Pereira, FP420 Note 2008-002.
[40] M. Carena, S. Heinemeyer, C. Wagner and G. Weiglein, Eur. Phys. J. **C 26** (2003) 601.
[41] [LEP Higgs working group], Phys. Lett. **B 565** (2003) 61.
[42] [LEP Higgs working group], Eur. Phys. J. **C 47** (2006) 547.
[43] J. R. Ellis, J. F. Gunion, H. E. Haber, L. Roszkowski and F. Zwirner, Phys. Rev. D **39** (1989) 844.
[44] R. Dermisek, J.F. Gunion. Phys. Rev. Lett. **95** (2005) 041801.
[45] U. Ellwanger, J.F. Gunion, C. Hugonie, arXiv:hep-ph/0503203.
[46] K. Belotsky, V. A. Khoze, A. D. Martin and M. G. Ryskin, Eur. Phys. J. C **36** (2004) 503.
[47] A. Abulencia *et al.* [CDF Collaboration], Phys. Rev. Lett. **98** (2007) 112001.
[48] A. Abulencia *et al.* [CDF Collaboration], in preparation.
[49] D. d'Enterria [PHENIX Collaboration], Proceeds. QM'05, Budapest, arXiv:nucl-ex/0601001.
[50] V.M. Budnev, I.F. Ginzburg, G.V. Meledin and V.G. Serbo, Phys. Rept. **15** (1974) 181.
[51] A. Baltz *et al.*, Physics Reports **458** (2008) 1
[52] F. Maltoni and T. Stelzer, JHEP **0302** (2003) 027; T. Stelzer and W.F. Long, Phys. Commun. **81** (1994) 357.
[53] A. Pukhov, Nucl. Inst. Meth. A **502** (2003) 596.
[54] S.P. Baranov *et al.*, in Proceeds. "Physics at HERA Workshop" (1991) 1478.
[55] T. Sjöstrand *et al.*, Comput. Phys. Commun. **135** (2001) 238.
[56] J. Ohnemus, T.F. Walsh and P.M. Zerwas, Phys. Lett. B **328** (1994) 369-373.
[57] J. F. Gunion and H. E. Haber, Phys. Rev. D **48** (1993) 5109.
[58] V.M. Budnev, I.F. Ginzburg, G.V. Meledin, V.G. Serbo, Nucl. Phys B **63** (1973) 519; A.G. Shamov, V.I. Telnov, Nucl. Instrum. Meth. A **494** (2002) 51; D. Bocian, K. Piotrzkowski, Acta Phys. Polon. B **35** (2004) 2417; M. W. Krasny, Nucl.Instr. and Meth. A **584** (2008) 42;

J. A. M. Vermaseren, Nucl. Phys. B **229** (1983) 347.

[59] V. A. Khoze, A. D. Martin, R. Orava and M. G. Ryskin, Eur. Phys. J. C **19** (2001) 313.

[60] J. Favereau de Jeneret, X. Rouby, K. Piotrzkowski, JINST **2** (2007) P09005; arXiv:0707.1198.

[61] G. Bélanger and F. Boudjema, Phys. Lett. B288 (1992) 201.

[62] G. Abbiendi *et al.* [OPAL Collaboration], Phys. Rev. D **70** (2004) 032005.

[63] O. Kepka and C. Royon, Proceeds. "Photon Workshop at the LHC 2008", to be submitted to Nuc. Phys. B Proc. Suppl.

[64] G. Bhattacharya *et al.*, Phys. Rev. D **53** (1996) 2371.

[65] M. Drees *et al.*, Phys. Rev. D **50** (1994) 2335.

[66] K. Piotrzkowski, hep-ph/9310223.

[67] J. Abdallah *et al.* [DELPHI Collaboration], Eur. Phys. J. C **31** (2004) 421.

[68] G. Abbiendi *et al.* [OPAL Collaboration], Eur. Phys. J. C **32** (2004) 453.

[69] M. Battaglia *et al.*, Eur. Phys. J. C **33** (2004) 273.

[70] K. Cheung, Phys. Lett. B **319** (1993) 244.

[71] T. Han and J.L. Hewett, Phys. Rev. D **60** (1999) 074015.

[72] S. Chekanov *et al.*, Phys. Lett. B **559** (2003) 153.

[73] J. Hollar, S. Ovyn, X. Rouby, CMS AN-2007/032.

[74] Y.Y Balitski and L.N. Lipatov, *Sov. J. Nucl. Phys.*, **28** (1978) 822; V.S. Fadin, E.A. Kuraev and L.N. Lipatov, *Sov. Phys. JETP* **44** (1976) 443.

[75] A. Brandt *et al.* [UA8 Collaboration], Phys. Lett. B **297** (1992) 417.

[76] V. Barone and E. Predazzi, *High-energy particle diffraction*, Springer, 2002.

[77] S. Alekhin *et al.*, "HERA and the LHC - A workshop on the implications of HERA for LHC physics: Proceeds. Part B", arXiv:hep-ph/0601013.

[78] M. Arneodo and M. Diehl, hep-ph/0511047 (2005).

[79] S. Chekanov *et al.* [ZEUS Collaboration], Nucl. Phys. B **658** (2003) 3.

[80] A. B. Kaidalov *et al.*, Eur. Phys. J. C **21** (2001) 52152.

[81] B. E. Cox and J. R. Forshaw, Comput. Phys. Commun. **144** (2002) 104.

[82] G. L. Bayatian *et al.* [CMS Collaboration], J. Phys. G **34** (2007) 995.

[83] "OSCAR: CMS Simulation Package", `http://cmsdoc.cern.ch/oscar`

[84] "ORCA: CMS Reconstruction Package", `http://cmsdoc.cern.ch/orca`

[85] V. A. Khoze, A. D. Martin and M. G. Ryskin, Phys. Lett. B **643** (2006) 93.

[86] M. Boonekamp and T. Kucs, Comput. Phys. Commun. **167** (2005) 217.

[87] CMS Collab., D. Acosta *et al.*, "CMS Physics TDR Volume 1, Section 2.6: Fast simulation", p. 55, CERN/LHCC 2006-001 (2006).

[88] C. Adloff *et al.* [H1 Collaboration], Z. Phys. C **76** (1997) 613.

[89] E. Accomando *et al.*, arXiv:hep-ph/0608079.

[90] M. Carena, J. Ellis, A. Pilaftsis and C.E.M. Wagner, Phys. Lett. **B495** (2000) 155; Nucl. Phys. B **586** (2000) 92.

[91] J. M. Maldacena, Adv. Theor. Math. Phys. **2** (1998) 231 [Int. J. Theor. Phys. **38** (1998) 1113]; E. Witten, Adv. Theor. Math. Phys. **2** (1998) 505.

[92] H. Liu, J. Phys. G **34** (2007) S361.

[93] R. C. Brower, M. J. Strassler and C. I. Tan, arXiv:0710.4378 [hep-th].

[94] A.R.White, Phys. Rev. **D72** (2005) 036007.

[95] A.R.White, hep-ph/0611262 and references therein.

[96] J. Monk and A. Pilkington, Comput. Phys. Commun. **175** (2006) 232.

[97] V. A. Khoze, M. G. Ryskin and W. J. Stirling, Eur. Phys. J. C **48** (2006) 797.

[98] A. Aktas *et al.*, [H1 Collaboration], Eur. Phys. J. C **48** (2006) 715.

[99] V. A. Khoze, A. D. Martin and M. G. Ryskin, Phys. Lett. B **650** (2007) 41.

[100] HERWIG 6.5: G. Corcella *et al.*, JHEP **0101** (2001) 010.

[101] J. M. Butterworth, J. R. Forshaw and M. H. Seymour, Zeit. für Phys. **C72** (1996) 637.

[102] S.N. White *et al.* [ATLAS Collaboration], CERN-LHCC-2007-001.

[103] X. Aslanoglou *et al.*, Eur. Phys. J. C **52** (2007) 495.

[104] O. A. Grachov *et al.* [CMS Collaboration], AIP Conf. Proc. **867** (2006) 258.

[105] V. A. Khoze, A. D. Martin and M. G. Ryskin, Eur. Phys. J. C **48** (2006) 467.

[106] R. Field [CDF Run II Collaboration], "CDF run II Monte-Carlo tunes", FERMILAB-PUB-06-408-E.

[107] PYTHIA 6.2: T. Sjostrand, L. Lonnblad and S. Mrenna, arXiv:hep-ph/0108264.

[108] A.Shuvaev, V.A.Khoze, A.D.Martin and M.G.Ryskin, in preparation.

[109] R. Engel and J. Ranft, Phys. Rev. **D54** (1996) 4244.

[110] P.J. Bussey and W. Plano, FPTrack, in preparation.

[111] I. Agapov, J. Carter, G. A. Blair and O. Dadoun, "BDSIM: Beamline simulation toolkit based on GEANT4", EuroTeV Report 2006-035.

[112] I.Azhgirey and V.Talanov, "The status of MARS program complex." in Proceeds. XVIII Workshop on the charged particles accelerators, Protvino, 2000, Vol. 2, p. 184.

[113] Minutes of the CERN Machine Induced Background Working Group, 14-Dec-2007, `http://indico.cern.ch/conferenceDisplay.py?confId=24799`.

[114] A.Rossi, "Residual Gas Density Estimations in the LHC Insertion Regions IR1 and IR5 and the Experimental Regions of ATLAS and CMS for Different Beam Operations", CERN-LHC-Project-Report-783 (2004).

[115] "Vacuum System, LHC Design Report, Vol. 1, Chapter 12", CERN-2004-003, CERN, Geneva, Switzerland (2004).

[116] "Beam Cleaning and Collimation System, LHC Design Report, Vol. 1, Chapter 18", CERN-2004-003, CERN, Geneva, Switzerland (2004).

[117] LHC collimation homepage, `http://lhc-collimation-project.web.cern.ch/`.

[118] G. Robert-Demolaize, “Design and Performance Optimization of the LHC Collimation System", LHC Project Note 981, CERN, Geneva, Switzerland (2006).

[119] I.Baishev, CERN LHC Project note 407, 2007.

[120] GEANT4: S. Agostinelli *et al.*, Nucl. Instrum. Meth. A 506 (2003) 250.

[121] S. Roesler, R. Engel and J. Ranft, arXiv:hep-ph/0012252.

[122] MADX homepage, `http://mad.web.cern.ch/mad/`.

[123] “LHC Design Report Vol. 1”, CERN-2004-003, CERN, Geneva, Switzerland (2004).

[124] T. Columbet, “Cryogenics preliminary calculation for the FP420 cryostat”, `https://edms.cern.ch/document/827775`.

[125] S. Pattalwar *et al.* “A New Connection Cryostat to insert FP420 Proton Tagging Detectors in the LHC Ring”, Proceeds APAC (2007) 103.

[126] R. Folch, “FP420 Cryostat Modules Workpackage”, `https://edms.cern.ch/document/823322`.

[127] K. Piotrzkowski and U. Schneekloth, ZEUS collab. meeting, march 1994, DESY, Hamburg.

[128] S. Chekanov *et al.* [ZEUS collaboration], Eur. Phys. J. C **26** (2003) 389; and Eur. Phys. J. C **11** (1999) 35; A. Aktas *et al.* [H1 collaboration] Phys. Lett. B **638** (2006) 422.

[129] Centre de Recherche du Cyclotron (CRC), UC Louvain, `http://www.cyc.ucl.ac.be/`

[130] V. Berardi *et al.* [TOTEM Collaboration], TOTEM TDR, CERN-LHC-2004-002, Jan 2004.

[131] A. Mapelli *et al.*, in 10th ICATPP Conference, ATL-COM-LUM-2007-008, ATL-LUM-PUB-2007-006.

[132] O. Aberle *et al.*, EPAC-2004-MOPLT008, Jul. 2004; R. Losito, A. Masi, RT2007-CM-EXIST04, Apr 2007; R.W. Assmann *et al.*, PAC07-MOPAN081, Jun 2007.

[133] A. Guerrero *et al.*,“CERN front-end software architecture for accelerator controls,” (ICALEPCS 2003), Korea, Oct 2003. in Gyeongju 2003, Accelerator and large experimental physics control systems, p. 342.

[134] D. Brandt and L. Vos, “Resistive wall instability for the LHC: intermediate review”, LHC-PROJECT-NOTE-257, CERN, Geneva, Switzerland (2001).

[135] D. Brandt, and L. Vos, Resistive Wall PAC, CERN.

[136] F. Caspers, “Impedance determination”, Handbook of Accelerator Physics and Engineering, World Scientific (1999).

[137] V. G. Vaccaro, “Coupling Impedance Measurements”, INFN/TC-94/023 (1994).

[138] Ansoft Corporation, URL: `http://www.ansoft.com/`

[139] Computer Simulation Technology, URL: `http://www.cst.com/`

[140] GdfidL Electromagnetic Field simulator, URL: `http://www.gdfidl.de/`

[141] F. Roncarolo, R. Appleby and R. M. Jones, “Beam Coupling Impedance Simulations and Measurements for the LHC FP420 Detector”, Proceeds 22nd Particle Accelerator Conference,

Albuquerque, NM (2007).

[142] E. Metral, “Overview of Impedance and Single-Beam Instability Mechanisms”, CERN-AB-2005-041.

[143] S.I. Parker, C. J. Kenney, and J. Segal, Nucl. Instr. and Meth. **A395** (1997) 328.

[144] C. Kenney, S. Parker, J. Segal, and C. Storment, Proceeds. 9th Meeting of the Division of Particles and Fields of the APS, Minneapolis, MN, 11-15 Aug 1996, World Scientific, 1998, Vol. 2, p. 1342.

[145] C. Kenney, S. Parker, J. Segal, and C. Storment, IEEE Trans. Nucl. Sci. **46** (1999) 1224.

[146] C.J. Kenney *et al.*, IEEE Trans. Nucl. Sci, **48** (2001) 189.

[147] S.I. Parker and C. J. Kenney, IEEE Trans. Nucl. Sci., **48** (2001) 1629.

[148] C.J. Kenney, S. I. Parker, and E. Walckiers, IEEE Trans. Nucl. Sci, **48** (2001) 2405.

[149] C. Da Vià, CERN Courier, Vol. 43, Jan. 2003, p. 223.

[150] C. Da Vià *et al.*, Nucl. Instr. Meth. **A 509** (2003) 86.

[151] J. Morse *et al.*, Nucl. Instr. Meth. **A 524** (2004) 236.

[152] C. J. Kenney, J. D. Segal, E. Westbrook, S. Parker, J. Hasi, C. Da Via, S. Watts, J. Morse, Nucl. Instr. Meth. **A 565** (2006) 272.

[153] S. I. Parker *et al.*, IEEE Trans. Nucl. Sci, **53** (2006) 1676.

[154] C. Da Via *et al.*, to be submitted to IEEE Trans. Nucl. Sci.; and C. Da Via *et al.* presented at the 6th International Symposium on the Development and Application of Semiconductor Tracking Detectors, Carmel (USA), Sept. 11-15 2006.

[155] C. Da Via *et al.*, to be submitted to IEEE Trans. Nucl. Sci.

[156] C.DaVia, S.Parker, G.Darbo, ATL-P-MN-0022, `https://edms.cern.ch/document/828969/1`

[157] H.E. Larsen, FP420 Note 2008-001.

[158] T. Wijnands (CERN-TS), private communication (2007).

[159] ATLAS: Detector and physics performance technical design report. Vol. 1 and 2, CERN-LHCC-99-14/15, ATLAS-TDR-14/15, 1999.

[160] Picosecond Timing Workshop, University of Chicago, March 2008, `http://www.hep.anl.gov/ertley/tof/`.

[161] A. V. Akindov *et al.* [ALICE Collaboration], Nucl. Inst. Meth. Res. **A 533** (2004) 178.

[162] M. Akatsu *et al.*, Nucl. Inst. Meth. **A 528** (2004) 763; K. Inami *et al.*, Nucl. Inst. Meth. **A 560** (2006) 303.

[163] Burle `http://www.burle.com` and Photonis `http://www.photonis.com` merged in 2005.

[164] `http://www.hamamatsu.com`

[165] M.Artuso *et al.*, SUHEP-10-2005, arXiv:physics/0505110.

[166] N. Kishimoto *et al.*, Nucl. Inst. Meth. **A 564** (2006) 204.

[167] We thank S.Baron and Jan Troska for information and design work.

[168] S.N. White, arXiv:0707.1500 (hep-ph).

[169] Univ. Chicago, Argonne National Laboratory, and Saclay, in particular.

[170] C. Bovet *et al.*, CERN-SL-97-069-BI.

[171] E. Calvo *et al.*, "The LHC Orbit and Trajectory System", Proceeds. DIPAC 2003 – Mainz, Germany, p. 187.

[172] H. Grote *et al.*, Proceeds. Workshop on Beam-beam Effects at Fermilab, June 2001, CERN-LHC-Project-Report-502.

[173] M. Slater *et al.*, "Cavity BPM tests for the ILC energy spectrometer", SLAC-PUB-13031.

[174] S. Walston *et al.*, Nucl. Instrum. Meth. **A578** (2007) 1.

[175] W. Coosemans *et al.*, CERN-SL-2001-022-BI.

[176] `http://meas-spec.com/myMeas/MEAS_download/ApplicationNotes/Position/SchaevitzCernWP_0507.pdf`

[177] F.C. Iselin, J.M. Jowett, J. Pancin, A. Adelmann, MAD, CERN-SL-2000-026.

[178] A. Abulencia *et al.* [CDF Collaboration], Phys. Rev. Lett. **98** (2007) 112001

[179] A. Aaltonen *et al.* [CDF Collaboration], in preparation.

[180] J. Poole (ed.), "Beam Instrumentation" CERN Report 2004-05-13, `https://edms.cern.ch/file/445861/6/Vol_1_Chapter_13.pdf`

[181] M. Gallinaro and K. Goulianos, CDF Internal note 7877 (2006).

[182] M. Gallinaro, in Proceeds. XIV International Workshop on DIS2006, Tsukuba, Japan, 20-24 Apr. 2006, arXiv:hep-ex/0606024.